Piezoresistive MEMS sensor arrays for tactile
applications

by

Shichao Yue

A thesis submitted in partial fulfillment of the requirements for the degree of

Doctor of Philosophy

Department of Mechanical Engineering
University of Alberta

**Abstract**

As common human computer interfaces(HCIs), touchscreen panels (TSPs) have been ubiquitously adopted in our daily life especially in the consuming electronics, and numerous industrial applications. However, force information has been a missing part in conventional TSPs, drawing limitations in the gesture strategy and user experiences. This void has led to weaknesses such as complex gestures, multi-level menus, waiting, etc. To fill this gap, the objective of this thesis was to study the feasibility of building MEMS-based multi-axis force sensor arrays for tactile applications.

Firstly, this work investigated the feasibility of the MEMS-based tactile sensor array for sensing the normal tactile force. The structural configuration of the sensor array has been studied by the numerical models using the finite element method. The outputs are corelated with the distance between the location where the force is applied and the tactel (tactile cell). The geometric parameters have been examined for the behavior of the sensor array.

The sensor array for the normal force has been built in a $2 \times 2$ configuration. Tactels in the sensor array have been optimized and fabricated for this tactile application. The fabrication process flow has been introduced, including the challenges encountered in the development. The sensor array for the normal force has four tactile cells packaged inside. By applying a known normal force on the sensor array, the sensor array has been tested. The test results agreed with the trend of the numerical simulation data. The tactile force and its location were quantified by a lookup table based on a least square method. A 2-mm location resolution has been accomplished in the force range of 0.01 - 0.25 N. The prototype-of-concept shed light on reducing the number of tactile cells. Further numerical analysis demonstrated the scalability of the sensor array for larger-area applications with the same number of tactile cells.

Moreover, the tangential forces can be introduced as complementary input gestures. To enrich touchscreen functions, the multi-axis tactile sensor array with the unique layered structure has been developed, sensing both the multi-axis tactile force and its location. This prototype has a functional area of 60 mm ✕ 60 mm, packaged by only four tactels. The development of the multi-axis tactile sensor array has been addressed in this work including the design, fabrication, packaging, and tests. Qualitative and quantitative tests have been performed to study the responses of the tactile sensor array with the force range of 0.1 - 0.5 N. The results of the proposed sensor array demonstrated promising potentials for future tactile applications.

Generally, the MEMS development entails different phases including fundamental design, mask preparation, process flow, packaging and tests. To finalize the solution for one specific application, engineers must go through several iterations of the development, which is time-consuming and high-cost. To shorten the development time/cost and explore broader applications, tuning the sensitivity of concurrent devices is merited for accelerating the development progress. Since two types of tactels for the sensor arrays have been developed, the sensitivity tunability of these devices has been introduced in their packaging phase. The force ranges of the original tactels have been altered to be more than 10-folds and 3000-folds by packaging the assembly with PDMS and PU, respectively. The tuned force sensors with different force ranges can be used for physiological signal monitoring applications.

# Preface

The research work related to the feasibility study of the tactile sensor array which is included in part of Chapter 3 and Chapter 4 has been published in Shichao Yue, Walied A. Moussa, L. Richard Williston "Feasibility on a piezoresistive tactile normal force sensor array", *Applied Physics A*, vol. 116, pp. 409-414, 2014/08/01 2014. Shichao Yue was responsible for the simulation, data collection and analysis as well as the manuscript composition. Walied A. Moussa was the supervising author. L Richard Williston contributed in the manuscript revision.

The research work related to the prototype of the normal force sensor array which is included in part of Chapter 3, Chapter 4 and Chapter 5 has been published in Shichao Yue, Walied A. Moussa "A pizeoresistive tactile sensor array for touchscreen panels", *IEEE Sensors Journal*, Volume: 18, Issue: 4, Feb.15, 15 2018 (DOI: 10.1109/JSEN.2017.2776936). Shichao Yue was responsible for the simulation, design, fabrication, packaging and tests of the sensor array, data collection as well as the manuscript composition. Walied A. Moussa was the supervising author and contributed in the revision.

The research work related to the prototype of the multi-axis sensor array which is included in part of Chapter 3, Chapter 4 and Chapter 5 has been published in Shichao Yue, Yang Qiu, Walied A. Moussa "A multi-axis tactile sensor array for touchscreen applications", *Journal of Microelectromechanical Systems*, Issue: 99, 10 January 2018 (DOI: 10.1109/JMEMS.2017.2778572). Shichao Yue was responsible for the simulation, design, fabrication, packaging and tests of the sensor array, data collection and analysis as well as the manuscript composition. Yang Qiu contributed in part of the packaging and manuscript revision. Walied A. Moussa was the supervising author.

The research work related with tuning the sensitivity of the normal tactile sensor which is included in part of Chapter 6 has been accepted for the publication in Shichao Yue, Yang Qiu, Walied A. Moussa "Packaging Induced Range Tunability of Tactile Sensors for Physiological Signal Monitoring Applications" *IEEE Transactions on Components, Packaging, and Manufacturing Technology*, 2018(Accepted). Shichao Yue was responsible for the simulation, design, fabrication, packaging and tests of the sensor array, data collection and analysis as well as the manuscript composition. Yang Qiu contributed in part of the packaging and manuscript revision. Walied A. Moussa was the supervising author.

# Acknowledgement

# Table of Contents

## List of Figures

## List of Tables

## Nomenclature

| | |
|---|---|
| MEMS | Microelectromechanical system |
| HCI | Human Computer Interface |
| 3D | Three-dimensional |
| API | Application programming interface |
| TSV | Through silicon via |
| AOI | Area of interest |
| ADC | analog to digital converter |
| CCD | Charge-coupled device |
| IR | infrared |
| FEM | Finite Element Method |
| FVM | Finite Volume Method |
| PDMS | Polydimethylsiloxane |
| PCB | Printed Circuit Board |
| PCBoG | Printed Circuit Board on Glass |
| DRIE | Deep Reactive Ion Etching |
| BOE | Buffered Oxide Etching |
| SNR | Signal to Noise Ratio |
| N | Newton |
| mN | Millinewton |
| $w$ | lateral deflection |
| $\sigma_r$ | stress in the axial direction |
| $Q$ | impurity dopants dose |

# Chapter 1.  Introduction

## 1.1 Thesis objective

Hands are one of human body's most dexterous organs [1]. Humans use their hands to execute complex tasks, and due to their tactile and sensory nature, hands mediate how humans interact and experience their surroundings. Not only do our hands help us communicate directly with others, but our hands help us interact with the digital world. In fact, smart devices have been designed based on the tactile capacities of our hands. The touch screen, for example, is ubiquitous. Numerous portable devices, tablets, and other Human-Computer-Interfaces (HCIs) that we use on a daily basis rely on the human capacity to touch. The touch motion, or put another way, this tactile gesture, represents the manner in which the user send commands to the smart system. An intuitive tactile event requires the location of the contact point and the interfacial force[2], i.e. the tactile force. The inclusion of tactile force between a human finger or a stylus, and a touch screen, is absent from conventional HCI devices[3]. This void has led to compromises in the gesture strategy, caused longer waiting times, required multi-level menus and complex gestures from multiple fingers, for example. Based on the assumption of a Cartesian coordinate when the finger or stylus contacts the working area of a tactile panel[4], tactile force is typically three dimensional, and includes a normal force component, as well as two-dimensional shear force components. The measurement of the three-dimensional tactile force is relevant when considering three-dimensional (3D) gestures in touch screen panels. Through the proper measurement of tactile force, it is hoped that better user experiences and diverse software programs can be designed. The objective of this thesis is 1) to measure the tactile force generated by fingers on the touchscreen panels, 2) to develop a tactile sensor array of these measurements. Based on these findings, the thesis also aims to develop a multi-axis tactile sensor and its concomitant array.

## 1.2 Motivations

This project builds on previous research on the use of tactile force as input gestures for smart systems[5-7]. Portable digital devices are ubiquitous to modern daily life, and include functional touch screen panels as part of HCIs[5]. The physical contact between devices and humans functions as a reliable link between users and digital information. Introducing force sensation as the input gesture, moreover, can enhance the functionality of touch screen panels. By using force

information, software developers can invent new gestures to diversify the application programing interfaces (APIs) [8]. Quick access to specific menu levels can also be achieved by combining the force input with conventional input gestures already in use. Force sensibility can also be used as complementary interfaces where common capacitive projective touch screens are limited. Such instances include underwater operations, as well as medical, automobile, and other contexts where gloves are required.

### 1.2.1 Force as the gesture

Using force amplitude as a complementary gesture with concurrent input systems will allow for more convenient human-machine interactions. An intuitive touch event entails both information about the location of the touch as well as its force amplitude. Researchers have been working on adapting the shear force, or the normal force, to allow for specific manipulation tasks on modified touch screen panels. These researchers have done so by focusing on tasks initiated by force sensitive resistors[9, 10], deformable gel[8, 11], joy sticks, or piezoelectric film[12]. Certain cellphone manufactures have released models with the force sensitive function, although most touchscreen panels on these devices can only sense normal force (pressing force). These devices categorize pressing force as either light or heavy, and can activate new features such as the "peek and pop"[13].

### 1.2.2 Introduction of the tactile force measurement

The measurement of the tactile force must accommodate the requirements of the application scenery. The tactile force typically generated by human fingers ranges from several hundred newton to less than 0.1 N[14]. Nonetheless, applying various forces on a touchscreen panel frequently throughout the day can cause finger fatigue and contribute to wear on the stylus. Given the frequency in which touch screens are used, it is not practical to set the threshold at large force level. Inasmuch as commonly used conventional projective capacitive touchscreens require very little contact force, the device will not be activated when the screen is touched by alien conductive objects. This is therefore advantageous in terms of its capacitance merit [6, 15]. According to the literature, the tactile sensor array for touchscreen applications usually has a force range of 1 N, specifically between 0.1 newton to 0.3N[16, 17]. Previous research has shown that a tactile cell is designed as a square shape, with an edge length of 1mm to 2 mm[18], these measurements define the targeted spatial resolution of the tactile force sensor array.

## 1.3 Methodology

Inasmuch as the objective of the thesis is to record multi-axis force by using a tactile sensor array, the research employs a methodology wherein the multi-axis tactile sensor is investigated as to its suitable sensitivity. The same tactile sensor array implement is used throughout these experiments in order to characterize and validate the functionality of multi-axis tactile force.
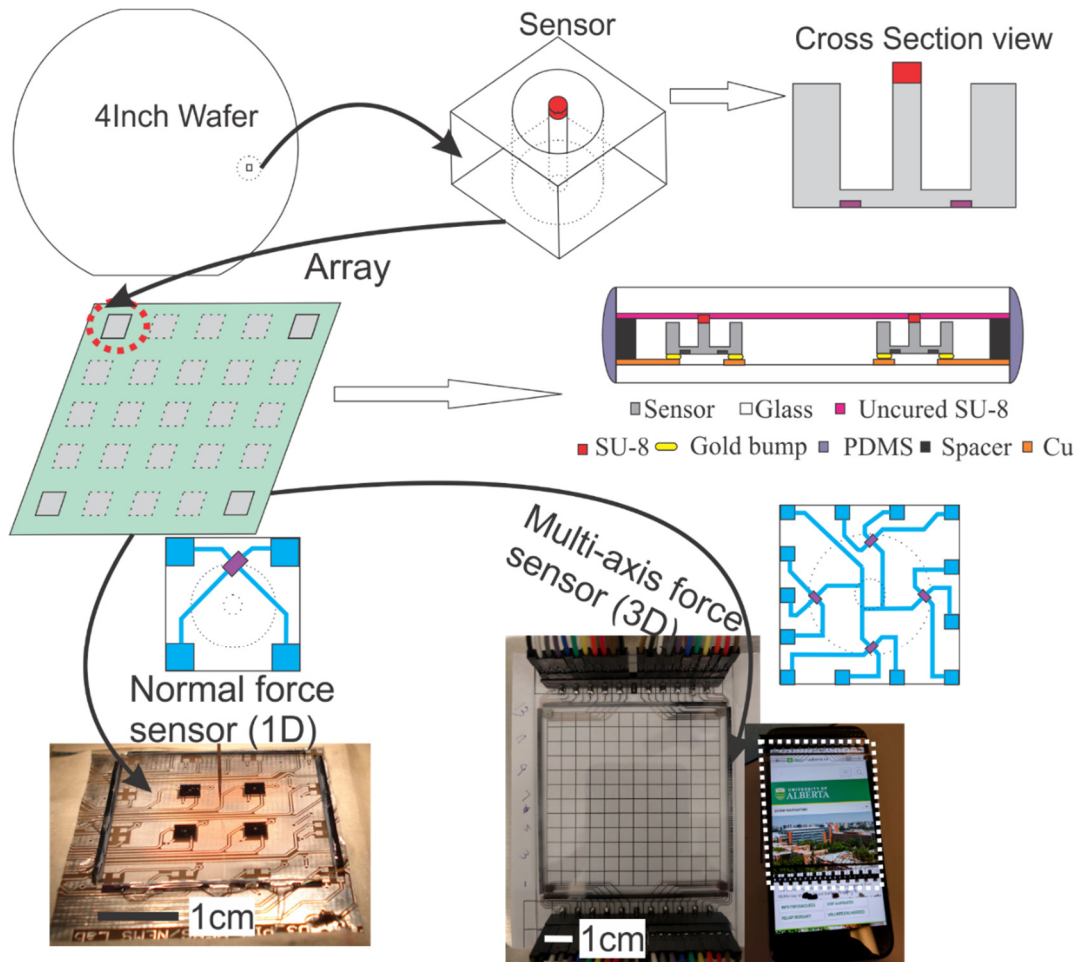


Figure 1-1 Overview of the methodology roadmap

### 1.3.1 Multi-axis force sensor

Measuring multi-axis force can be accomplished by using force sensors employing various materials. These include, piezoresistive material[19, 20], piezoelectric film[21], infrared light[22], capacitance changing[23], optical fibers[24], and various others. The range of force measurement ability can be altered by changing the geometry of sensor design[25], or by different packaging solutions[26]. To comply with the requirements for sensing sub-newton level of forces in a compact size, the piezoresistive MEMS force sensor was determined to be the tactile cell that

would form the sensor array. Its advantages include its miniature and intrinsic design, simple conditioning circuits, low power consumption, and its advanced fabrication standards.

### 1.3.2   Sensor array configuration

For most conventional touch screen panels and tactile sensor arrays, the digitization of an area of interest (AOI) is usually accomplished using a straightforward configuration. This is possible because the area in question is covered by numerous tactile cells or electrodes[27] that sense changes of resistance or capacitance from the stimuli of tactile events[18, 28-31].   However, because the experimental application involves a larger working area, the number of tactile cells and/or electrodes will increase dramatically. This results in more complex peripheral electronic circuits and signal processing procedures. For example, more ADCs (analog-to-digital converters), high frequency multiplex switches, and high sampling rates/bandwidths will be required. As such, this research uses four tactile sensors to form a multi-axis sensor array with a proven scalability of the working area that can sense multi-axis forces. It does so with the objective of determining the tactile location in a manner that reduces the number of signal channels.

### 1.3.3   Sensor array calibration

The calibration of digitized tactile sensor arrays is commonly accomplished by characterizing the performance of each individual tactile cell, the results of which are used to form a lookup table[17]. During the application deployment, the output from each cell being tested is compared with its corresponding value in the lookup table; it is then plotted in greyscale or colour into a figure mapping the entire area [30, 32]. This approach is employed in the research reported in this thesis. Although the tactile sensor array in question is made up of four physical tactile cells, the rest of the central area comprises virtual tactile cells. This allows the four tactile cells to sense locational and behavioral changes at every point of the area. Employing this approach, a similar lookup table can be built that maps the sensitivity signature of each characterized tactel. By searching the lookup table, the location and force amplitude of the tactile event can be solved. Drawbacks to this approach include that it uses a one-point multi-axis force measurement, in which shear force response comes from the glass film cover that only moves in a rigid and horizontal direction.

## 1.4 Thesis organization

The following chapters describe the development of the tactile sensor array as per the above-mentioned objectives and methodology. Chapter 2 reviews literature related to the core aspects of the thesis objectives, including the piezoresistive sensing element, tactile force measurements, TSV or TSV-less packaging, and the structural analytical model of the tactel. Chapter 3 describes the simulations performed on the tactile cell and tactile sensor array in order to parametrically study its geometric influences. Chapter 4 discusses the fabrication procedures including the mask design, challenges faced when manufacturing the devices, and how the sensor array was packaged according to the micron-level coplanarity required to form a functional array. Chapter 5 discusses the characterization of both the individual tactile cell and the packaged sensor array, as well as explains the tests undertaken to evaluate the functionality of the sensor array. Chapter 6 outlines a methodology for tuning the measurement range of the tactile sensor through modifications to the packaging procedure, that would broaden its applicability. Chapter 7 provides an overview of this research, its contributions, and offers directions for future research.

# Chapter 2. Literature review

*On looking back over the history of science one realizes that most of us can only hope to place one small brick 一if that 一in the edifice 一and even that may get knocked out by following generations.* [33]

**Albert Edward Green** *(1912-1999)*

## 2.1 Multi-axis force sensor in tactile applications

A large amount of engineering research has focused on questions of force measurement. Unmodified commercially available load cells have been used widely to measure one-axis or multi-axis forces or torques in multi-directions. The tactile force involves contact between at least two objects such as human fingers or robotic actuators, and the surface that is contacted. The contact generates interfacial forces, including the normal force, shear force (friction), and moments or torques. To measure the amplitude of the contact force, multi-axis force sensors are often used to quantify the interactions between these objects.

Research on tactile sensors has been occurring for multiple decades and grew concurrent with that on dexterous robotics. Harmon [34] has surveyed academic researchers and industrial manufacturers to determine their tactile sensing requirements and the potential implications of their work. Harmon found that ideally transducers should have a low mass, be small in size, easy to use, cosmetically attractive, and not hinder regular movement patterns. Desired sensor performances were found to have a spatial resolution of 2 - 3 mm, a load range of 0.1 to 100 N, a response time of 0.1 to 10 ms, in addition to having a low hysteresis, being compliant, and being robustly packaged.

Research on tactile sensors has not been limited to robotics[1, 28, 35], but has investigated for its application for biomedical engineering[14, 36], minimally invasive surgery[37, 38], human computer interfaces (HCIs)[16], and artificial skin[39, 40]. Abundant applications such as finger mounted force devices[23, 41, 42], palmer mounted devices[43], cellular force measurement[44], and biomaterial characterization[45], use multi-axis tactile sensors.

Tactile sensors are developed according to various mechanisms meant to accommodate specific applications. The compact footprint is a core consideration for HCIs. Fundamentals for developing multi-axis tactile sensors have been outlined. Theories on sensing vary according to structure and material, but can include those on piezoresistors[19], capacitive elements[46],

piezoelectric materials[47], optical fibers[24], optical modules[48], and inductors[49]. Piezoelectric sensors are usually inadequate in detecting static force[50]. Optical force sensors are usually bulky because of their CCD cameras[51], or because other optical materials used for analysis  are connected by optical fibers. As such, the most commonly employed fundamentals are based on piezoresistive or capacitive sensing elements.

Piezoresistive elements or piezoresistors work based on a change in resistance of materials. Materials can include metal strain gauges[52-54], doped silicon, doped polysilicon[55], carbon nanotube adhesive[56, 57], coated nanowire, resistive microfluidic channels[58], and others. Metal strain gauges are usually mounted in groups onto optimized metal structures that allow for the detection of multi-axis force [59]. The force range of this type of sensor can be as large as a few hundred newtons or more. Other types of strain gauges can be etched using a thin metal film directly on the sensor structure, this process allows for the miniaturization of the sensor footprint [60, 61].The doped single crystal silicon is another piezoresistor material commonly used in the manufacturing of multi-axis force sensors. These piezoresistors are can formed using a thermal diffusion process at a high temperature. Single crystal silicon piezoresistors can also be made by implanting the ion into a silicon membrane or cantilever. This then works as a resistor in the Wheatstone bridge[20, 25, 62-64], as a four-terminal gauge [65], or as a combination of both [66]. Overall this provides the capacity for the device to sense multi-axis force. The Wheatstone bridge and the four-terminal gauge will be further discussed in section 2.2.

Multi-axis force sensors have also been developed based on change in capacitance. The strain or displacement induced by a force changes the distance (or area) between two electrodes in the capacitor. The electrodes are constructed by creating a comb drive using silicon [44, 45, 67] or a metal coated membrane [68]. Electrodes can also be formed by using metal ribbon as the electrode material; copper has been used for such a purpose[14]. Multiple capacitors are designed to allow for multi-axial detections[23, 42, 69].

The force range and the die size of multi-axis sensors are highly dependent on the specific applications for which the device will be deployed. Previous research has found that forming devices using a metal strain that is mounted on structures produces a larger force span that can be hundreds to thousands newton levels higher[52-54]. These sensors are usually larger than 10 mm, or can be a few centimeters in size. MEMS-based silicon sensors, however, can be delicate and highly sensitive to forces at the  millinewton [25, 64] or nano-newton level [44]. MEMS-based

sensors can also be made to be very small, including those at the millimeter level[68] or even micrometer level[65]. MEMS-based approaches are then chosen in research requiring footprint compactness and good sensitivity at a sub-newton force range. The typical force range for tactile sensor array applications will be discussed in section 2.3.

The geometric structure of multi-axis sensors varies according to changes in capacitance and resistance. The geometric structure can be categorized as comb-drive based[44], membrane based[68], and beam based[59]. The comb-drive based device is often made by using several directional comb-drives on one die[44]. A probe is then added or fabricated for when force is applied, which then triggers displacement changes between interdigital electrodes. Due to the planar feature of comb-drive based sensors, they are usually fragile, sensitive, and have a larger in footprint size. Membrane based multi-axis force sensors measure the normal load by the lateral deformation. The transversal load is commonly applied to the membrane by a boss or mesa placed on either the front or back of the membrane. This creates a differential stress distribution in the membrane, or different gap distances between the membrane electrodes and the fixed[70]. Location, size, and the number of mesa applied can be optimized to meet specific sensitivity requirements when designing multi-axis sensors[25, 64].

In summary, the development of a multi-axis tactile sensor is highly application-oriented. As such, the force range varies and can be customized for the application in question. As well, the sensor die size can be miniaturized to the millimeter or micrometer level by changing common fundamentals such as piezoresistance or capacitance.

## 2.2 A Piezoresistive element: the four-terminal gauge

This section provides a review of the literature pertaining to the piezoresistivity of silicon, the four-terminal gauge, differences between work modes, and the state of the field as to its design parameters.

### 2.2.1 Piezoresistivity of silicon

Piezoresistivity is present in engineering materials that exhibit a change in resistivity when mechanical stress is applied. This phenomenon is significant in crystalline silicon, where the gauge factor related to a change in the resistance following the application of strain is 100 times greater than common metal piezoresistive strain gauges[71]. The piezoresitivity of a single crystal silicon and germanium has been investigated following their discovery by Smith in 1954[72]. The

temperature dependency of the piezoresistive coefficients of silicon and germanium has been studied by Tufte and Stelzer *et. al.* [73]. The authors then studied the unique behavior of the shear piezoresistance coefficient ($\pi_{44}$) of n-Si, with respect to its doping concentration[74]. An analytical and graphical representation of the piezoresistive coefficients was then presented[75, 76]. Following that, the unique behavior of the shear piezoresistance coefficient ($\pi_{44}$) of n-Si was described [77]. The fundamental of carrier-transfer mechanism explains the piezoresistance effects of n-type and p-type silicon, as well as its change in mass. Graphic explanations of the piezoresistance coefficients of doped silicon have been provided[75, 78]. Because piezoresistors are well understood and easy to deploy, these devices have been used in applications including force sensors[64], stress sensors[79, 80], and inertial sensors[81, 82].

### 2.2.2 The four-terminal gauge

The four-terminal gauge, a pseudo-hall effect sensing element, was introduced in 1976[78]. Kanda *et. al.* have described the device using numerical models[83], and discussed its optimal design parameters [84]. Bao *et. al.* derived an analytical model of the four-terminal gauge for the pressure sensor, and introduced several optimal design rules[85, 86]. Gridchin *et. al.* compared the sensitivity of the four-terminal gauge to the common bridge circuit. Both were found to be quite similar, and the authors concluded that the four-terminal gauge was advantageous due to its smaller geometric size, and fewer points of electrical contacts[87, 88]. Doelle *et. al.* studied the optimal design rules that were based on the Finite Volume Method (FVM), and introduced a nonconductive island into the center of the four-terminal gauge, which resulted in its improved sensitivity[79]. The four-terminal gauge has also been investigated as a three-terminal gauge when it works in current mode. When the four-terminal gauge (which can be considered as a full Wheatstone bridge), is compared to the three-terminal gauge, it can be considered as a half-bridge circuit[89]. Additionally, multi-terminal gauges based on the shear piezoresistance coefficient have been designed; these allow for higher sensitivity and a more agile performance[90, 91]. For instance, an ultra-miniaturized piesoresistvie sensor was developed for intra-cranial pressure monitoring[92].Benfield *et. al.* used the four-terminal gauge to develop a series of force sensor for biomedical applications[93-96].

The objectives of the research herein reported are to measure the normal force and multi-axis forces using two proof-of-concept prototypes. To do so, normal force sensors and multi-axis force sensors were implemented and contained either one sensing element or four sensing elements on

the deformable membranes, respectively. The details of which will be further addressed in Chapter 3.

### 2.2.3 Temperature compensation of piezoresistive sensor

Although piezoresistive devices have merits such as miniaturization, simple circuits, and mature fabrication, their performances can be dependent on temperature. The main reason for such dependence is because that the piezoresistance coefficients has been found to be inversely proportional to temperature changing[76, 77]. The dependence can alter the performance of piezoresistive devices such as sensitivity and offset. Without the temperature compensation, consequently, this will compromise the applications where the sensors are deployed. Commonly used techniques for doing such corrections includes self-temperature compensation[97, 98], span compensation using added piezoresistive thermistors[99]. Other techniques involves advanced algorithms such as Artificial Neural Networks[100] (ANN), Machine Learning[101]. Peripheral electronics solutions can also be used for temperature compensations, including analog circuits[82, 102] and digital IC circuits[103].

## 2.3 Tactile sensor array and tactile panels

This section contains the state-of-art tactile sensor arrays and touch screen panels, including the flexible or rigid sensor arrays.

Using a tactile panel as the user interface/HCI is one of the commercialized applications of various types of tactile sensors. Tactile sensors are devices that sense information such as texture, shape, temperature, softness, vibration, normal and shear force by physical contact[14]. The reviews of Harmon *et. al.*[34] and of Nicholls *et. al.*[2, 104] introduced diverse types of tactile sensors, involving fields such as robotics, medical system, food processing, fingers, grippers, probes and whiskers, as well as haptic perception. The practical concept of the tactile panel as a user interface was first built in 1967 for an automatic data-processing system to assist control operations [105]. Given the convenience of tablets, cellphone, trackpads of laptops the tactile panel has become prevalent in daily life as a part of human-computer interfaces (HCIs). For the sensing fundamentals, a variety of principles have also been employed for implementing tactile panels, such as the resistive[106, 107], capacitive[6, 108], infrared[109], surface acoustic wave[110], electromagnetic[111], near field imaging[112], piezoelectric[12]. The resistive tactile panel has been produced by numerous manufactures and widely used in consumer electronics,

industrial HCIs, and automobiles. This conventional resistive touch panel consists of one or two resistive layers separated by a spacer layer[5]. The force from a finger or stylus causes contact between layers, leading to resistance changes, transferring the position information to a voltage drop signal through the conditioning circuit [107]. However, due to the working principle, it is commonly limited by the single point touch detection [113]. The capacitive tactile panel works based on the capacitance changes between electrodes[27]. To introduce the capacitance changes, capacitive tactile panels can be categorized into several groups according to sensing methods, such as the surface capacitive[114, 115], projected capacitive or mutual capacitive[116, 117] and self-capacitive[118, 119]. Tactile panels for multi-point detection, based on projected capacitance have been released by Apple Inc. since 2007 and emerged quickly in the consuming electronic market. However, the capacitive tactile panel was limited to using bare fingers or the conductive stylus, and the surface of the tactile panel was compromised by water, and contamination. Infrared (IR) technology has been used for the tactile panel since the PLATO Computer Aided Learning project[120], which detected the interruption of the IR light beam by fingers between the light emitter and receiver. Hlady *et. al.* introduced a tactile panel based on a surface acoustic wave[121], which achieved high resolution but was limited by its sensitivity to irregularities such as scratches or contaminants on the sensing surface. Piezoelectric touch panels utilize piezoelectric materials in devices that can detect dynamic contact motion[3, 122] but cannot sense static forces. Similar devices utilizing triboelectric mechanism for tactile application[50, 123, 124], are also limited by dynamic force. Tactile sensor array that imitate the flexibility of human skin, soft, stretchable have also been introduced[32]. Self-destructive tactile sensor array has also been built for time-critical applications. Notably, most of the tactile sensor arrays have digitized the AOI with groups of tactile cells (tactel). These have many signal channels, which is useful if needed for larger applications while maintaining reasonable spatial tactile resolution. In this way, the embodiment of the sensor array should reduce the number of tactels needed.

Prior research on tactile panels for sensing both the applied force and the location have been limited to either the normal force component[16] or the shear force component[8], and few have included multi-axis force design in one system. Utilizing forces such as gestures for input devices drawn attention and many prompts have been implemented using force sensitive resistors[125], capacitors[114], deformable gels[11], piezoelectric films[3], frequency tags, or even bulky joy sticks. Kim *et. al.* demonstrated a polymer-based sensor array with the resistance variation rate at

2%/N[18]. However, the force can only be applied on the mesa, leaving a blind area between mesas where the tactile information of the applied force cannot be interpolated. Huang *et. al.* introduced a transparent force sensing array using the liquid crystal which can detect tactile force up to 360mN. However, the resolution of the location depended on the cell size and was limited by the different power requirements for each cell[17]. Hong-Ki Kim *et. al.* introduced a transparent and flexible tactile sensor array that can capture the touch force of fingers or objects, but the resolution was still limited by the size of the sensor cell[16]. The development of the tactile panel based on piezoresistive force sensors is meaningful and will fill in this gap, in terms of limitations on multi-axis force detection of tactile force measurement. Therefore, to capture the normal force and the shear force on the user interface, this work to embody the tactile panel within the multi-axis force sensor array.

## 2.4 TSV and force sensor packaging

Through-Silicon-Via is a technique which enables silicon chips to be connected electrically with peripheral electronics while the functional surface remains exposed to interactions by extending conductive traces or pads to the other side of chips using vials filled with conductive materials such as the metal[126, 127], doped polysilicon, or other conductive materials[128, 129]. TSV techniques have been widely practiced for the IC industry[130]. Approaches to filling approaches those materials can vary due to their physical or chemical characteristics, including electroplating[131], vacuum suction[132], pressure assisted[133], printing. These approaches are are usually tedious, time intensive, or messy in terms of cleaning up. Besides, the etching process to penetrate through the thickness of wafers can be costly due to tight pitch, vertical side wall requirements, or wafer materials. Therefore, eliminating the TSV procedure would be beneficial for system integration[134]. From the perspective of the tactile panel application, the sensor design is more compact without need for TSV, and the fabrication process is shortened by achieving the membrane and structural mesa with one DRIE etching process, instead of two[135].

## 2.5 Plate theory with boundary conditions

This section reviews conceptual models of a circular plate with the edge clamped and a rectangular plate simply supported or with four clamped edges (clamped-clamped-clamped-clamped, CCCC).

### 2.5.1 Circular plate with clamped edge

Since both the normal tactile sensor and the multi-axis tactile sensor are chosen to be membrane-based force sensors, literature on models of a circular plate subjected to a concentrated load in the center should be reviewed. Assuming the diameter of the circular plate is $a$ with the edge clamped, carrying a concentrated load $P$ in the center, the deflection of the plate at a distance $r$ is governed by the following equation [136]:

$$w = \frac{P}{16\pi D}\left[\frac{3+\gamma}{1+\gamma}(a^2 - r^2) + 2r^2 \log\frac{r}{a}\right]. \tag{2-1}$$

Using Hooke's law to express stress distribution:

$$\sigma_r = \frac{E}{1-v^2}(\varepsilon_r + v\varepsilon_\theta) = -\frac{Ez}{1-v^2}\left(\frac{d^2w}{dr^2} + \frac{v}{r}\frac{dw}{dr}\right) \tag{2-2}$$

$$\sigma_\theta = \frac{E}{1-v^2}(\varepsilon_\theta + v\varepsilon_r) = -\frac{Ez}{1-v^2}\left(v\frac{d^2w}{dr^2} + \frac{1}{r}\frac{dw}{dr}\right). \tag{2-3}$$

Since the sensor structure is formed by a membrane with a stand-alone mesa at the center, this geometry could be abstracted with a built-in circular membrane subjected to concentrated lateral force on the base in the center before being ruggedized with polymer in the void (see Figure 2-1) and could be written in equation(2-4)[136]:
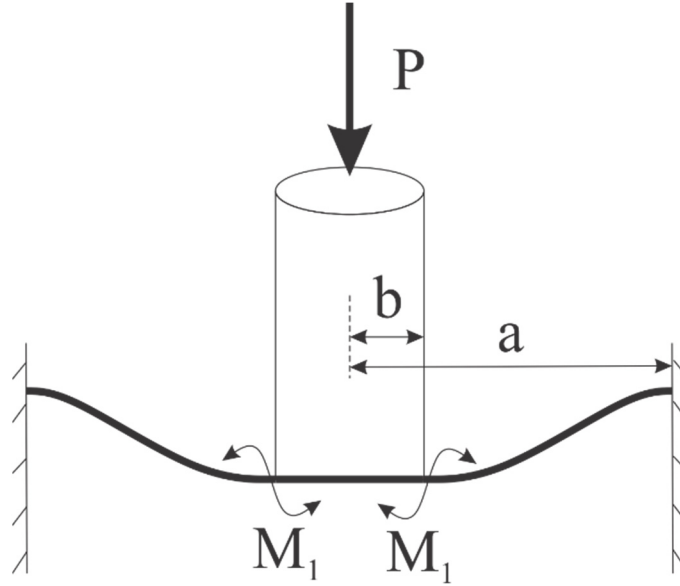


Figure 2-1 Model of the tactile sensor

$$M_1 = \frac{P}{4\pi\left[(1+v)\frac{a^2}{b^2}+1-v\right]}\left[(1-v)\left(\frac{a^2}{b^2}-1\right) + 2(1+v)\frac{a^2}{b^2}\log\frac{a}{b}\right], \tag{2-4}$$

where $M_l$ stands for the moment, $P$ stands for the concentrated lateral load, $a$ stands for radius of the membrane, and $b$ stands for the radius of the cylinder boss, which is the mesa here. The maximum stress and deflection can be expressed empirically as (2-5) and (2-6)[136]:

$$\sigma_{max} = \frac{kP}{h^2} \tag{2-5}$$

$$w_{max} = k_1 \frac{Pa^2}{Eh^3}, \tag{2-6}$$

where $k = 0.993$ and $k_l = 0.092$ are empirical index, $h$ stands for the thickness of membrane.

### 2.5.2 Rectangular plate

For a simply supported plate under pressure, $P_0$, the deflection at any point $(x, y)$ on the plate is governed by the following equation[136]:

$$w = \frac{4P_0 b^3}{\pi^4 aD} \sum_{m=1}^{\infty} S_m \sin\frac{m\pi\xi}{a}. \tag{2-7}$$

Where $S_m = \sum_{n=1}^{\infty} \frac{\sin\frac{n\pi\eta}{b}\sin\frac{n\pi y}{b}}{\left(\frac{m^2 b^2}{a^2}+n^2\right)^2}$, $\xi$ and $\eta$ are location of the load, $a$ and $b$ are the width and length of the plate. $D$ is the flexural rigidity of the diaphragm:$D = \frac{Eh^3}{12(1-v^2)}$.

## 2.6 Tactile sensor calibration and tests

This work requires two calibrations, for the individual tactile sensor and the sensor array, respectively. The methodologies on the calibration of multi-axis force sensor and sensor array are reviewed in this section.

### 2.6.1 Force sensor calibration

The main purpose of calibration is to obtain a functional relation between the input force and output voltage of the multi-axis force sensor. Based on Wheatstone bridge for multi-axis force sensor, given the vector of sensor piezoresistors *fractional change in resistance*$\Delta R/R$, and the corresponding loading vector, $F$ in $N$, the linear transformation matrix $K$ between them,

$$F = K\frac{\Delta R}{R}, \tag{2-5}$$

can be determined by evaluating the Moore-Penrose least-square error solution to over-determined set of equations[70]. The experimental sensitivity matrix $S_E$ is the pseudoinverse of matrices $K$, which is calculated by fitting with the Least-Square Method. Similarly, by writing the equation using voltage outputs from several sensing elements of the multi-axis sensor and by

applying directional force along *x, y, z* axis respectively, the force and voltages relation can be written as:

$$\begin{pmatrix} F_x \\ F_y \\ F_z \end{pmatrix} = \begin{pmatrix} k_{11}V_{11} + k_{12}V_{12} + k_{13}V_{13} + k_{14}V_{14} \\ k_{21}V_{21} + k_{22}V_{22} + k_{23}V_{23} + k_{24}V_{24} \\ k_{31}V_{31} + k_{32}V_{32} + k_{33}V_{33} + k_{34}V_{34} \end{pmatrix} \qquad (2\text{-}6)$$

### 2.6.2 Tactile sensor array characterization

Tactile sensor arrays are usually characterized in their group form. For a digitized sensor array, a common approach for characterization is to calibrate each tactile cell is to determine the sensitivity table for cells within the array[31]. In the realistic application, since the working area has been divided into pieces or pixels according to the territory taken by each tactile cell, forces are calculated based on this table after acquiring sensor outputs with the location intrinsically known by the existence of signal. However, this approach dramatically increases the signal channels as the sensing area increases. To map the working area for performance evaluation, a color scale plane plot is commonly employed. In other words, each cell is depicted as a square pixel with the force amplitude shown by the color bar. The proposed work would refer to this method to plot the tactile event trajectory.

# Chapter 3. Sensitivity analysis on the sensor and sensor array[1]

*"...premature optimization is the root of all evil..."* – **Donald Knuth**

## 3.1 Uniaxial (Normal) force sensor geometry

The normal force (one dimensional force, uniaxial force) sensor is designed as a piece of square-shape silicon chip, consisted of a membrane-boss structure. The structure of the sensor is shown in Figure 3-1. At the edge of the circular membrane, a four-terminal gauge as the sensing element is analyzed for the optimal performance. To apply a force at the center of the membrane, a cylindrical pillar which is named as the mesa, stands at backside of the membrane. At top of the membrane, a structure called flow-stopper is added for preventing adhesives from overflowing on the membrane and degrading sensor performances in the packaging procedure.
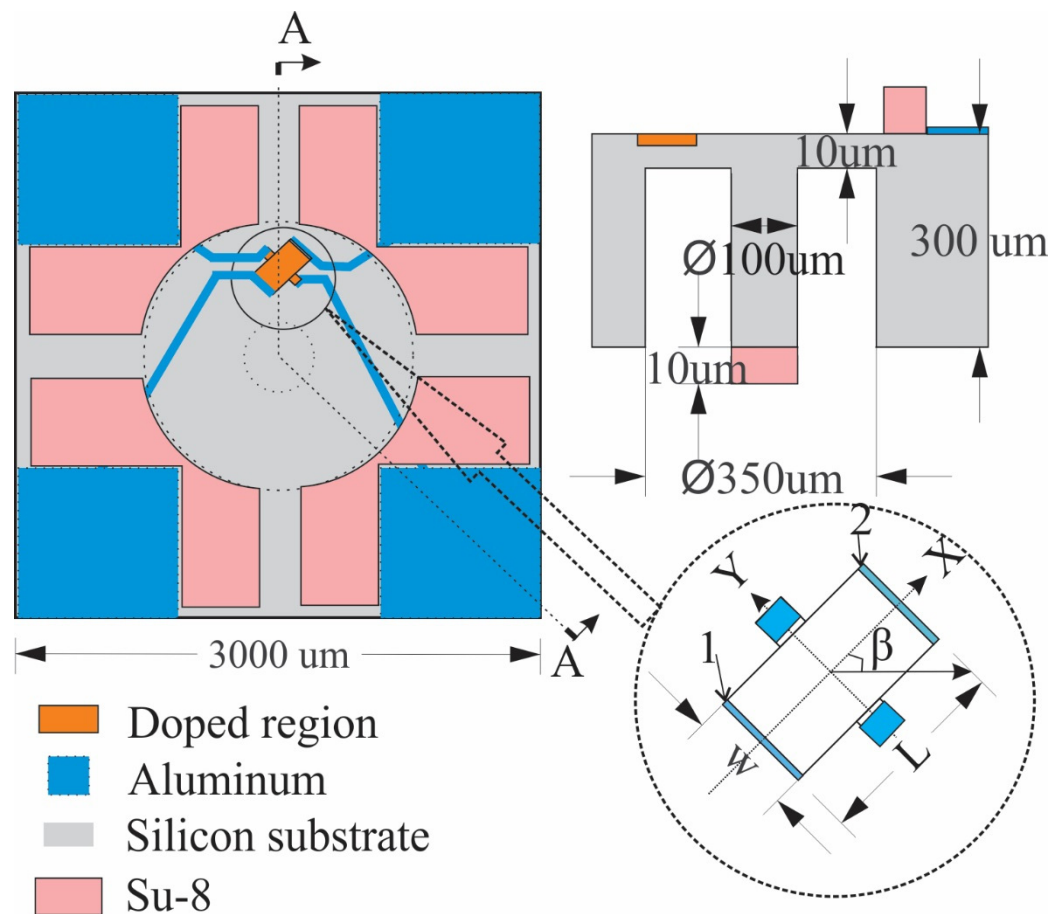


Figure 3-1 Structure of a normal force sensor[137] © [2014] Springer. Reprinted, with permission.

---

[1] Some of the materials in this chapter has been published by Yue *et.al.* [137][140][141]

The previous study for scoliosis applications has a dome-geometry mesa on top of the membrane[138], as shown in Figure 3-2 b. This work is more compact in terms of the device height because the mesa is implemented at the backside of the chip. Moreover, the via structure as shown in Figure 3-2 c, has been removed due to the change of mesa location. Therefore, the fabrication cost becomes more economical by eliminating the deep cryo-etching procedure.
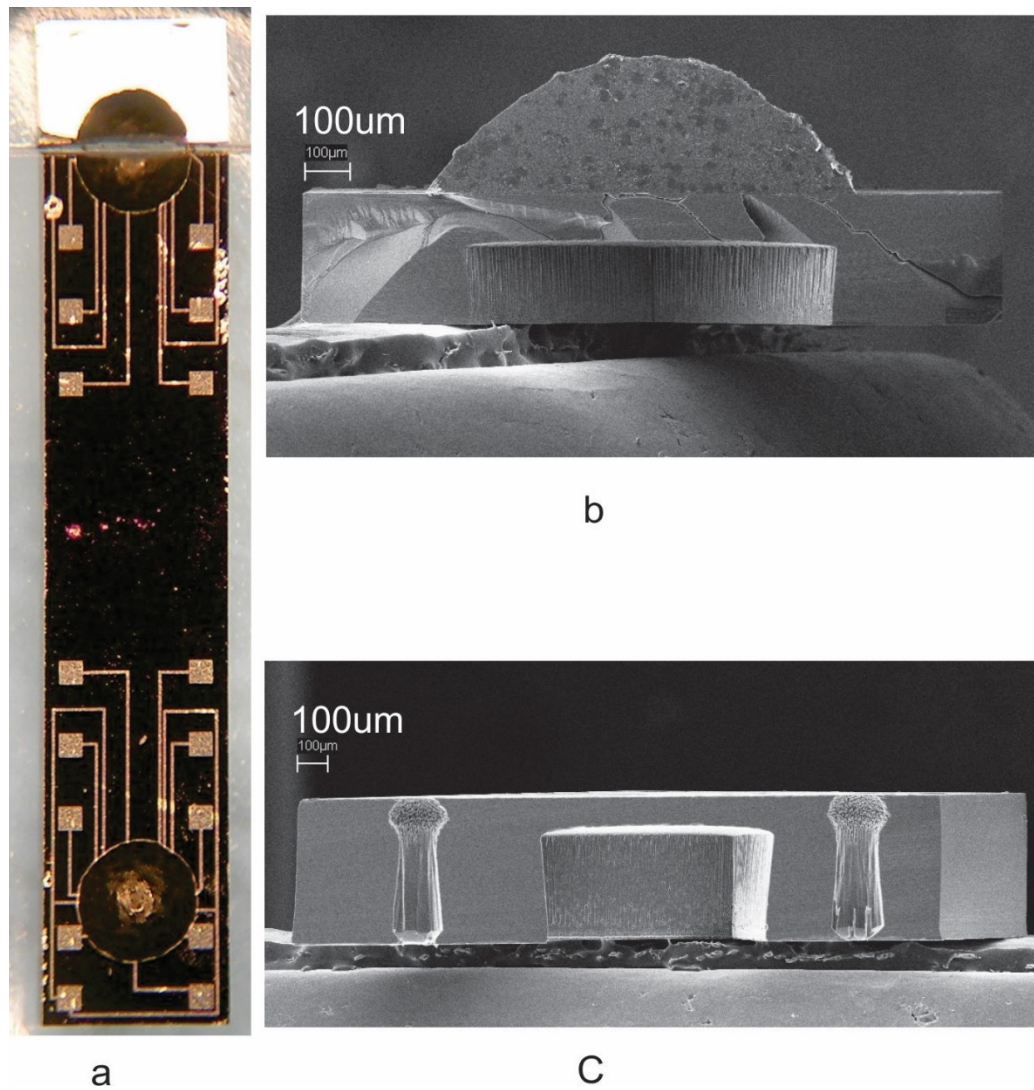


Figure 3-2 Force sensors for scoliosis application [94]

## 3.2 Sensitivity analysis on the uniaxial sensor

To enhance the performance of a sensor design, the geometrical parameters related to the sensitivity of this sensor need to be optimized systematically. Therefore, numerical models with different geometric parameters have been analyzed by finite element method (FEM) using

ANSYS®. Chosen values of key parameters such as diameters of the membrane and mesa, size of piezoresistive element, thickness of the membrane are listed below in Table 3-1.

Table 3-1 Parametric study on various designs of normal force sensors

| Membrane Diameter (um) | Mesa Diameter (um) | Element Size (um) | Thickness of Membrane (um) |
|---|---|---|---|
| 350, 400, 450, 500, 550, 600, 700, 800, 900, 1000 | 90, 100, 110, 120 | Width: 35, 40, 50, 60, 80, 100 Length: 40, 50, 60, 65, 70, 80, 100 | 6, 7, 8, 10, 12 14, 16, 18, 20, 22, 25 |

Generally, the outputs of the sensor increase as the size of the membrane expanding in the sensor. No typical correlation has been observed between the size of the four-terminal gauge and outputs, according to numerical simulations. As shown in Figure 3-3, the outputs from the normal force sensor increased from 24.3 mV to 43.1 mV, as the membrane diameter enlarged from 300 um to 900 um. Therefore, the membrane of the sensor worked as a signal amplifier to the applied force, owing to the raised stress level.
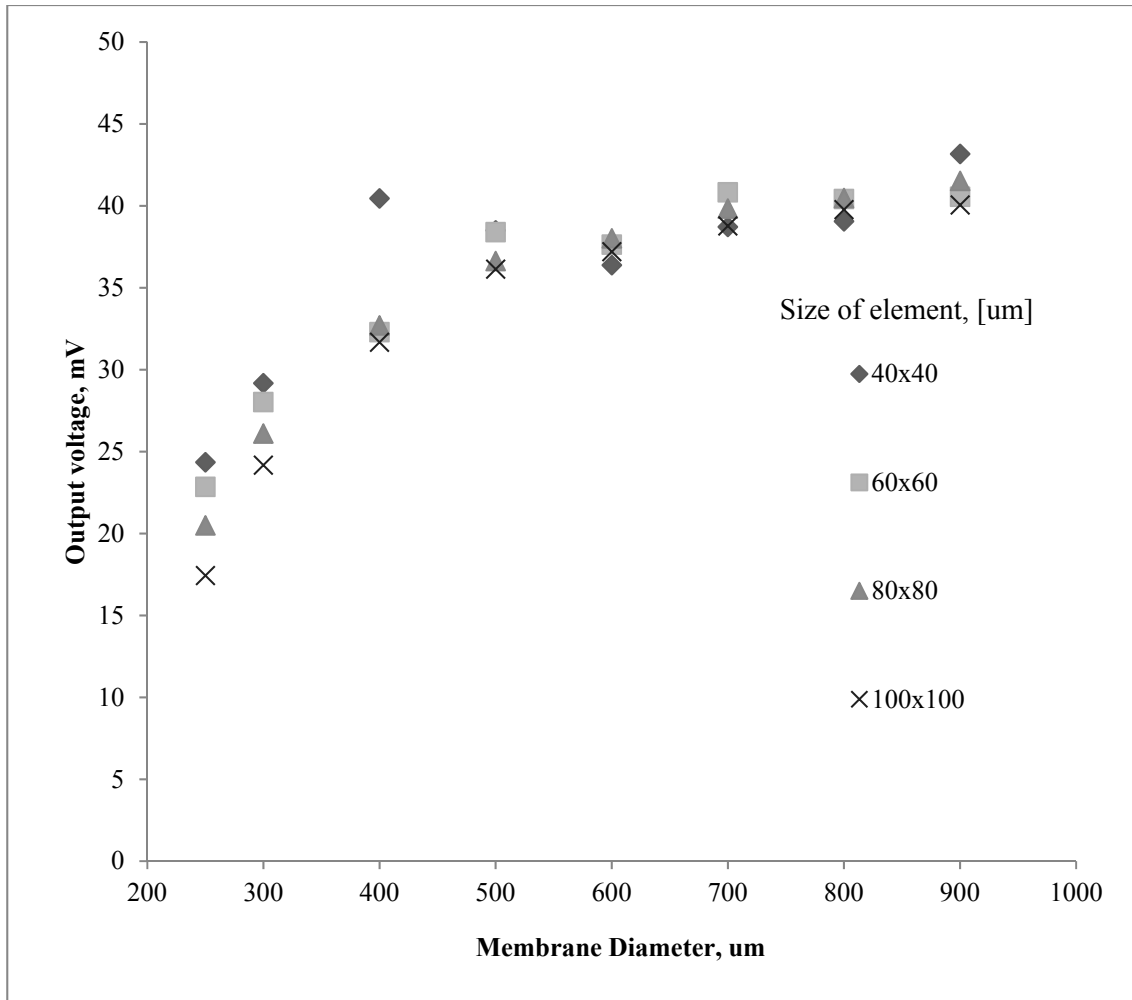
Figure 3-3 Correlation between membrane diameter and output voltage

The location of the four-terminal gauge on the membrane and the thickness of the membrane affect the sensor output. These parameters have been studied through numerical models. As shown in Figure 3-4, the location of the four-terminal gauge is simulated from the edge of the membrane toward the circle origin, within the range from 0 um to 60 um. The optional performance was found to be around 20 um from the edge of the membrane. The study of various membrane thicknesses demonstrated that the outputs increased as the membrane was thinned until about 10 um, which indicated as the optimal membrane thickness.
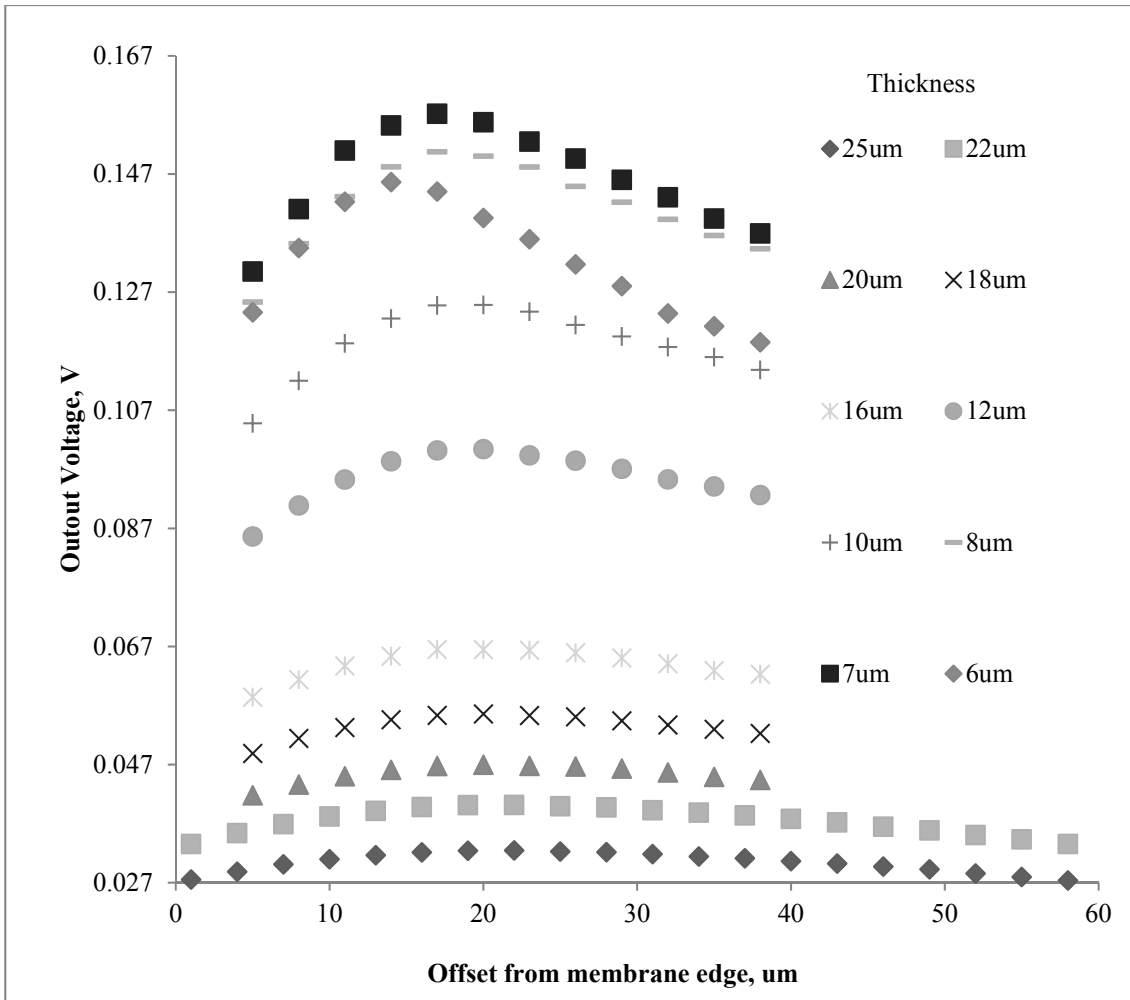
Figure 3-4 Membrane thickness effects on outputs voltage
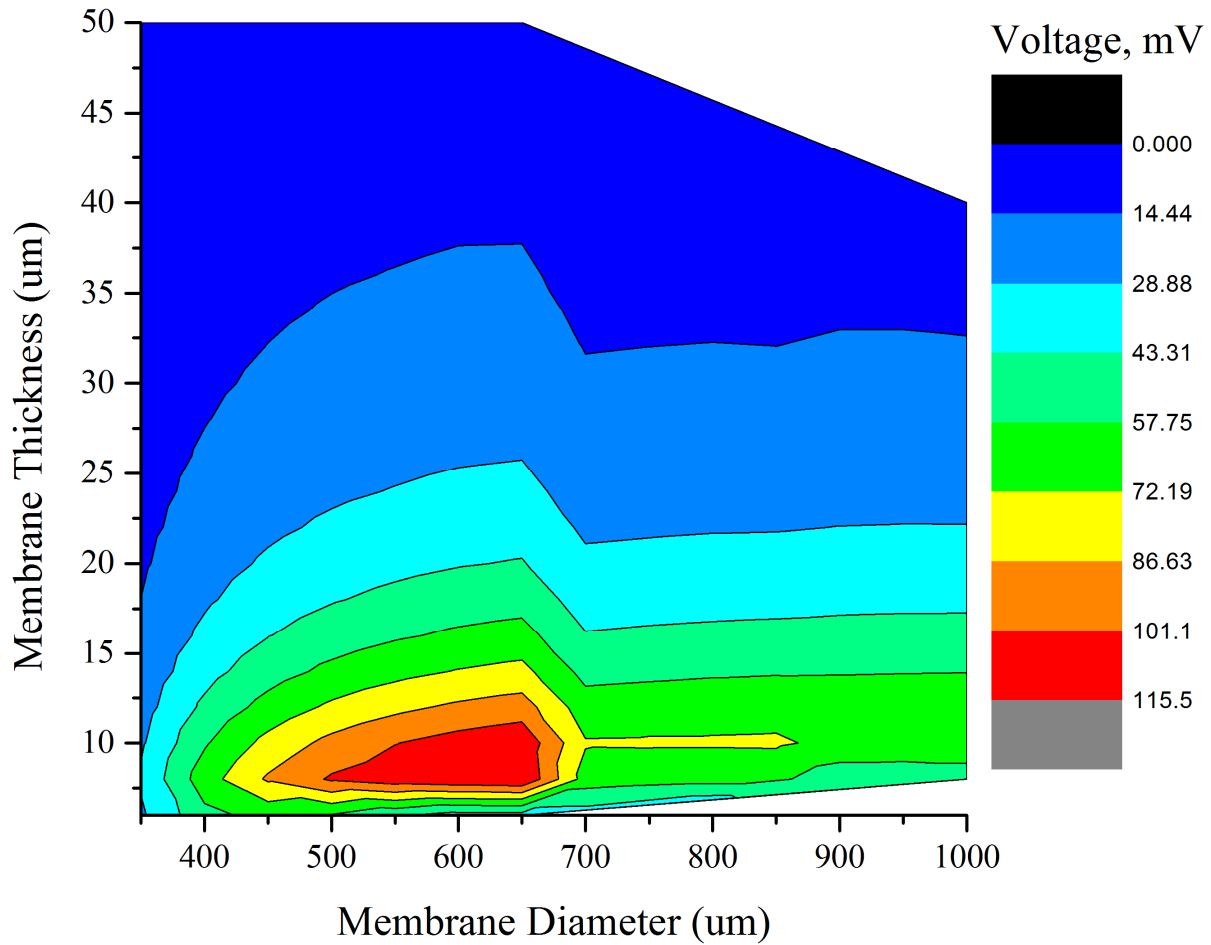
Figure 3-5 Output voltage metrics due to the membrane diameter and membrane thickness

Since the influence on the sensitivity of the sensor due to the membrane diameter and thickness is significant, the metrics of changing both parameters should be investigated. Therefore, a set of more complete simulations has been done regarding this issue. The results have been depicted in Figure 3-5. The optimal performance could be found within the diameter size of 350 um -700 um and membrane thickness of 8 um - 15 um.
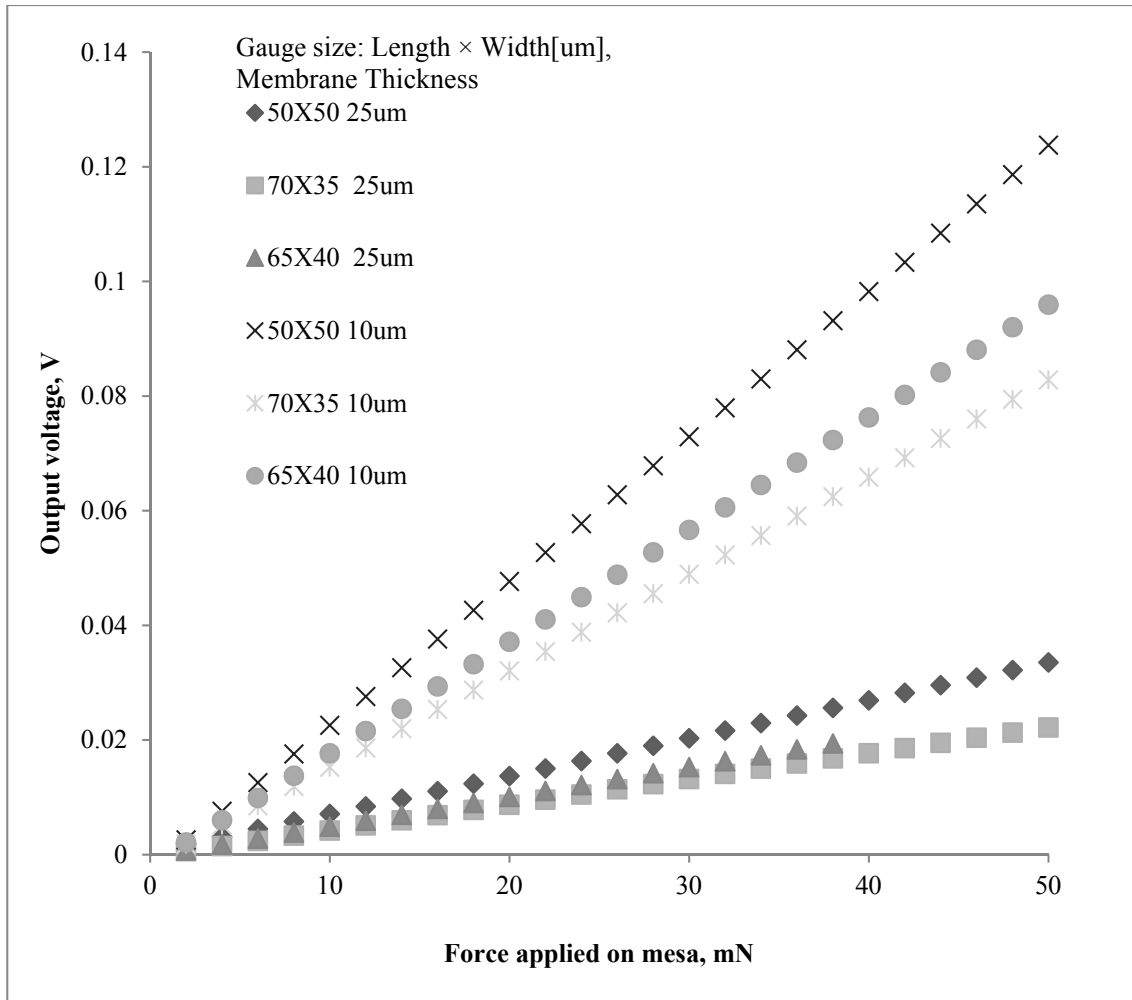
Figure 3-6 Gauge size effects on outputs voltage

The aspect ratio (AR), defined as the element length divided over the width, is also known for changing outputs proportionally[86]. The maximum output can be found if the aspect ratio equals to one from the development of a pressure sensor[85]. To study the aspect ratio effect on this work, several designs with different AR have been simulated on 10-um-thick and 25-um-thick membranes, respectively. Results in Figure 3-6 showed the highest output occurred with AR equal to one while on the 10-um membrane.

The piezoresistance coefficient changed as the sensor temperature varied in the ambient environment, which would cause outputs change accordingly. As shown in Figure 3-7, as the temperature increased from -40 °C to 40 °C, the outputs from this sensor decreased from 70.9 mV to 53.9 mV, due to temperature induced piezoresistance coefficient variations. In practical applications, the sensor performance change caused by temperature variations can be solved by adding another piezoresistor on the device where there is no stress changing due to the applied

force. This place is usually on the bulk part of the device. The added piezoresistor can act as the compensation thermistor[102, 139].
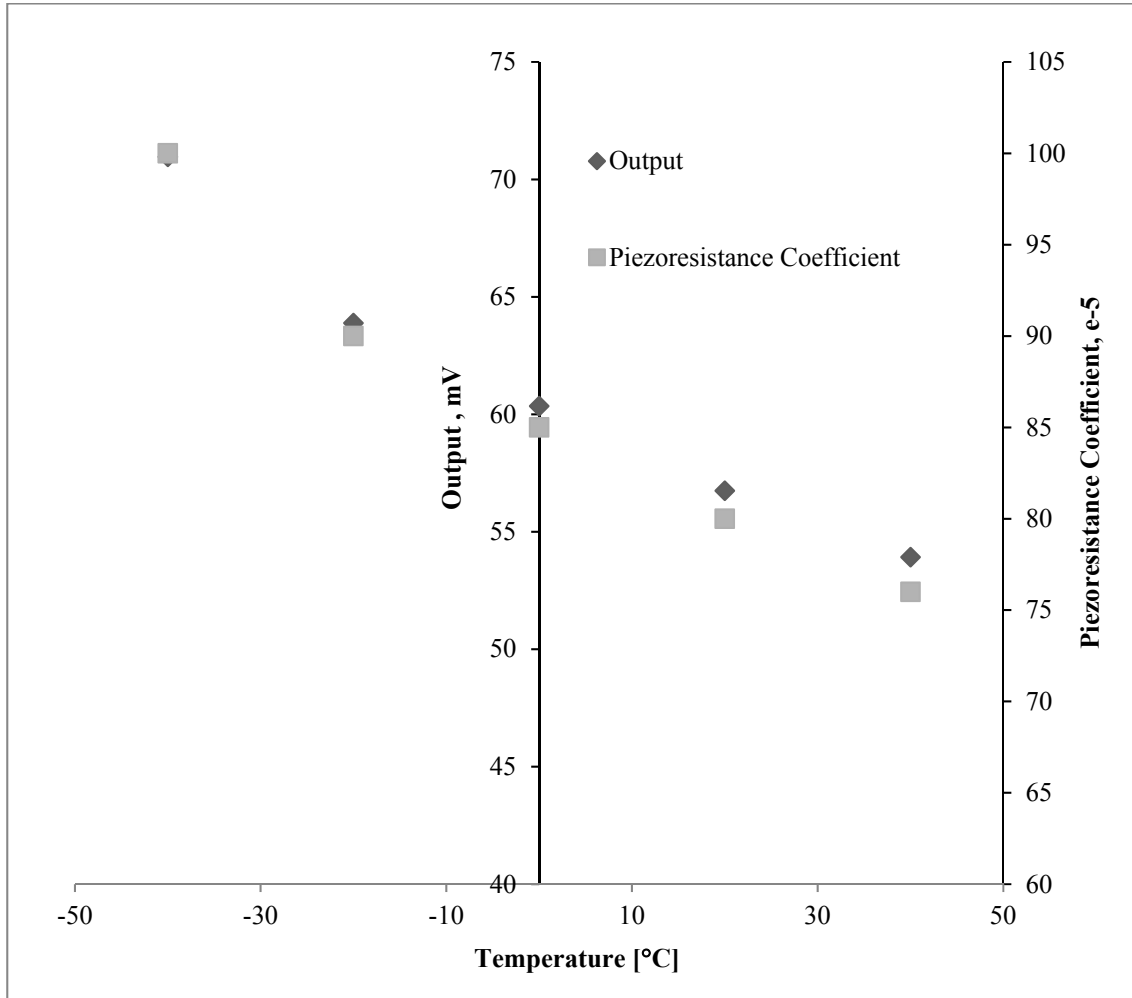


Figure 3-7 Piezoresistance coefficients effects on outputs voltages at various temperatures

The stress distribution in a membrane can be changed by placing a boss on it. This has been used as an approach to improve the pressure sensor performance in the literature[38]. The mesa for applying forces on the sensor membrane in this work, therefore, can also change the stress distribution within membrane region. Consequently, this stress distribution change can alter the sensor sensitivity. Simulation results have been plotted in Figure 3-8, showing that the sensitivity of force sensor decreases as the diameter of mesa increases.
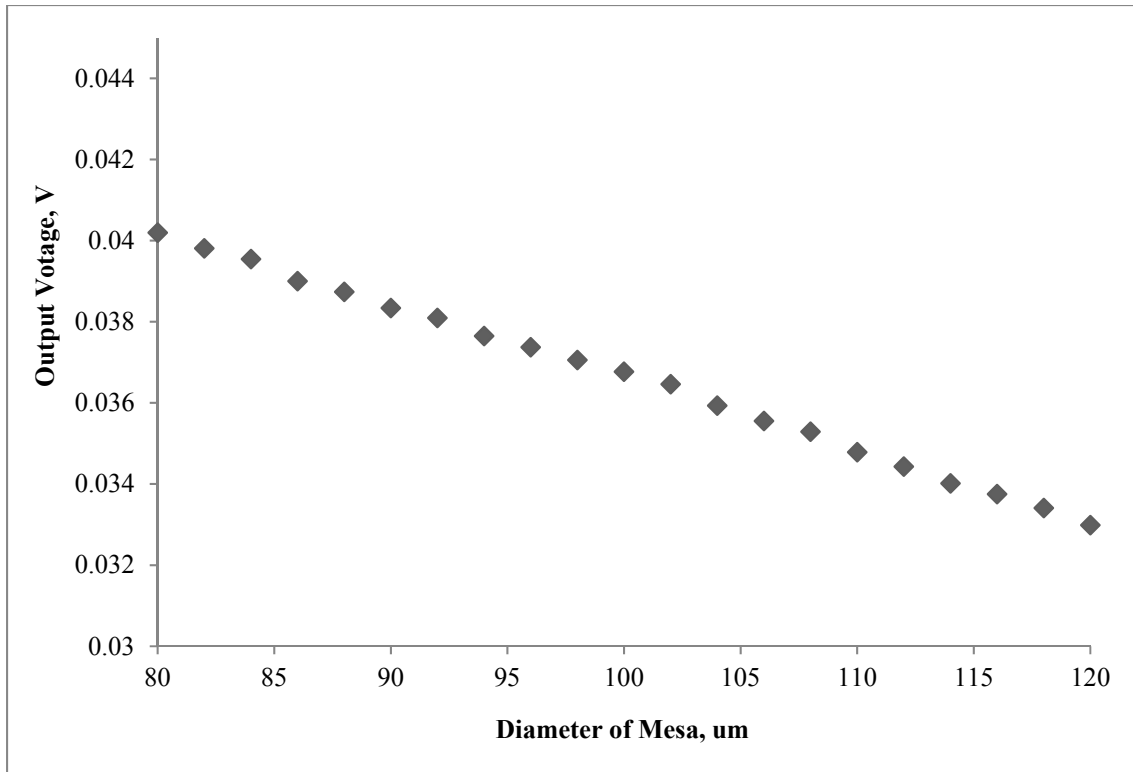
Figure 3-8 Mesa diameter effects on sensor outputs, done by simulations on a membrane with 500um in diameter, 10 um in thickness

Practically, forces applied on the sensor are not always ideally normal to the membrane plane. To study effects of an inclined force on the normal force sensor, three series of simulations have been done by applying forces with an elevated angle θ at 5°, 10° and 15°, respectively. At each test, the force was rotated at an angle ψ. Then responses were acquired from all surrounding directions until tests for one revolution were finished. In Figure 3-9, the results of the simulation were plotted, indicating a quasi-sinusoidal behavior from different directional forces with an inclined angle. The peak-to-peak output increased as the tilted angle was enlarged. As the amplitude of applied force was fixed at 50 mN, notably, three neutral points of the sinusoidal behavior maintained unchanged according to this simulation. More discussions would be introduced for the multi-axis force sensor in terms of this sinusoidal feature. Advantages of this feature also involved in the latter analysis on the sensor array characteristics.
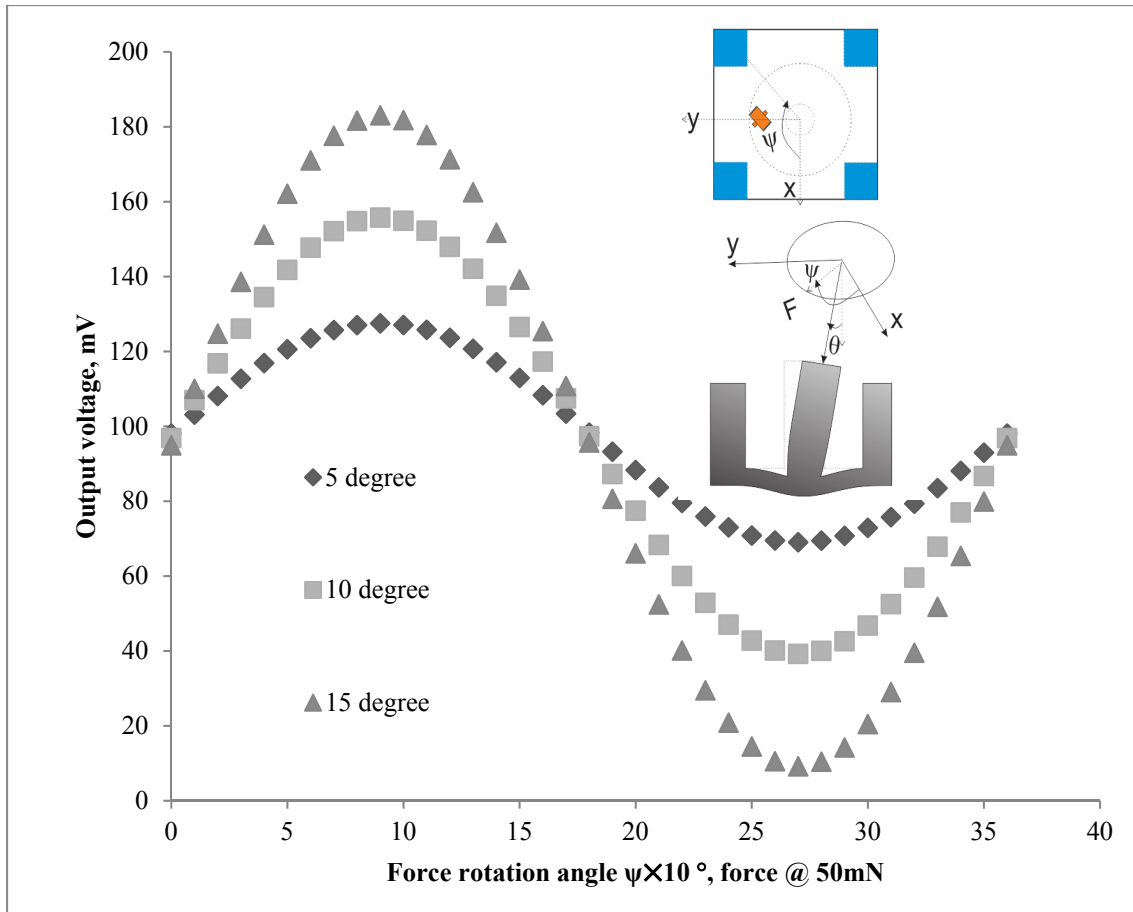
Figure 3-9 Effects on sensor performance by force misalignments to normal direction

## 3.3 Uniaxial sensor array layout

The layout of the sensor array was depicted in Figure 3-10. From previous simulations such as Figure 3-6, the output voltage from the normal force sensor has shown to be proportional to the applied force. The applied force generated the local stress induced by the membrane deformation. This was also the lateral displacement of the mesa. Therefore, the correlation between the applied force and voltages can be interpreted as the function between the lateral deformation and voltages. Hereby, the deformation of the thin plate caused by a lateral force was feasible to be detected if an array of uniaxial force sensors was assembled beneath it.
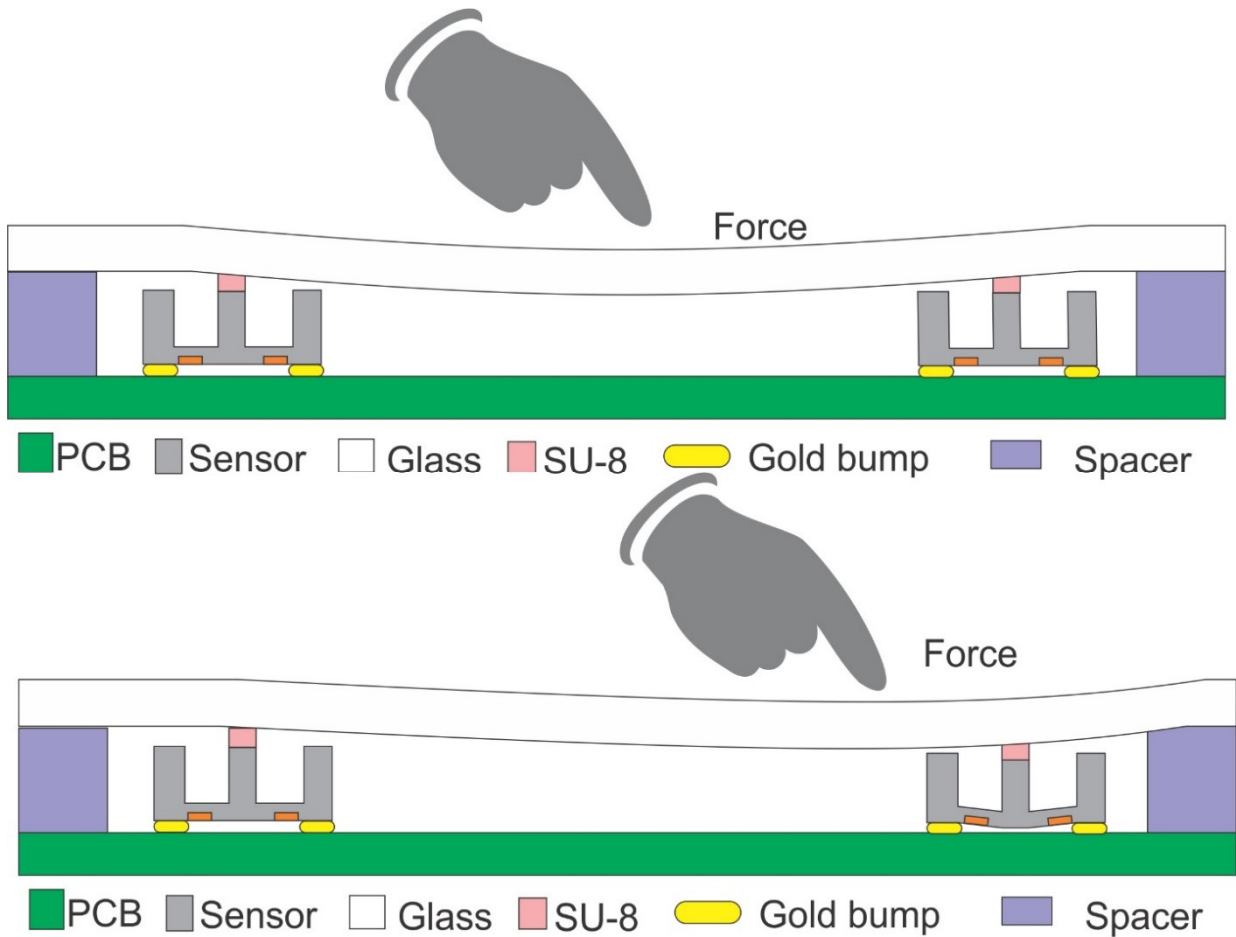
Figure 3-10 Conceptual scheme of packaged sensor array © [2018] IEEE

The sensor array was embodied with four piezoresistive tactile cells underneath a glass film, which could be replaced by a display or a conventional touch screen (hybrid solution) in future practical applications. The four tactile cells were placed on top of a piece of PCB precisely by a flip-chip machine. If a finger or stylus touched the film surface, the glass film would be deflected. The deflection could be sensed by the piezoresistive sensor array. The schematic layout of this embodiment has been depicted in Figure 3-11 below. The gap between the glass film and PCB at four edges was sealed by silicon strips and polymers.
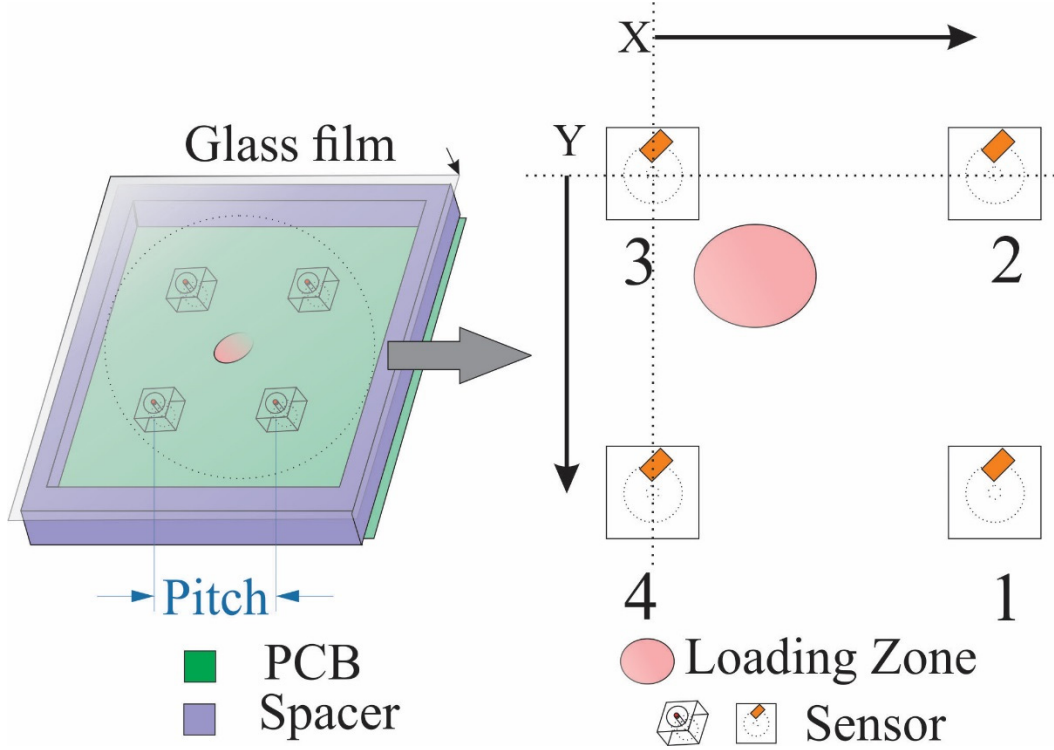
Figure 3-11 Schematic definition of the basic sensor array © [2017] IEEE

For a thin plate (length = $a$, width = $b$) with four edges fixed subjecting to a lateral load $q$, the vertical displacement $w$ of the plate can be described as an equation as [136]:

$$w = \frac{4qa^4}{\pi^5 D} \sum_{m=1,3,5,..}^{\infty} \frac{(-1)^{\frac{m-1}{2}}}{m^5} \cos\frac{m\pi x}{a} \left(1 - \frac{\alpha_m \tanh \alpha_m + 2}{2\cosh \alpha_m} \cosh\frac{m\pi y}{a} + \frac{1}{2\cosh \alpha_m}\frac{m\pi y}{a}\sinh\frac{m\pi y}{a}\right)$$

(3-1)

where the coefficient $\alpha_m$ given by: $\alpha_m = \frac{m\pi b}{2a}$, and $x$, $y$ standing for the location of the force. Inspired by the equation above, the normal (uniaxial) sensor array prototype was used for demonstrating the feasibility of the sensor array configuration as the proof-of-concept.

## 3.4 Sensitivity analysis on uniaxial sensor array

To study the feasibility, the numerical analysis by the Finite Element Method (FEM) has been employed according to the sensor array layout described in the previous section.
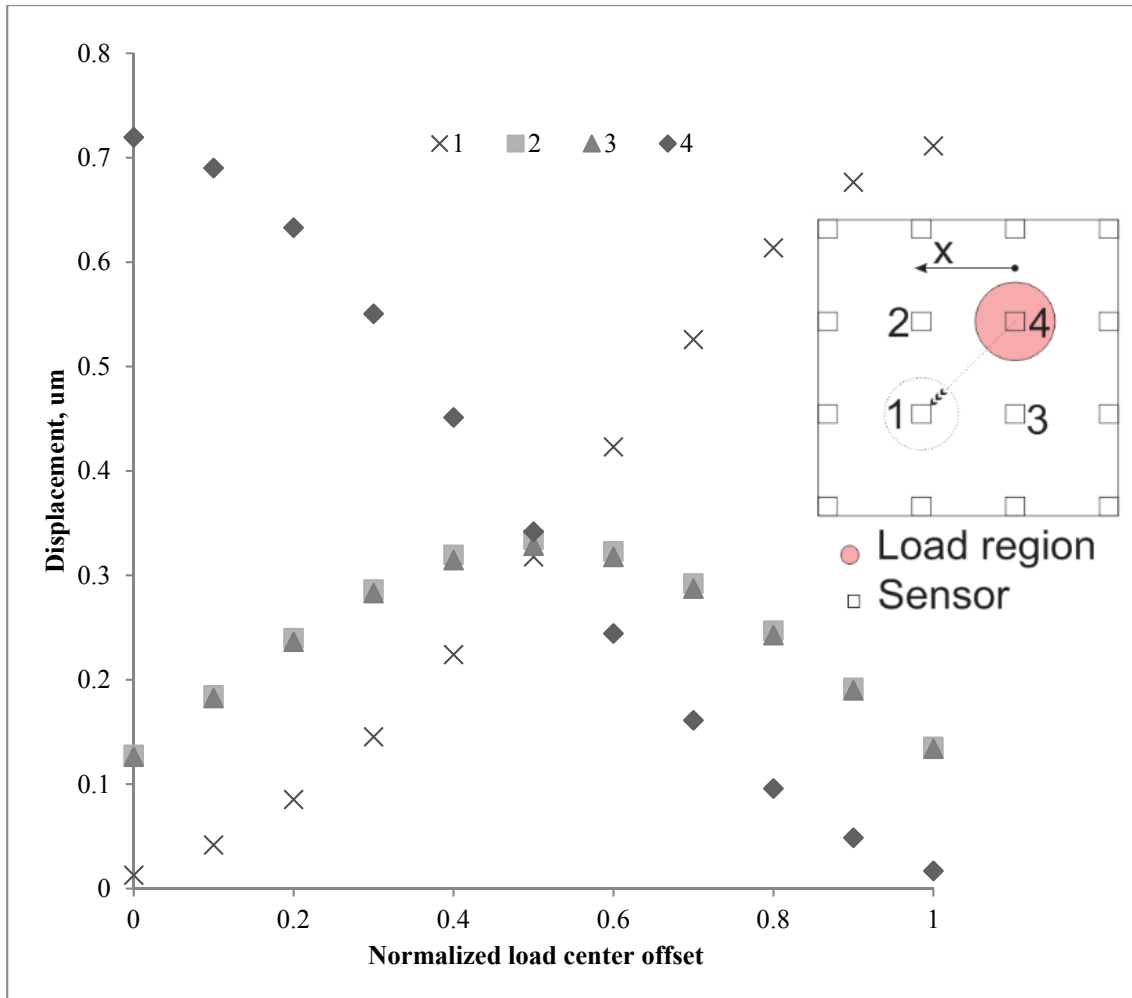
Figure 3-12 Displacement on mesas of sensors with load at 100mN © [2014] Springer. Reprinted, with permission.

As shown in the legend from Figure 3-12, the circular load center was moved from top of sensor 4 diagonally to sensor 1. The displacements from sensor 2 and sensor 3 presented the similar trend with their calculated voltage outputs owing to the symmetry of the sensor array layout. For sensor 1 and sensor 4, the displacements were inversely proportional to the approximate distance between the loading center and the sensor mesa.
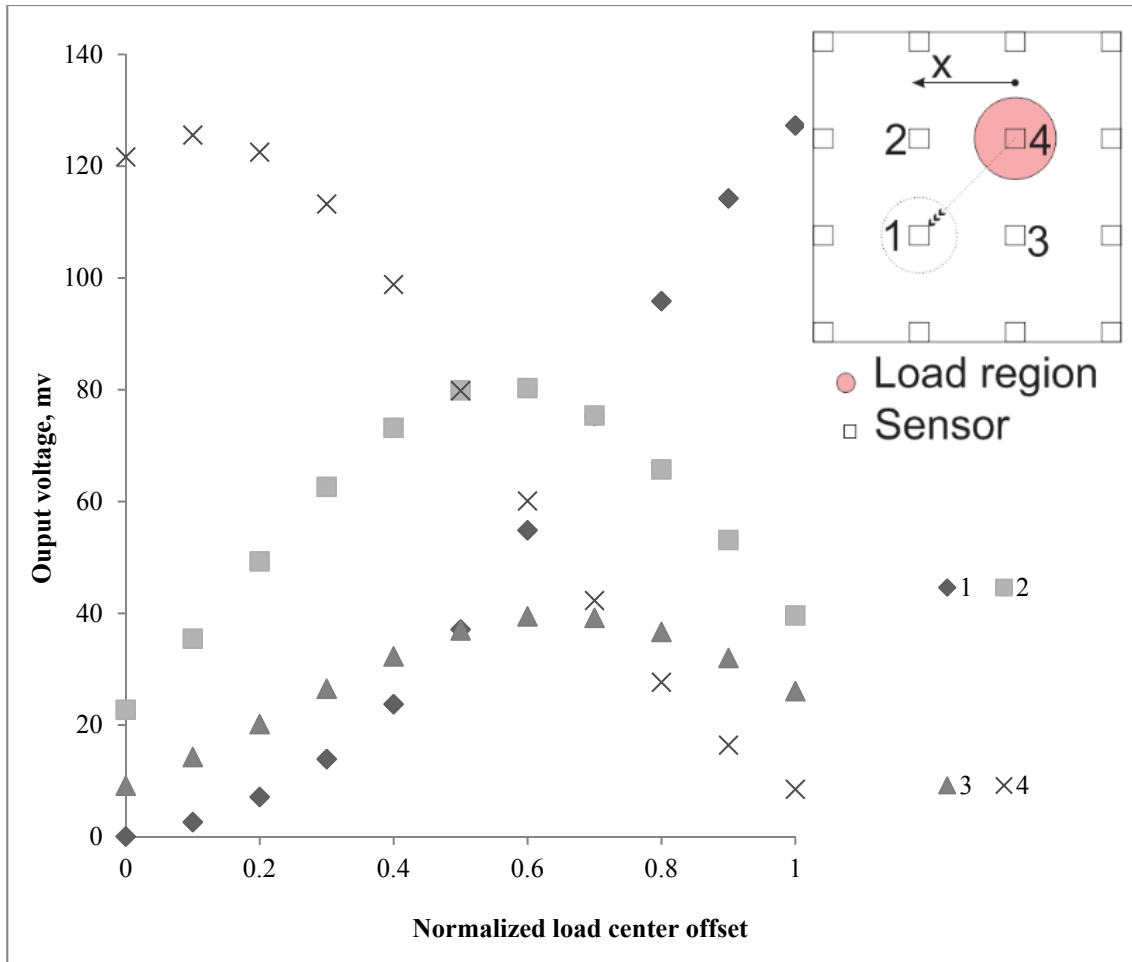
Figure 3-13 Voltage output with load at 100mN © [2014] Springer. Reprinted, with permission.

As shown in Figure 3-13, sensor 4 had the largest output when the load center was applied on its top. In contrast, sensor 1 showed the lowest output as it had largest distance to the load center on the top of sensor 4. As moving the load center from the top of sensor 4 to sensor 1, the output from sensor 1 increased while the output from sensor 4 dropped, similarly as the previous displacement simulation. This demonstrated the feasibility of the sensor array, which was the ability of sensing both the force amplitude and the location information of a tactile event. Furthermore, the outputs of sensor 2 and sensor 3 trended to different peak values of 80mV and 40 mV, respectively, at the center of the diagonal line connecting them. This asymmetric behavior was because the sensing element was located at the edge of circular membrane, which led to unevenly distributed stress.
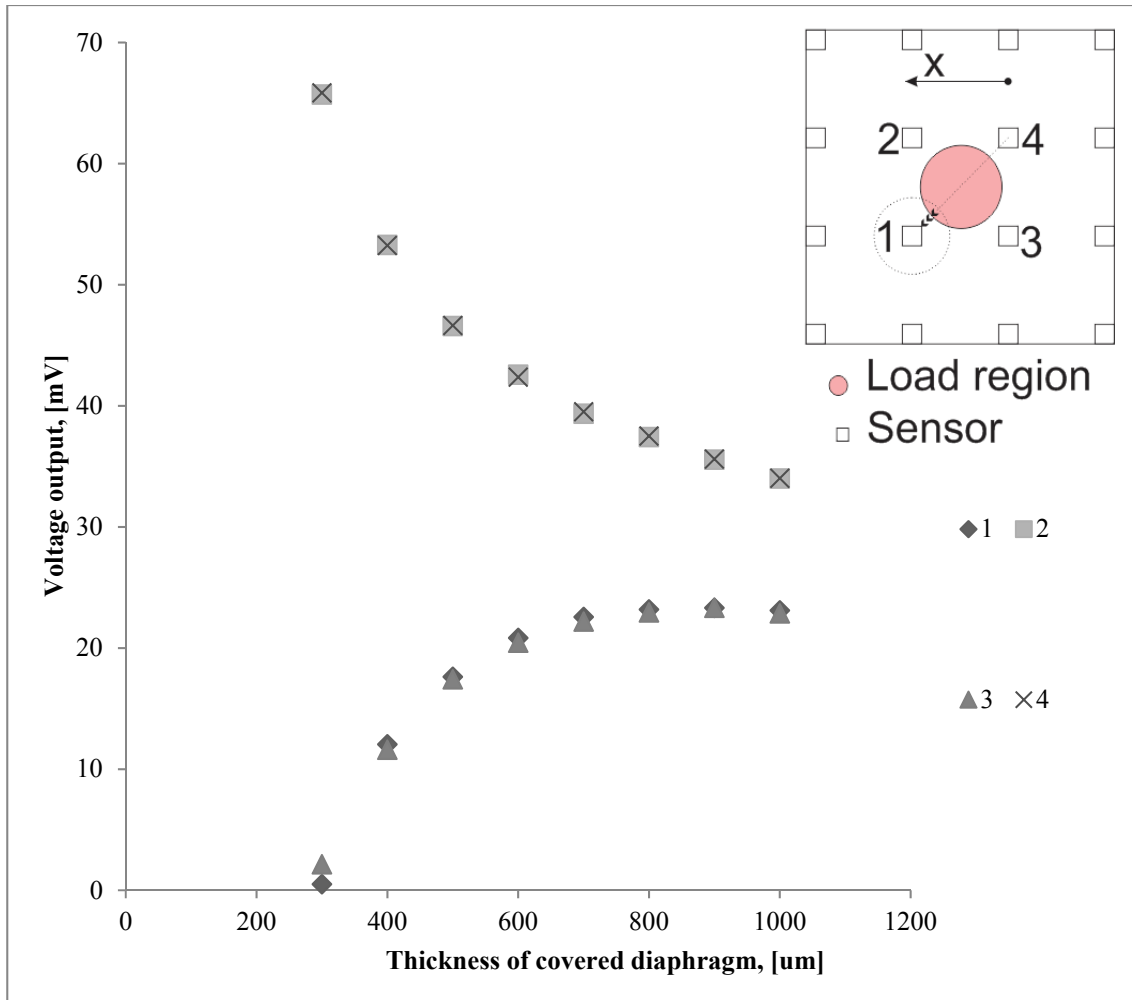
Figure 3-14 Voltage outputs with varying diaphragm thickness © [2014] Springer. Reprinted, with permission.

Another key parameter which affected the sensitivity of the packaged sensor array was the thickness of covered glass diaphragm. It was shown in Figure 3-14 that as glass plate thickness increased from 300 um to 1000 um, the outputs of sensor 2 and sensor 4 decreased from 65.8 mV to 34 mV. In contrast, the outputs of sensor 3 and sensor 1 increased with using a thicker diaphragm. This effect was due to the force-angle-related (FAR) property with respect to the location of sensing element on each normal tactile sensor.
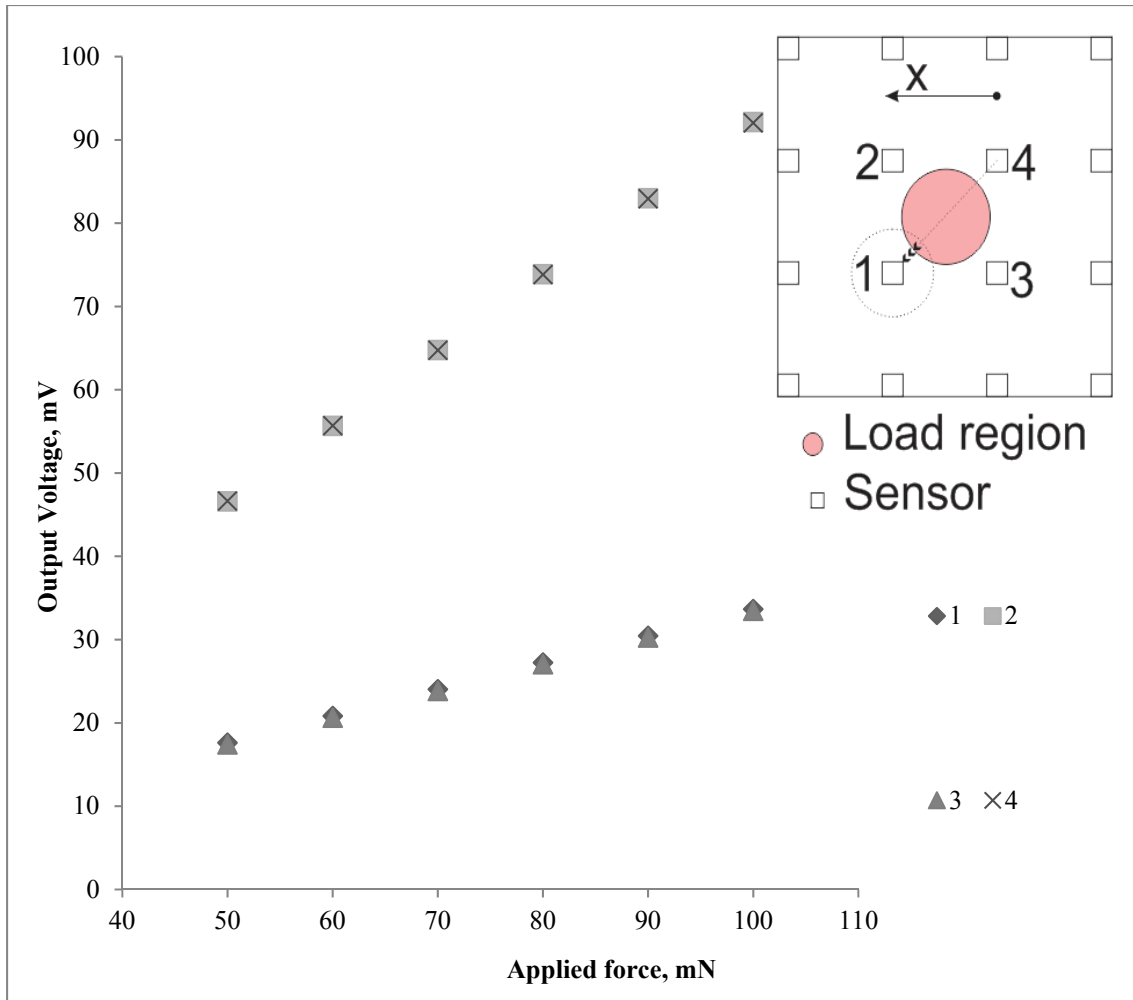
Figure 3-15 Outputs from different amplitude forces at fixed position © [2014] Springer. Reprinted, with permission.

The sensor responses at a fixed location have been investigated as shown in Figure 3-15. The results showed that as the amplitude of the applied force increased, all the sensor outputs grew linearly. Moreover, as the applied force increased from 50 mN to 100 mN, the sensor 2 and sensor 4 outputs increased faster, trending together from 46.6 mV to 92.04 mV while the sensor 1 and 3 increased slower, from 17.4 mV to 33.4 mV. This could be explained by the curvature of deformed cover glass transformed the pressing force as an inclined force onto each sensor mesa, although the applied force was in a normal direction. The angular force could cause generally two different effects on sensor outputs, either enhancements or reductions. These applied forces, for sensor 2 and sensor 4, were in the enhancement region, but in the reduction region for sensor 1 and sensor 3.

31
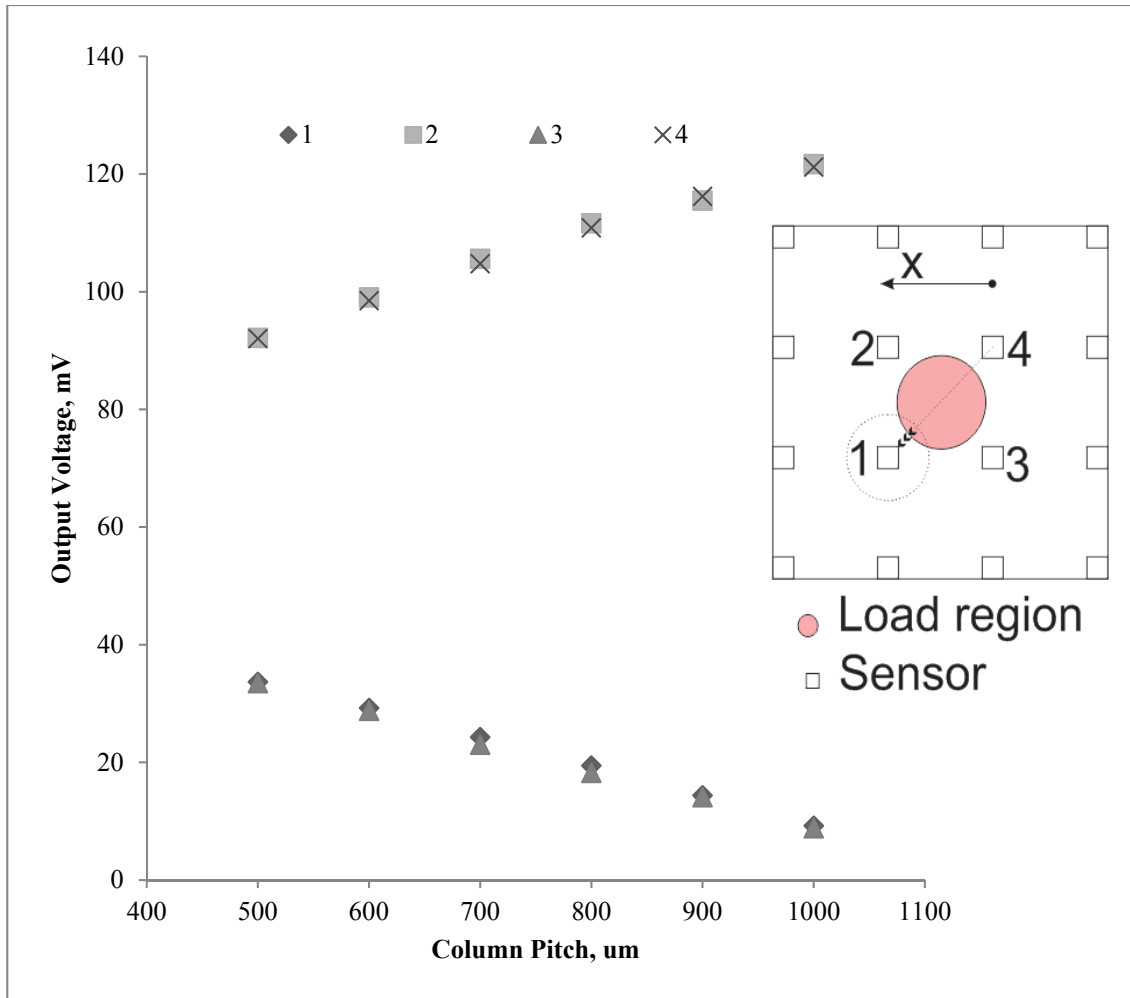
Figure 3-16 Correlation between the column pitch and outputs by a normal force at a fixed location ©
[2014] Springer. Reprinted, with permission.

Definition of the column pitch was the distance between two sensors in the same row or column.
The sensor array was assembled in a square configuration. From Figure 3-16, the outputs of sensor
2 and sensor 4 increased from 92.04 mV to 121.18 mV, while the outputs of sensor 1 and sensor
3 dropped down from 33.4 mV to 8.8 mV, respectively, as the column pitch increased from 500
um to 1000 um. This phenomenon indicated that the force-angle-related property was enhanced
with increasing column pitch, causing more discreteness in terms of sensor outputs.

*Analysis on enlarged sensor array pitch*

Further numerical analysis on the sensor array by FEM (finite element method) has been done
at larger *pitch* values. Results from the sensor array demonstrated consistent responses in terms of
larger *pitch* configurations. As shown in Figure 3-17, the outputs from the four sensors in the

sensor array increased as the *pitch* expanding (the distance between two neighborhood sensors in the array). Notably, the maximum outputs from those four sensors doubled in the amplitude while the pitch was enlarged from 10 mm to 60 mm. The sensor array responded to the normal force in a similar behavior pattern as it did when the *pitch* was 10 mm. In other words, the sensor outputs increased as the loading was placed closer from the mesa of the sensor and decreased while the loading was placed further. This consistency revealed the potential for larger area applications.
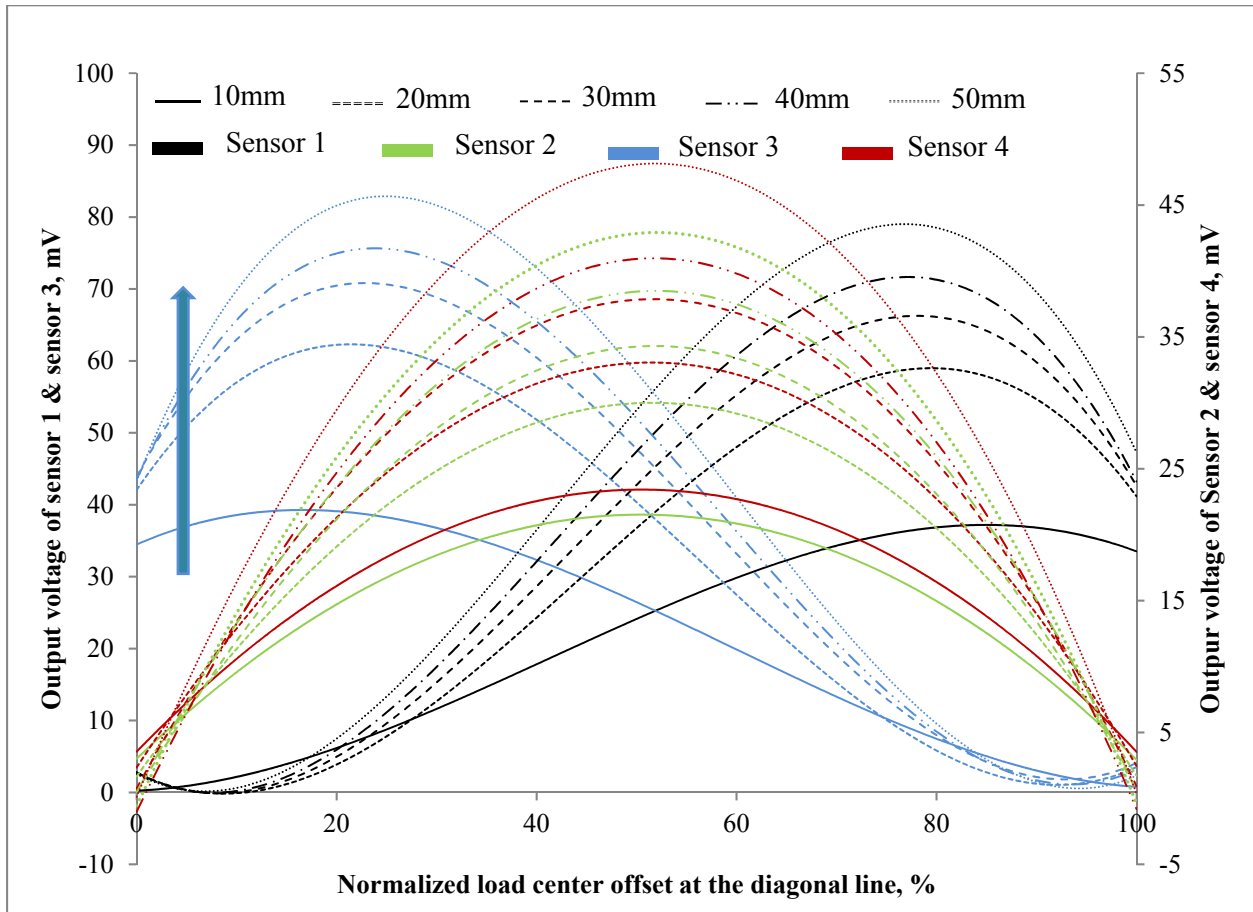


Figure 3-17 Response of sensor array at various pitches between sensors [140] © [2017] IEEE

## 3.5 Multi-axis force sensor geometry

In this section, multi-axis force sensors were designed by adding three extra sensing elements in the membrane of the previous normal force sensor. As depicted in Figure 3-18, four sensing elements were distributed evenly on the membrane, orienting perpendicularly to the adjacent one. The outputs from these four sensing elements would have differences if an inclined force was applied at the center of the sensor membrane. The force might be with a pitch angle $\theta$ and a yaw

33

angle $\phi$. The multi-axis sensor would be diced into square chips at the size of 2.5 mm $\times$ 2.5 mm. The circular membrane had a diameter of 350 um with a 100-um cylinder mesa.
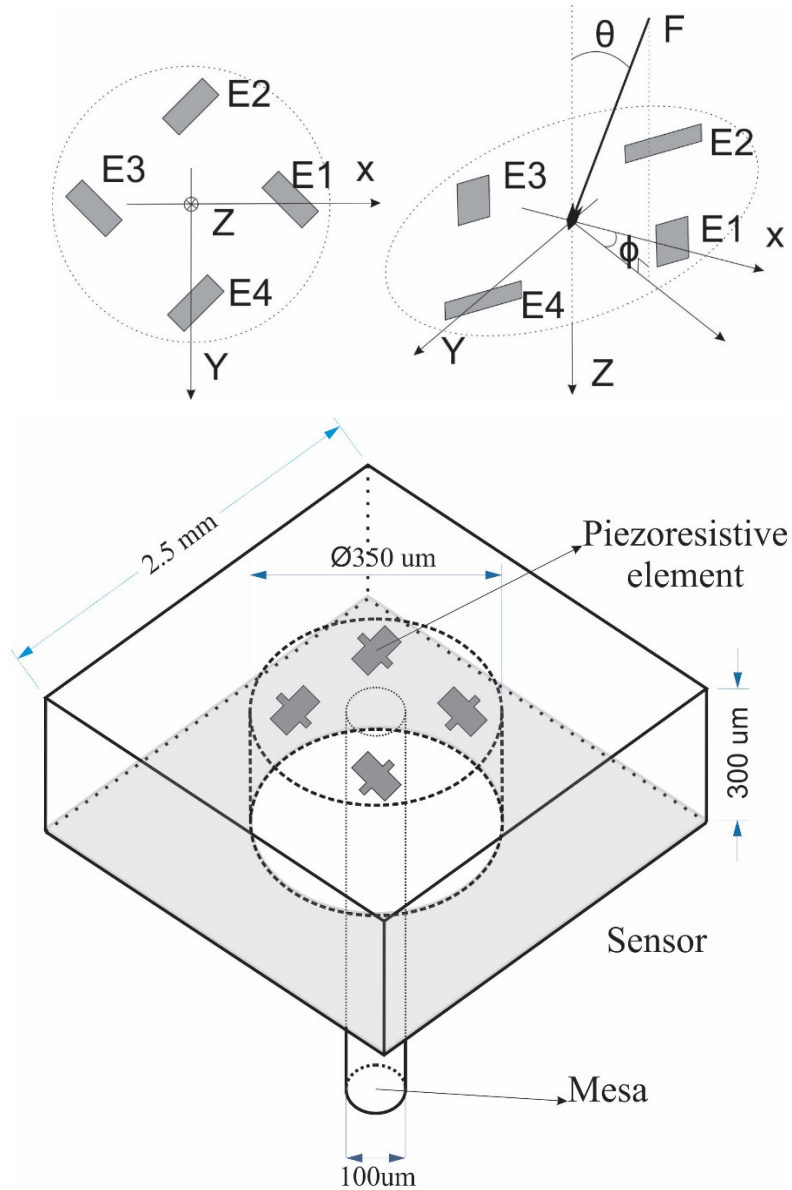


Figure 3-18 Sensing elements distribution and sensor geometry of the multi-axis force sensor

© [2018] IEEE

## 3.6 Sensitivity analysis on the multi-axis tactile sensor

Numerical analysis has been done to evaluate the performance and characteristics of the multi-axis force sensor. Firstly, an inclined force with an angle $\theta$ of 5° was applied onto the mesa. The force amplitude was increased from 0 to 50 mN. Results plotted in Figure 3-19 have presented a high linearity of the multi-axis force sensor, with outputs discreteness from four sensing elements.

Specifically, outputs from sensing elements E1 responded with higher voltages while element E3 with lower voltages. This was because the force had a component parallel to the axis where the element E1 and E4 were located.
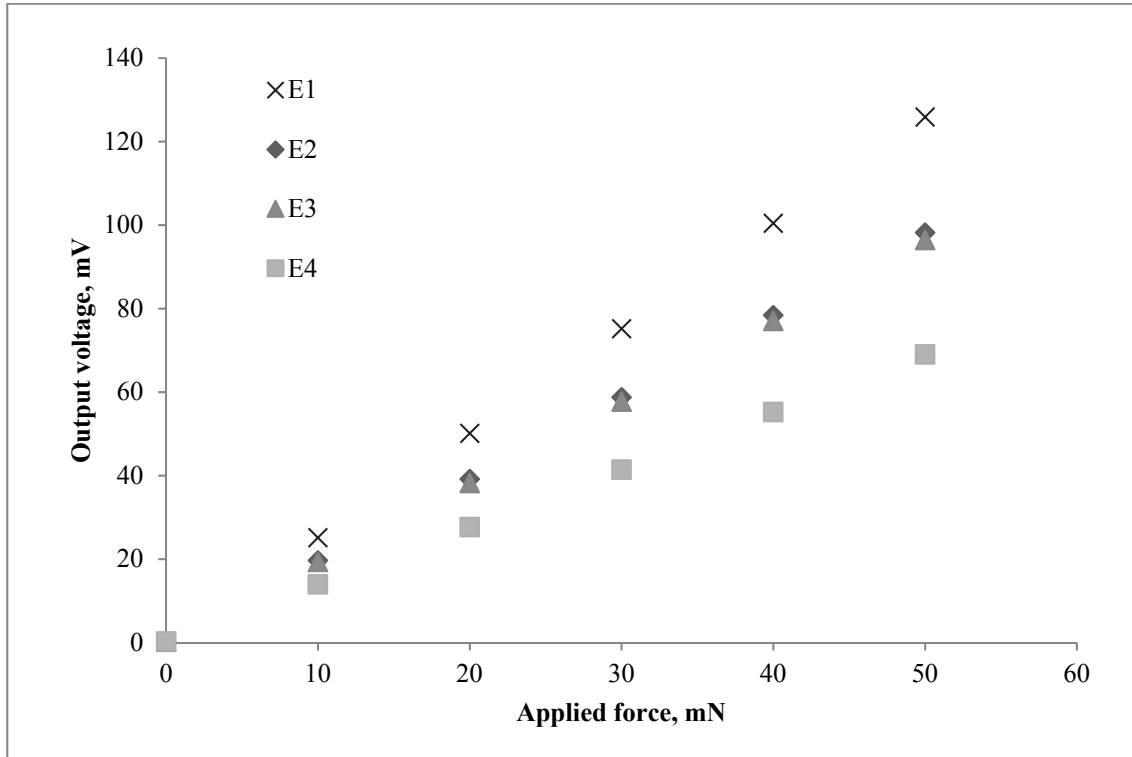


Figure 3-19 Sensor performance on an inclined force with a fixed angle θ = 5°

Elevated inclined forces were generated by the deformation of the cover glass plate due to the structural feature of the sensor array packaging. In the application scenario, these inclined forces could be oriented into various directions, put another way, with different values of $\phi$. Therefore, a study using FEM by rotating the inclined force at $\theta = 5°$ was performed. The results shown in Figure 3-20 indicated a sinusoidal behavior from each sensing element. The phase shift corresponded to the stress phase changes on the membrane. The simulations were initiated from pointing the angular force towards sensing element *E1*, by rotating the direction of this force sequentially until passing by elements *E2, E3, E4* as one complete revolution.
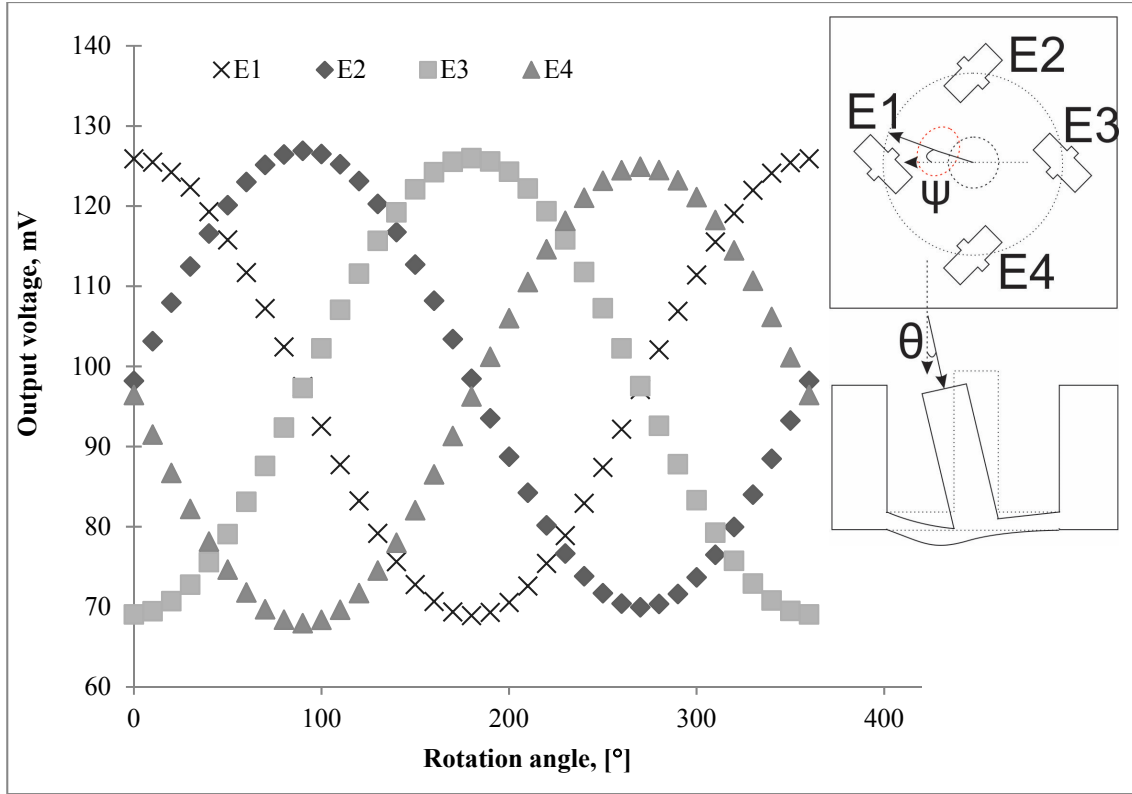
Figure 3-20 Sinusoidal outputs from multi-axis force sensor

Furthermore, for each sinusoidal output from the sensing element, the voltage value could be denoted as equation:

$$V_{out} = A\theta \sin \varphi_1 + V_{Nout} \tag{3-2}$$

Where $V_{out}$ standing for output voltage, $A$ was amplitude tweaking factor which acquired by the regression curve fitting, and $V_{Nout}$ was the output voltage noted as $V_{Nout} = kF$, if the force was a normal force $|F|$ with the same amplitude as $F$.

Since there were four elements on the membrane, the results yielded four equations if a random force was applied on the mesa:

$$\begin{cases} V_{out1} = 5.9\theta \sin \varphi_1 + 1.192F \\ V_{out2} = 5.9\theta \sin(\varphi_1 + \pi/2) + 1.192F \\ V_{out3} = 5.9\theta \sin(\varphi_1 + \pi) + 1.192F \\ V_{out4} = 5.9\theta \sin(\varphi_1 + 3\pi/2) + 1.192F \end{cases} \tag{3-3}$$

For a random force $F$ applied at the mesa with an elevated angle $\theta$ and an orientation angle $\phi$, the above equations could be solved as it had three unknowns but four known voltages.

Notably, the outputs sum from this multi-axis force sensor remained unchanged by if the amplitude of the force was fixed. Calculations on the sum were plotted in Figure 3-21, which was

the flat dot line. This characteristic would be helpful for the multi-axis force measurement applications. Because the outputs sum of the sensor would not be affected by tilting the force to different directions. Besides, the output from individual element did respond to the orientation changes. This feature would be further used and discussed in following sections regarding of the multi-axis sensor array characterization.
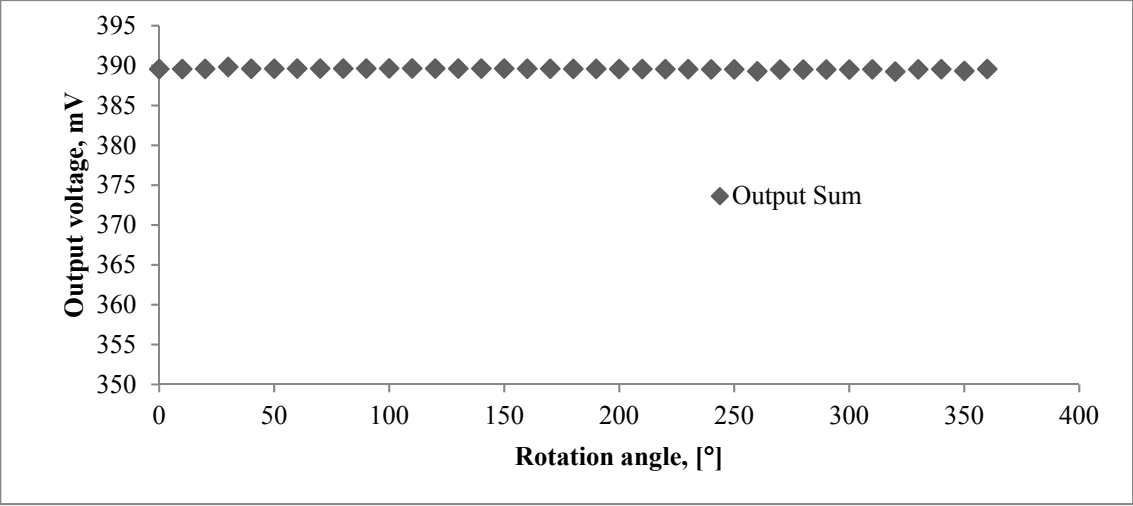


Figure 3-21 Sum of the outputs from four sensing elements
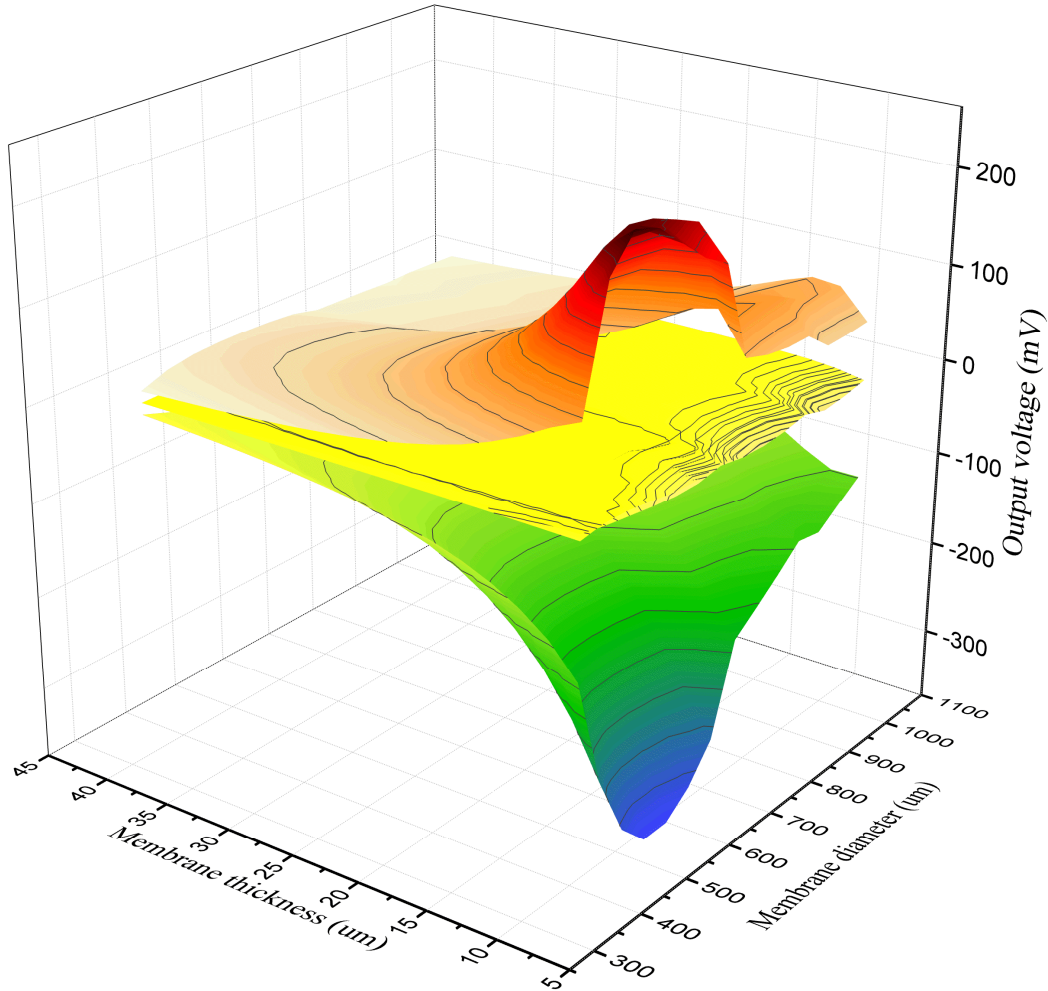
Figure 3-22 Multi-axis force sensor response on the shear force

The response characteristics of the multi-axis force sensor regarding of the membrane diameter and the membrane thickness have also been simulated by applying a pure shear force on the mesa, see Figure 3-22. The optimal sensitivity of the sensor was found from the similar region as the uniaxial tactile sensor described in section 3.2.

## 3.7 Multi-axis tactile sensor array design

The multi-axis tactile sensor array was a continuous work inspired by the proof-of-concept structure of the normal force sensor array with a larger configuration. A 2 × 2 highly sensitive piezoresistive sensor array was embodied on a printed-circuit-board (PCB), covered by a thin glass plate which would be replaced by a display for practical applications. Four edges of the cover glass were sealed with a ring-shape spacer, bonding to the PCB with the PDMS. Its working principle was that as the cover subjected to a force applied by a finger or stylus, the lateral deformation and

tangential movement of the cover glass would be sensed by the sensor array which was underneath the cover. The prototype has been developed with the schematic geometry shown in Figure 3-23. The distance between two individual sensors was defined as the *pitch*, which was 60 mm in this demonstration prototype. The space (bezel) between the mesa and the edge of the assembling was 2.5 mm which could be further reduced in the future.
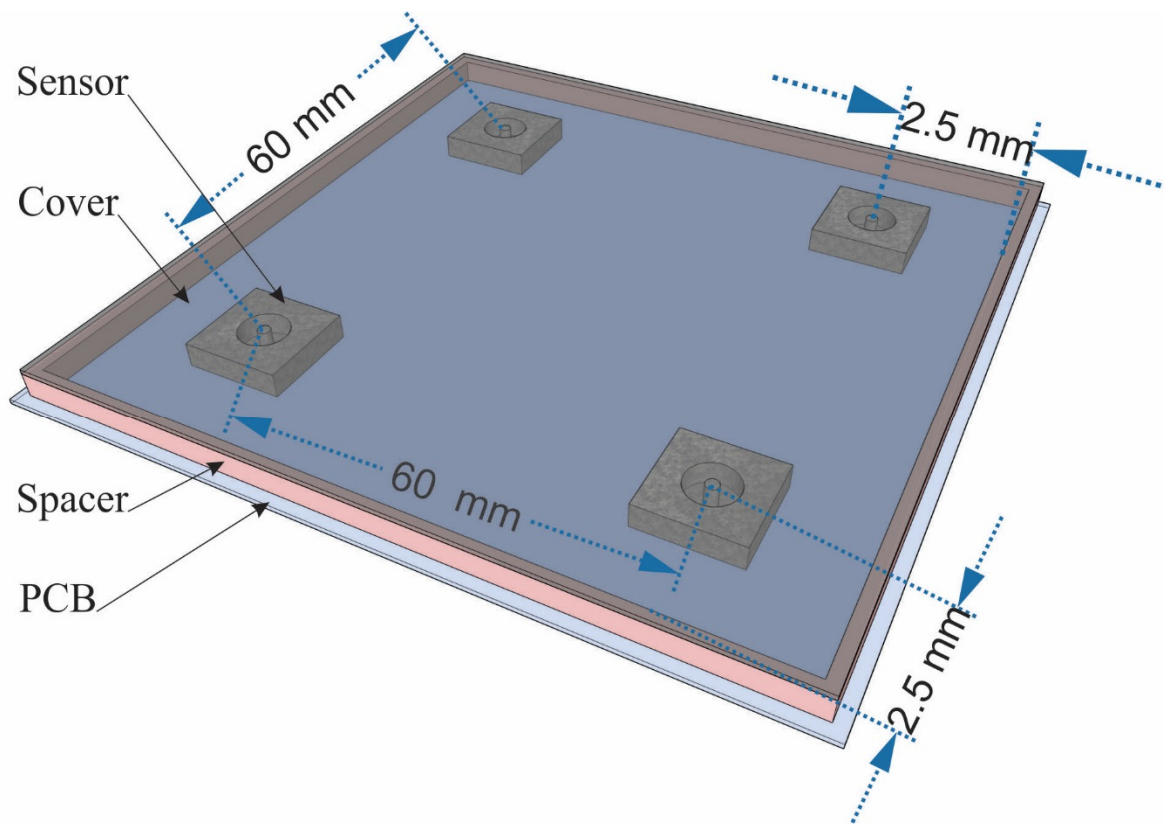


Figure 3-23 Geometric scheme of the sensor array [141] © [2018] IEEE

## 3.8 Sensitivity analysis on the multi-axis sensor array

Numerical studies on the response from the multi-axis sensor array have been done by ANSYS in terms of a fixed-amplitude normal load and a pure shear load applied at various locations on the working area, respectively. The sensing elements were powered by 3 volts DC. A 300-mN normal force was applied on the cover glass plate of the sensor array. The response data at different locations have been collected with probing incremental steps of 5 mm in either x or y directions for evaluating the whole 60 mm × 60 mm area. Outputs from four sensing elements of the sensor 1 has been plotted in Figure 3-24. The highest output was generated as the probe applying force at the top of sensor 1 and much lower outputs existed if the force was located at the rest of three

39

corners. The average outputs from the four tactels have been extracted and plotted in Figure 3-25 if the sensor was powered by 1 volt and the force was 200 mN. The simulation results trended similarly as the normal force sensor array. Specifically, as the force moving closer to the top of the mesa, the outputs of the sensor increased till they reached peaks. The performance of the sensor array was functional at the working area of 60 mm × 60 mm. Notably, the outputs showed some differences comparing the four channels from the same tactile cell. The peak sensitivity was found at four corners of the assembling, with value of 0.35 mV/mN•V.
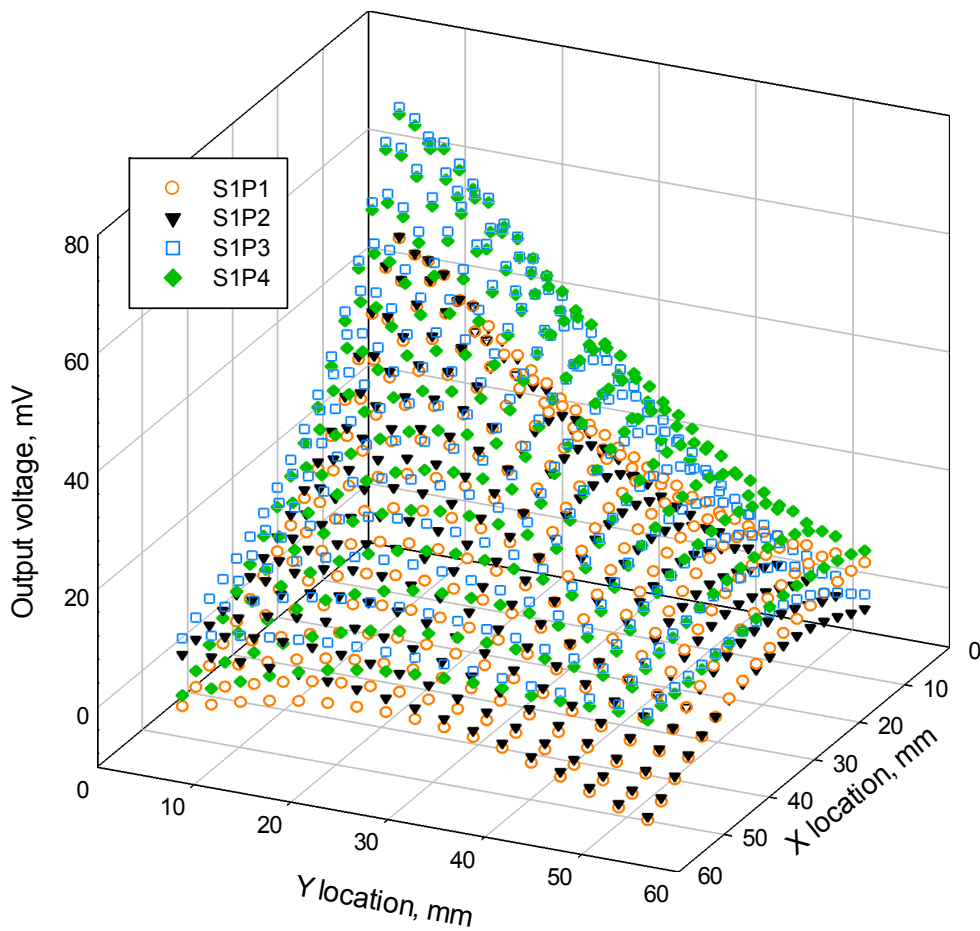


Figure 3-24 Outputs from four sensing elements of sensor 1
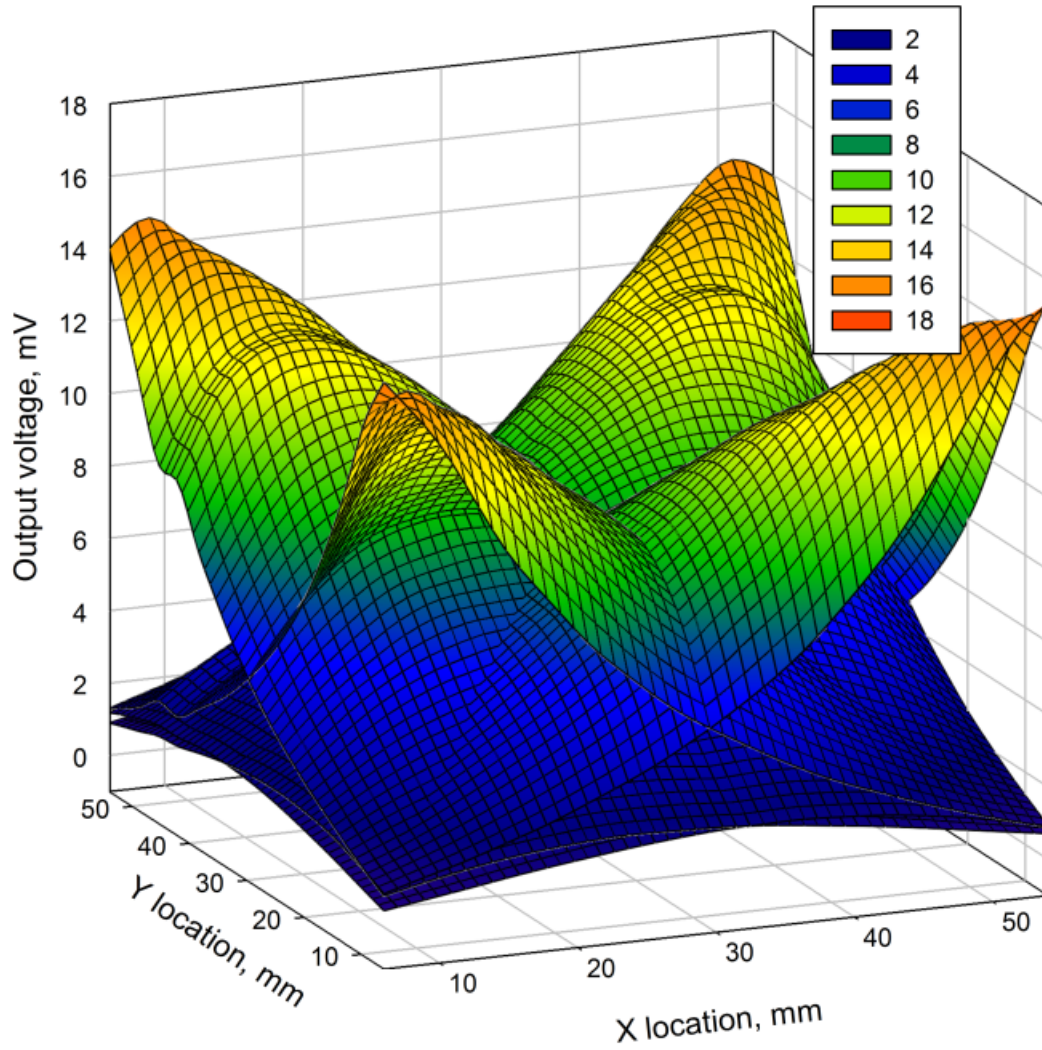
Figure 3-25 Average output voltage at various locations from four sensors
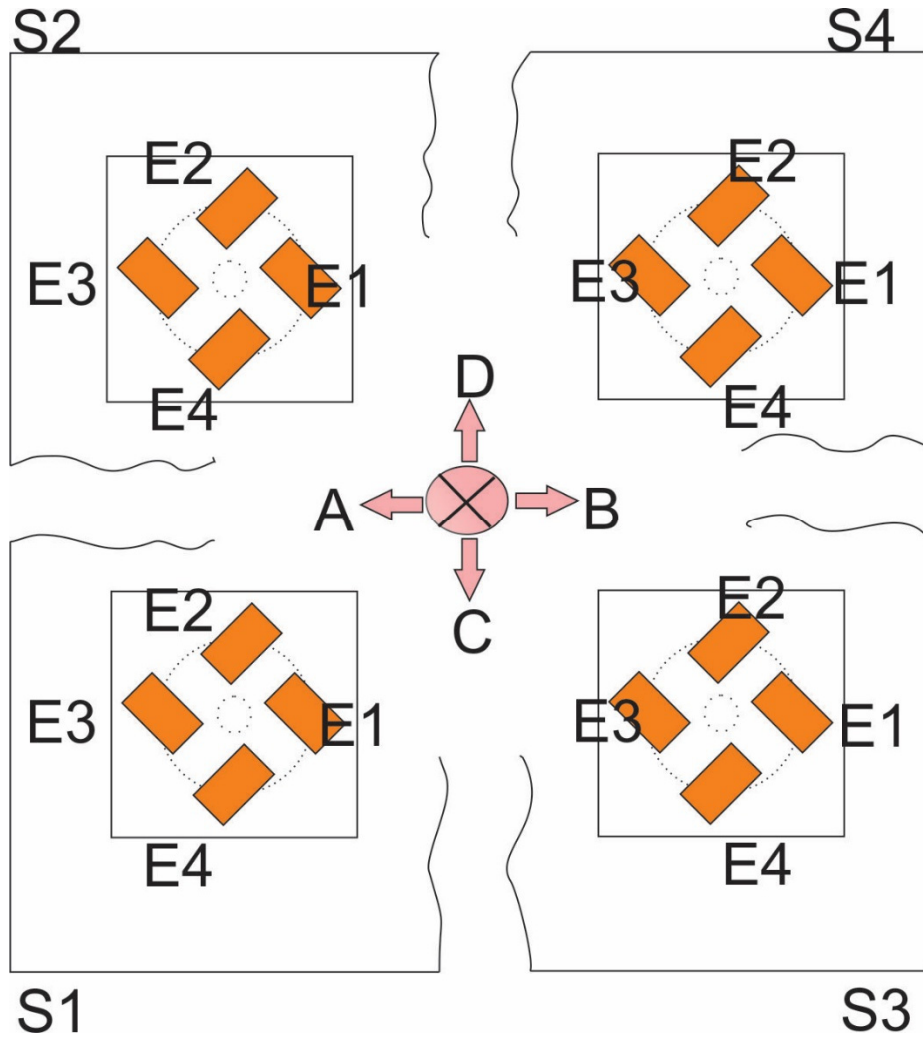
Figure 3-26 Evaluation scheme on shear force at the center of the sensor array in four directions (A, B, C, D respectively) with preloading of normal forces

Table 3-2 Qualitatively anticipated responses of all 16 elements in terms of the shear force in four directions with a preloading normal force, ++ stands for increasing of output voltage, -- stands for decreasing of output voltage, o stands for slightly changing either increasing or decreasing © [2018] IEEE

|  | A | B | C | D |  | A | B | C | D |
|---|---|---|---|---|---|---|---|---|---|
| S1E1 | -- | ++ | o | o | S2E1 | -- | ++ | o | o |
| S1E2 | o | o | -- | ++ | S2E2 | o | o | -- | ++ |
| S1E3 | ++ | -- | o | o | S2E3 | ++ | -- | o | o |
| S1E4 | o | o | ++ | -- | S2E4 | o | o | ++ | -- |
|  | A | B | C | D |  | A | B | C | D |
| S3E1 | -- | ++ | o | o | S4E1 | -- | ++ | o | o |
| S3E2 | o | o | -- | ++ | S4E2 | o | o | -- | ++ |
| S3E3 | ++ | -- | o | o | S4E3 | ++ | -- | o | o |
| S3E4 | o | o | ++ | -- | S4E4 | o | o | ++ | -- |

Shown in Figure 3-26, a qualitative evaluation scheme was depicted. In this schematic figure, one finger was employed to press the central area of the sensor array. Shear force was applied whilst keeping the normal force (pressing) as a preloading. Four scenarios were prompted with the shear force component in four different directions. The four sensors in the array were labeled as *S1, S2, S3, S4*, respectively. Each sensor had four elements marked as *E1, E2, E3, E4*. Table 3-2 showed the anticipated responses from the sensor array corresponding to shear forces in four directions, according to the previous shear test scheme shown in Figure 3-26. A conclusion could be drawn that the four sensors responded identically to the shear force; Applying forces in different directions would swap the voltage increments to corresponding elements. This phenomenon would be used for further characterizations of the shear force later. The anticipated responses of the sensor array had been examined by simulations results as shown in Figure 3-27.
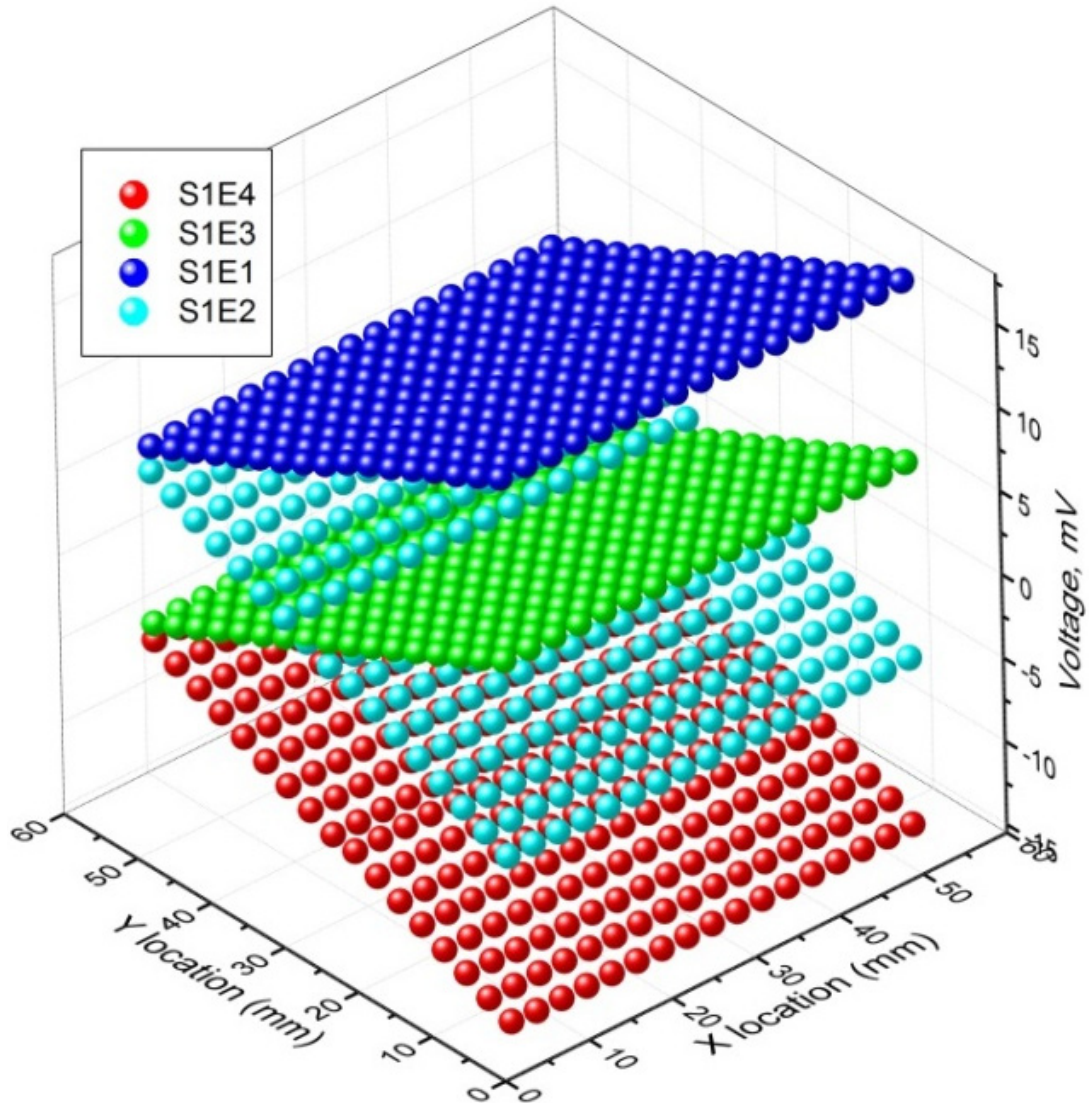
Figure 3-27 Response from one sensor in the sensor array on a shear force along the x

direction © [2018] IEEE

Since the embodiment of the sensor array was consisted of four multi-axis tactels, the performance of the sensor array on sensing the shear force could be evaluated. The numerical analysis has been modeled by applying a 300-mN shear force at the x direction. The results from one tactel were shown in Figure 3-27 above. The results from four elements (denoted by *E1, E2, E3, E4*) within one tactel indicated that the outputs remained the same if the force stayed in the same coordinate at y-axis with changing x-location. Notably, responses of the shear force from each piezoresistive element formed a flat plane, which showed that the sensor performed linearly. Moreover, the output was related with the location in the direction perpendicular to the applied force in a Cartesian coordinate. The sum of outputs from one sensor at any point within the sensing

44

area, in terms of a shear force, remained as zero. This was the similar behavior as using the sensor solely for measuring pure shear forces (refer to Figure 3-20). This characteristic was taken as the signature of this configuration of the sensor array, which proved to be useful for decoupling the force and location information, especially when the normal force and shear force are combined as a multi-axis force.

# Chapter 4.  Fabrication and Packaging[2]

## 4.1 Overview

This chapter discussed several aspects on the fabrication and packaging of the sensor array, including Boron diffusion, mask design, process flow and some obstacles confronted during the development phase. The normal (uniaxial) force sensor was tentatively fabricated using DSP (Double-Side Polished) wafers to establish a reliable process flow. After solving initial challenges, the devices were eventually fabricated by adopting SOI (silicon on insulator) wafers to accomplish a uniform membrane. Most of the fabrication procedures were done in the nanoFAB except the Boron diffusion, which was performed in MEMS/NEMS Advanced Design Lab of University of Alberta. The normal force sensor design was implemented by using 6 layers of masks for the proof-of-concept. Similarly, the multi-axis force sensor has also been fabricated using SOI wafers with another set of masks. Packaging solutions have been developed for both sensor arrays. Some in-process characterizations have also been elaborated in this chapter.

## 4.2 Boron diffusion

Silicon diffusion is a fabrication procedure in which the dopants are added into the wafer, which will change its electronic property as a semiconductor. Common ways for doing the diffusion include the thermal diffusion and the ion implantation. Following sections will discuss these two diffusion approaches, considering both have been adopted in this research.

### 4.2.1 Thermal diffusion

Diffusion happens faster in a high temperature environment. Thermal Boron diffusion was achieved by a typical two-step thermal diffusion processes including the pre-deposition and annealing[142]. The pre-deposition was also named as the constant-source diffusion.  Because the ambient environment was saturated by the boron dopants and maintained at the highest concentration at that temperature. Whilst, the annealing was also named as the limited-source diffusion or drive-in. Because without the dopant source, no extra dopant atoms were added into the doping furnace chamber. This high temperature environment was usually obtained in a quartz furnace which was automatically controlled by its controller.

---

[2] Some of the materials in this chapter has been published by Yue *et.al.* [137][140][141]

The concentration of dopants for the constant-source diffusion can be obtained by the complementary error function which is given by[143]

$$N(x,t) = N_0 erfc(x/2\sqrt{Dt}) \tag{4-1}$$

The total number of impurity atoms per unit area in the silicon was called the dose $Q$, with the unit of atoms/cm$^2$, was given by equation:

$$Q = \int_0^\infty N(x,t)dx = 2N_0\sqrt{Dt/\pi} \tag{4-2}$$

Where $D$ standing for the diffusion coefficient which could be obtained by equation:

$$D = D_0\exp(-E_A/kT) \tag{4-3}$$

For the Boron diffusion, $D_0$ was 10.5 cm$^2$/sec and $E_A$ was 3.69 eV. The doping temperature was 900 °C, which was equivalent to 1173K, and $k$ was a constant equal to 8.614 $\times 10^{-5}$. $N_0$ was $10^{20}$ /cm$^3$ depending on the solid solubility of Boron at the doping temperature. The diffusion coefficient was eventually calculated as $1.45\times10^{-15}$ cm$^2$/sec and $Q$ as $2.23\times10^{14}$/cm$^2$.

For the annealing process, the concentration in silicon was calculated by the Gaussian distribution:

$$N(x,t) = \left(\frac{Q}{\sqrt{\pi Dt}}\right)exp - (x/2\sqrt{Dt})^2 \tag{4-4}$$

As the temperature in annealing increased to 1000°C, $D$ was changed to $2.55\times10^{-14}$cm$^2$/sec. The background doping concentration of n-type silicon wafer was given by the equation:

$$\rho = \frac{1}{q\mu_e n}, \ n = N_D - N_A \tag{4-5}$$

The junction depth, at which the concentration of boron dopants was equal to the concentration of the background n-type dopants, was calculated by the equation:

$$N(x,t) = C_B \tag{4-6}$$

Where $C_B$ denoting the background dopants concentration. Therefore, the junction depth was equal to 1.437um. But during the oxidation procedure, the thickness of silicon would be consumed by 45%. Therefore, the junction depth decreased to 1.212um which was described as following equation: 1.212 um = 1.437 um - 0.5 um $\times$ 45%.
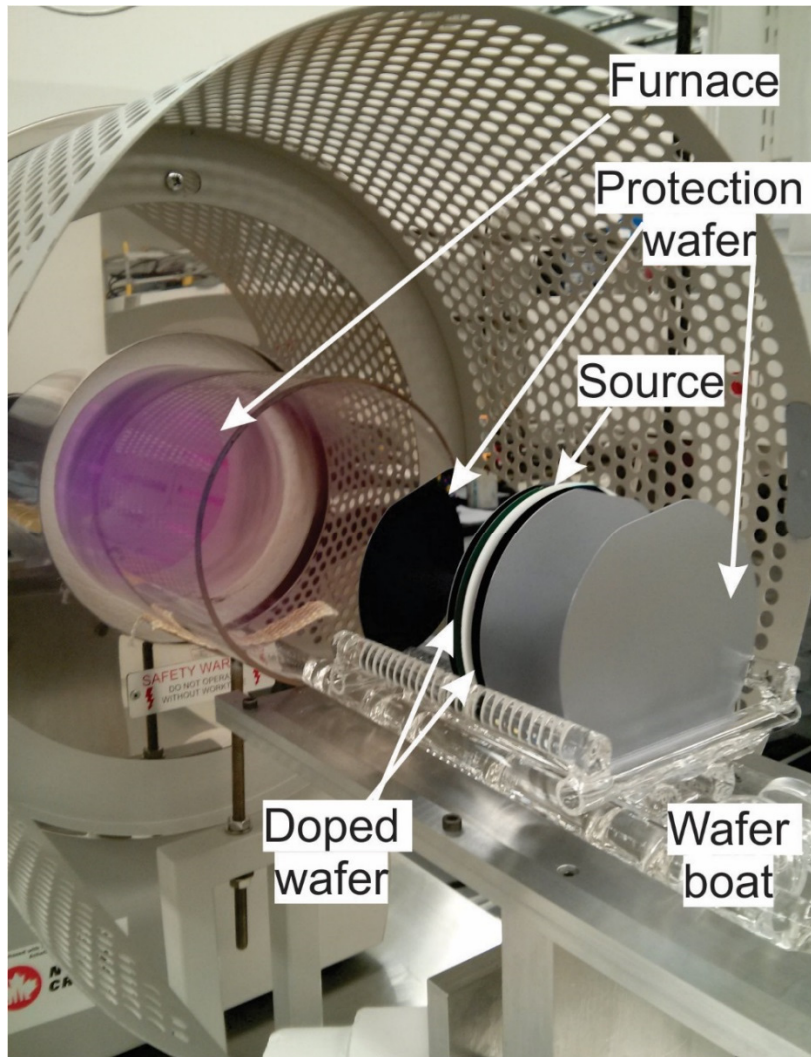
Figure 4-1 Thermal doping setup

The diffusion process was conducted in an isolated quartz furnace with a temperature control module. The temperature of the furnace was firstly raised up to 700 °C and kept as it for one hour to eliminate any moisture with a nitrogen flow at a speed of 10 L/minute. As shown in Figure 4-1, the white plate was the Boron source (BoronPlus® GS-126), encompassed by two pieces of device wafers which were to be doped. Two or more pieces of protecting wafers were placed outside the device wafers, to withstand the thermal shock and potential nitrogen turbulent flows, which could disturb the uniform saturated Boron atmosphere across the device wafer. All the wafers and the source were located on a wafer boat which was made of quartz owing to its stability and inertness even at a high temperature. The quartz boat together with wafers and the source were pushed inside the furnace at a speed of one inch per15 seconds[71], to avoid the dramatic thermal shock induced by the temperature difference between the inside of the furnace and the ambient. The

furnace was capped by a thermal isolating lid after loading the boat and wafers. Then the temperature of the furnace was raised up to 900 °C, at which point the nitrogen flow rate was changed to 5 L/minute. As shown in Figure 4-2, the temperature profile was plotted. The wafers were doped for 45 minutes at 900 °C.
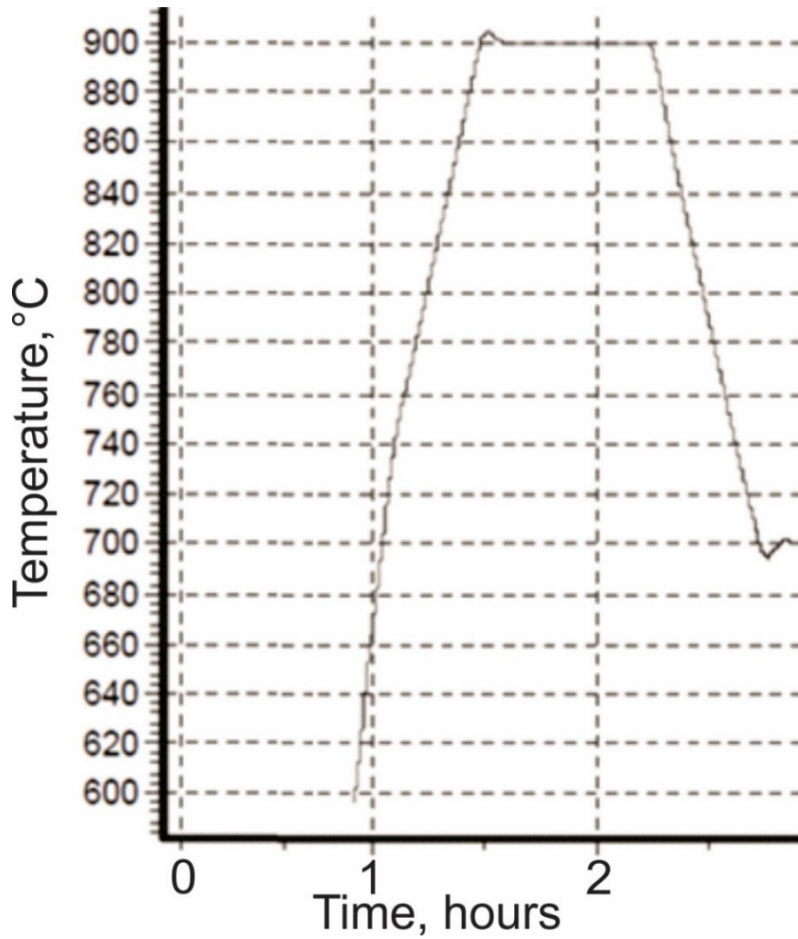


Figure 4-2 Temperature profile for the doping
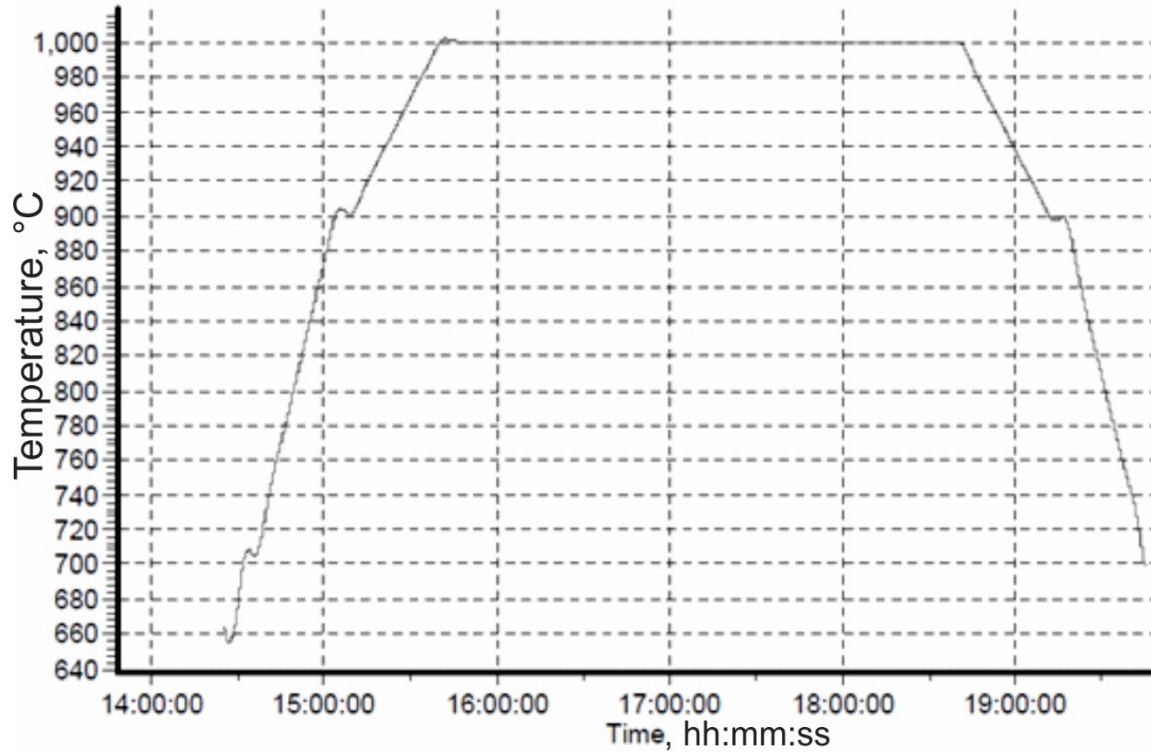
Figure 4-3 Temperature profile for the annealing

After diffusing the wafer with the boron source, the annealing process was performed by taking the source out of the furnace at around 700 °C first. As shown in Figure 4-3, the annealing was done in the same furnace for 3 hours at 1000 °C. The profile contained the ramp-up and ramp-down processes, which were inevitable for this procedure. This was also the key reason leading to the variations on the doping concentration comparing with those theoretical models.

To further understanding the profile of dopants inside silicon wafer after the pre-deposition and annealing processes, calculations have been simulated using MATLAB® and results were plotted in Figure 4-4. At the device surface where the distance $x$ was equal to zero, the dopant concentration was equal to the maximum solubility of the Boron dopant at 900 °C. It dropped down to the level equal to the background concentration value. Since the order of the dopant number had significant differences between the boron dopants and background dopants, the net impurity of carriers here was considered as the number of dopants (Boron).
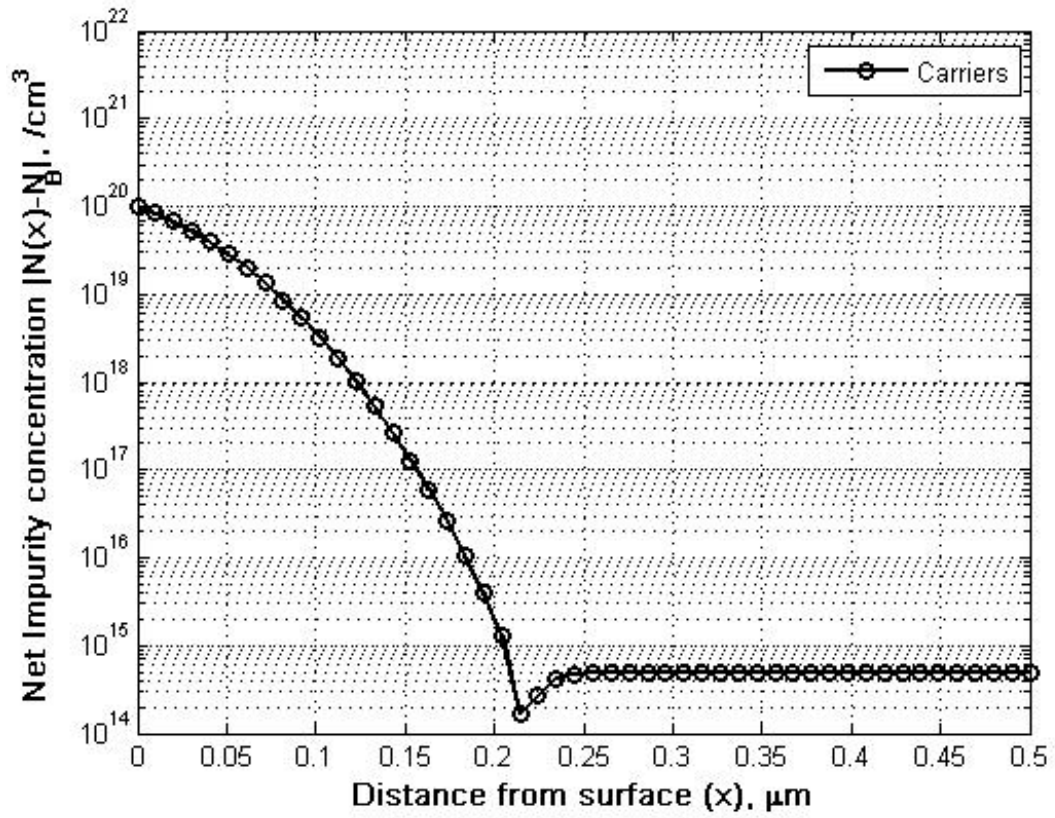
Figure 4-4 Simulated profile of carriers (Boron) in silicon after thermal doping
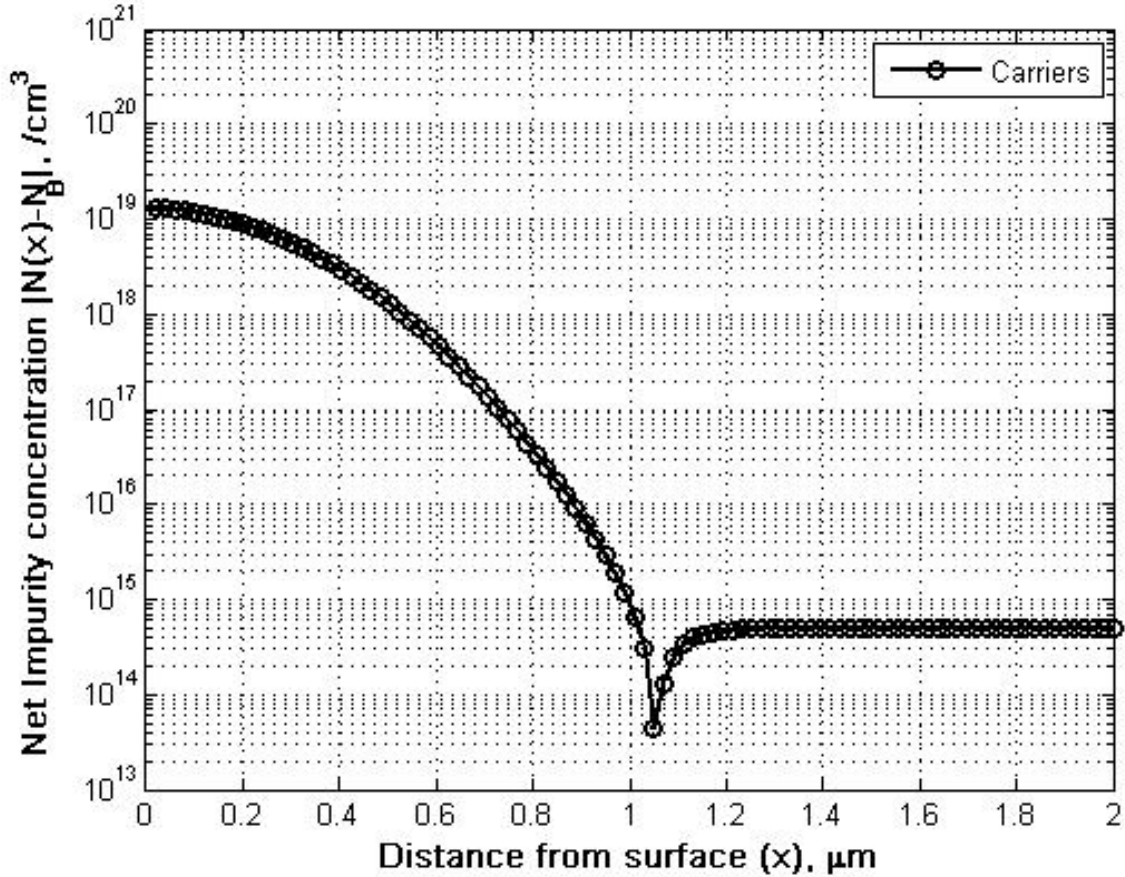
Figure 4-5 Simulated profile of carriers (Boron) in silicon after thermal annealing

The concentration profile of the dopants would be changed by the annealing. During the annealing procedure, the surface concentration of dopants would decrease because part of the dopants escaped from the silicon wafer by the nitrogen air flow. The rest of Boron atoms diffused deeper inside the silicon wafer. A profile depicting this change was simulated as shown in Figure 4-5. Notably, the surface concentration of the dopants has dropped one log order. The junction depth moved to 1 um.

### 4.2.2 Ion implantation

The ion implantation was a procedure introducing bombardments of high-energy ions into a wafer, to mix the dopant elements with the silicon atoms. The accelerated dopant ions were controlled by a biased electric field and penetrated the wafer surface and stopped at a certain depth due to a series of electronic and nucleic collisions. Based on LSS theory, the profile of ions below the wafer surface can be approximately predicted as[144]

$$C(x) = \frac{Q_{tot}}{\sqrt{2\pi}\Delta R_p}\exp(\frac{-(x-R_p)^2}{2(\Delta R_p)^2}) \tag{4-7}$$

where $R_p$ was the projected range and $\Delta R_p$ was the standard deviation or projected straggle. $Q_{tot}$ was the total dose of ions, which was monitored by a Faraday cup[145]. A simulation was provided below demonstrating the profile of the net-concentration from 4 times of implantations to achieve the required junction depth and the surface doping level. The sharp trophy indicated the junction interface where was the concentration of the background Phosphorous overthrown the Boron.
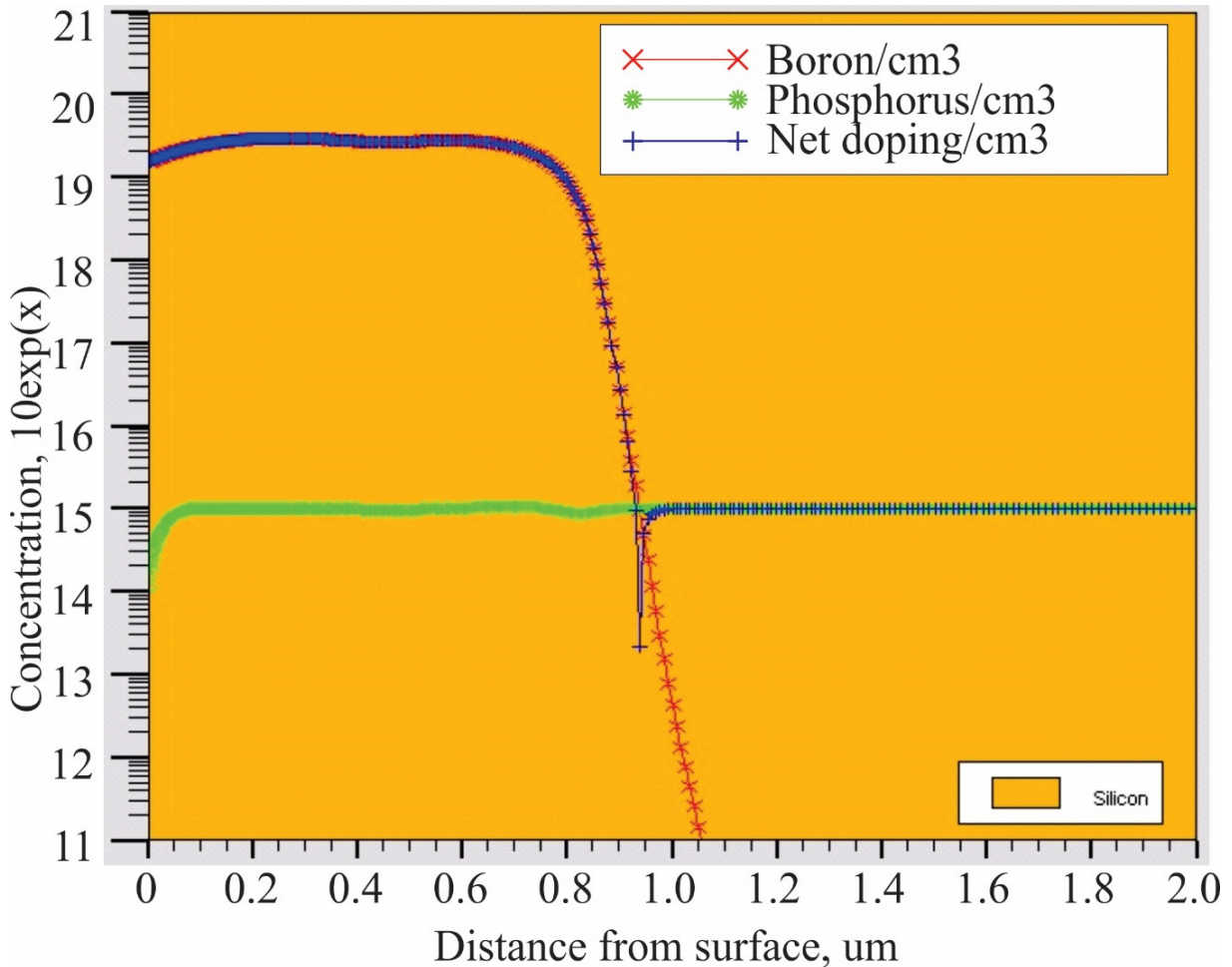


Figure 4-6 Simulated profile of implanted dopants (Curtesy of inex Inc.)

Advantages of ion implantations are significant since the surface concentration of dopants can be controlled by the dose of ionized dopants; the depth of the doped region can be monitored by tuning the ion acceleration. Besides, a uniform doping profile across the doped layer can be achieved by the combination of several precisely deployed sub-procedures, as adopted in this work, which would produce the high-quality doped piezoresistor. The crystalline damage caused by high

energetic ions could be recovered by performing a rapid thermal annealing(RTA) procedure to the wafers.

## 4.3 Mask design for the uniaxial force sensor

Two sets of masks have been designed for the uniaxial force sensor, using the L-Edit which is a mask designing tool in the software suite, the MEMSPro 6.0®. As shown in Figure 4-7, the uniaxial force sensor was designed to be a square-shape die with the size of 500 um × 500 um, with four aluminum pads which were 125 um × 125 um. The size of the rectangular four-terminal gauges was 50 um × 65 um in this figure. The membrane diameter was 350 um with a mesa in the diameter of 100 um. The aluminum trace width was 10 um. This set of masks was printed in an outsourcing manufacture named *inex Inc.* in Newcastle, UK.
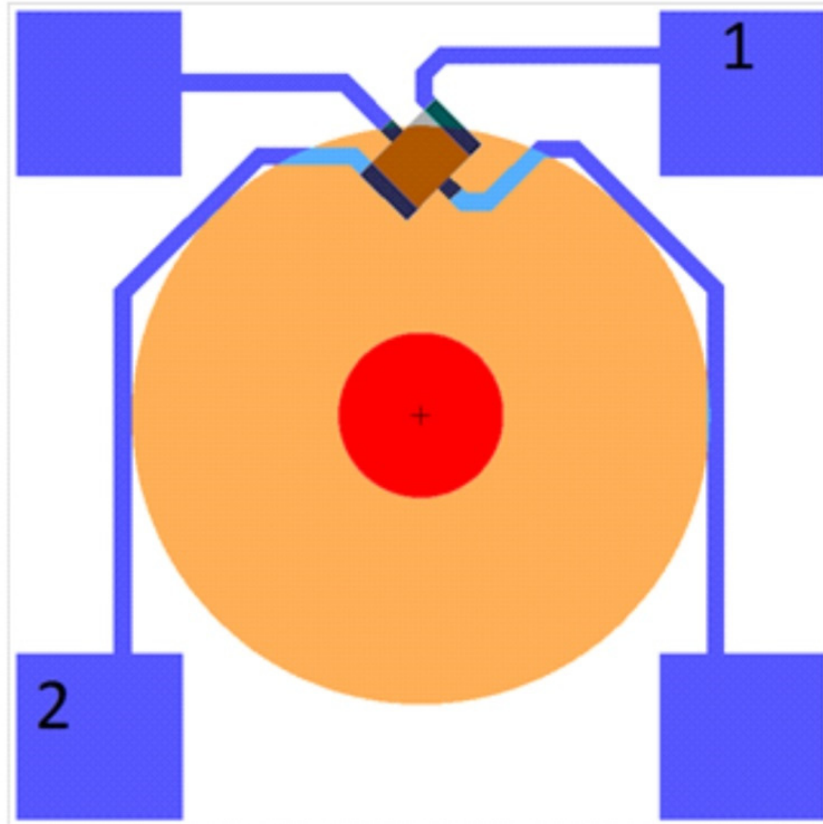
Figure 4-7 Mask of a normal force sensor for inex Inc.

To easily manipulate the sensor after dicing and accommodate to the equipment on campus, another set of masks (see Figure 4-8) was designed and used in nanoFAB for fabricating the die with the size of 3 mm × 3 mm. In this mask set, the size of the aluminum pads was changed to 1 mm × 1 mm. The pad size change would not affect the sensitivity of the sensor, since the pads were only used for electrical connections and the changes of the connecting resistance caused by the geometric variation was neglectable. Other critical parameters determining the sensitivity of the sensor, such as the geometry of the four-terminal gauge, the membrane diameter and the mesa diameter were the same as the previous smaller-footprint design.
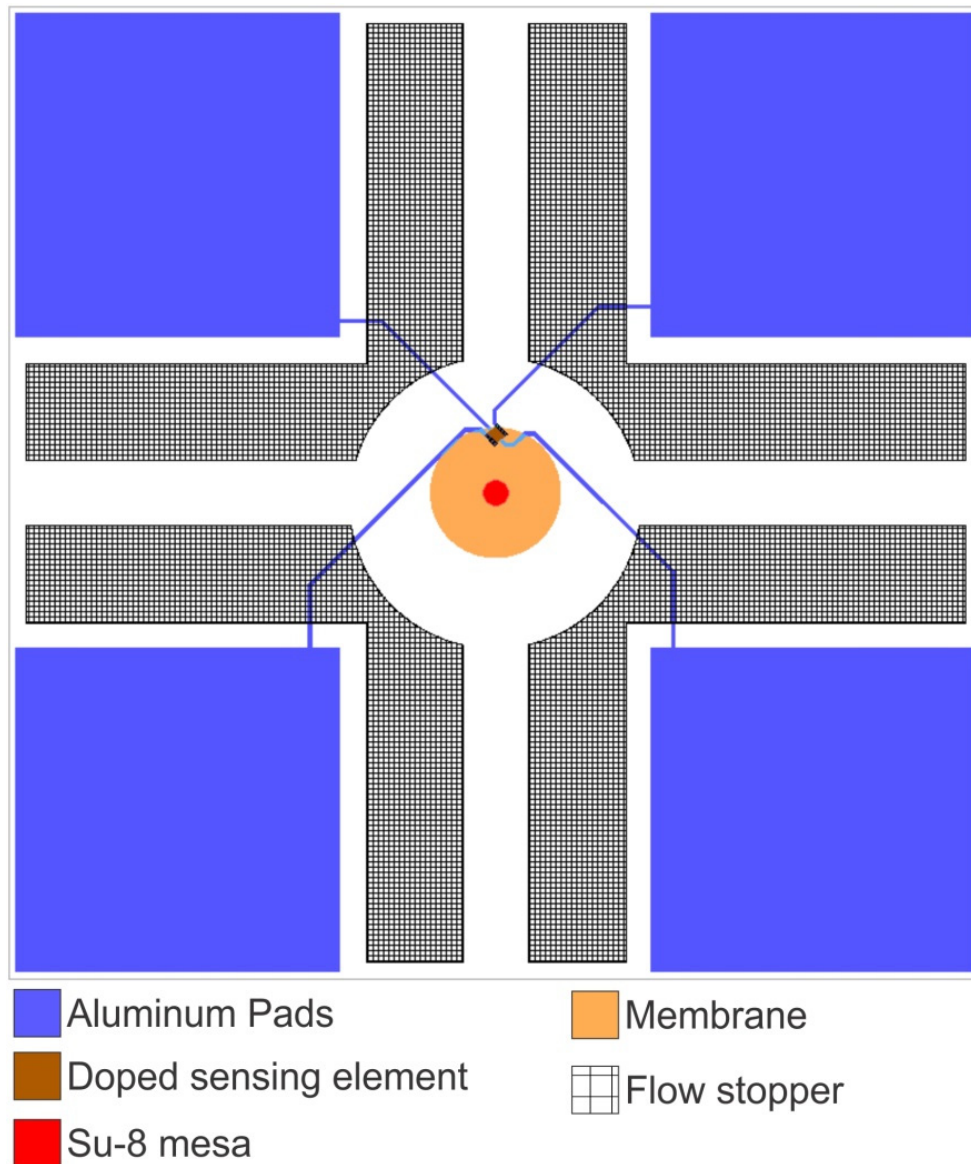
Figure 4-8 Mask of a normal force sensor used in nanoFAB

## 4.4 Mask design for the multi-axis sensor

The following section described the design of the mask set for fabricating the multi-axis sensor. The multi-axis (3D) force sensor had four sensing elements on the circular membrane. Owing to additional four-terminal gauges, the total number of output terminals were 8 channels with two power input terminals if the four sensing elements shared one common ground and one power supply, making 10 metallized pads. To use the planar space on the surface of the sensor and maintain the symmetry in the layout, 12 pads were designed on the top of the multi-axis force

sensor. The size of each pad was 450 um ✕450 um which was for having enough space for nine gold bumps. The geometric parameters of the multi-axis sensor have been discussed in Chapter 3. As sketched in Figure 4-9, the mask set has 6 layers, which were for the processes such as the boron doping, contact via, aluminum pads, membrane etch, SU-8 mesa and SU-8 flow stopper.
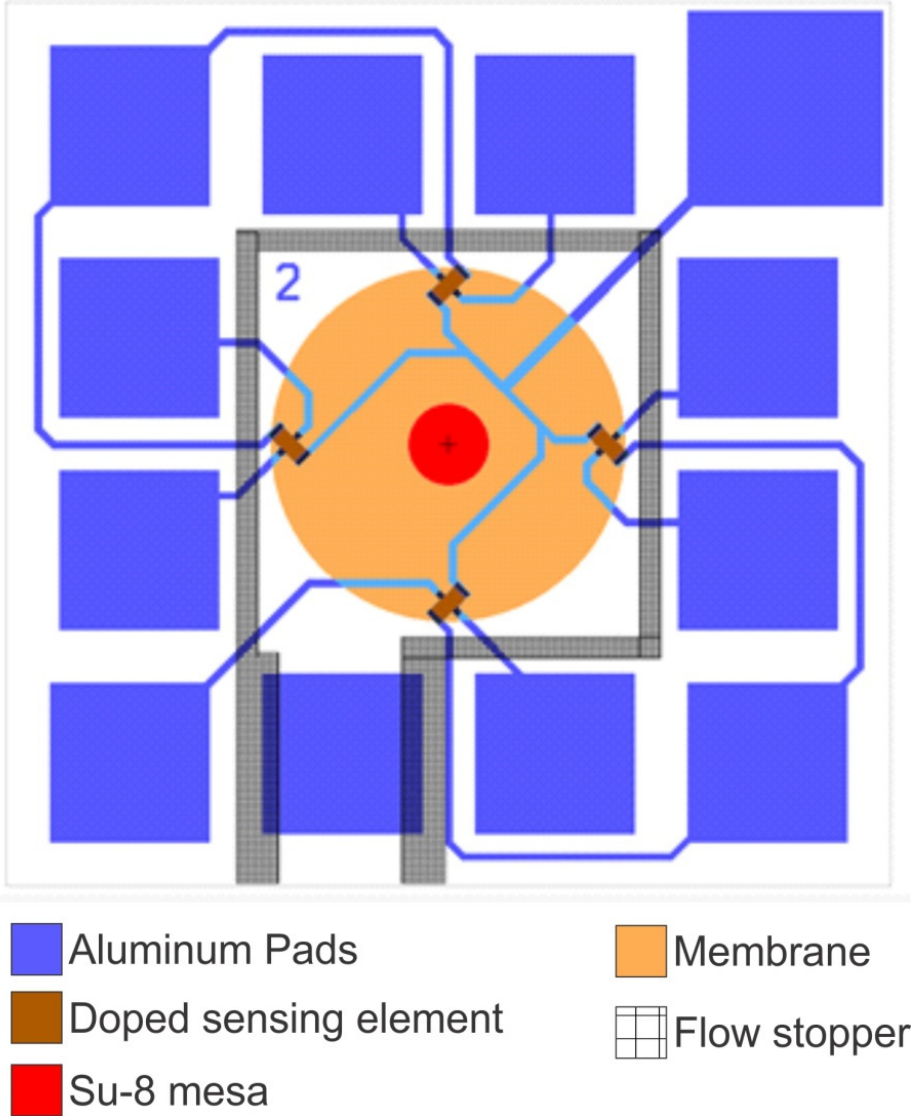


Figure 4-9 Mask of the 3D (Multi-axis) force sensor

## 4.5 Process flow of the fabrication

This section discussed the fabrication and its improvements involved in this project, including the initial process with the DSP wafer, the process flow designed for the outsourcing vendor, and the one adopted in nanoFab. Challenges and issues confronted during this phase has been introduced as well as modifications and solutions were included in this part.

**4.5.1 Process flow operated in nanoFAB**

(1)Oxidation

(2)Pattern Doping Windows

(3)Boron Doping

(4)Annealing

(5) Strip Oxide

(6) Oxidation

(7)Pattern Contact Via

(8)Sputtering Al

(9)Pattern Al

(10)Chromium Lift-off

(11) SU-8  Flow Stopper

(12)SU-8 Mesa

(13)DRIE

- ☐ Silicon
- ☐ Silicon Oxide
- ☐ Doped silicon
- ☐ Aluminum
- ☐ Chromium
- ☐ SU-8
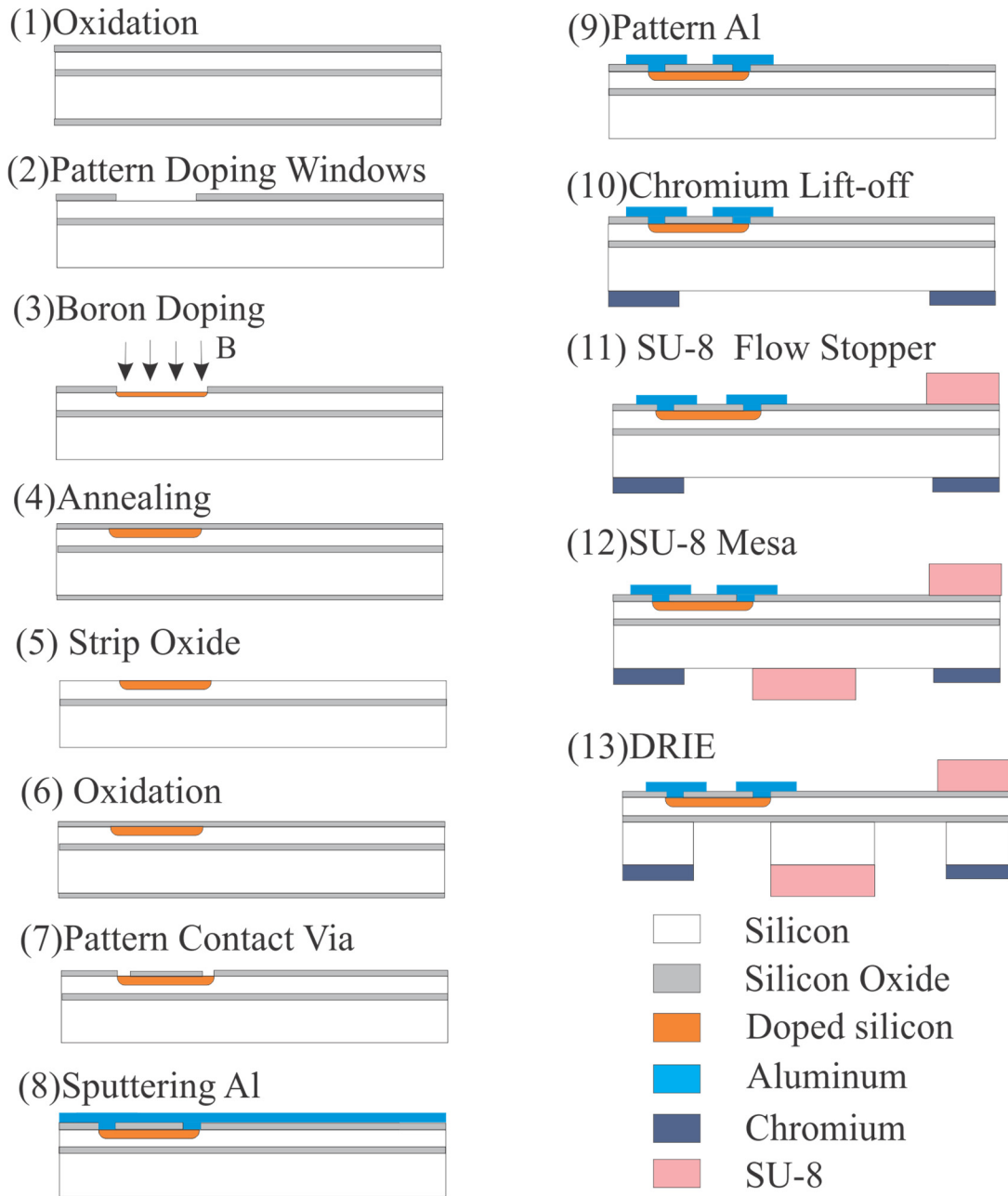
Figure 4-10 Process flow for both uniaxial force sensor and multi-axis force sensor © [2017] IEEE.

**1 Cleaning and Oxidation**

The cleaning of the SOI wafer was done by rinsing it in the Piranha Etch. The Piranha was a mixture solution of concentrated Sulfuric Acid (98%) and concentrated Hydrogen Peroxide (50%), with the volume ratio of 3:1. The wafer was immersed inside the Piranha solution for 15 minutes, removing any organic or metallic contaminations. Then the wafer was cleaned by DI water and

placed into a furnace for the thermal oxidation. A layer of silicon oxidation was formed by the wet thermal oxidation process. The wafer was placed into a furnace. Afterwards, the furnace temperature was ramped up to 1000 °C, and kept for 85 minutes, with a moist nitrogen inlet from a water bubbler heated at 95 °C. The flow rate of the humid nitrogen was set at 5 L/min. This procedure would yield the thickness of silicon oxide at around 500 nm.

### 2 Pattern doping windows

The first step for patterning the doping windows was to perform the lithography on the top of the oxide. Before the lithography, a HMDS procedure was recommended to improve the adhesion between the photoresist and the silicon oxide. Then the photoresist HPR-504 was spread on top of the wafer with a spinner at the speed of 500 rpm for 10 seconds, then span for 40 seconds at the speed of 4000 rpm, resulting a thin photoresist film with the thickness around 1.25um. After baking the wafer at 115 °C for 90 seconds in the vacuum chamber of the YES baking station and cooling down to the room temperature, the doping windows were patterned by the optical lithography with an exposure time of 3 seconds. The features would show up after developing the exposed wafer in the Developer 354 for 25 seconds. Rinsing the wafer with DI water to ensure no contaminants on the wafer surface was necessary for the following procedures. Patterns of the doping window should be checked under a microscope for the lithography quality.

This oxide layer was etched by an etchant named as the Buffered Oxide Etchant (BOE). Due to the small size of the doping window and the viscosity of the liquid etchant, the residual oxide usually existed at the doping region by the common protocol of BOE, since it only involved immersing the wafer inside BOE. To avoid this defect, the etchant was stirred carefully by an electromagnetic-driven bar at a rate of 130 rpm for about 14 minutes to 17 minutes, while the wafer was immersed inside it with the designated side facing down. After etching the doping window, the photoresist was removed by spraying Acetone on it. Then the wafer was rinsed by IPA firstly, followed by rinsing for five times with DI water to remove any residual hydro fluorides or organic solvents.

### 3 Boron Doping

The wafer was doped by the Boron source in the furnace at MEMS/NEMS ADL. The furnace was firstly ramped up to 700 °C, before loading with the source and wafers as described in Section 4.2. After loading the wafer and source, the temperature inside was ramped up to 900 °C. The

setup inside the furnace was kept for 45 minutes with a nitrogen gas flow at the rate of 5 L/minute. More details involving this procedure could refer to Section 4.2.

### 4 Annealing

After doping for 45 minutes, the furnace was cooled down to 700 °C and the source was taken out of the furnace, leaving the wafers inside. Then the furnace was ramped up to 1000 °C and maintained at this temperature for three hours. After cooling down the furnace below 150 °C, wafers could be safely moved out of the furnace for further procedures.

### 5 Strip the oxide

The oxide layer for doping windows needed to be removed after the doping was done. Due to the large area of oxide to be etched, the wafer was put into BOE for 20 minutes, with an electromagnetic bar stirring at the speed of 220 rpm. Then the wafer was rinsed 5 times by the DI water. The water would not form a thin film on the surface of the wafer if the oxide had been completely removed. Because the bare silicon surface was hydrophobic. This feature could be used as the sign of the complete removal of the oxide mask instead of actually measuring the residual oxide thickness.

### 6 Wet thermal oxidation

A layer of oxide was synthesized by the wet thermal oxidation in the furnace at the temperature of 1000 °C for 85 minutes. The thickness of the oxide was about 500 nm. It needed to be measured using an equipment named Filmapper®. This oxide layer would be used as the insulator layer between the metal and the silicon.

### 7 Pattern the contact via

Similarly, as patterning the doping window, the contact via was etched on the oxide layer. Firstly, an HMDS procedure was span on the wafer to enhance the adhesion of the photoresist on the silicon oxide. The HPR-504 photoresist was applied and patterned by the optical lithography. After developing the pattern of the contact via, the wafer was put into the BOE for about 15 minutes to etch the via. Then the photoresist was removed, and the wafer was rinsed and dried by a spinning dryer.

### 8 Sputtering Aluminum and pattern the Aluminum

The bare silicon could be easily oxidized if it was exposed to the ambient air even for a few minutes, due to its chemical activity, forming an intrinsic layer of oxide with thickness of a few nanometer[146]. As the exposed time elapsed, the thickness of this native oxide layer grew. A fair

solution to this issue was to sputter the Aluminum film immediately after the procedure #7, when the contact via was just etched and the wafer was cleaned by water rinsing. The Aluminum sputtering was done for 50 minutes with the sputtering system (from Kurt J. Lesker Company) called the Floyd in nanoFAB. This Aluminum layer was patterned by the photolithography using the HPR-504 photoresist. This procedure was similar as patterning the doping windows. After developing the photoresist for traces and pads, the wafer was immersed into the aluminum etchant for 25 minutes while manually shaking the wafer rack, to get a uniform etching. After etching the aluminum, the wafer was rinsed with DI water for 5 times and dried in a spinning dryer.

To get ohmic-contact[147] between the doped silicon and the aluminum, and electrically broken the native oxide layer, an annealing procedure was done in the furnace. The wafers were loaded in the furnace at the 450 °C and kept inside for 45 minutes, then moved out of the furnace. During the annealing procedure, a nitrogen flow at the rate of 10 L/minute was used for protecting the wafer and metal from the oxidation. However, the oxidation of the silicon at the backside has inevitably happened when the wafer was taken out of the furnace for cooling down to room temperature. This thin layer of silicon oxide was about 30 nm. This was found to affect the performance of the Deep Reactive Ion Etching(DRIE). To remove this thin layer of silicon oxide, a BOE procedure was performed afterwards. Firstly, a layer of HPR-504 was applied as a protection layer on the surface which had the aluminum traces and pads. Then the wafer was immersed with BOE for 3 minutes to etch the oxide.

## 9 Chrome lift-off

At the etched surface of the wafer from the process section 8, the negative photoresist AZ5214 was applied at a spreading velocity of 500 rpm for 10 seconds and a spinning velocity of 4000 rpm for 40 seconds. The photoresist was baked for 40 seconds at 90 °C. It was cooled down and rehydrated for 15 minutes. Then the photoresist was patterned by the optical photolithography with 5 seconds of exposure time. The wafer was baked for 60 seconds at 110 °C and left aside for 15 minutes again to rehydrate the baked photoresist from the moisture in the ambient environment. This rehydration could also be achieved by rinsing it in DI water. After the rehydration, the photoresist was exposed without any mask for 60 seconds, which was also called the flooding exposure. Ultimately, the photoresist was developed by the developer MF 319 for 30 seconds.

A layer of Chromium was sputtered on top of the AZ5214, using the Floyd sputtering system for 7 minutes. The thickness of the Chromium was about 161 nm, according to the sputtering rate

which was 23 nm/minute. The wafer with Chromium was immersed into the Acetone for bathing more than 20 hours with the Chromium side facing down. Most of the Chromium on the AZ 5214 would fall off naturally inside the Acetone solution due to the gravity. To remove the residual Chromium and reveal clean patterns, the Acetone bath setup was moved into an ultrasonic generator and bathed for 3 to 5 minutes with the ultrasonic wave on. Then wafers were rinsed and dried after all the residual Chromium removed within the to-be-etched regions.

**10 SU-8 flow stoppers**

SU-8 2050 was used for making the flow stopper on the top of the device surface. This negative photoresist was spread on the wafer at a speed of 500 rpm for 10 seconds, under the fume-hood protection from the UV light contamination emitted by the lab light bulb. The speed of the spinner ramped up to 3500 rpm and kept for 30 seconds, to thinning the photoresist film further. Ultimately, the SU-8 was span at 5000 rpm for another 30 seconds. The measured film thickness was around 25um. The wafer was pre-baked for 3 minutes at 65 °C then baked at 95 °C for 5 minutes.

Due to the viscosity of the SU-8, an SU-8 residual ring region would form at the edge of the opposite side of the wafer. This residual would cause sealing issues on the vacuum chuck of the lithography machine. Therefore, it had to be removed carefully by wiping the wafer edge with the acetone. After cleaning the unintended SU-8 residual, the wafer was patterned using the optical photolithography by an exposure time of 12 seconds. Then the wafer was baked at 65 °C for one minute, which preheated the photoresist before the post-bake at 95 °C for four minutes. After cooling the wafer to room temperature, and the SU-8 was developed for 4 minutes with the SU-8 developer.

**11 SU-8 Mesa**

To install the SU-8 mesa in the central region of the circular area where was no chromium, the wafer was bonded on the top of a carrier wafer. The bonding material was the crystal bond (Crystalbond$^{TM}$ 555 from TED PELLAR Inc.). SU-8 2050 was spread on the wafer at a speed of 500 rpm for 10 seconds, firstly. Then the speed of the spinner was ramped up to 3500 rpm and kept for 40 seconds. Similarly, as the flow stopper, the photoresist was pre-baked and baked at 65 °C for three minutes and at 95 °C for 5 minutes, respectively. After 15 minutes of the rehydration, the SU-8 was exposed for 12 seconds on the lithography machine. Then the wafer was post baked at 65 °C for one minute and at 95 °C for four minutes. On the baking deck, the SOI wafer was separated from the carrier wafer by heating the stacked wafers. Ultimately the SU-8 was developed

for four minutes and the wafer was rinsed with DI water and dried by blowing compressed air on it. Some crystal bond residual on the wafer could be removed by rinsing the wafer in boiled DI water for two times.

**12 Deep Reactive Ion Etching**

The device layer of the SOI wafer used for fabricating the sensor was 10 microns, by which defined the thickness of the membrane. The membrane was done by Deep Reactive Ion Etching (DRIE). Because the generated pressure difference between two sides of the wafer in the procedure could compromise the completeness of the thin membrane, ie. causing the breakage. Therefore, the SOI wafer was bonded to a carrier wafer before the DRIE, using the crystal bond. Typically, the membrane was accomplished by about 400 to 600 cycles of BOSCH processes within the DRIE machine. This etch cycles could change due to different etching rates accounted for various machine conditions.

Then the wafer was separated from the carrier wafer, cleaned, flipped and bonded on top of another carrier wafer for dicing. A layer of HPR 504 was spread on the surface of the wafer for the protection of the Aluminum traces and pads before putting the wafer onto the dicing machine. More details on the dicing would be discussed in the section 4.6.6 later.

**4.5.2 Process flow operated in outsourcing foundry**

Another process flow has also been adopted as the device-development-round for accommodating the outsourced foundry. This process flow has fewer procedures than what have been done in nanoFAB described in previous section 4.5.1, if taking considerations of changing the Boron diffusion into the ion implantation. The ion implantation was chosen for the Boron diffusion in this process flow. The fabrication (see Figure 4-11) started with an SOI wafer by doing the lithography for patterning the doping window, that meant the photoresist layer was used as the mask for ion implantation. The Boron ion implantation was performed to add Boron dopants inside the wafer, building piezoresistors with a surface sheet resistance at around 50 $\Omega$/sq with a junction depth of about 1 um. After removing the photoresist mask, a rapid thermal annealing(RTA) needed to be done to recover the damaged crystalline structure. To add an insulation layer, a wet thermal oxidation was done to form a layer of 500nm oxide on the wafer. The lithography and BOE were performed on the oxide to etch the contact via. A 700nm Aluminum layer was then sputtered on the top of the oxide and patterned to define the conductive pads and traces. The Chemical-Mechanical-Polishing (CMP) was supposed to be performed for thinning the wafer down to 100

um to get a thinner profile. However, this was not completed due to equipment limitations and budget issues. At the surface of the handle layer, the Chromium lift-off was done to define the membrane geometry. At the front side of the wafer, an SU-8 layer was used for constructing a flow stopper around the membrane region. By flipping the wafer again, the mesa was installed in the center of the exposed region in the Chromium layer. Ultimately, the membrane was etched by the DRIE until the reduction of the silicon reached the insulator layer in the SOI wafer.
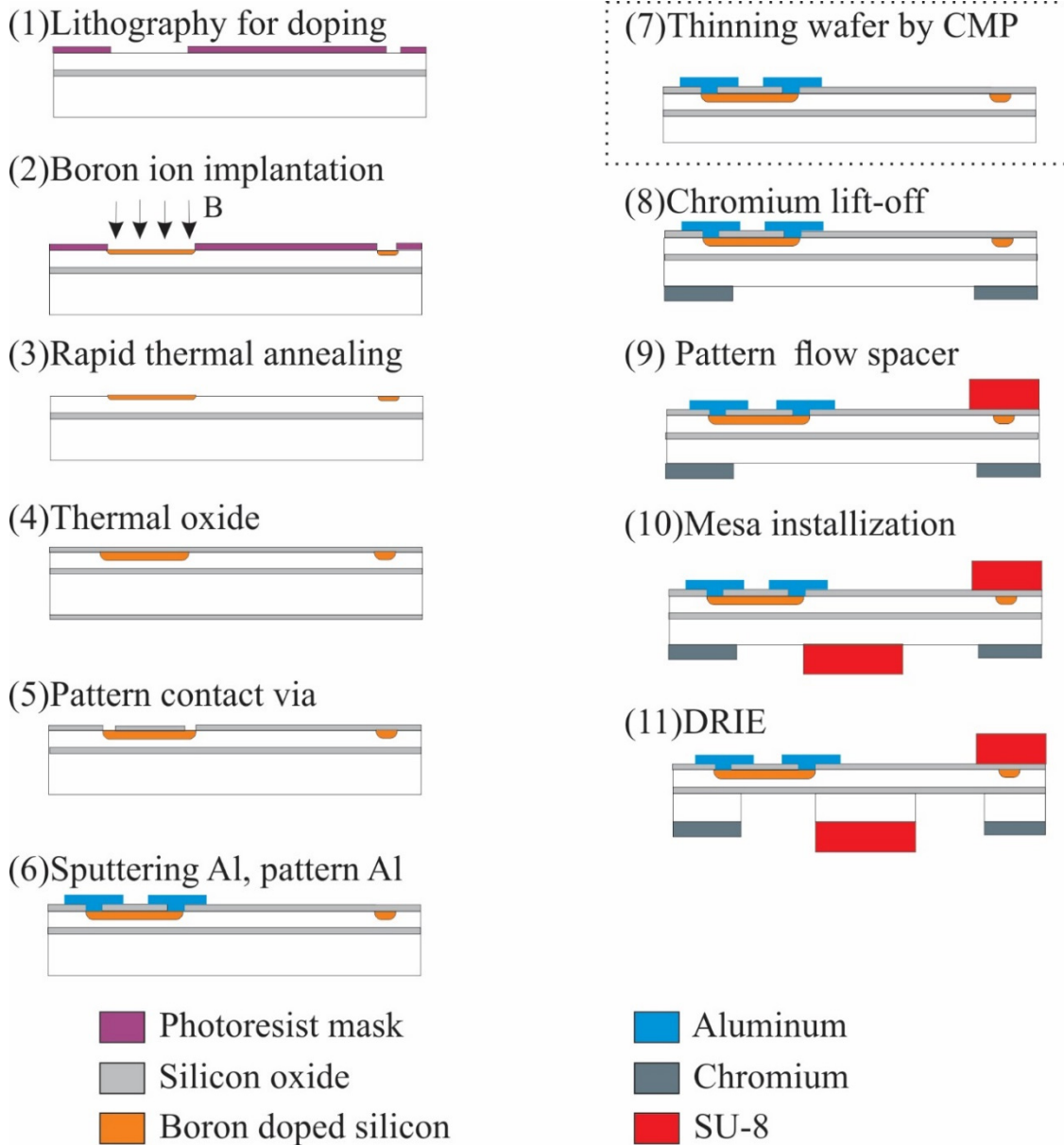


Figure 4-11 Process flow developed for outsourcing vendor

## 4.6 Challenges and modifications in fabrication

A successful and stable process flow can hardly be established from one trivial fabrication, that iterations from failures to successes have been experienced before getting a consistent fabrication flow. As shown from the previous articles, the fabrication of the sensor was completed through several main milestone-procedures, which were consisted of more than 24 sub-experiments. The successful delivery of the fabrication mainly relied on the hands-on experiences and attentive skills, such as operating the equipment, techniques of handling wafers and referring to the protocols, and tweaking recipe parameters. As sensor developments moving forward, some modifications have been made in the fabrication, which ultimately was finalized as the process flow in previous section 4.5. Hereby, this section would recall the amendments. Common failures and challenges of the fabrication process would be described in this section, which included solving issues such as the oxide residual in the openings, poor quality of Chromium lift-off, mesa incompleteness due to etching procedures, and the dicing yield enhancement.

### 4.6.1 Fabrication modifications

*Modifications on alignment marks:*

(1)Oxidation

(2)Pattern Doping Windows

(3)Boron Doping

(4)Lithography

(5) STS ICP RIE

(6) Strip Oxide

(7)Annealing, Oxidation

(8)Pattern Contact Via

(9)Sputtering Al, Pattern Al

(10)Chromium Lift-off

(11)Mesa Installization

(12)DRIE

(13) Pattern Flow Stopper

Photoresist mask
Silicon oxide
Boron doped silicon
Aluminum
Chromium
SU-8
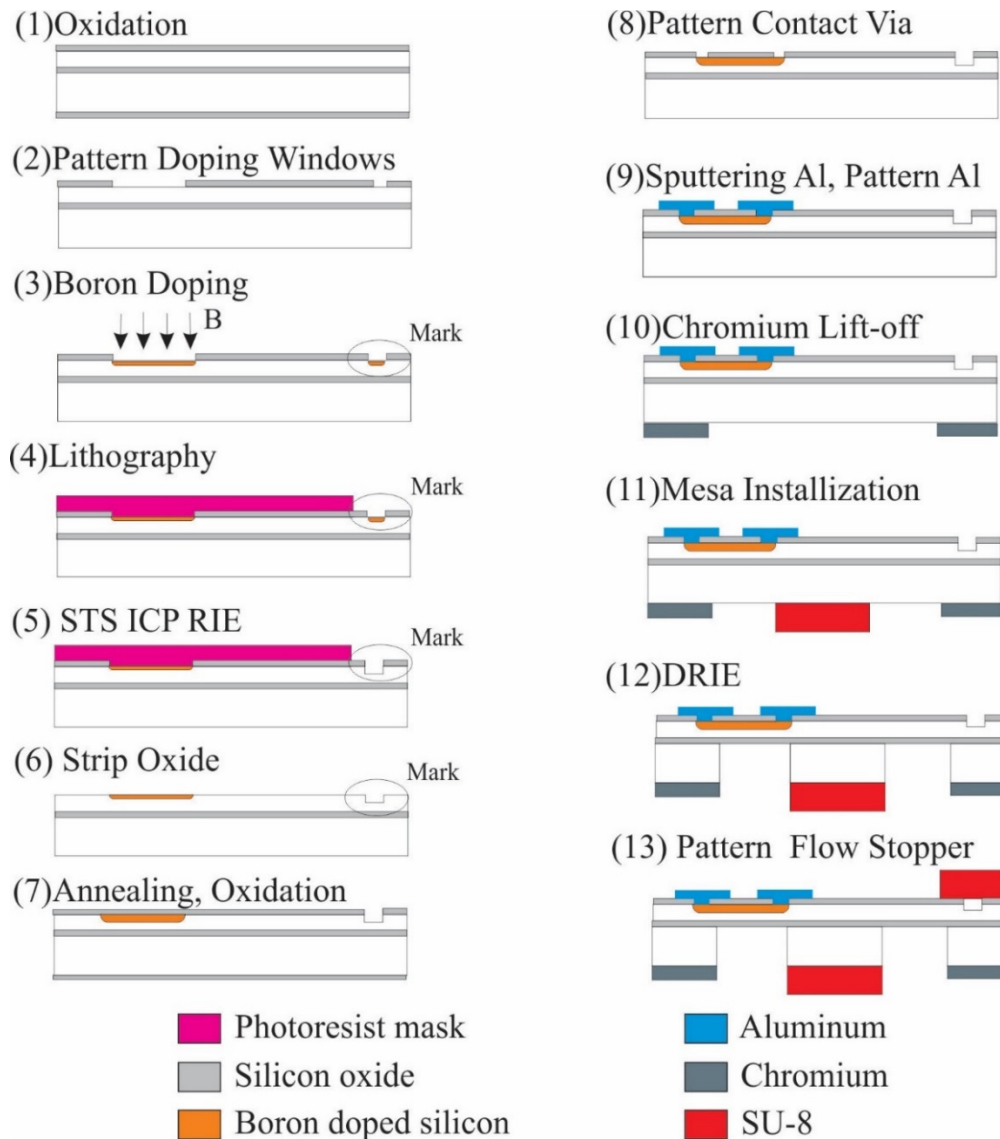
Figure 4-12 Modifications on alignment marks for the doping process

The process flow started with the wet thermal oxidation to get a layer of 500 nm oxide. After patterning the doping window, the boron doping was performed to form the four-terminal gauges on the device. The oxide layer was used as a mask for the doping. In trial fabrications, the mask oxide was removed immediately, and the bare silicon was exposed. However, there was no obvious difference between the boron doped regions and the undoped silicon surrounding them, observed either under a microscope or by naked eyes directly. To transfer alignment marks to procedures after the doping, a lithography procedure was added to cover the rest of the wafer except for the alignment marks (see Figure 4-12). Afterwards, the wafer was put into the DRIE machine for 20 cycles of fast-etch, etching the exposed alignment marks whilst using the photoresist as a

protection mask. Due to the selectivity difference between the silicon and photoresist, the feature of alignment marks in the oxide layer was transferred into the bulk silicon, with a depth of about a few microns which was sufficient to be recognized for the following optical lithography. The following procedures were performed based on the transferred alignment marks. However, after multiple rounds of fabrications, recognizable boundaries have been observed at the oxide layer after the thermal oxidation. Therefore, this alignment mark transfer step was opted out in the formal process flow described in section 4.5.

Another main amendment on the process flow was switching the sequence of doing the DRIE and patterning the Flow stopper. In this recipe (see procedures #12 and #13), the flow stopper was done after the DRIE. A carrier wafer was needed in DRIE. To do the flow stopper patterning, the carrier wafer had to be removed from the SOI wafer. The detachment procedure increased the risk of sabotaging the membrane. Moreover, after separating the carrier wafer from the device wafer, the residual crystal bond caused by the bonding had to be washed away before spreading SU-8 on the wafer. The device wafer had to be flipped and bonded to a carrier wafer again, since the voids in the wafer after the DRIE leaking the chuck vacuum in the spinner.

### 4.6.2 Residual oxide in openings

The fabrication process flow has three procedures of etching the oxide, which are for doping windows, stripping doping mask, and patterning the contact via. The common approach for etching the oxide in nanoFAB is to merge the wafer in the BOE until the oxide is completely etched away. However, due to the small size of doping windows, especially for the contact via, the oxide within the etching region is difficult to be etched completely. In fact, observing through the microscope, within the openings of the contact via, clusters of purple dots indicated the existence of residual oxide. The residual oxide was firstly overseen, not until the in-process characterization revealing a huge resistance (Megaohm level) of the four-terminal gauge which was unrealistic comparing with the anticipated resistance level based on the doping source datasheet. To solve this residual oxide issue, before putting the wafer into the BOE, the DI water was sprayed on the surface of the wafer for a few seconds. The reason for doing this was that the oxide layer was hydrophilic, and a thin layer of water film allowed less air bubbles generated in the opening region. A stirring machine was used to make a better chemical reaction environment, which meant the etchant flowing abundantly across the wafer and closer to the opening region.

**4.6.3 Chromium lift-off**
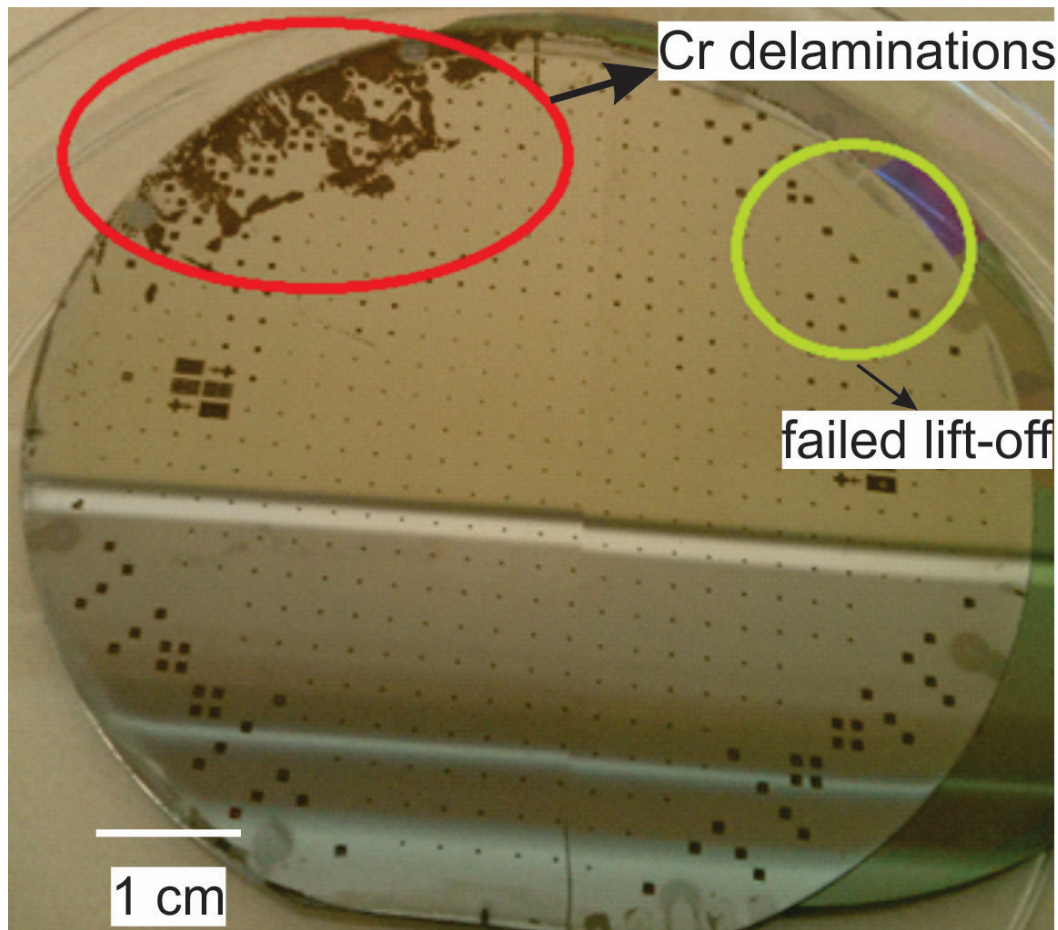


Figure 4-13 Lift-off defects

The chromium thin film was used as the mask layer for DRIE after going through a process named as the lift-off. As described in section 4.6, the negative photoresist AZ5214 was used for defining the etching region. A critical procedure for using the AZ5214 after spreading was to get the photoresist rehydrated for 15 minutes in the ambient environment or by rinsing the wafer with DI water. The rehydration was done again after exposing the photoresist before the flooding exposure. If the lithography was not done properly, the chromium layer would be not removed completely. Then a higher grade and longer time of ultrasonic bath would be needed. But the consequences of introducing the higher strength and longer time of ultrasonic bath was illustrated in Figure 4-13. Without a proper rehydration, the Chromium film would stick with the silicon wafers, leaving etching region unopened.

### 4.6.4 DRIE and mesa completeness
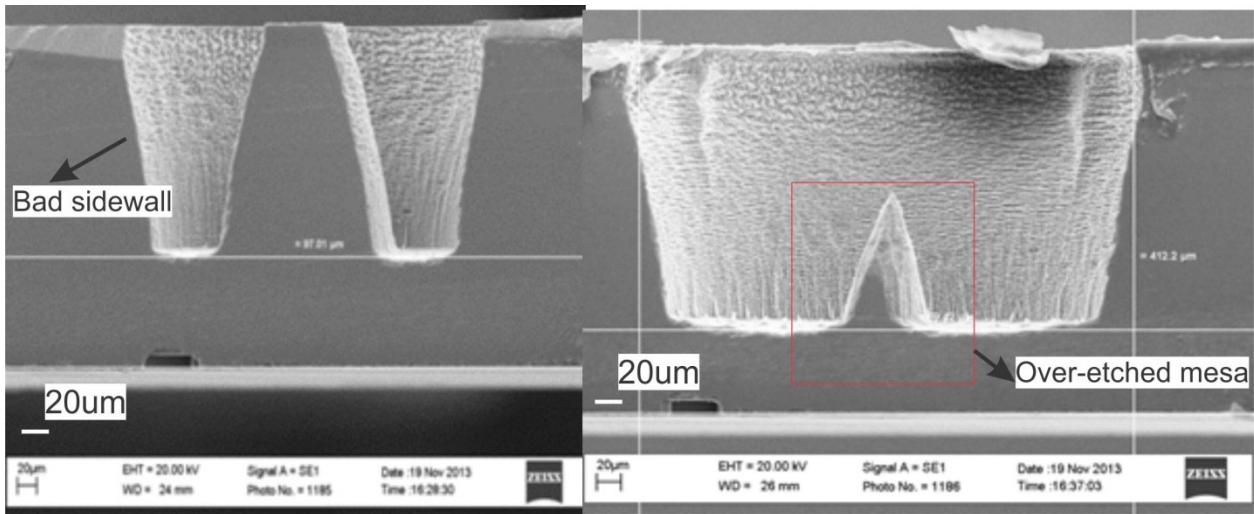


Figure 4-14 Mesa and sidewall etching defects

As key structural and geometric elements, the completeness and uniformity of the membrane and mesa were essential for the performance of the devices. Both the uniaxial force sensor and the multi-axis force senor were designed based on the membrane-mesa structure. The sensing element, which was the four-terminal gauge, was formed by the Boron doping inside the membrane. The stress distribution affected the outputs of the sensor, consequently including the sensitivity of the sensor, which depended on the uniformity of the membrane. The mesa at the center of the membrane was the structure where the forces would be applied. Moreover, the membrane and mesa were fabricated in one procedure, which was the DRIE. Therefore, a few rounds of trial fabrications had to be done to overcome the defects and concluded a reliable procedure. The common defects have been depicted in Figure 4-14, showing that the SU-8 mesa had been etched away even before the etching reached the insolation oxide of the SOI wafer. The right picture demonstrated that the mesa had been over-etched, leaving a pyramid residual at the center of the membrane.

The defects were due to the heat transfer issue during DRIE, which required the substrate temperature to be maintained at a low level (around 0 °C). The membrane thickness was 10 um, which was fragile comparing to the turbulent cooling system by the helium underneath the etching chamber of the DRIE (Estrelas from Oxford Inc.). Preventing the membrane from broken due to drastic pressure changes, using a carrier wafer was mandatory for the etching process. A few of bonding solutions were available in the nanoFAB, including the photoresist (for instance, HPR

504), double-side bonding tape, and the crystal bond (555-HMP, TED PELLA Inc.). Owing to the simplicity of using the double-side bonding tape, it was chosen to be the bonding material in the first place which caused the defects above. Therefore, other two bonding solutions have been tried. The comparison among these three bonding approaches has been described in Table 4-1.

Table 4-1 The comparison of trial DRIEs based on various bonding approaches

| Bonding solution | Etching depth | Mesa completeness |
| --- | --- | --- |
| Double side tape #1 | 150um | Poor |
| Double side tape #2 | 150um | Poor |
| HPR 504 | 150um | Poor |
| Crystal bond #1 | 150um | Good |
| Crystal bond #2 | 150um | Good |

### 4.6.5 DRIE and membrane uniformity

The membrane geometry was demanding in the fabrication as it was essential for defining the sensitivity of the sensor. Therefore, SOI wafers were chosen for the sensor fabrication on purpose to improve the membrane uniformity. Because the insulator layer could be used as an etching stop in DRIE.  In the DRIE process, as the etch approaching the insulation layer, due to the selectivity difference between the silicon oxide and the silicon, the etching rate turned to be extremely slow at the interface of the silicon and the buried silicon oxide. Figure 4-15 below showed the etching profile if common DSP wafers were used. This was DRIE without an etching stop. The green eclipse highlighted the curved profile at the bottom of the etching.
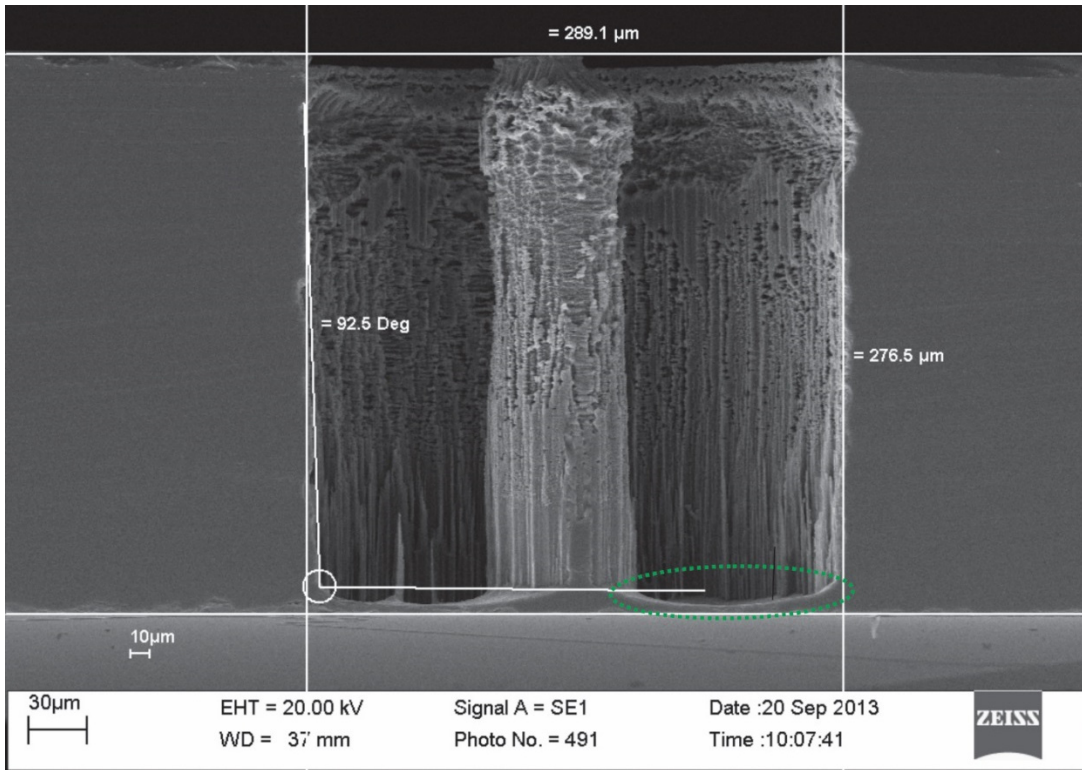
Figure 4-15 Non-uniform membrane etched using DSP wafers
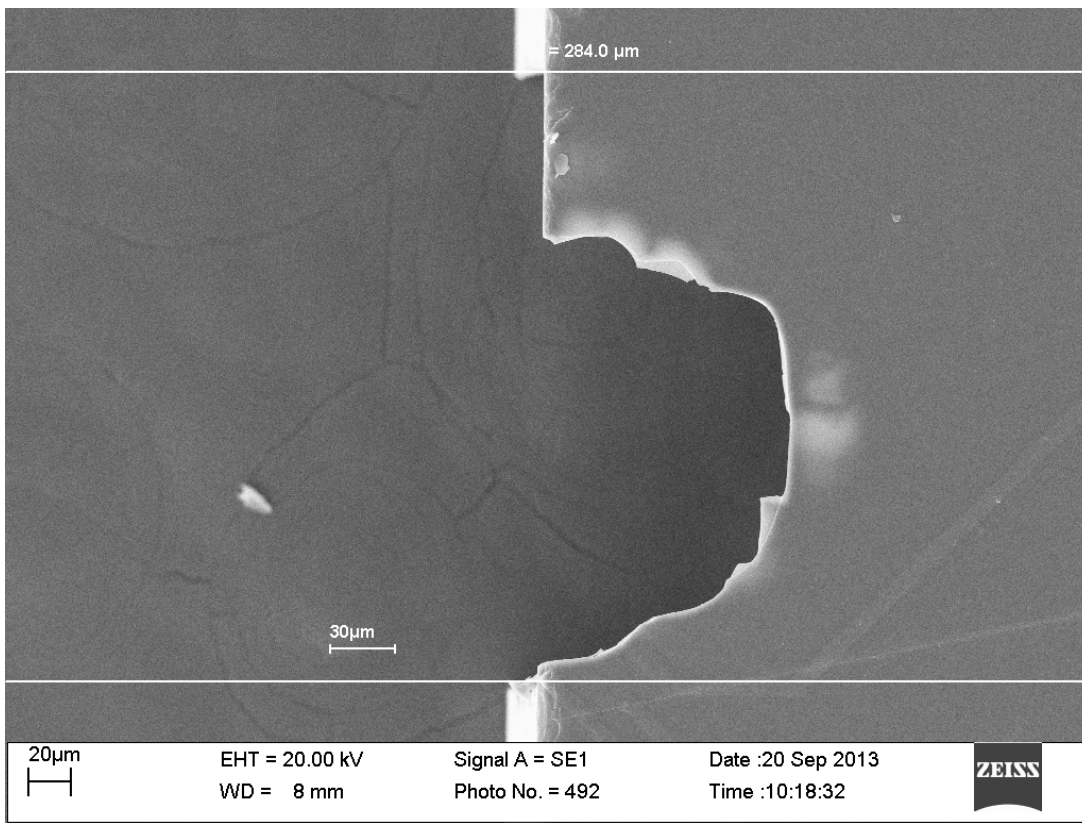


Figure 4-16 Over etched membrane on DSP wafers

Due to the etching rate differences which were also call the lagging effect across the wafer diameter, devices located at the central part of the wafer could be over-etched as shown Figure 4-16, whilst the outer part of the wafer still did not reach the membrane thickness. However, the flatness and uniformity of the membrane were preserved by introducing SOI wafers, which was shown in Figure 4-17.
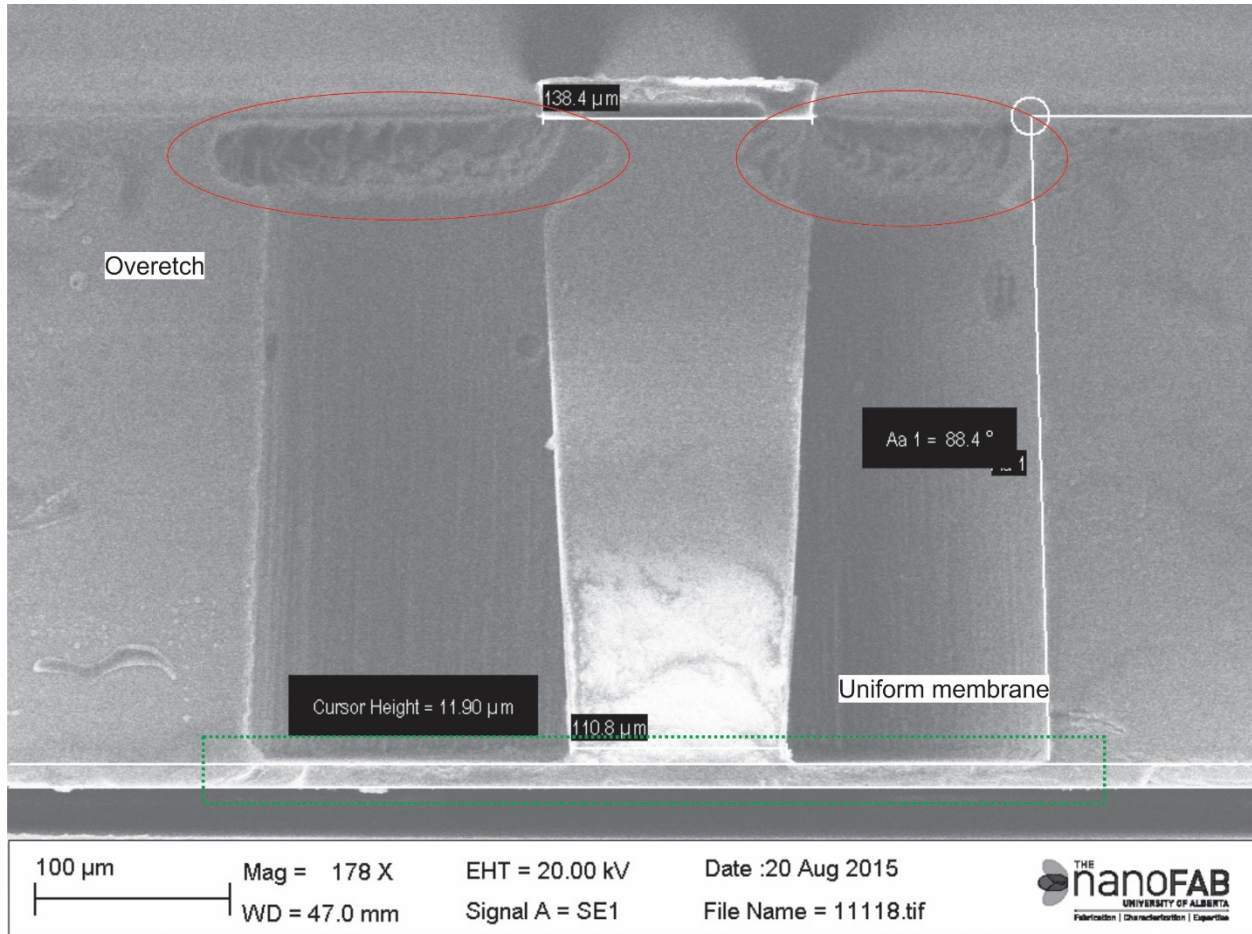


Figure 4-17 Device fabricated from SOI wafers © [2017] IEEE

Moreover, using the SOI wafer for the membrane uniformity was not automatically granted without modifications on the etching process. The etching process happened in the vacuum chamber of the DRIE machine, without a direct observation on the progress of the etching. And the etching rate varied due to the systematic characteristics along the feature depth. Therefore, the number of etching cycle was a varying parameter. The residual silicon existed at the bottom of the membrane if not enough cycles were done, as depicted in Figure 4-18 using a white-light interferometry microscope (Zigo® interferometer in nanoFAB). The top of the mesa could possibly be over-etched if more than enough etching cycles were added. This issue was captured

in Figure 4-17, although the membrane of the device was uniform. The solution to solve this was imperial, that was to pause the etching near the calculated etching cycles, then take the observation of the wafer and resume etching until a satisfied uniformity was achieved. Eventually, most of the devices had few residual silicon on the membrane.
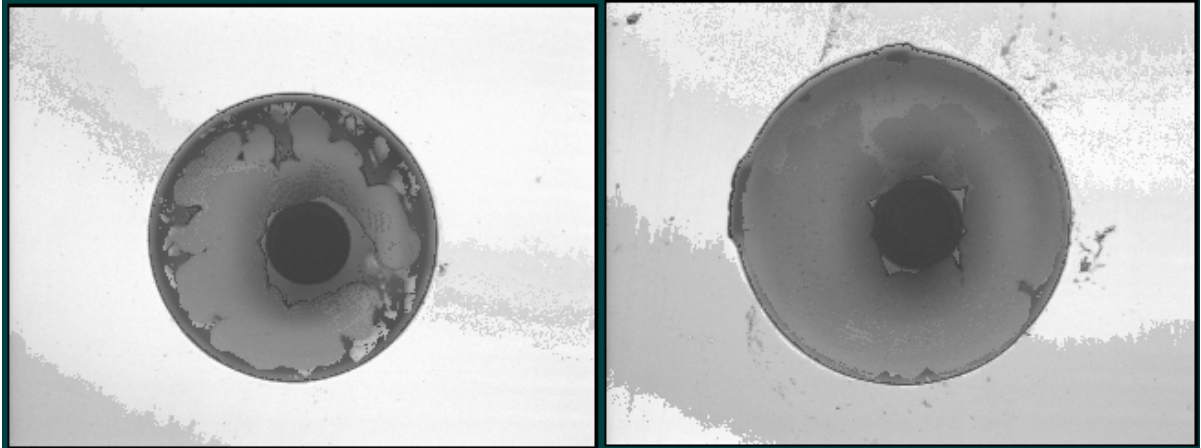


Figure 4-18 Residual silicon at the bottom of membrane

### 4.6.6 Yield loss on dicing

The dicing was the last procedure in the fabrication process flow, during which devices were cut out individually from the SOI wafer. Hereby, all the previous experiments and efforts cohered in each single die. Many ways of dicing can be used for separating the wafer into pieces of chips, including scribing and breaking which means naturally cleaving the wafer along the silicon crystalline, the mechanical dicing by a saw rotating at an extremely high velocity, or laser cutting. The cleavage method was easy to perform with a cleavage knife, however, it required experiences and was inefficient if the die size was small. The laser cutting approach required a high-power laser generator and a precise position controller, which consequently increased the cost on the dicing, although it had the merits of less mechanical damages, environmental friendly and the capability of smaller cutting. Mechanical dicing saw (DAD 3420) was chosen by adopting the machine in nanoFAB, due to its access convenience and low cost. Before addressing the challenge generated by the dicing, a brief introduction on yield was described below.

*Yield*

From a perspective of products, the total number of working devices can be successfully fabricated from one piece of SOI wafer is an important factor to considerate. The concept *yield* is defined as the ratio of success, which can be calculated at any stage of the process flow. The final

yield can be calculated as the ratio of successful devices among all the devices on the wafer. Many models have been used for quantifying the yield. For instance, a general model takes defects clustering into the consideration and can be expressed as[148]

$$Y_{random} = \left(1 + \frac{AD_0}{\alpha}\right)^{-\alpha}$$

Where the $A$ is the chip size and $D_0$ is the defect density, $\alpha$ is the cluster factor.

Another yield model is known as Murphy's model, which is

$$Y = \left(\frac{1 - e^{(-AD)}}{AD}\right)^2$$

Where $D$ is defect density.

*Dicing with saw*

Dicing was performed as the last step after DRIE, that the 10 um membrane and cylindrical mesa have already been machined. Both the membrane and mesa out of the brittle silicon would not survive under the coolant injection due to its high velocity. Tempts have been made to protect the mesa by spreading a thick layer of adhesive (Crystalbond™ 555, melting temperature 55 °C) at the side of etching, which later could be removed by hot DI water. However, the heat generated in the dicing by frictions between two substrates and the saw would melt the adhesive, which caused the membrane and mesa directly confronting the impact of the coolant. Besides, the SOI wafer was already warped during the fabrication, as the result of residual stress caused by the oxide layer on the wafer. Once the curved SOI wafer with etched wells in one side was placed on the dicing saw, it cracked instantly as the vacuum was turned on. This vacuum was for fixing the wafer on the cutting chuck. The schematic description of this scenario has been depicted in Figure 4-19. To solve these issues such as adhesive melting and wafer crashing, the wafer was flipped on a carrier wafer bonded by another layer of adhesive with a higher melting temperature (Crystalbond™ 509, flow point at 121 °C). The carrier wafer was place on the top of a hotplate at the temperature of 120 °C. Crystal bond adhesives were spread on the top of the carrier wafer, followed by flipping the SOI wafer on the adhesives with the side of aluminum trace facing up. Eventually the stacked two wafers were ready for dicing after cooling down to the room temperature.
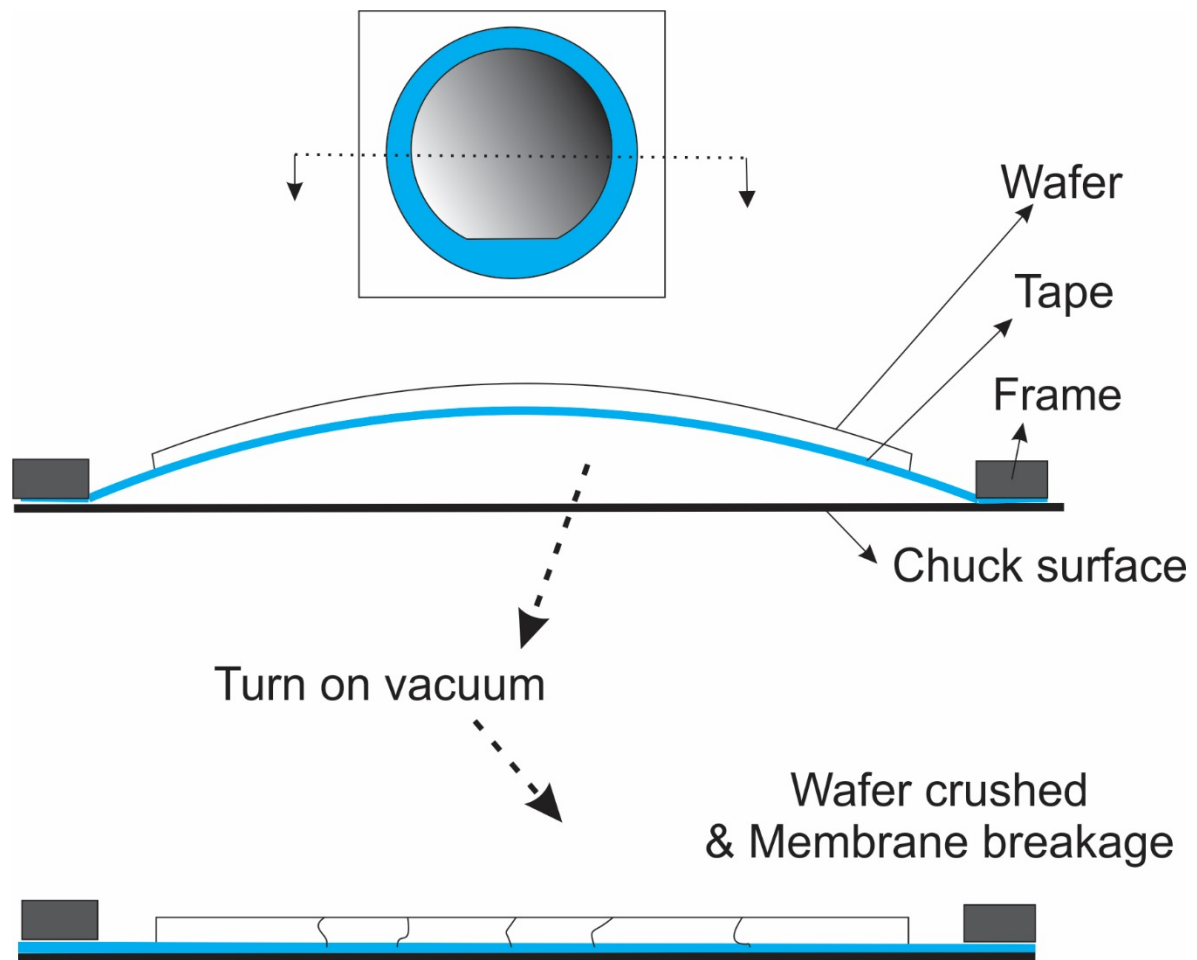
Figure 4-19 Damage caused by the vacuum of the dicing saw (exaggerated view)

Bonding the device wafer on the top of a carrier wafer for the dicing solved the issues of being crushed on the stage. As the chips were square shapes, the dicing directions were two perpendicular paths along device edges. Assuming the two directions were called horizontal and vertical in the wafer plane, after cutting the horizontal direction, the wafer was rotated 90° for dicing in the other direction. Some devices started falling off the carrier wafer during each cutting motion, as shown in Figure 4-20. Regions where devices were missing have been addressed using a red dash line. The fallen devices could be found from the filters in the drain of the machine. However, most of devices found there were not testable cause the mesa was damaged, or the membrane was cracked, or aluminum traces was scratched.
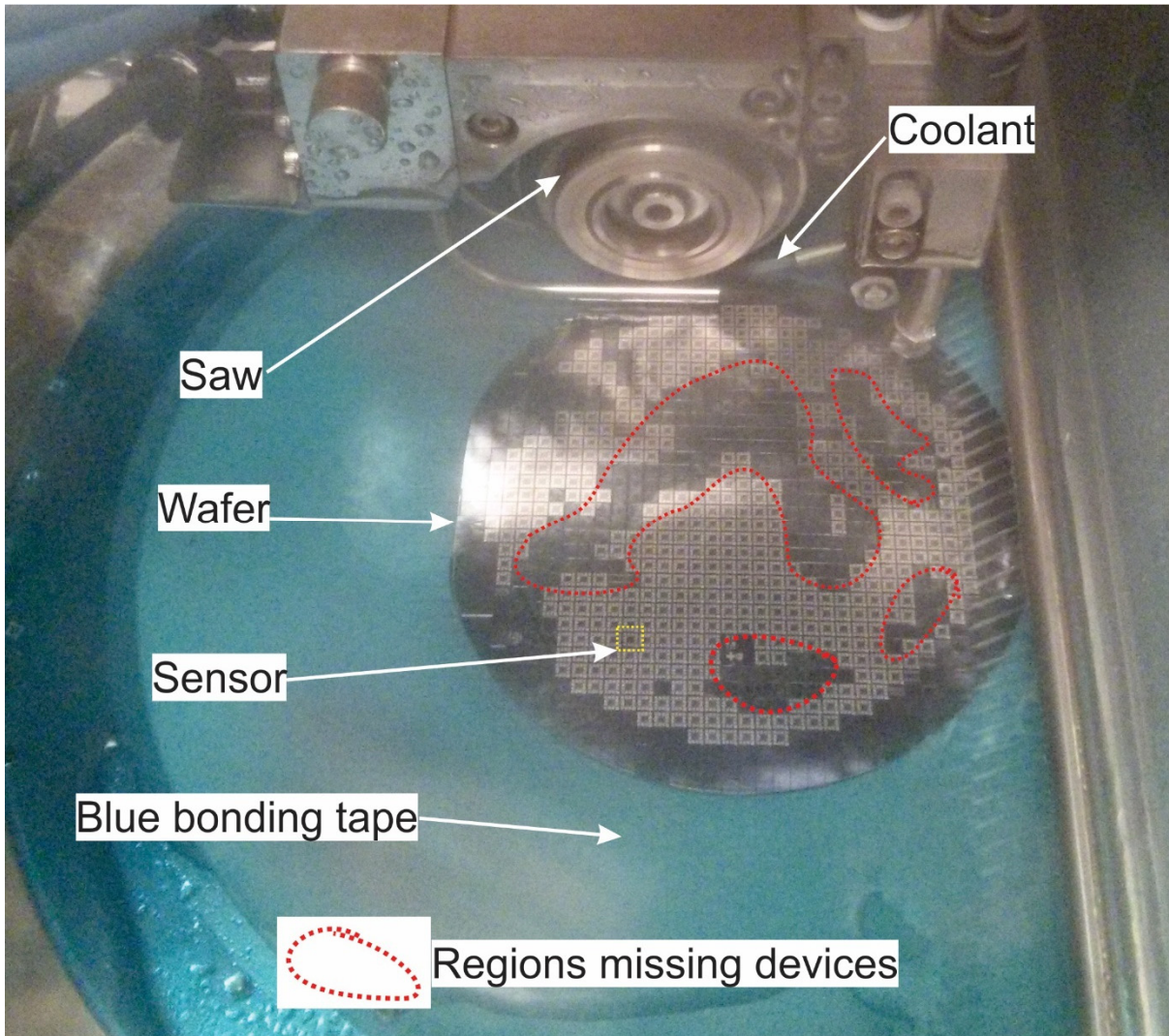
Figure 4-20 Missing devices due to cooling water and bonding material delamination in the dicing procedure

## 4.7 Characterization in fabrication

All the fabrication was done by following the equipment protocol, modifying the process recipe. Therefore, characterizations in-process were necessary to track the experimental quality. Most of the cases involved imperial observations by bare eyes or under the microscope. For instance, the issues addressed in section 4.6 such as residual oxide, poor quality lift-off, mesa and membrane geometry, those geometric or appearance parameters can be characterized by observations. Another key parameter of the sensors, the piezoresistance of the four-terminal gauge, must be characterized during the process flow, in order to ensure that the rest of the processes for the wafer were meaningful to proceed.

### *Characterizations on Thermal diffusion by Four-point tests on wafer*

The level of diffusion represents the piezoresistance coefficients. This was characterized by testing the resistance of the doped region. Visually, no significant difference was shown comparing the color between the doped silicon and the un-doped, except the doped one became a bit darker in grey scale, which was almost unnoticeable. Based on design requirements, the sheet resistance of the doped region should be 50 $\Omega$/sq. The four-point test method has been employed to test the sheet resistance of the doped wafer. The schematic structure of the four-point test was drawn in Figure 4-21. Four sharp probes were aligned in one line and contacted with the surface of the wafer. The distance between two neighborhood probes was denoted as *S*. A DC current source was applied on the two outer probes. The voltage output was measured from the inner two probes. The resistance of the doped region can be written as the equation[149]:

$$\rho = C\frac{V}{I}$$

Where *C* is an imperial constant related with the ratio of sample size and the testing distance *S*.
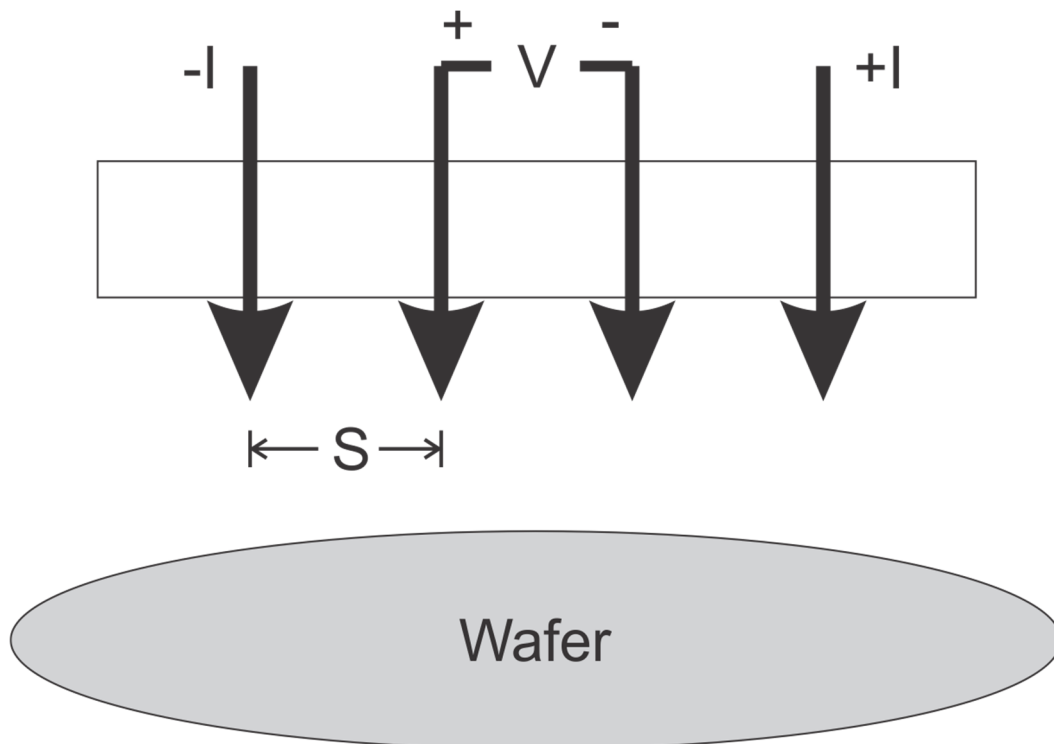


Figure 4-21 Four-point test for the resistance characterization (not of scale)

The resistance of the doped wafer was tested by a four-point probe equipment (Pro4, LUCAS LABS) with a source-meter (Keithly 2400 ), automatically calculated by the software package (see Figure 4-22). The source meter applied currents and calculated the ratio of the voltage divided by

the current. 9 points on the wafer have been tested. Assuming the center of the wafer was the origin of a Cartesian coordinate, locations of these nine points have been listed below in Table 4-2, with the calculated sheet resistance $R$, and the resistivity. The average sheet resistance was 64.36 ohm/sq, from which the wafer was doped at 900 °C for 45 minutes.

Table 4-2 Sheet resistance test data of doped wafer

| X (mm) | Y (mm) | R (ohm) | Resistivity [ohm-cm] | V/I | Thickness [um] |
|--------|--------|---------|----------------------|-----|----------------|
| 0 | 0 | 64.14613 | 3.367672 | 14.19251 | 525 |
| 40 | 0 | 62.18629 | 3.26478 | 13.75889 | 525 |
| 18.856 | 18.856 | 67.86852 | 3.563097 | 15.0161 | 525 |
| 0 | 40 | 66.10696 | 3.470615 | 14.62635 | 525 |
| -18.856 | 18.856 | 66.48148 | 3.490278 | 14.70921 | 525 |
| -40 | 0 | 64.40215 | 3.381113 | 14.24916 | 525 |
| -18.856 | -18.856 | 64.27286 | 3.374325 | 14.22055 | 525 |
| 0 | -40 | 61.45911 | 3.226603 | 13.598 | 525 |
| 18.856 | -18.856 | 62.32807 | 3.272224 | 13.79026 | 525 |
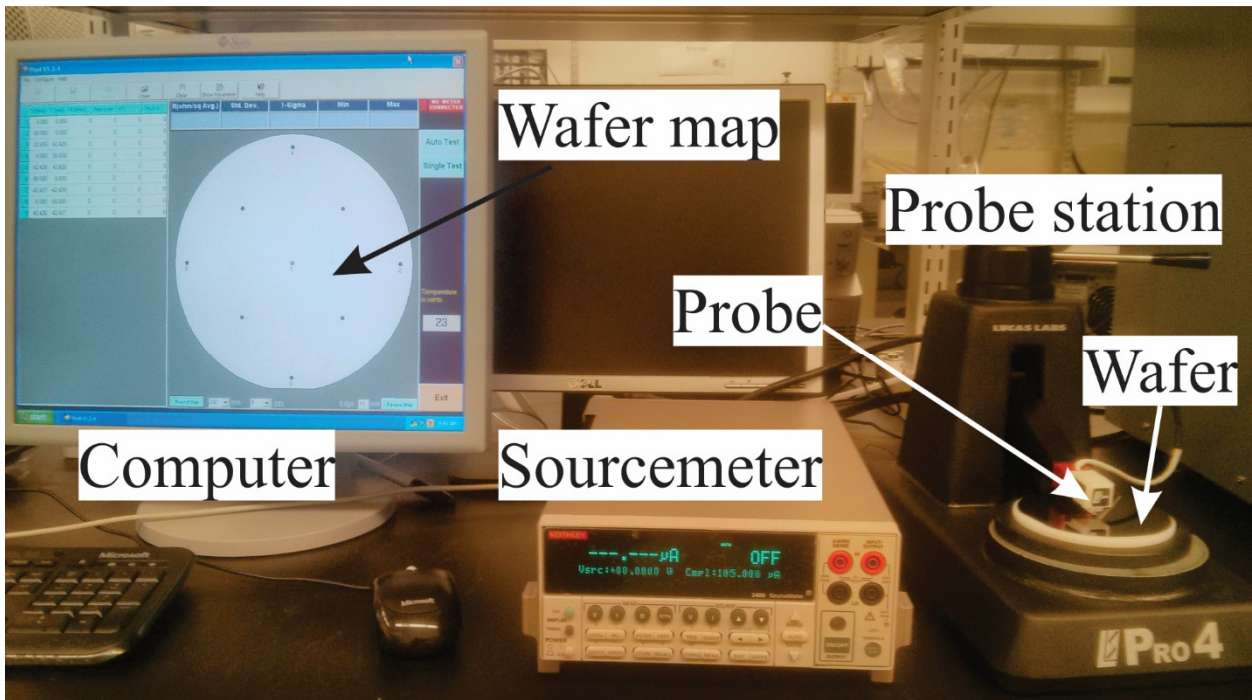


Figure 4-22 Four-probe test setup

***Characterization on the resistivity of the piezoresistor***

After determining the doping time and temperature by characterizations from the doped wafers, the characterization on the doped piezoresistors was deployed by measuring the resistance of the

resistors on the wafer. Resistor structures have been added on the doping mask as shown in Figure 4-23. This included six locations where resistors were placed on the wafer.
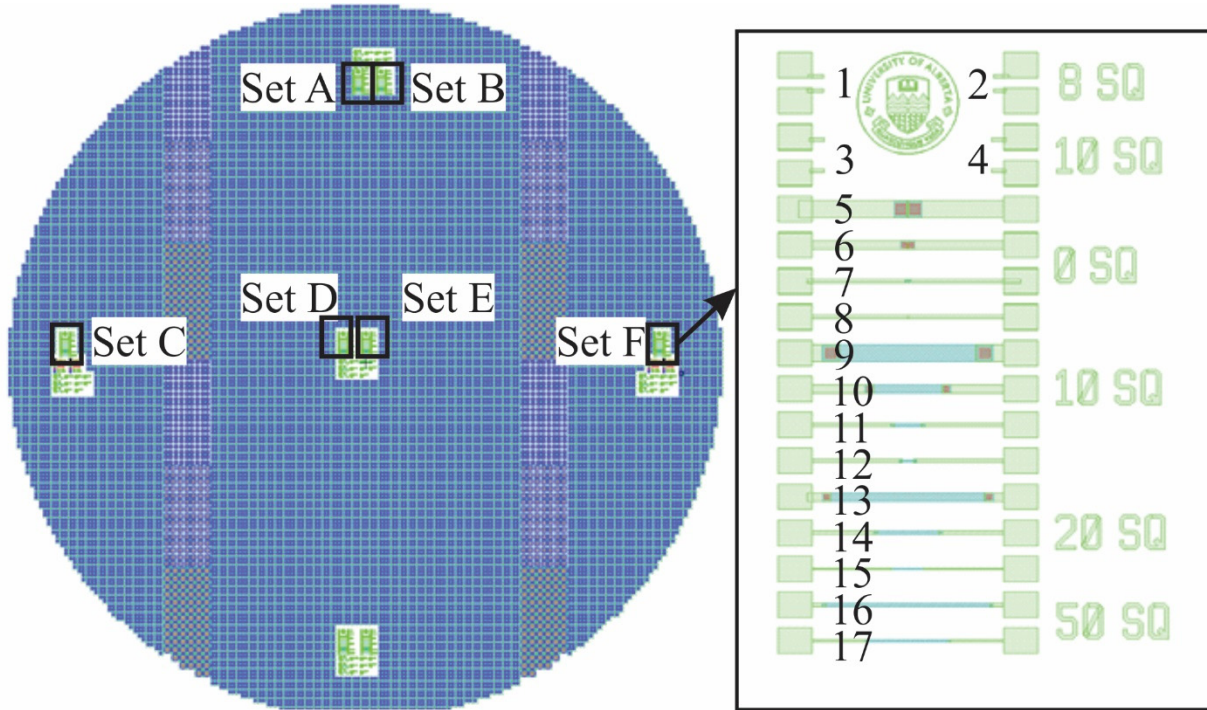


Figure 4-23 Locations and structures of characterization resistors

5 locations of where the resistor groups were placed and part of them have been marked from Set A to Set F. 17 resistors were included in each resistor set. Here, the concept of the aspect ratio was the length divided by the wideth of the resistor. Several designs of different aspect ratios have been made in the resistor set, including aspect ratios of 0, 8 sq, 10 sq, 20 sq and 50 sq.

The average resistance increases propotionally as the aspect ratio becomes bigger. Plotted in Figure 4-24, the average resistance of resistor with aspect ratio of 8 sq was about 380 ohm. This was reasonable comparing with the value around 450 ohm from resistors of 10 sq, which includes No. 3, No. 4 and from No. 9 to No. 12. As the aspect ratio increased to 20 sq, the average resistance from No. 13, No. 14 and No.15 was around 950 ohm. This was the double-value of the 10-sq-resistor. Moreover, with the aspect ratio was equal to 50 sq, the resistance is about 2500 ohm, which was 2.5 times the value of the resistance from resistors of 10sq. Noticably, the resistance values tested from Set F varied dramatically and did not fit the propotional trend, indicating fabrication defects on the condutivity. According to the data, the average of the resistance can be calculated as around 50 ohm/sq.
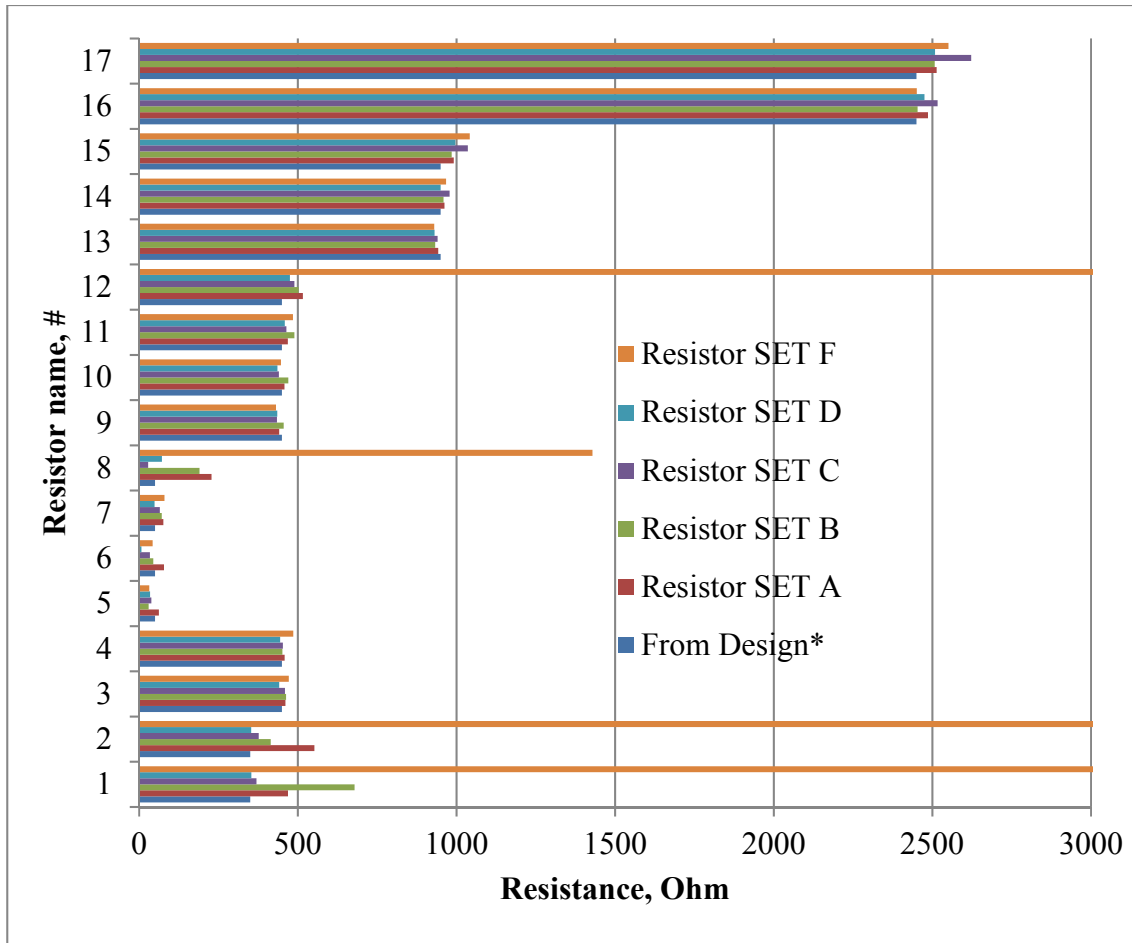
Figure 4-24 Resistance of characterization resistors at different locations; *From Design group represent the calculated value at the aspect ratio based on the assumption of 50 ohm/sq

### *Resistance test of the sensor*

The resistance of four-terminal gauge on the membrane of the sensor has been tested for evaluating the doping level. The test setup was shown in Figure 4-25 which was also used for testing the resistor structure discussed in previous section. A current source was applied at two ends of the sensing element. Then the voltage was measured at both ends. The probe was moved under microscope to ensure its contact and positions on the pads array. Schematic electric structure for the test has also been included in the photo. Figure 4-26 listed a few data samples from the four-terminal gauges on several force sensors, randomly picked up and tested from a wafer. Most of the resistance values fell within the range of 100 ohm to 200 ohms, which was reasonable according to their aspect ratios and the sheet resistance. The original current and voltage data can be referred to Appendix A 1.
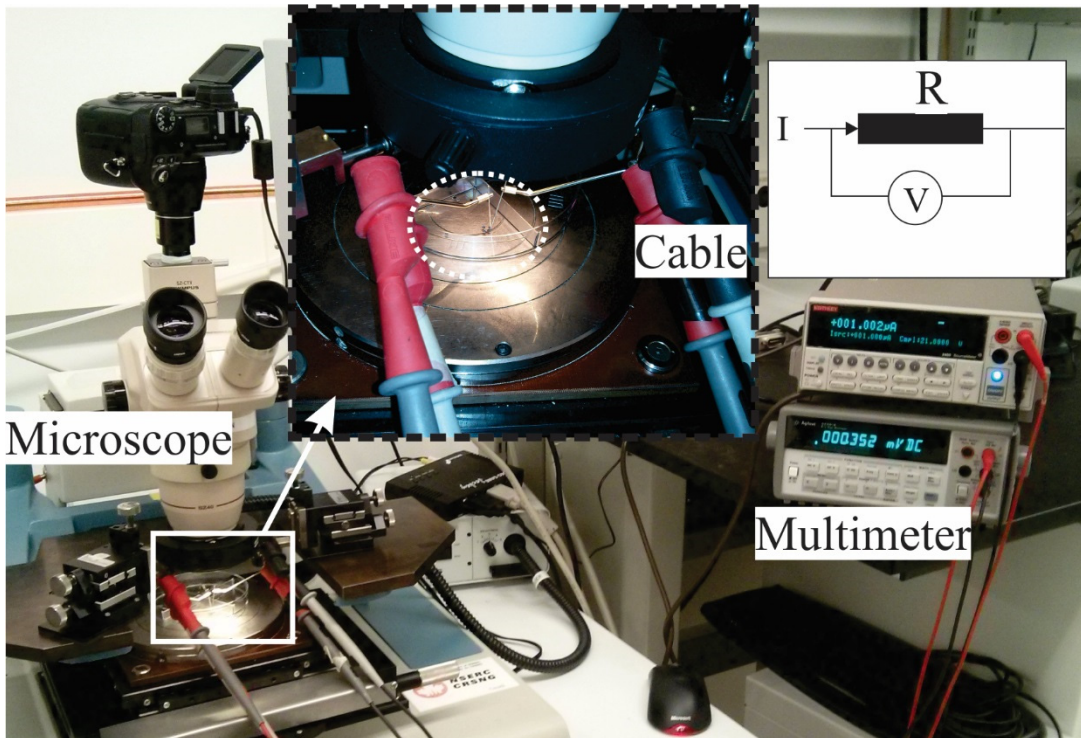
Figure 4-25 Resistance test of sensors
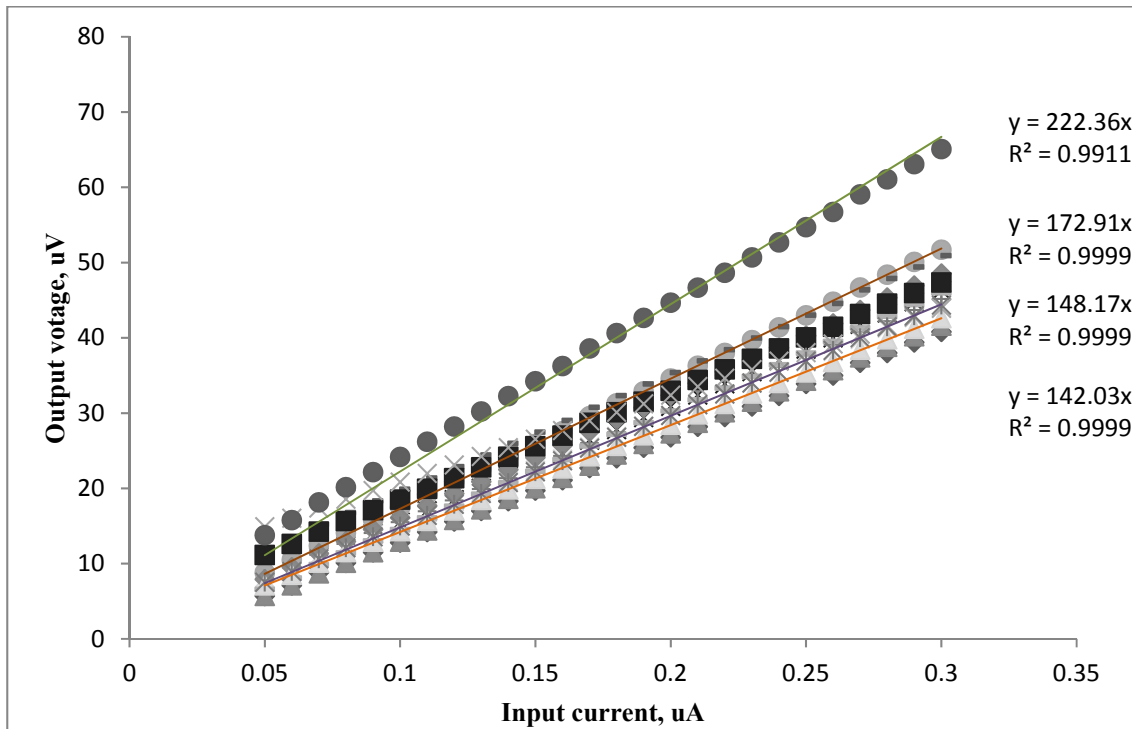


Figure 4-26 Resistance tests on sensing elements in force sensors

**Geometry characterizations with SEM**

Scanning Electron Microscope (SEM) was used for observing the geometry of fabricated sensors. As shown in Figure 4-27, a fragment of the device wafer has been captured by a magnification of 65. Undercuts existed at the side wall and the mesa post, with the angle range from 1.88 degree to 2.19 degree, which caused by the DRIE as a systematic feature. Comparing with other cryo-etching approaches or anisotropic etching, this sidewall introduced by DRIE was sufficient to be claimed as vertical for building the membrane and defining the void of the sensor geometry.
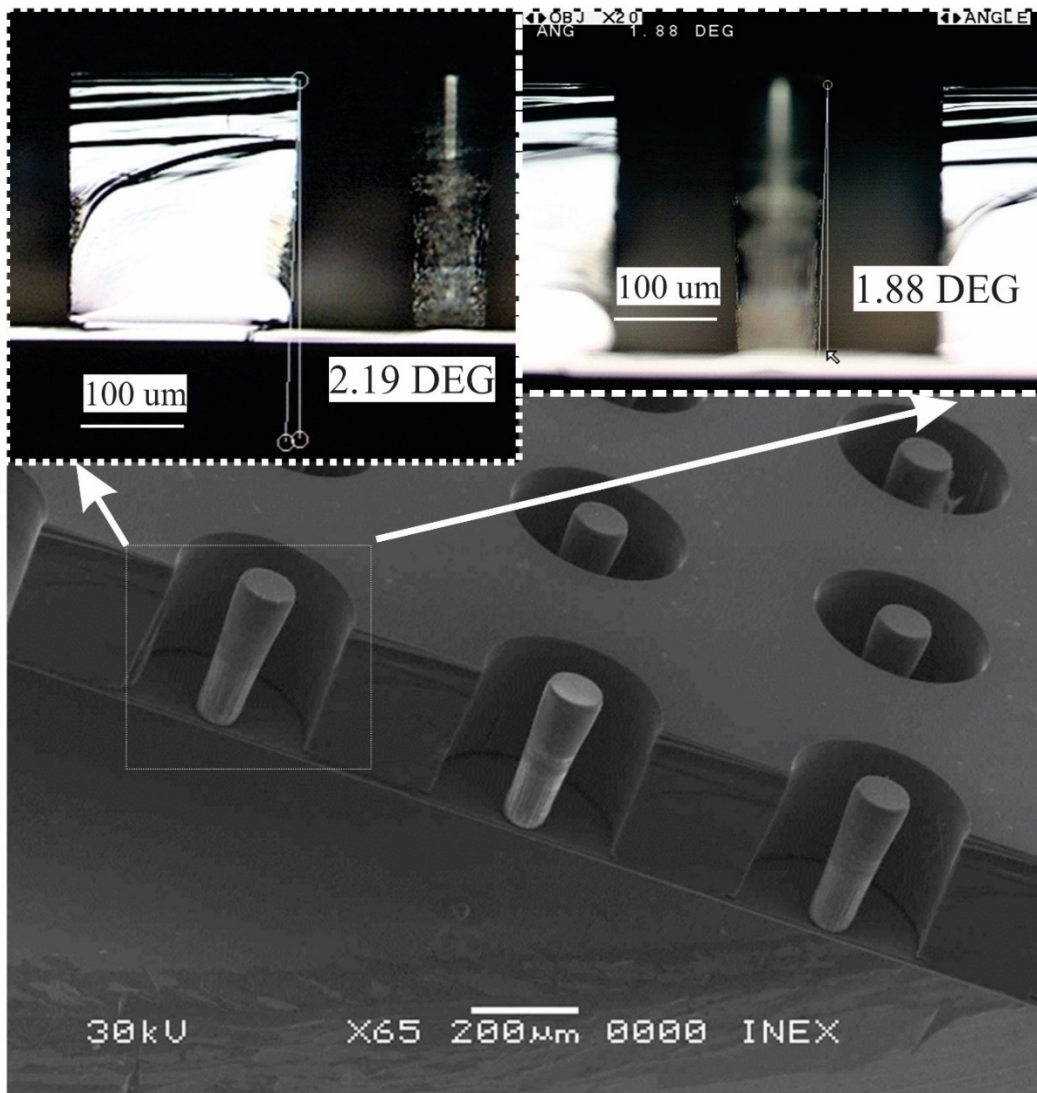


Figure 4-27 *Bottom:* SEM image of un-diced wafer; *Top left:* Undercut of sidewall; *Top right:* Undercut of the mesa

## 4.8 Packaging of individual force sensor

### 4.8.1 Packaging by stacked gold bumps

*Bumps installation and chip cleaning*

After dicing, the device chip was still attached with a carrier chip by the crystal bond, as shown in Figure 4-28. The stacked chips were firstly tested for the resistivity as an initial characterization of the sensor function on the probe station. If the sheet resistance falls into the reasonable range around 50ohm/sq, the following gold bumps installation would be proceeded. Gold bumps were installed on top of the aluminum pads with a wire tail, then coined to a flat surface by the wire bonder using a coining tool. The coined bump has been shown in Figure 4-29. The bumps had the diameter of about 90 um and the height from 40 to 50 um, which depended on the voltage and the force employed during the installation. Figure 4-30 demonstrated four gold bumps on the aluminum pads of a device.
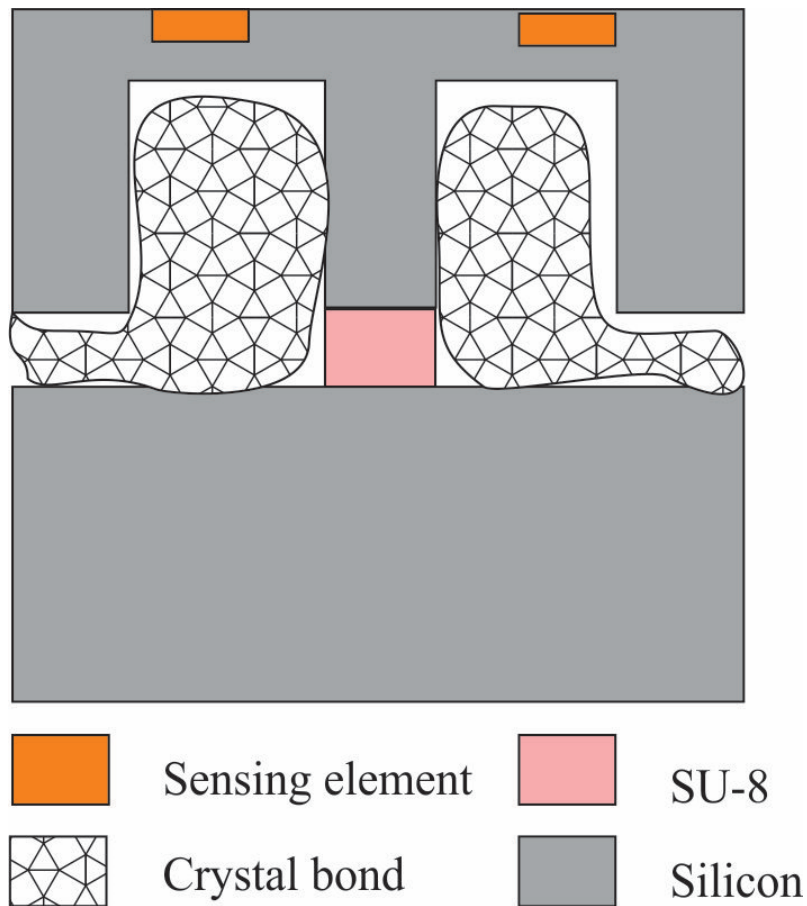


Figure 4-28 The diced chip on a carrier chip
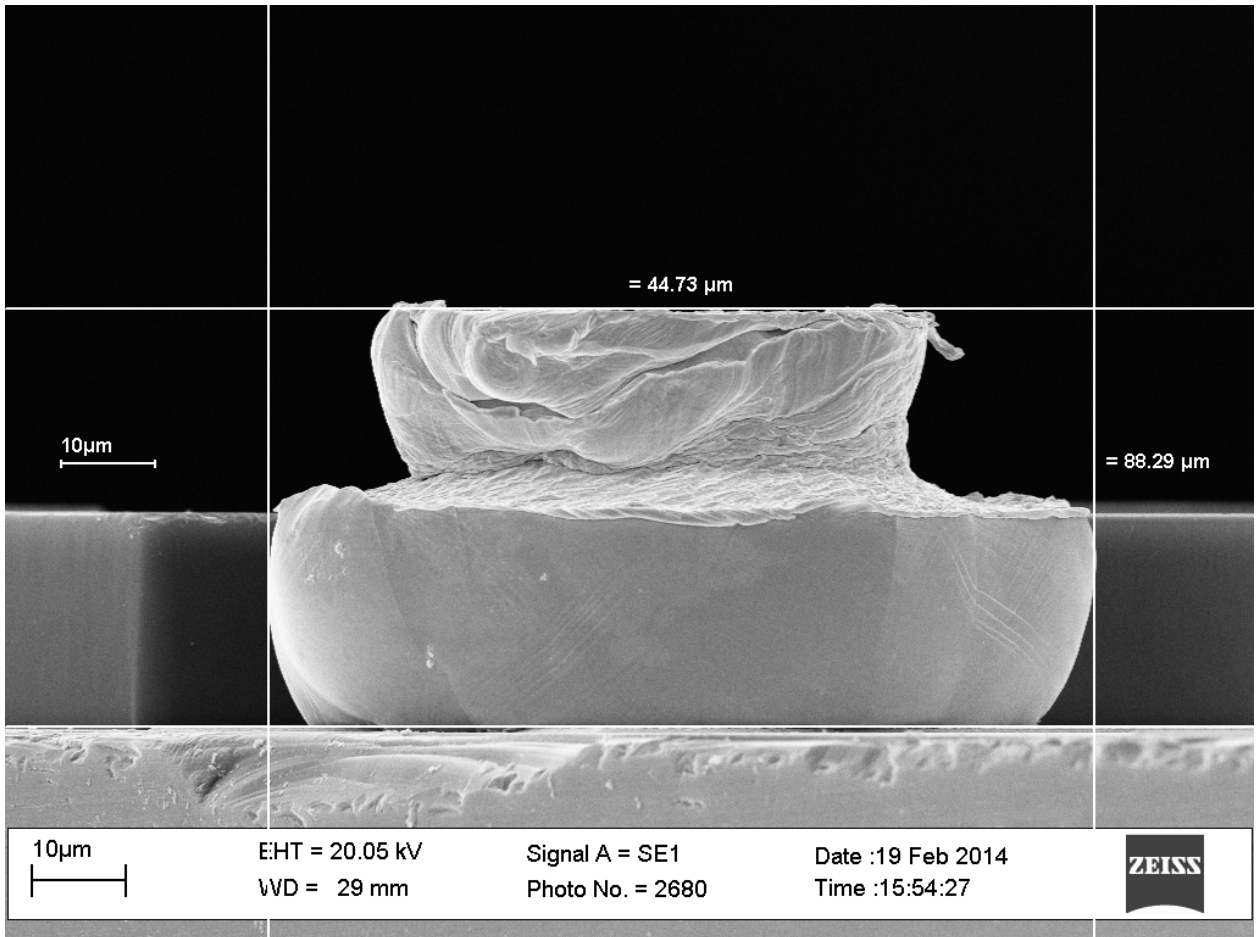
Figure 4-29 A coined gold bump on the Aluminum pad
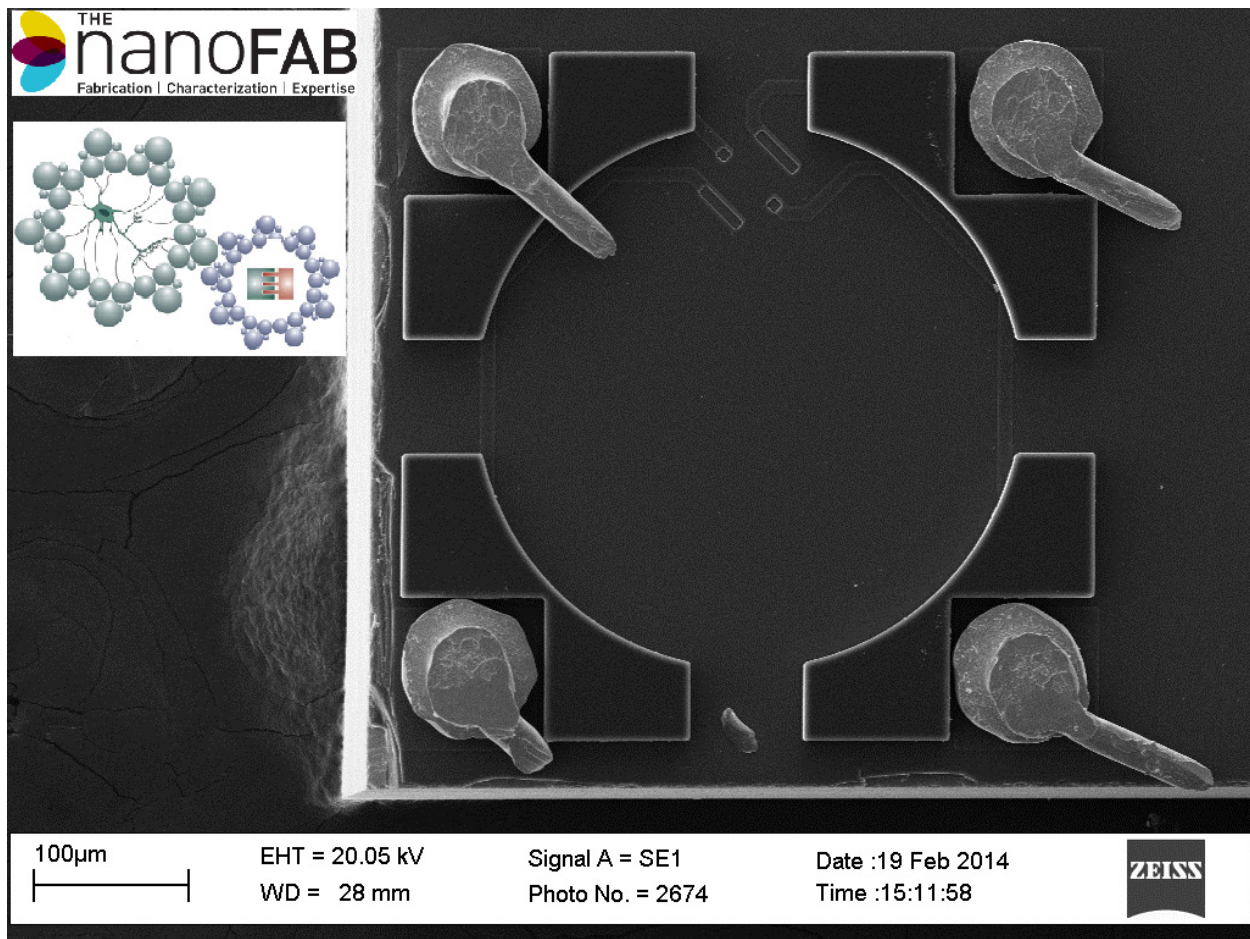
Figure 4-30 A device with four gold bumps on the pads (device size: 500um×500um) ©
[2014] Springer.

After installing gold bumps on the aluminum pads of the device, the sensor was detached from the carrier chip using a hot plate heated up to 120 °C. Therefore, the sensor needed to be cleaned to remove the residual crystal bond at the back side, where the mesa and the DRIE void were located. To clean the crystal bond, firstly, the sensor was rinsed by spraying Acetone for about one minute, holding by a carbon-tip tweezer, followed by the IPA rinsing for about 45 seconds to wash away the Acetone. Ultimately, the device was rinsed by the DI water flow for about one minute to remove the residual IPA and dried by blowing with the compressed air. The Acetone bath could be longer than one minute, which was for a complete removal of residual crystal bond in the void. Improper cleaning would lead to the malfunction of the sensor owing to the residual crystal bond left on the membrane or the mesa, as shown in Figure 4-31.
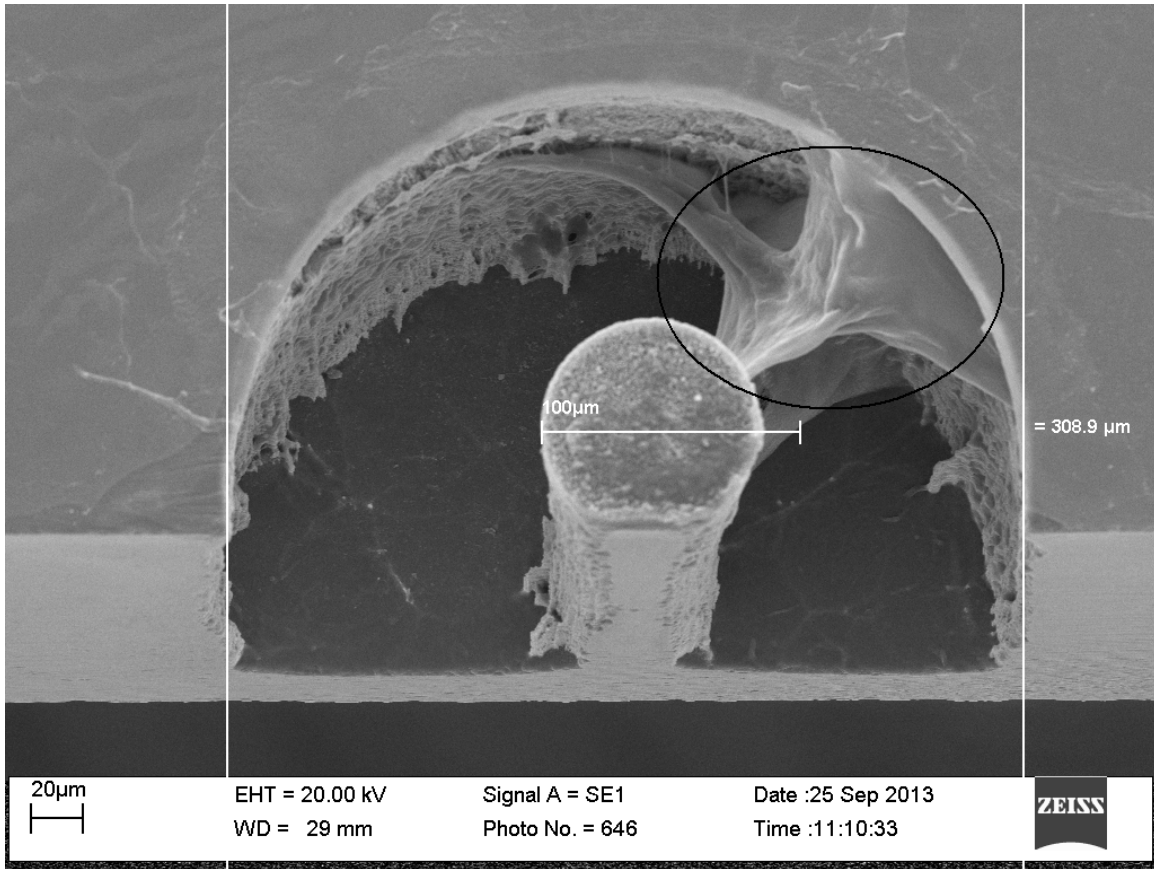
Figure 4-31 Residual crystal bond in the etching void after an improper cleaning

***Flip-chip using stacked gold bumps***

The conductivity between pads on the device and the copper pads on the PCB was essential for the function of sensors. This sensor design was scaled down to 0.5 mm for economic considerations in the future massive production. Therefore, its size was limited by the small bonding pad, on which only one gold bump could be installed. The connection between the sensor and the copper trace on the PCB relied on one gold bump per bonding pad. Using one gold bump on each pad to make conductive connection was challenging and unreliable. This was realized by the author after packaging more than 30 devices. Most of them were partially connected. The reason for these unsuccessfully packaged devices was because the geometric variations aggregated. These variations included binding two surfaces of devices, manufacturing defects (warpage) of the PCB, height variations among four gold bumps, and the degradation of the quality of the extremely small volume of ACA. Figure 4-32 showed a piece of chip containing four devices, one of which was installed with four gold bumps. The chip was mounted on a carrier chip by the crystal bond. The reason of these four devices were diced into one piece was because limitations of the dicing

equipment. Sophisticated dicing approaches adopted in industry such as the laser cutting could solve this issue in future.
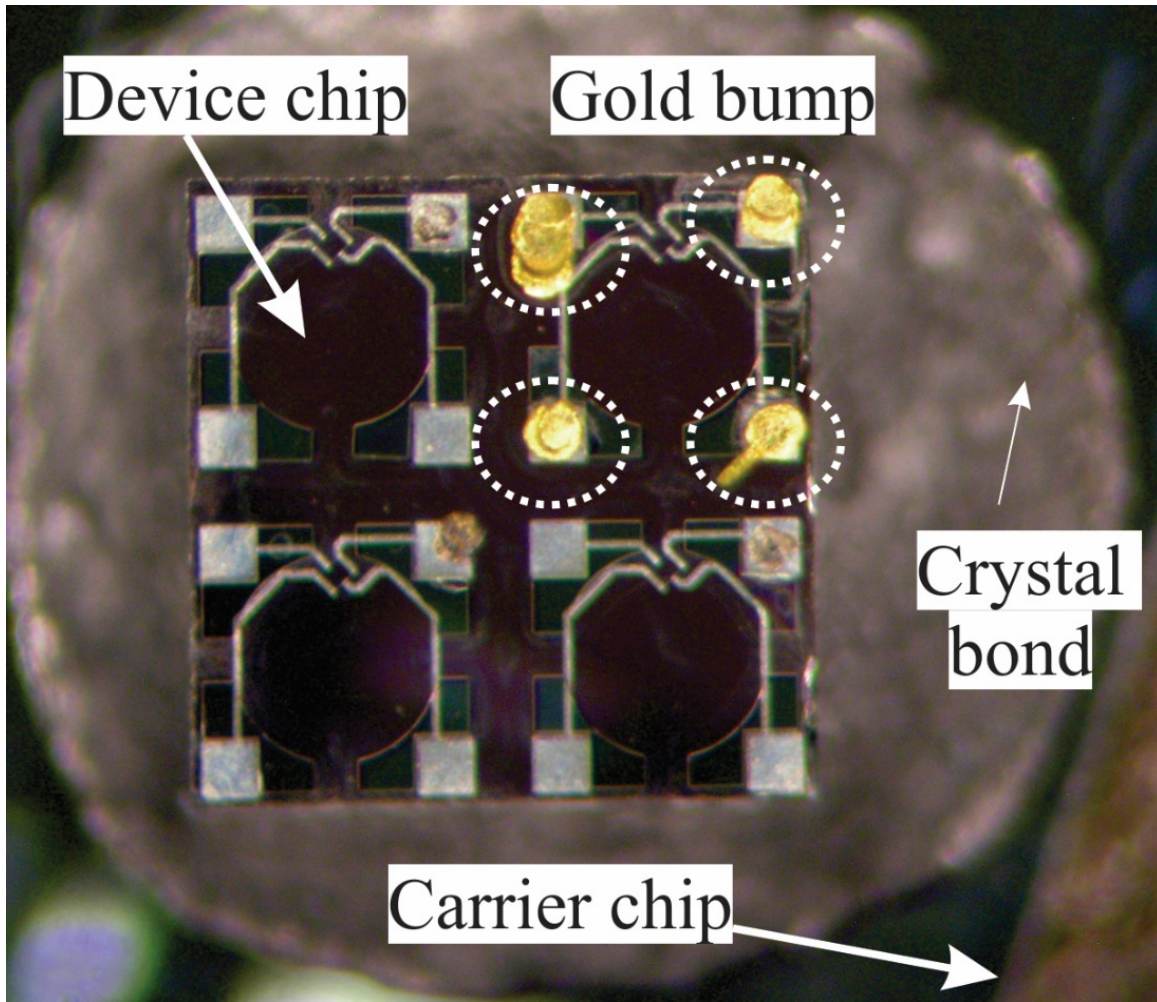


Figure 4-32 Gold bumps on one device of the four-device-group chip

Spreading ACA on the top of a device manually was difficult as the chip size was 1 mm × 1 mm. Moreover, one device size was 0.5 mm × 0.5 mm, although the chip mounted on a larger carrier chip. The ACA was separated into several 1 ml syringes from the original syringe for separated storage. Logically, a small needle could produce small droplets of ACA. However, the ACA was so viscous that the liquid could not be ejected out of the needle if its tip diameter was smaller than 0.006inch (152um). The 0.008inch (200um) needle (TIP 27GA GP 45D .008 CLR 50PC, Nordson EFD Inc.) was chosen for dispensing the ACA. As the diameter of the needle tip was almost equal to double size of the aluminum pad, nearly half size of the device, the injection under microscope was challenging. This caused the ACA overflow on the membrane region and the rest space of the chip, which has been depicted in Figure 4-33.
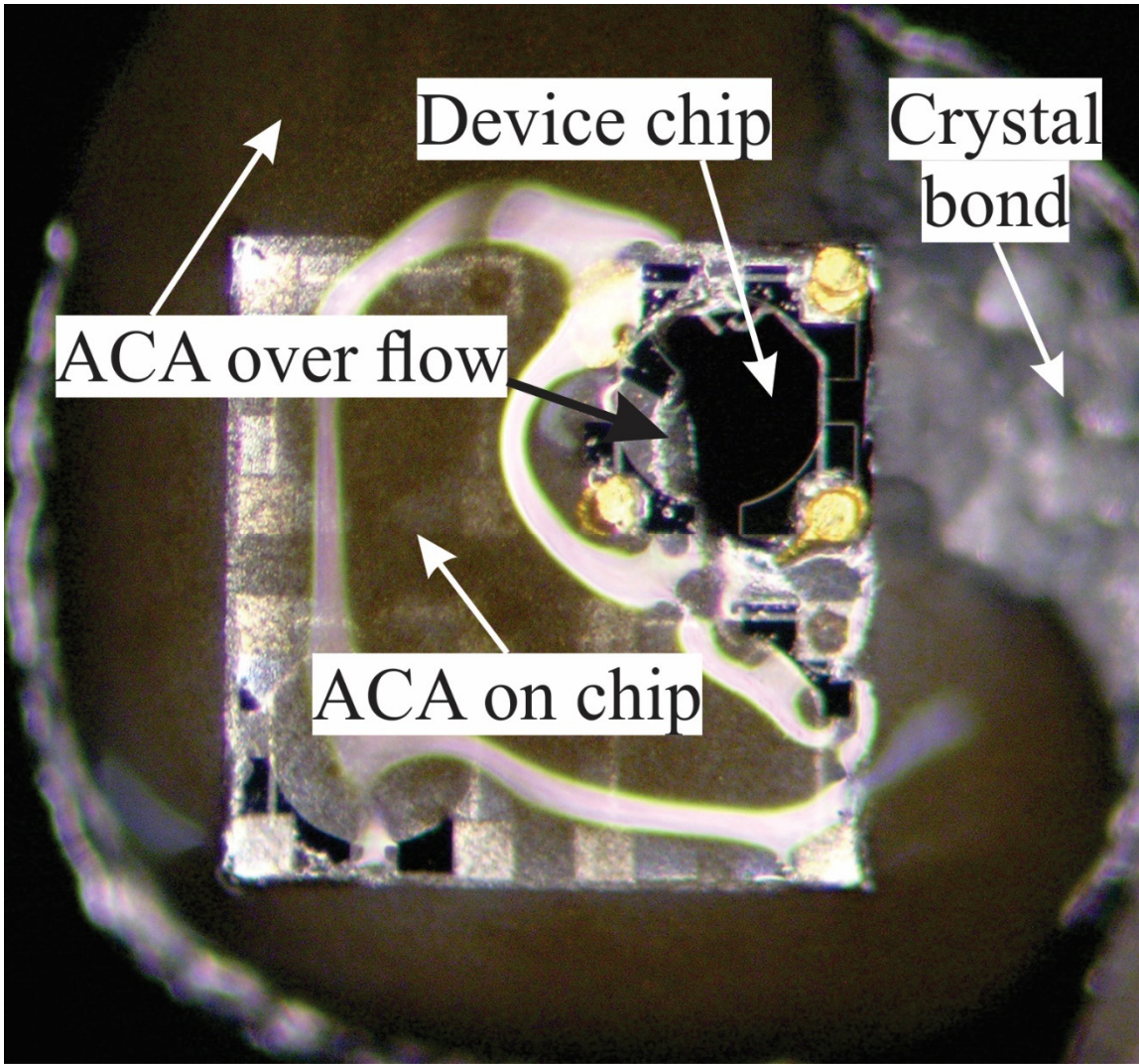
Figure 4-33 Device dispensed with ACA
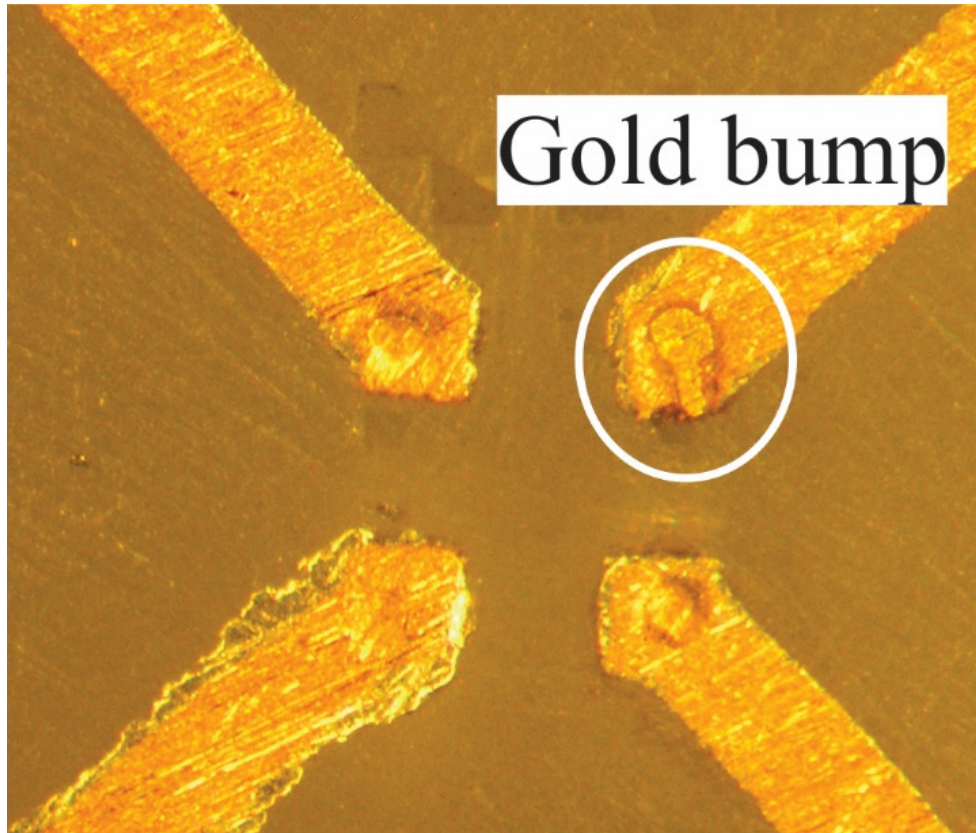
Figure 4-34 Gold bump on copper pad of PCB

Despise of the challenges mentioned above, the protocol of packaging the normal force sensor has been established. In the current design, commercially manufactured PCBs were manually polished to remove the solder covering on the copper traces, which could partially reduce the height differences among those copper pads. This height differences among copper traces caused variable gaps between copper traces and gold bumps in flipping the sensor onto the PCB. To solve this challenge, a dual-gold-bumps method has been developed. An SU-8 flow stopper was planted on the surface of the sensor to prevent the ACA from spreading onto the sensor elements.

As shown in Figure 4-34, one gold bump was planted on each bonding pad in the sensor. The ACA was spread on gold bumps of the sensor die. To achieve better assembling, the PCB has been manually polished with fine sandpaper (600 grit). Then gold bumps were precisely positioned on the polished copper pads under the microscope. The intent was to flip the die onto the PCB. Hereby, gold bumps on both sensor chip and the copper trace would align with each other in vertical direction. Under the pressure applied by the flip-chip machine, relatively soft gold bumps would be squeezed into each other, compensating variations in the height by the stacked gold bumps[150].

With conductive adhesive ensuring electrical connection should any variations occur in alignments. The procedure was shown conceptually in Figure 4-35.
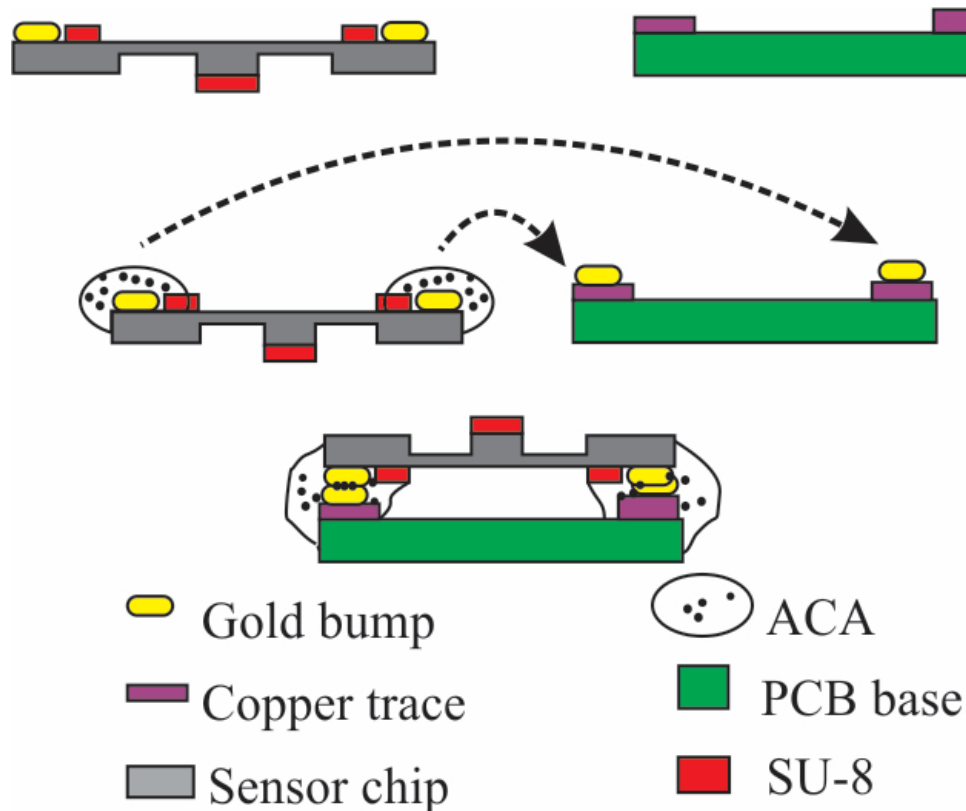


Figure 4-35 Scheme of flip-chip with stacked bumps approach[151]

### 4.8.2 Packaging with larger aluminum pads

The packaging approach described in the previous section has been modified to accommodate the larger design, which was the die size of 3 mm × 3 mm, owing to the larger pad size. On the aluminum pad, which was 1 mm × 1 mm, at least 9 gold bumps were installed (see Figure 4-37). With several gold bumps on each pad, this dramatically increased the conductive quality of the connection. As shown in Figure 4-36, the packaging started with installing gold bumps on chips, and sanding the PCB. The ACA was then spread on the copper pads of the PCB, instead of on aluminum pads of the device, which was different comparing with the previous packaging approach with stacked gold bumps. After aligning both the device and the PCB, the sensor was packaged onto the PCB by curing the ACA. The heating profile applied by the flip-chip machine (FINETECH Inc.) was captured in  Figure 4-38.
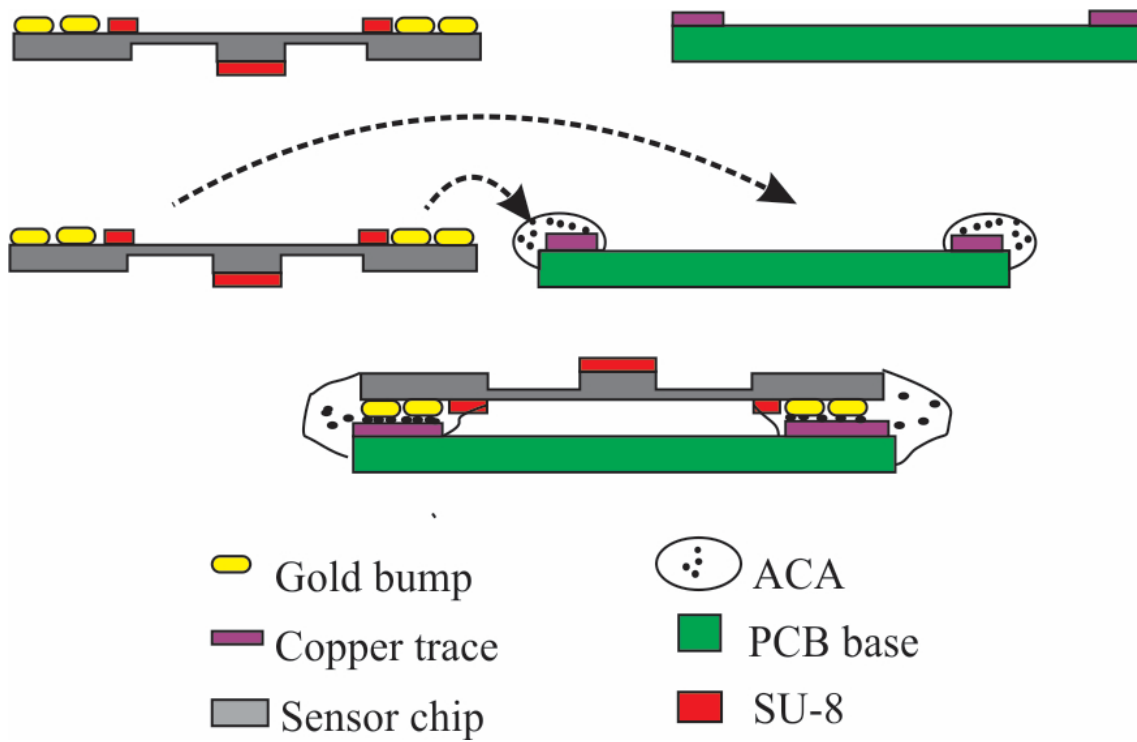
Figure 4-36 Modified flip-chip process for normal force sensor and multi-axis force sensor
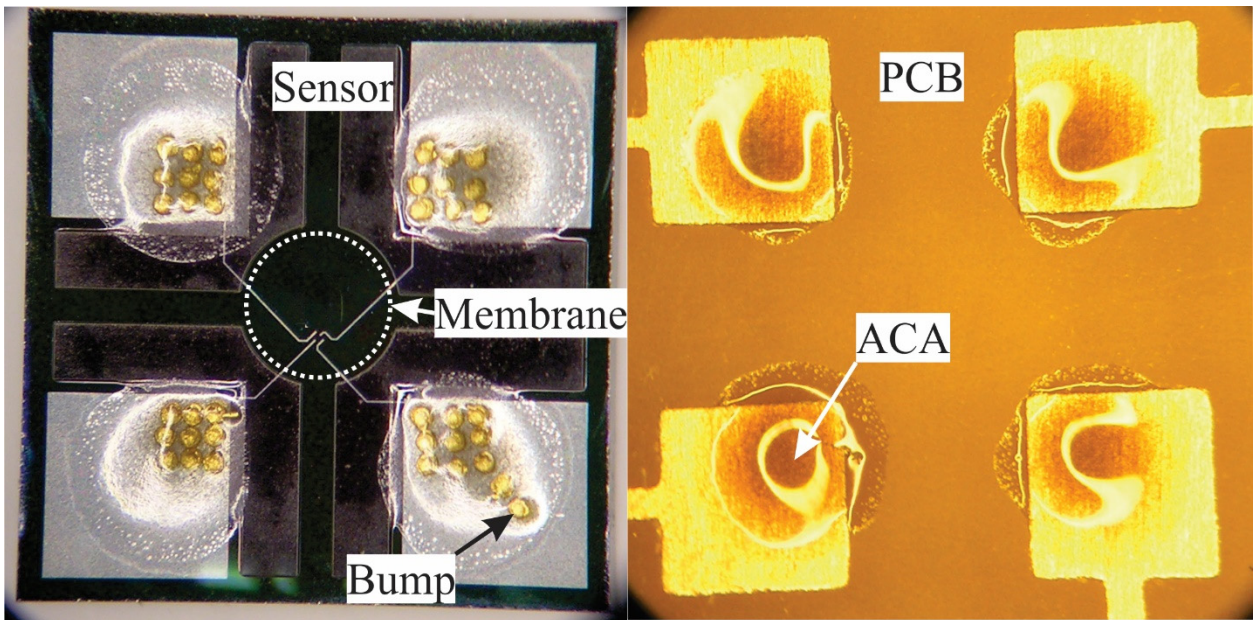


Figure 4-37 Unfolded package of a normal force sensor © [2018] IEEE
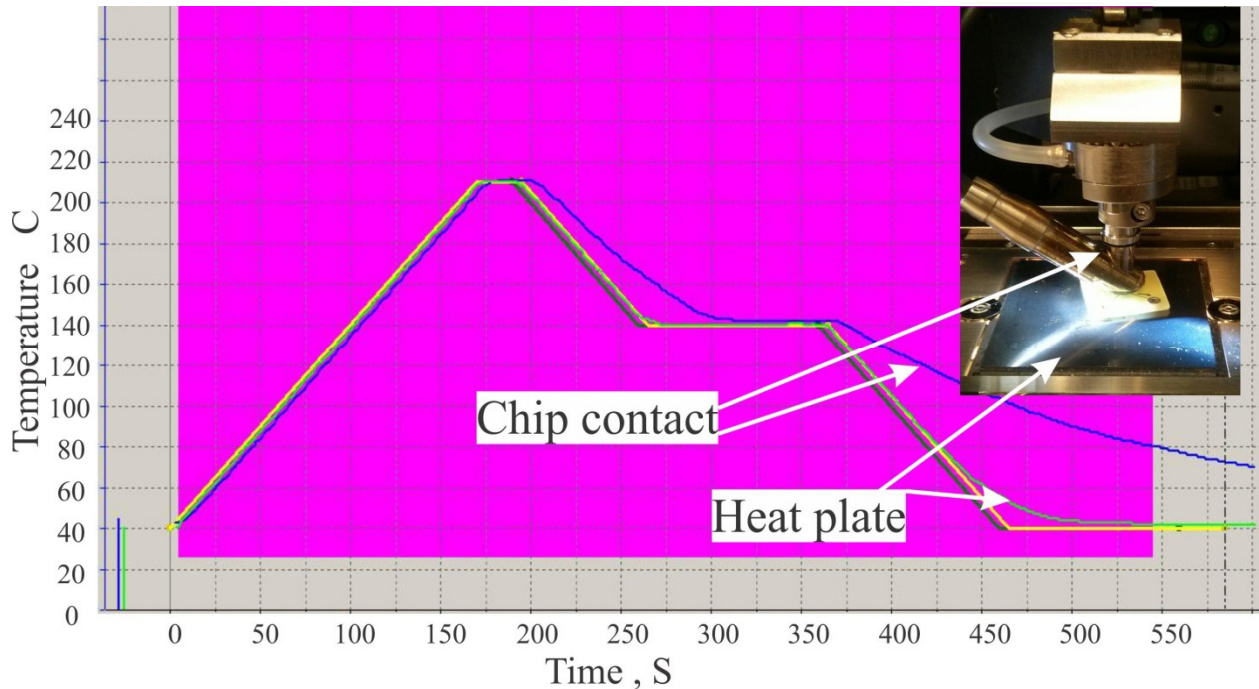
Figure 4-38 Temperature profile of the Flip-chip process

## 4.9 Packaging the sensor array for the uniaxial tactile force

As the proposed design, four tactile sensors were arranged as a 2 × 2 sensor array. Therefore, the four sensors were firstly packaged onto the same piece of PCB, using the same flip-chip approach described before for the individual sensor packaging. To sense the lateral deformation or the horizontal displacement of the thin glass plate to recognize the inclined force, the mesa of each sensor should be fixed at the bottom surface of the glass plate. The uncured SU-8 was chosen for the merits of its simplicity, transparency and ease to be span on the glass using the spinner machine. This thin layer of uncured SU-8 on the glass plate would be melt again by blowing the hot air on it, bonding the mesas of four devices. Figure 4-39 has shown the difference between a mesa glued to the glass film and an unattached mesa underneath the glass. The glued one has an annular circle outside the mesa top.
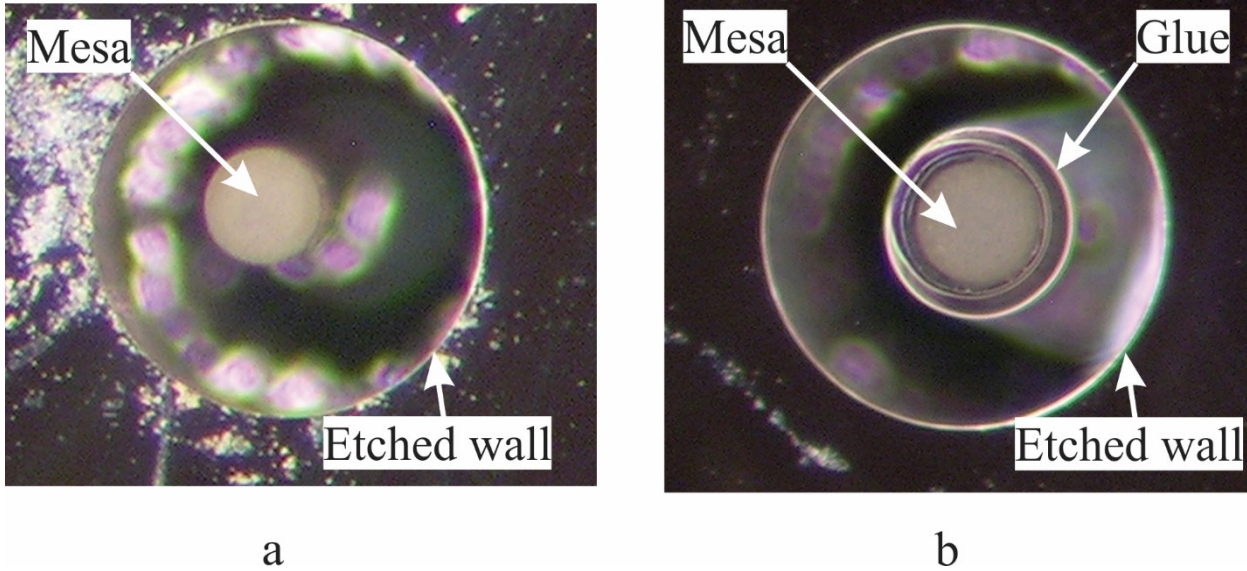
Figure 4-39 a. Free standing mesa underneath a thin glass plate; b. Glued mesa under glass

The four edges of the cover glass plate on the sensor array should be fixed, according to the proposed uniaxial array design. Several experiments using a thermal glue to fix the edges of glass film have been tried but failed, accountable for several possible reasons. Melted thermal glue was viscous and sticky liquid. However, it solidified quickly (in about 10 seconds) once it was squeezed on to PCB in the ambient environment. To deploy a proper volume of the glue was challenging if it was done manually. Besides, a rough joint would be formed at the corner of the glass film as shown in Figure 4-40 a. Besides, the thermal glue shrank to some extent when it changed from a liquid to a solid. This deformation caused the glass film dislocated from the original place after spreading and cooling, and pushed the mesas or membranes to break, since the mesa had already been glued with the glass film. Another prompt has been made, which was to deploy the thermal glue around the edges of glass film before attaching the mesas. Then the assembly was put into a furnace and annealed at 150 °C for 2 minutes. The thermal glue reflowed and distributed along four edges of the glass film uniformly, without rough corners or voids. The mesa was glued to the glass film as well in this procedure. However, the conductivity between sensor and PCB suffered a significant damage or degradation, which made this approach improper for the packaging. Hereby, a room temperature cured adhesive and sealing spacer needed be taken into considerations for packaging the sensor array.
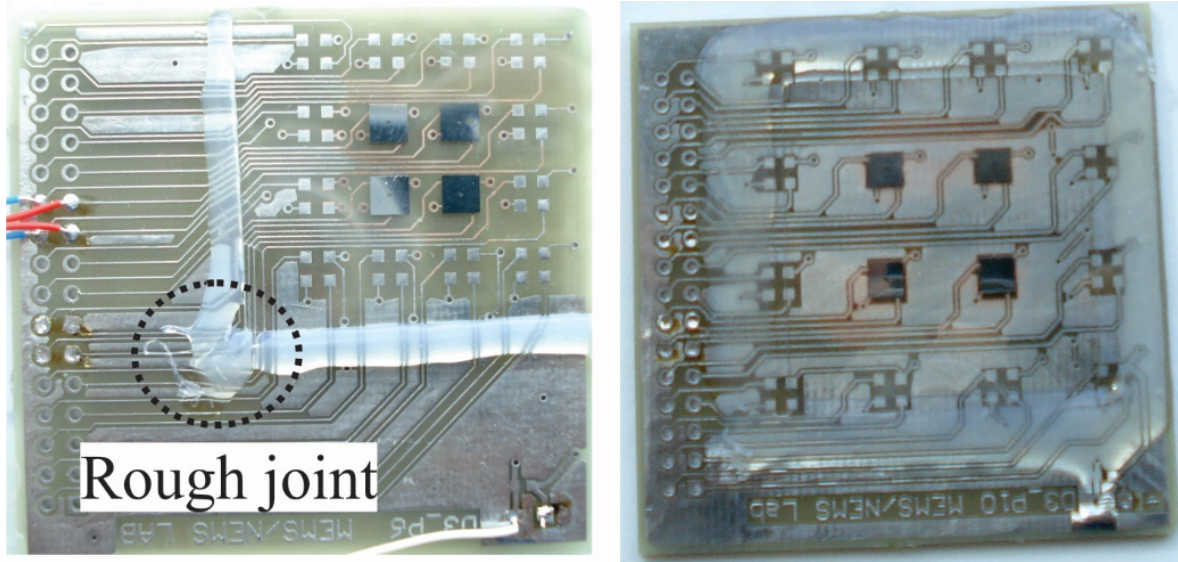
Figure 4-40 a. rough joint in the thermal glue; b. thermal reflowing of the glue

A feasible protocol for packaging the prototype of sensor array has been developed eventually, which was illustrated in Figure 4-41. The packaging started with the flip-chipping of four sensors onto one piece of PCB. The flip-chip procedure was the same as described before for packaging the individual sensor. Then SU-8 2010 was poured onto a piece of glass film. This SU-8 2010 was spread on a spinner machine for 10 seconds at the speed of 500 rpm and followed by spinning for 40 seconds at the speed of 4000 rpm to achieve the film thickness at around 10 um. This glass film was carefully flipped onto the PCB which was assembled with four sensors, with the SU-8 layer contact with four mesas. The hot air flow at the temperature of 150 °C was blowing on the surface of the glass plate for one to two minutes, which liquidized the uncured SU-8 layer. Owing to the gravity of the glass and the surface extension of the liquid SU-8, the top surface of each mesa would be immersed into this thin layer of SU-8. After cooling down to the ambient temperature, the bonding of the mesa and the glass film was done. Placing silicon strips under the edge of the glass film as the seal spacers, several drops of adhesives (Loctite 407®) were spread at edges of the glass film and on the silicon strip, to fix the edges of the glass plate and complete the prototype packaging in a few hours. Figure 4-42 showed a packaged sensor array with normal force sensors.
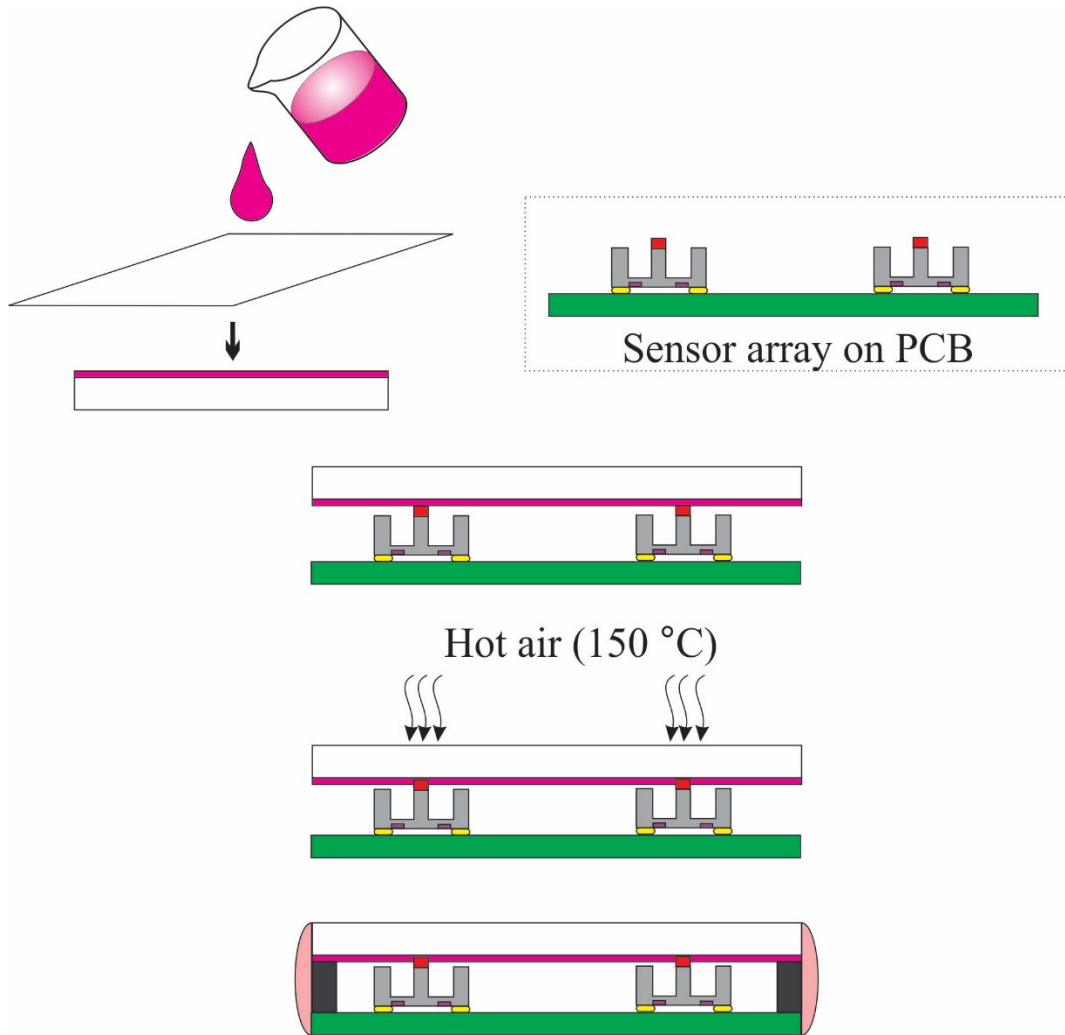
Figure 4-41 Packaging protocol of uniaxial sensor array

Using SU-8 as the adhesive to attach the mesa to the cover glass was a temporal solution for the development of sensor array prototype. Other adhesives could be used if they were compatible with the current protocol, i.e. using other thermal plastic polymers could also work.
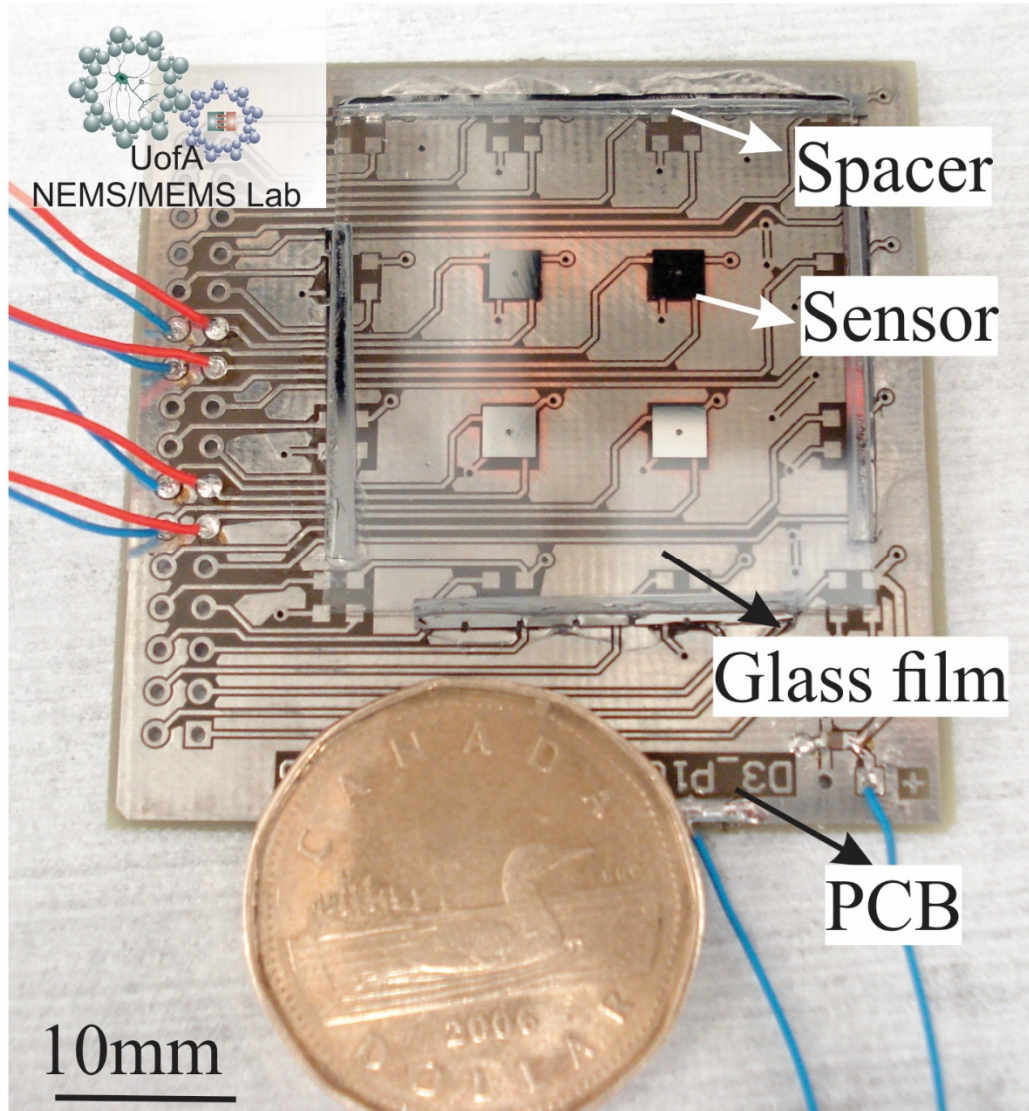
Figure 4-42  uniaxial sensor array prototype © [2017] IEEE

## 4.10 Packaging multi-axis tactile sensor array

As discussed before in the sensor array design section, the multi-axis sensor array has been proposed as the configuration of 60 mm × 60 mm. Therefore, common PCB was firstly used to develop the prototype as shown in Figure 4-43. This packaging approach was similar as what the author did in section 4.9 (see Figure 4-41) with a few differences including the expanded layout and sensor footprints. However, for larger packaging comparing with previous uniaxial sensor array, the previous packaging approach was not successful as the cover glass film could not contact with four mesas simultaneously. The reason of this packaging challenge was that the warpage of regular PCBs could reach several hundred micrometers. The mesa height extending above the

etching well was only around 30um. As the layer of SU-8 melted, the glass film touched edges of sensors first and bonded with the sensor body instead of the mesas, leaving the sensor array malfunctional.
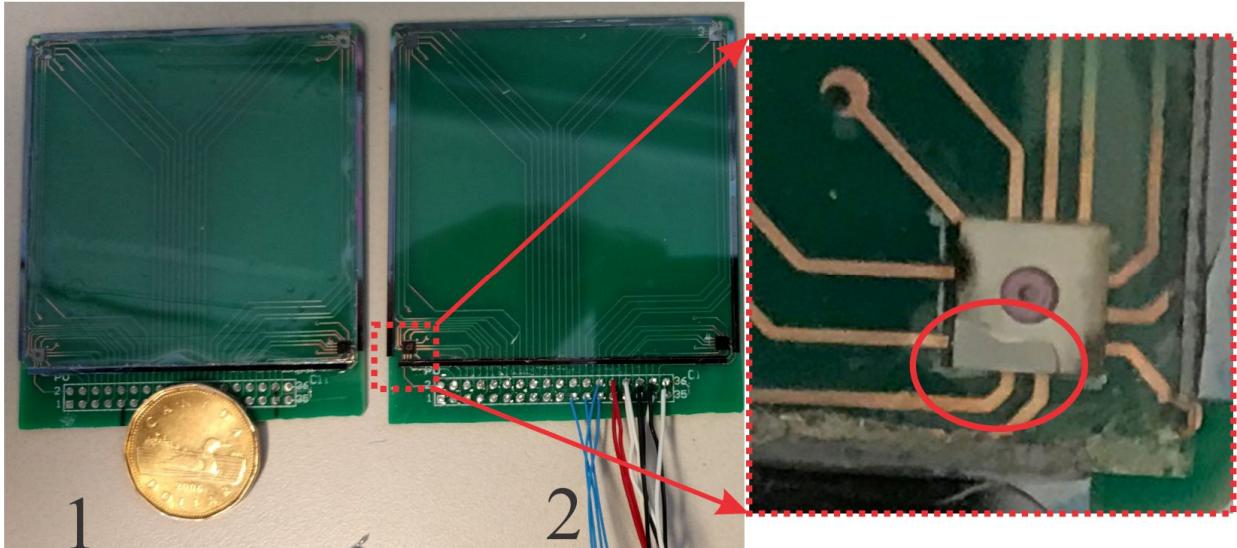


Figure 4-43 Prototype samples of multi-axis sensor array

An exaggerated schematic drawing attached below also explained the possible reason of misalignments between sensor mesas (see Figure 4-44).



Figure 4-44 Exaggerated view of mesa leveling differences

To avoid the malfunction of the sensor array caused by leveling differences of mesas, the warpage of PCB substrate needed to be solved. Usually, a super flat PCB could be customized from the manufacture, but which would be expensive and arising delays on the schedule. Therefore, a glass substrate has been chosen to make the circuit of the sensor array by the author as an alternative way, owing to its super flatness (about 5 um). The reason of this super flatness was because of the manufacturing process of glass, which was pouring melted glass on top of melted metal to get self-leveling caused by the gravity. This was a standard industrial approach which was economic.

Therefore, Boro float® glass substrates were added to the packaging protocol for the multi-axis tactile sensor array. A procedure of lift-off was used for making the super flat PCBoG (PCB on Glass, see Figure 4-45). Along with this, the adhesive to seal the gap between the glass cover and the silicon spacer has been changed to the PDMS, which offered the top thin glass plate a degree-of-freedom to move around the x-y plane. Therefore, the sensor array could sense the horizontal displacement, consequently, getting the shear force information. The modified protocol of packaging has been depicted in Figure 4-46.
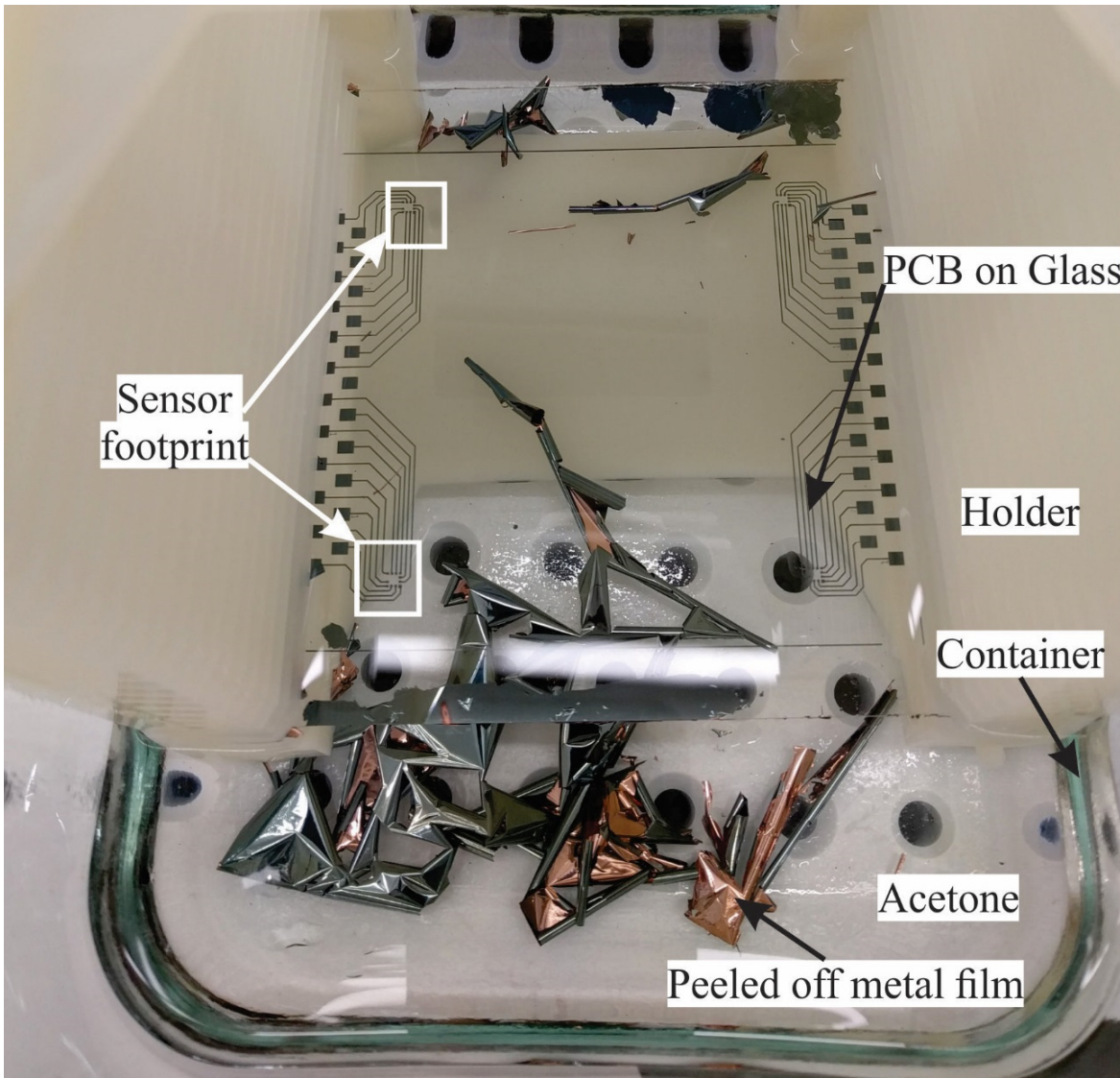
Figure 4-45 PCB on glass (PCBoG) by the lift-off

Apply Photoresist

Pattern

Sputtering metal

Lift-off

Sensor array on PCBoG

Hot air (150 °C)

■ Sensor   □ Glass   ■ Uncured SU-8   ■ SU-8
⬭ Gold bump   ■ PDMS   ■ Spacer   ■ Cu
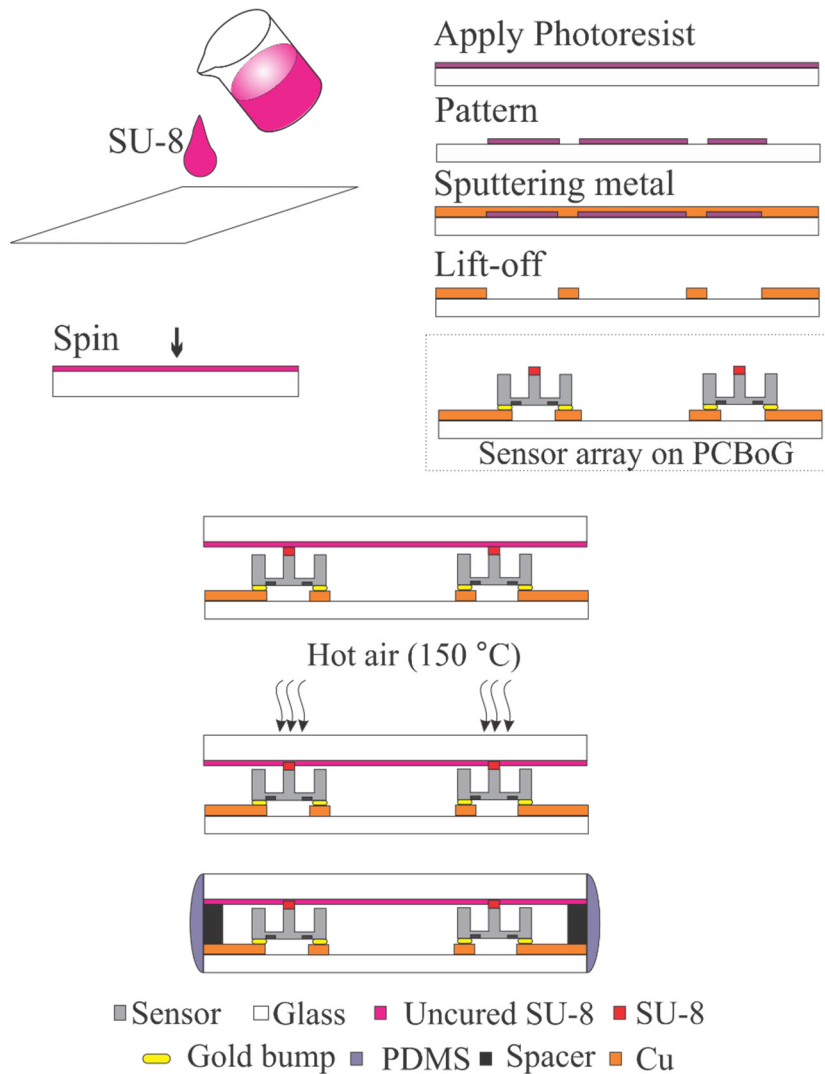
Figure 4-46 Modified packaging protocol for multi-axis sensor array © [2018] IEEE

With the PCBoG approach utilized in the modified packaging protocol, the sensor array is transparent in most the working area (see Figure 4-47). This was convenient for following characterizations and tests because the probing points could be monitored by mounting a printed grid under the sensor array.

100
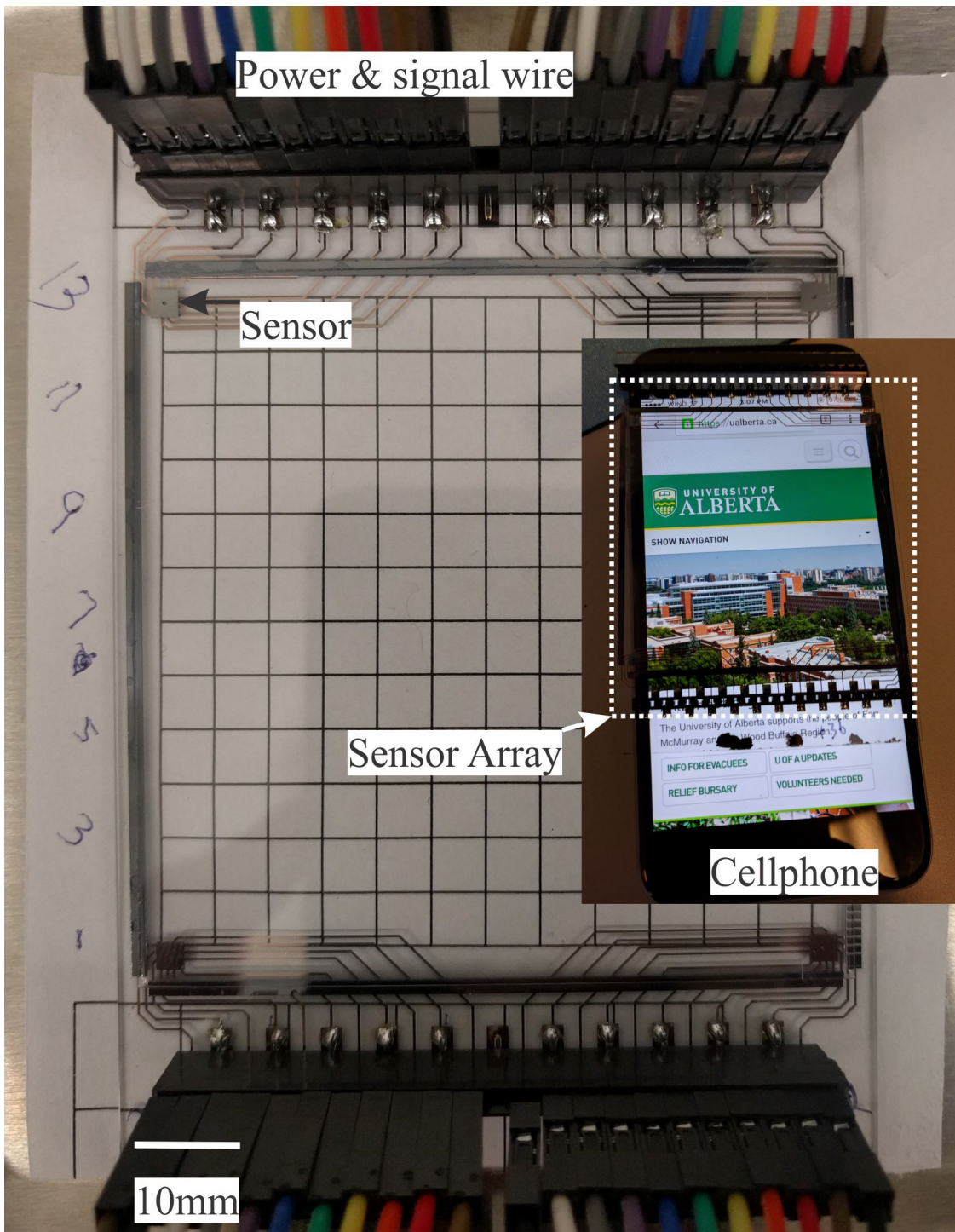
Figure 4-47 Packaged multi-axis sensor array and its transparency on a cellphone

# Chapter 5. Characterization and test[3]

*All models are wrong, but some are useful.*

**George E.P. Box**

(1919-2013)

## 5.1 Characterization and test on the uniaxial (normal force) sensor

Characterizations on force sensors can be done by applying a known force on them and calculating the sensitivity according to their responses. The normal force sensor was characterized by applying a normal force on the mesa with a probe whilst the sensor was placed on the top of a microbalance with a resolution of 1 mN. The manipulation of the probe was done under a microscope, which ensured that the sharp probe was in the center of the mesa tip. Characterization platform has been depicted in Figure 5-1.
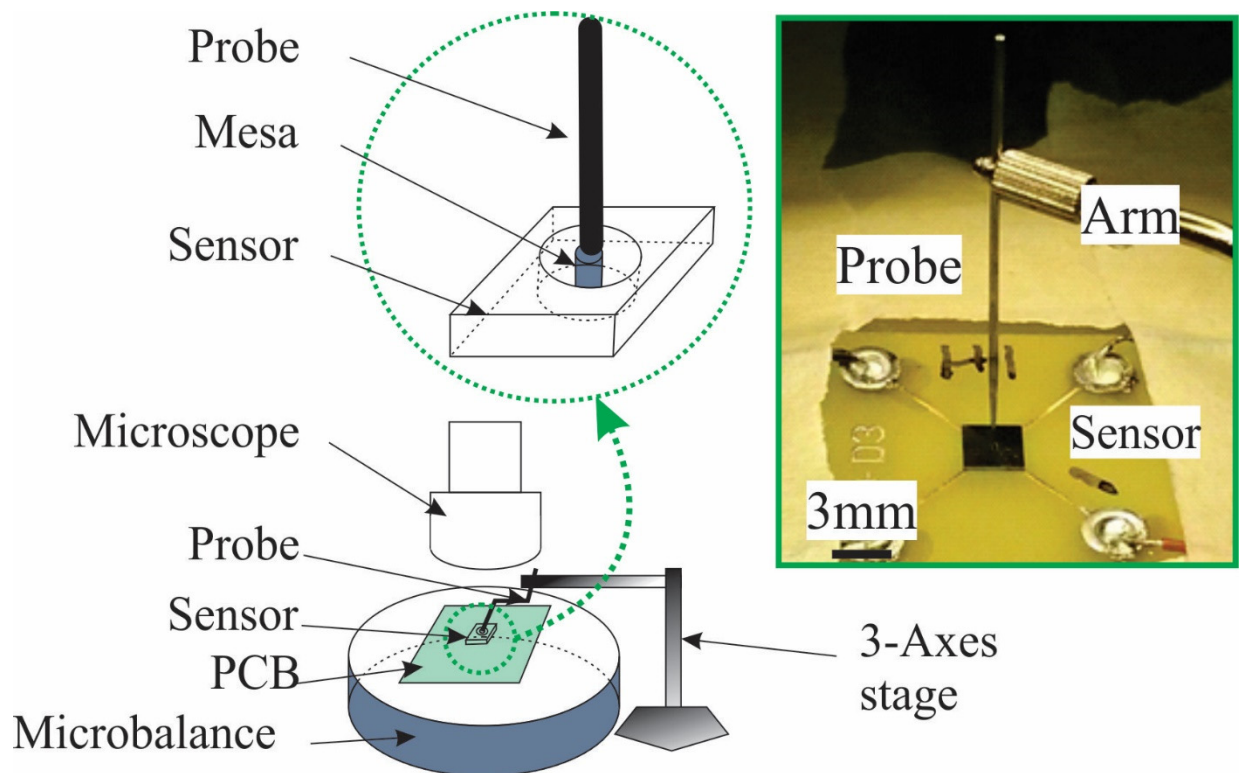


Figure 5-1 Scheme of normal force sensor characterization platform

Since normal force sensors have been implemented by two sources, which are the outsourced from the manufacture and the fabricated by the author in the nanoFab. Therefore, two series of characterizations on those sensors have been done. As presented in Figure 5-2, the performance of

---

[3] Some of the materials in this chapter has been published by Yue *et.al.*[137][140][141]

normal force sensors from 500 um × 500 um dies lay within the range of simulations, and demonstrated a sensitivity about 0.5 mV/mN•V with high linearity. This plot proved the feasibility of designed sensors on sensing tactile force at the mN level.
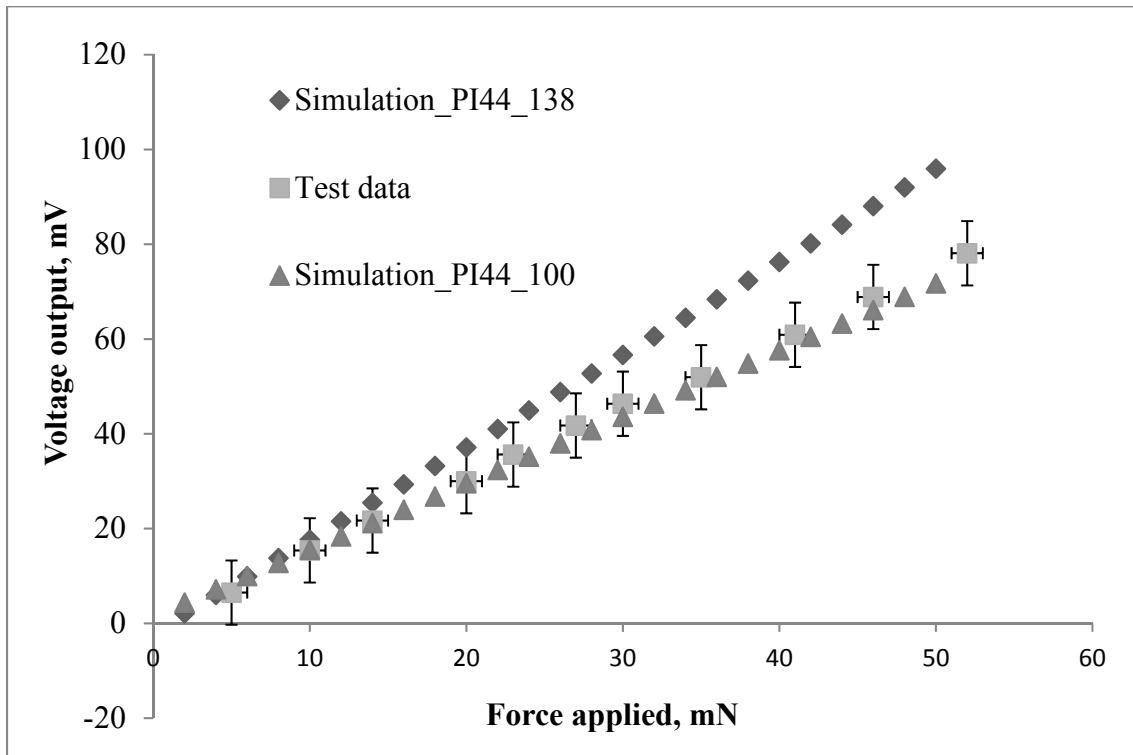


Figure 5-2 Results acquired from a normal force sensor outsourced from manufacture[137] ©
[2014] Springer
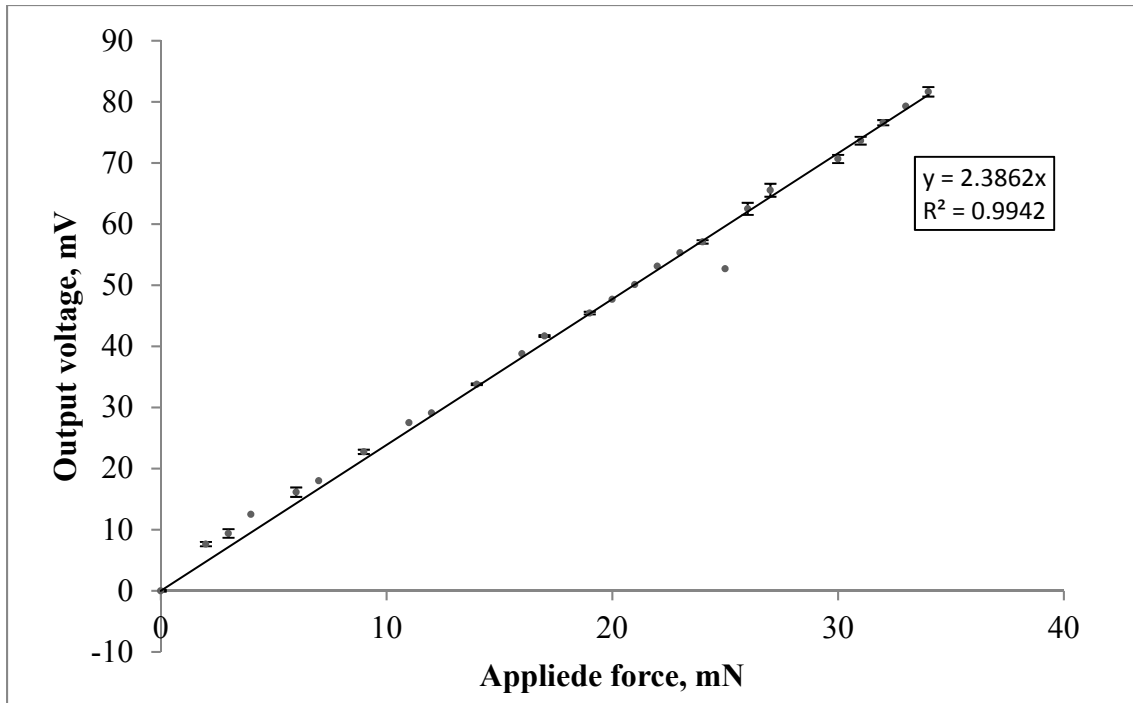
Figure 5-3 Sensor outputs from normal loads on the mesa

Sensors fabricated from nanoFab and diced in a larger footprint have been characterized using the same platform as described above. Collected data have been shown in Figure 5-3. This sensor has a larger sensitivity, which is 0.79 mV/mN•V, comparing with previous devices from the vendor. This could be explained by doping variations caused in the thermal doping and sensor geometrical differences by the DRIE, respectively.
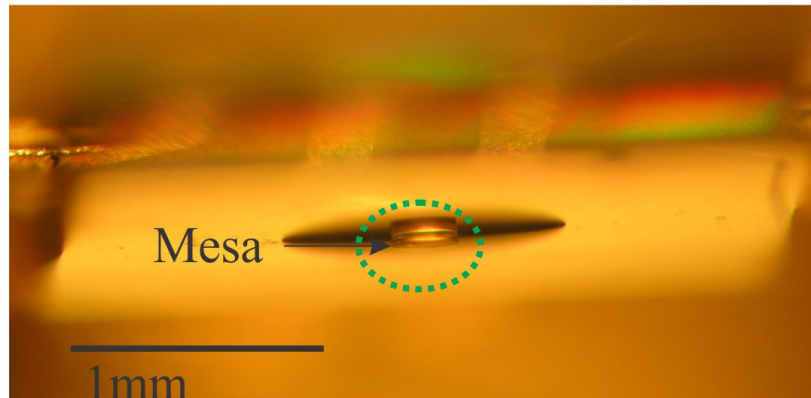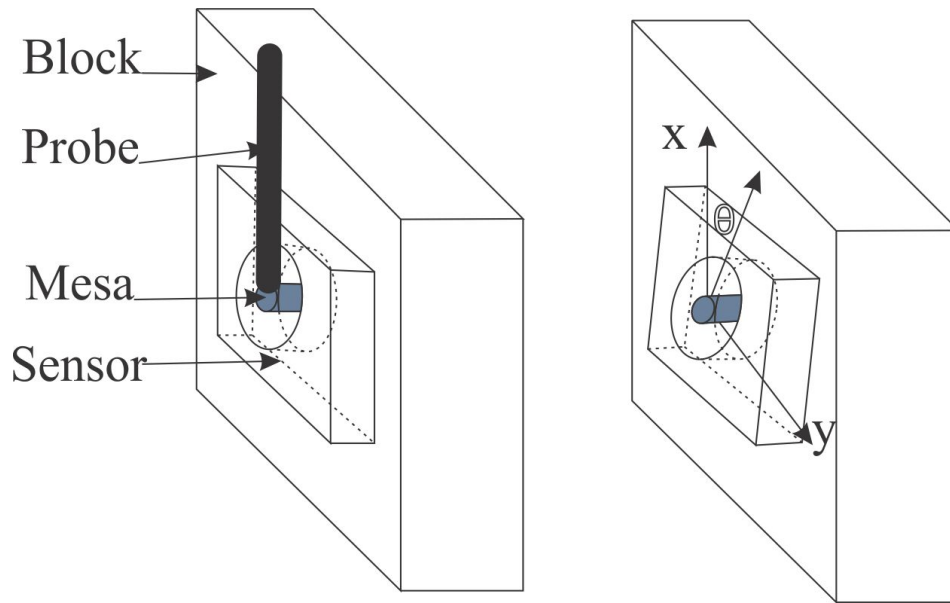
Figure 5-4 *Top:* Test scheme of a uniaxial force sensor behaving on a shear force; *bottom:* Sensor photo from a vertical perspective

In the sensor design phase, the sensor outputs exhibited a sinusoidal feature in responses to shear forces. To validate this simulation observation, a test scheme has been developed as presented in Figure 5-4. Since the mesa structure extended out of the sensor body at the backside, a straightforward way of applying a shear force would be pushing the mesa horizontally using a sharp edge. However, to find a sharp blade and control the blade edge to align with the standing-out part of the mesa was not viable due to the vertical layout of the microscope. Hence, an alternative way was proposed. The sensor was bonded on a wood block; the bonded test vehicle was placed vertically on a microbalance. The mesa can be observed clearly under the microscope. The force was applied perpendicularly to the mesa axis at its tip and parallel to the gravity (see Figure 5-4 *bottom*). After collecting one group of test data, the sensor was detached and re-bonded

onto the block with a rotated angle $\theta$ for the next round of test until the sensor was tested within a full resolution.
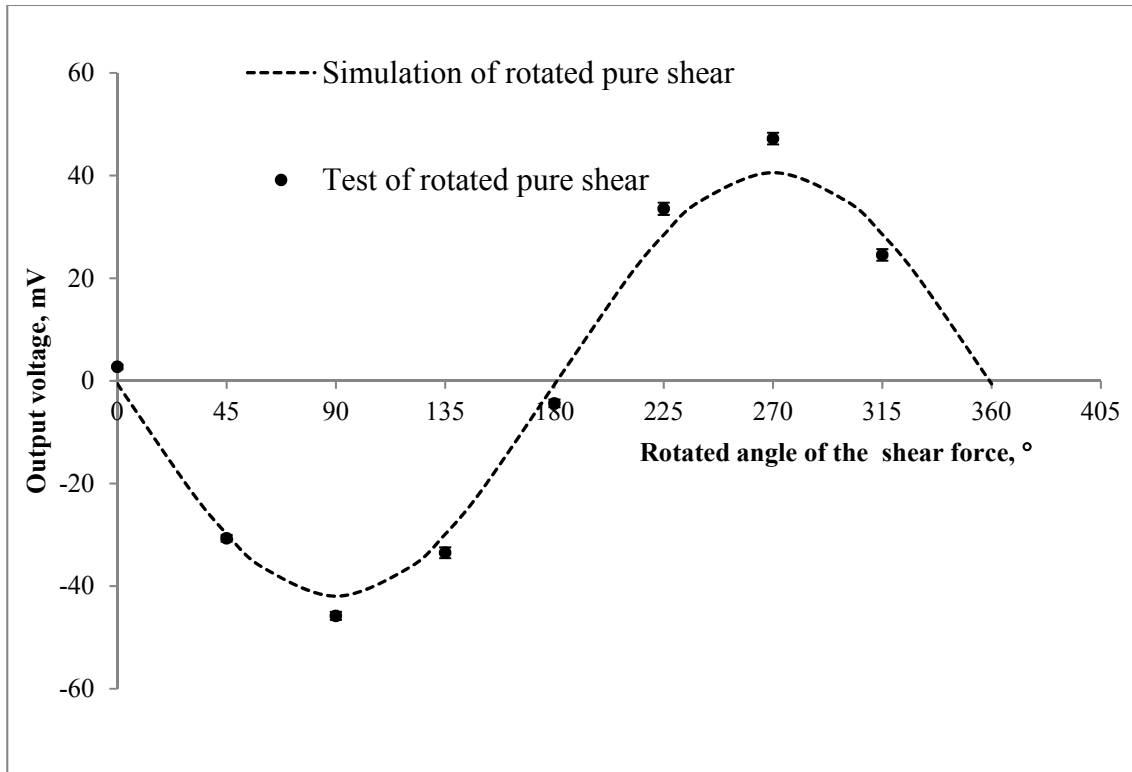


Figure 5-5 Sinusoidal behavior with respected to a rotational shear force © [2018] IEEE

See Figure 5-5, eight different orientations have been chosen for mounting the sensor to evaluate the shear force performance, which included *0°, 45°, 90°, 135°, 180°, 225°,270°,* and *315°,* with respect to the gravitational direction. Notably, the data points were not exactly fell on the sinusoidal simulation curve. This could be explained by the force misalignment during the tests. More precise testing platforms for shear force could be found in literature[42]. However, as a proof of concept, our testing results are sufficient for validating the sinusoidal behavior.

The maximum force that the sensor could tolerate was evaluated by raising the applied force until the destructive damage occurred. The damaged happened when a 350-mN normal force direction was applied, leading to the mesa broken as shown in Figure 5-6.
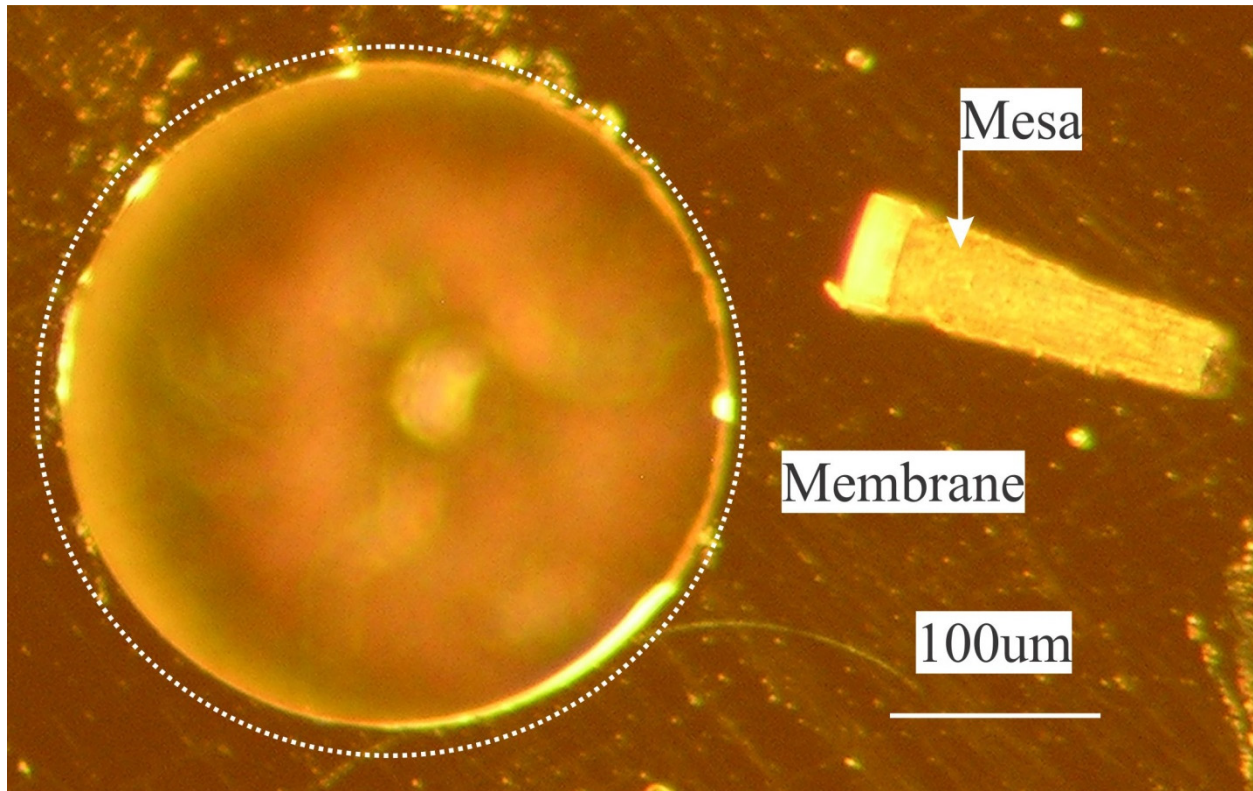


Figure 5-6 Mesa broken during destructive test for maximus force ability

As displayed in Figure 5-6, the shape of mesa was tapered at the root due to the sidewall profile from the DRIE. This tapered feature affected the maximum strength of the mesa. The maximum shear force was tested to be around 100 mN. Both the maximum strengths of the senor in the normal and shear direction have been improved by the packaging approaches of assembling them into an array, which could be found in following sections.

## 5.2 Characterization and test on the uniaxial sensor array
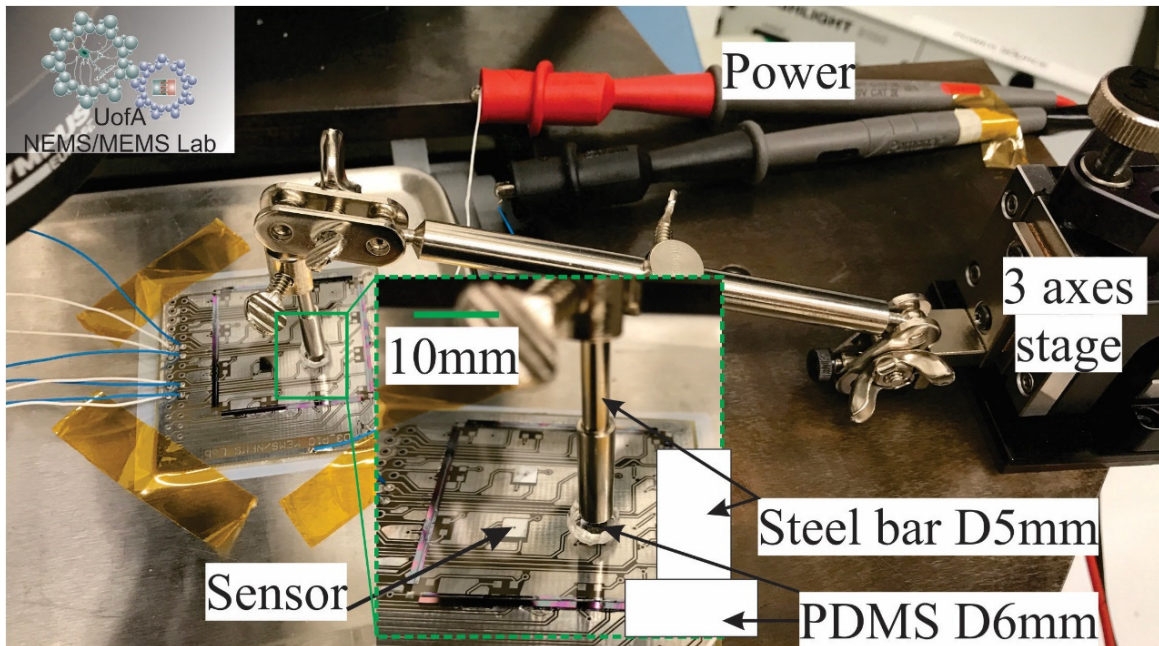


Figure 5-7 Probe test structure using a PDMS cushion as emulation of finger palm contact ©
[2017] IEEE

As the sensor array was designed to sense both the location and force information, which were the known variables in the characterization. Usually, finger tips contact with touchscreen panel at a small area with a distributed load. However, to apply a distributed load at the prototype at a controlled location could be challenging without robotic arms incorporated with computer vision feedbacks. The author would like to continue using sharp probe as the core part to apply the load on the sensor array in an easy and cost-effective manner. Considering the area difference of a fingertip and the probe tip, whether the loading area would affect the outputs or not became questionable. Therefore, see Figure 5-7, a PDMS cushion has been used as an emulation of the contact area between the fingertip and the sensor array. The normal force was applied by a steel bar installed on a 3-axes stage, with contact locations controlled manually from the view in the microscope.
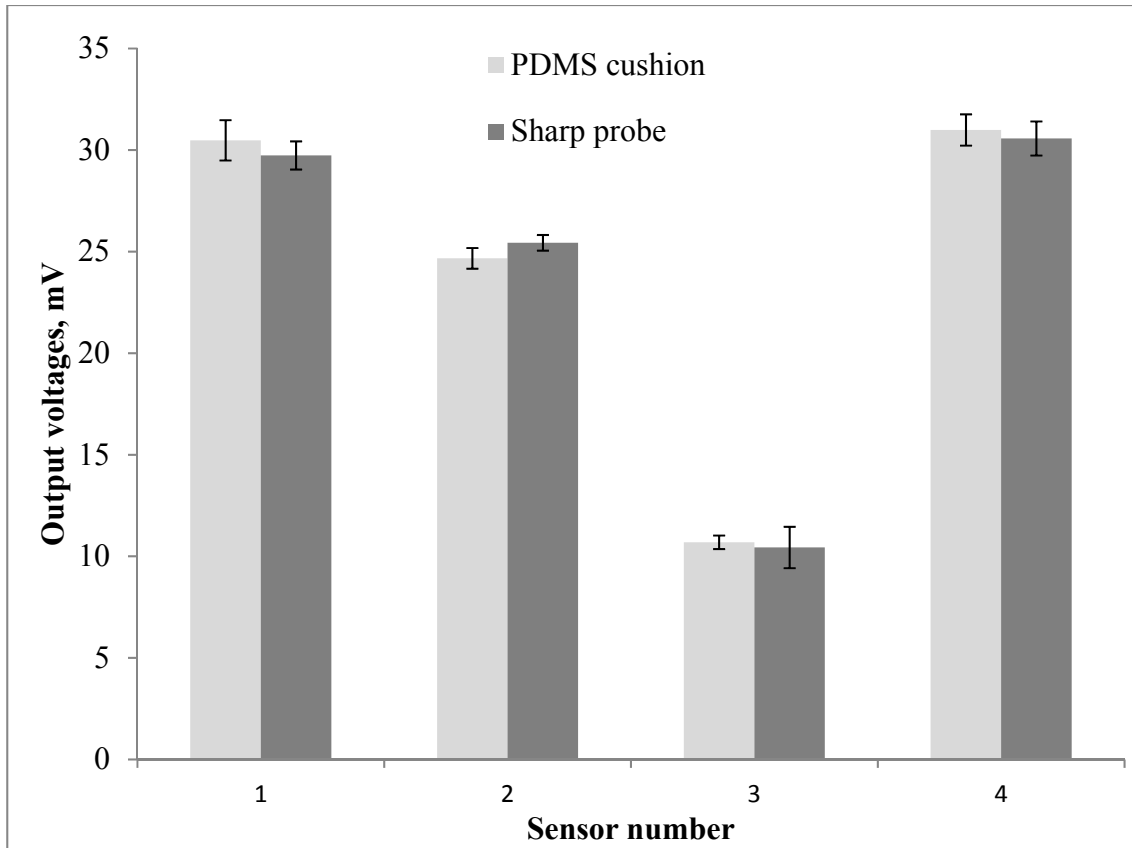
Figure 5-8 Comparison between tests using a sharp probe and the steel bar with a PDMS cushion © [2017] IEEE

The Young's modulus of the glass was typically more than 70 GPa (according to the Corning Willow® glass datasheet). The human finger tissue has the Young's modulus below 0.25 MPa if the applied force was smaller than 10 N[152]. The deformation of the fingertip would comply with the profile of the glass cover at a low tactile force level within the scope of this work. The glass cover deformation would remain the similar although intuitively the contact area caused by a fingertip was larger than by the probe. This conclusion could be also confirmed by the results (see Figure 5-8) tested by using a circular PDMS (polydimethylsiloxane) cushion with thickness of 5 mm (see setup in Figure 5-8) to mimic the fingertip, since the Young's modulus of PDMS was within range of 0.36MPa - 1MPa[69]. This value was close enough to the finger tissue in literature. The outputs from sensors remained at the same level with/without the PDMS cushion if applied 0.1N normal force on top of sensors. Therefore, for the ease of manipulating the location of the applied load, the rest of characterizations were done using a sharp probe under the microscope.
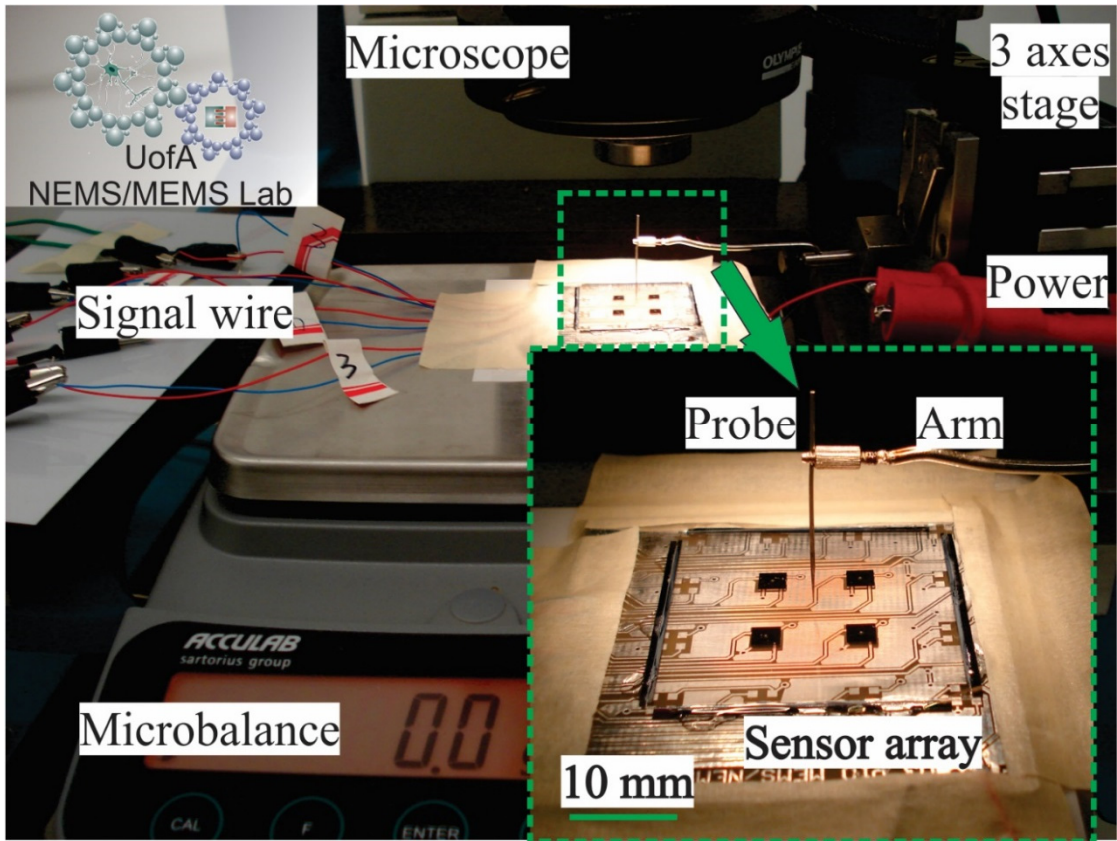
Figure 5-9 Probing setup for characterizations and tests © [2017] IEEE
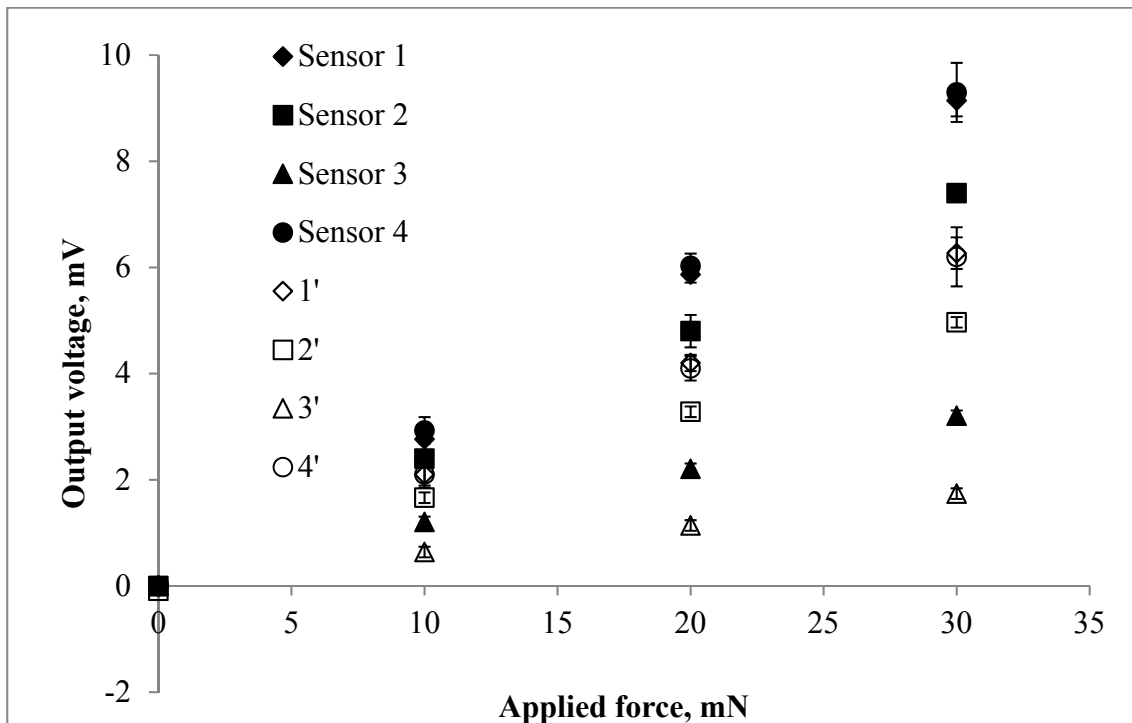


Figure 5-10 Sensor array outputs with/without cover glass © [2017] IEEE

The sensors were tested individually after they were assembled on the PCB, before covering the glass plate on them. This data has been shown in Figure 5-10, which was plotted by the solid dots. According to the test, four sensors in the array demonstrated a high linearity. The sensitivity range of the four sensors was from 0.31 mV/mN•V to 0.11 mV/mN•V, although more than 200% discreteness existed. Moreover, sensor 1, sensor 2 and sensor 4 had the similar level of sensitivity, with their ranges changing from 0.31 mV/mN•V to 0.25 mV/mN•V, which were less than 20% discreteness. This discreteness was mainly caused by the doping level differences across the wafer, which introduced the variation on the piezoresistive properties of the four-terminal gauge. After packaging the array with the glass plate, these four sensors were tested again with the same amplitude of normal forces. The data was shown in Figure 5-10 by the hollow dots. About 30% drop of the sensitivity was observed from the sensors, due to the support from the elastic glass plate. The accordance of the sensitivity decreasing from those four sensors could be explained by the global symmetry in terms of the sensor array layout.
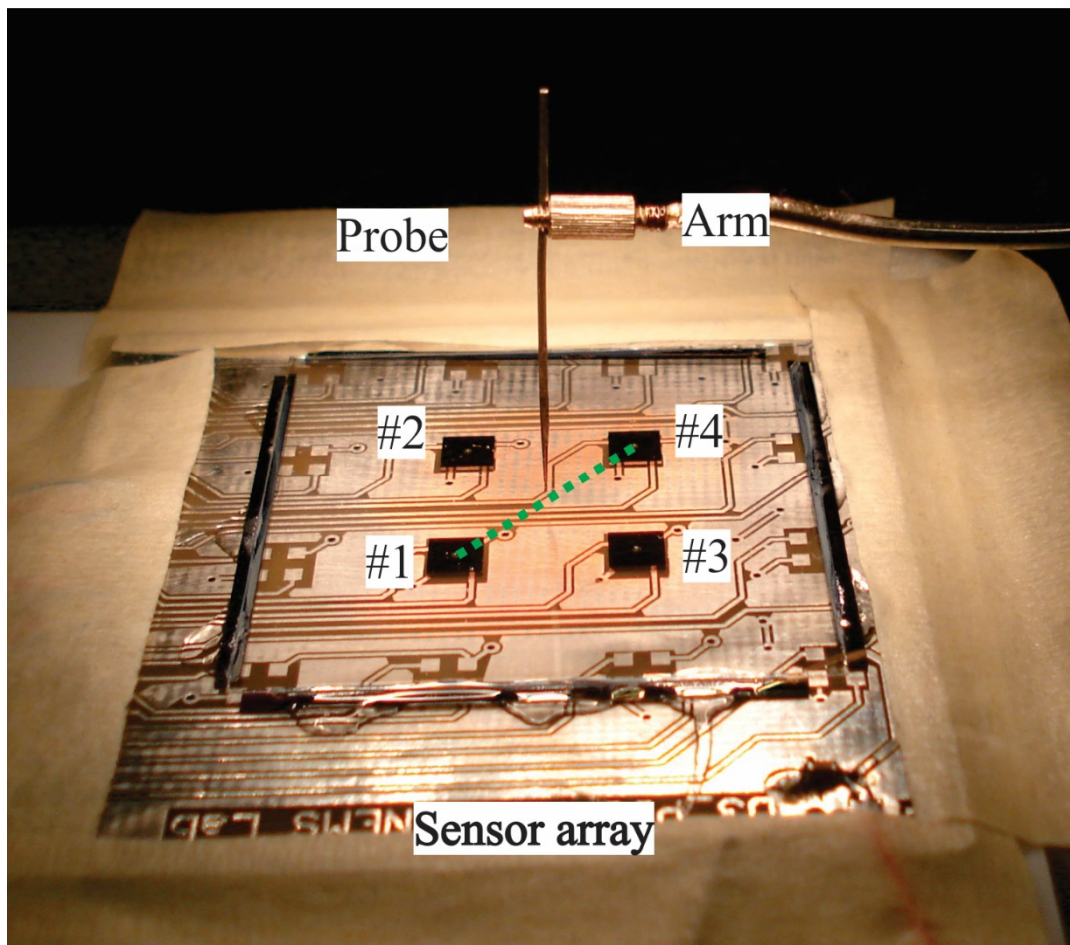


Figure 5-11 Probe trajectory from sensor 4 to sensor 1
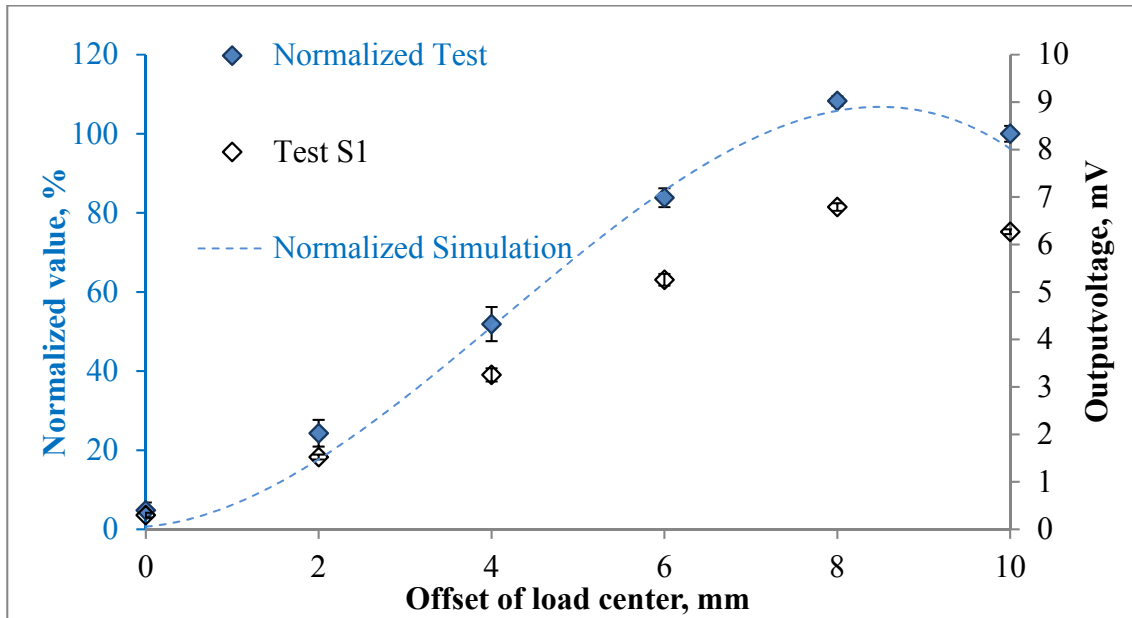
Figure 5-12 Data from sensor 1 © [2017] IEEE
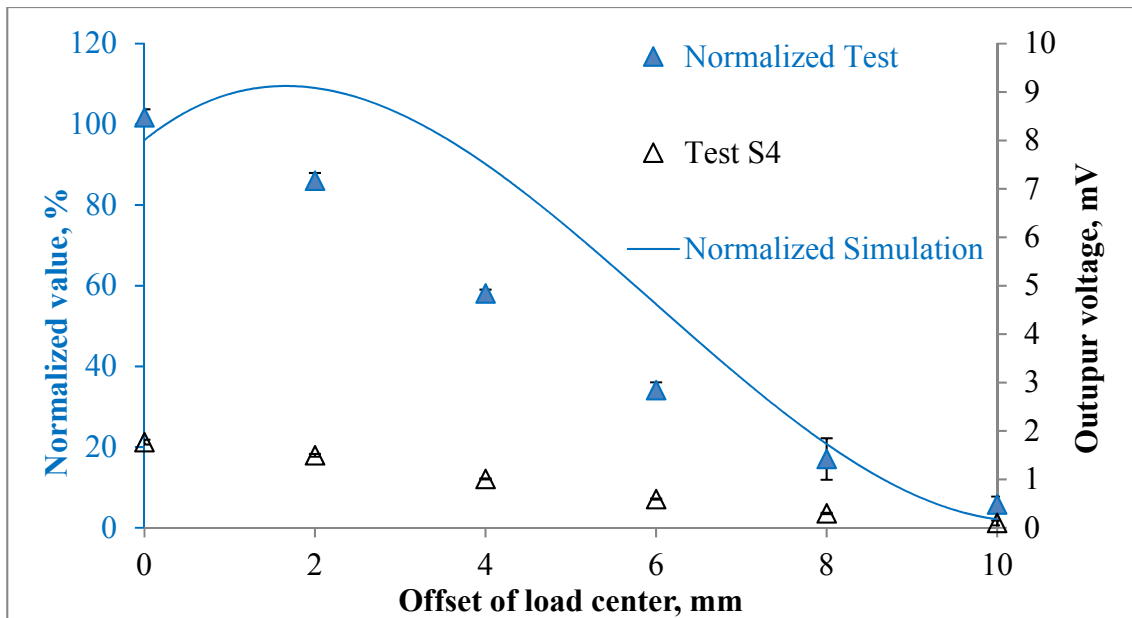


Figure 5-13 Data from sensor 4 © [2017] IEEE
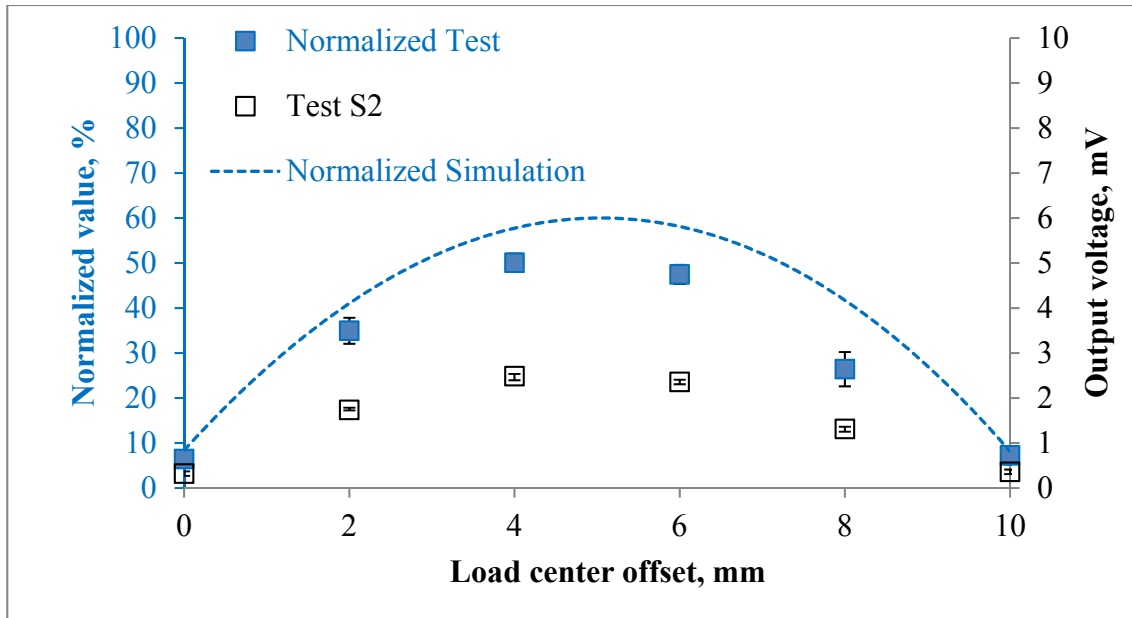
Figure 5-14 Data from sensor 2 © [2017] IEEE
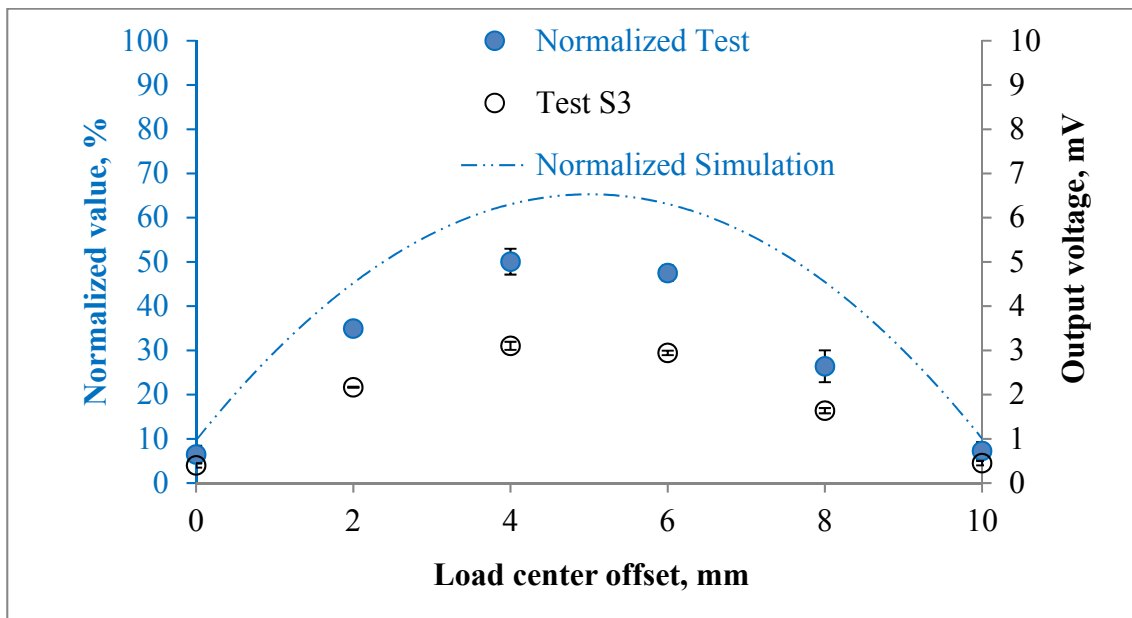


Figure 5-15 Data from sensor 3 © [2017] IEEE

The test data from four tactels have been shown in Figure 5-12 - Figure 5-15, which plotted the responses of moving the load center from the top of sensor 3 toward the sensor 1. As the load moving closer to sensor 1, its output increased from 0.3 mV to 6.27 mV. Before getting to the peak value, the output increased more than 25% at each step of the load center moving, indicating that the output increment was sufficient for differentiating the location information at a resolution of 2 mm. As the load moving from the top of sensor 3 to the top of sensor 1, the sensor 3 output dropped

from the maximum value to the minimum value. This was due to the changing distance between the load center and the sensor. However, the normalized value of the sensor 3 did not quite fit with its normalized simulation. About 20% discreteness existed among the locations where the distances between the load and the sensor 3 were 2 mm, 4 mm, and 6 mm, respectively. This might be caused by its low sensitivity and fabrication variations. To avoid such discreteness, all sensors in the same array should have been chosen to be the similar sensitivity before the flip-chip procedure or mitigating the fabrication variations by ion implantation in the future. Similarly, both outputs of the sensor 2 and sensor 4 increased as the load moved closer to the sensors and dropped as the load moving further from them. Both normalized test values of the sensor 2 and sensor 4 were lower comparing with their normalized simulation values, indicating the sensor array demonstrated higher stiffness than the simulation. Moreover, the normalized test values demonstrated similar trend as the normalized simulation, which was essential for force calculations and location decoupling. The output changes were between 16% and 34% for 2 mm location variations when the force was moved closer to or further from the sensor 2 and 4. Notably, the outputs from sensor 2 and sensor 3 were not symmetric with respect to the central position at 5 mm. Such phenomenon was due to the sensing element location on the membrane. The sensing element was at the edge of a circular membrane, therefore, those four tactels were not symmetrically orientated at those four corners. The prototype sensor array demonstrated the ability to sense the force applied on the glass cover. Besides, for a force applied between the individual sensors, the sensor array can sense the force and location differences, indicating the potential of having a smaller space resolution at mm level if more characterization data was collected. The test results agreed with the FEM numerical simulations.
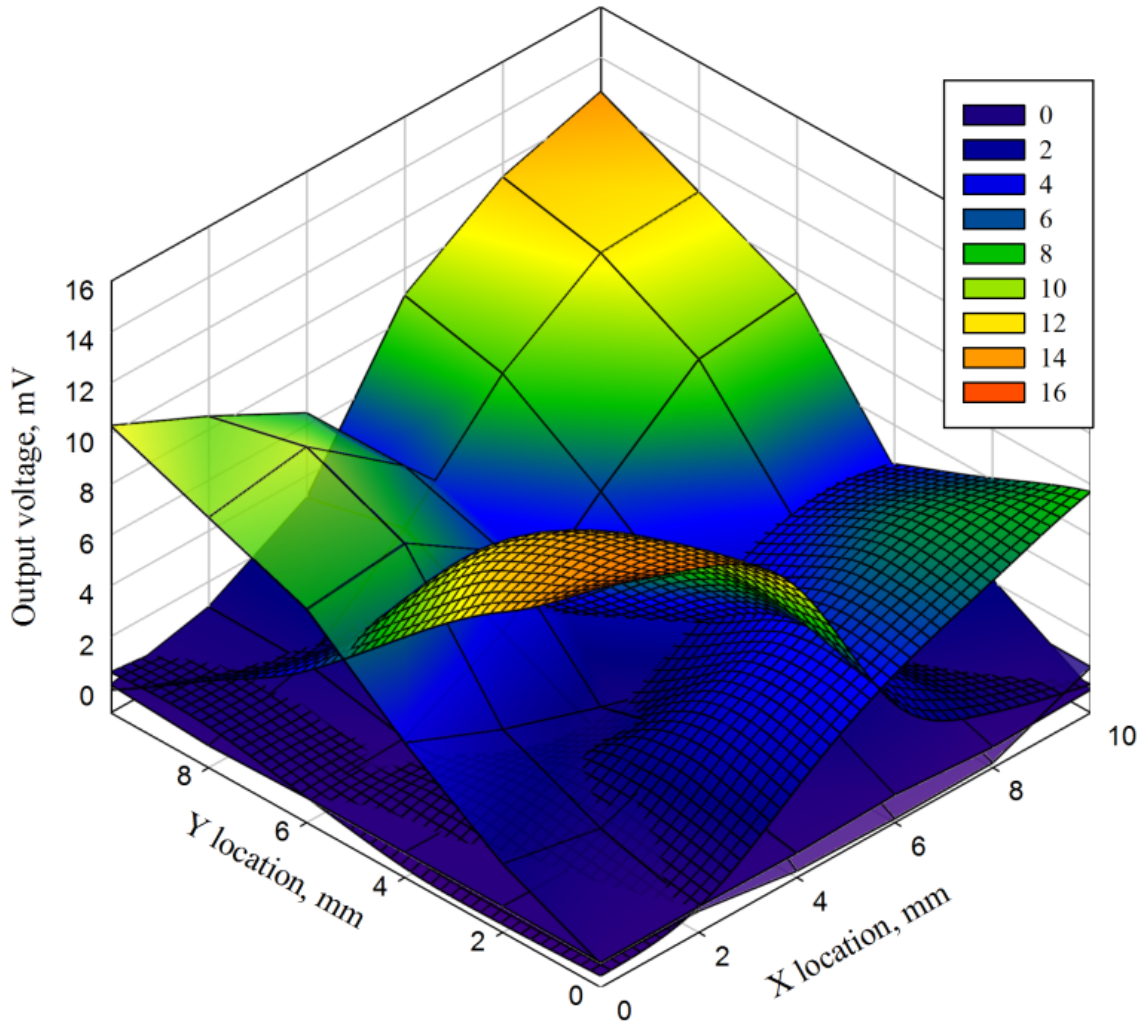
Figure 5-16 Data form complete probe test over the sensor array © [2017] IEEE

To quantify the response of the sensor array, outputs from the sensor array within the functional area were to be evaluated. A complete probe test has been done on the sensor array by applying a 50-mN normal force at various locations with a coordinate increment of 2 mm in either *x* or *y* directions respectively, yielding 36 sets of data. The data has been plotted in Figure 5-16. Notably, four surfaces plotted in the figure representing series of outputs from the four tactels. Each surface could be found symmetric to each of the two diagonal lines of the square region. Therefore, a triangular quarter of the region could be characterized by the outputs from two closer tactels (two larger signals out of the four) with a unique *output fingerprint* (sensitivity). Based on this observation, a lookup table was formed to quantify the corresponding force and location as shown in Table 5-1. The overlapping region by two adjacent tactels has been marked in the same color within the triangular quarter. By searching through the lookup table, the force and location

corresponding to a specific tactile event was calculated. Moreover, the two larger outputs from four tactels could also accelerate the searching procedure for four times faster by narrowing the polling region to one specific triangular quarter instead of the whole. The searching algorithm was based on the least square method which was to minimize the square error between the actual output signal and elements in the lookup table, expressed in equation:

$$\begin{cases} f_{i,j} = \min_{i,j} \Sigma_{k=1}^{2,3,4}(S_{tk} - S_k^{i,j})^2 \\ \quad a = i * d \\ \quad b = j * d \end{cases}$$ 5-1

where $S_{tk}$ standing for sensitivity calculated from test results and $S_k^{i,j}$ standing for the element in lookup table at $i_{th}$ column and $j_{th}$ row, $d$ standing for the step distance for probe tests. Once the index numbers $i$ and $j$ were found using the least square method, the location of the force could be calculated as well as the corresponding force.

Table 5-1 Lookup table scheme built from probing test at each key point on the sensor array; (a, b) representing the location (mm, mm) on the sensor array; S1,S2,S3,S4 representing the sensitivity acquired from tactels © [2017] IEEE

| S3,S4 | S2S3 | S2S3 | S2S3 | S2S3 | S2S3 |
|---|---|---|---|---|---|
| (0,10) | (2,10) | (4,10) | (6,10) | (8,10) | (10,10) |
| S3S4 | S3S4 | S2S3 | S2S3 | S2S3 | S1S2 |
| (0,8) | (2,8) | (4,8) | (6,8) | (8,8) | (10,8) |
| S3S4 | S3S4 | S3S4 | S2S3 | S1S2 | S1S2 |
| (0,6) | (2,6) | (4,6) | (6,6) | (8,6) | (10,6) |
| S3S4 | S3S4 | S1S4 | S1S2 | S1S2 | S1S2 |
| (0,4) | (2,4) | (4,4) | (6,4) | (8,4) | (10,4) |
| S3S4 | S1S4 | S1S4 | S1S4 | S1S2 | S1S2 |
| (0,2) | (2,2) | (4,2) | (6,2) | (8,2) | (10,2) |
| S1S4 | S1S4 | S1S4 | S1S4 | S1S4 | S1S2 |
| (0,0) | (2,0) | (4,0) | (6,0) | (8,0) | (10,0) |

Therefore, this lookup table algorithm treated the sensor array as if it had 6 × 6 virtual tactile cells, although physically only with four channels of data. This dramatically reduced the workload of the signal processing. Based on this lookup table algorithm, three tactile events were identified

with positions and input forces in Figure 5-17. These three tactile events were tested individually. The sensor array design would be meaningful for applications of one-point tactile sensing.
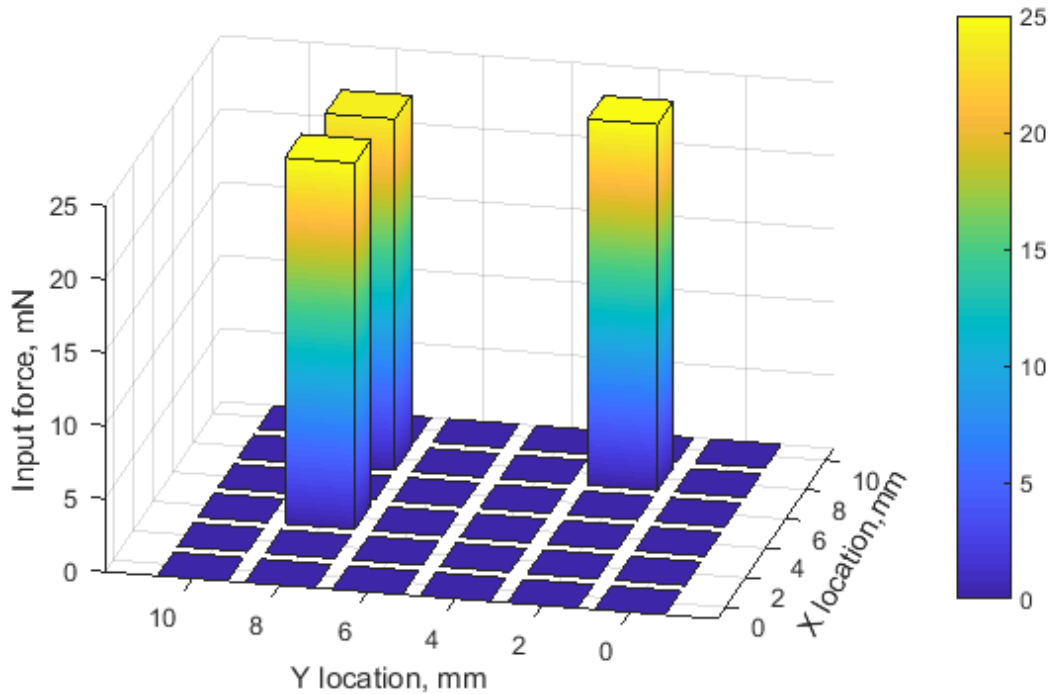


Figure 5-17 Plotted forces and locations information © [2017] IEEE

Signal-to-Noise Ratio (SNR) can be calculated as the power of the signal divided by the power of background noise. For the simplicity, forces were applied on top of one sensor. A peak voltage value from this sensor could be found as 58.8 mV. The background noise level was 1.5 mV as shown in Figure 5-18, with the profile of the applied normal force. The SNR was 39.2 by the equation $SNR = P_{Signal}/P_{Noise}$. The SNR ratio could be improved in the future by adopting a better power supply and a low-pass filter for the signal processing. Hereby, the load profile was also calculated with a peak force of 250 mN, indicating the force range of the sensor array could be 0.25 N.
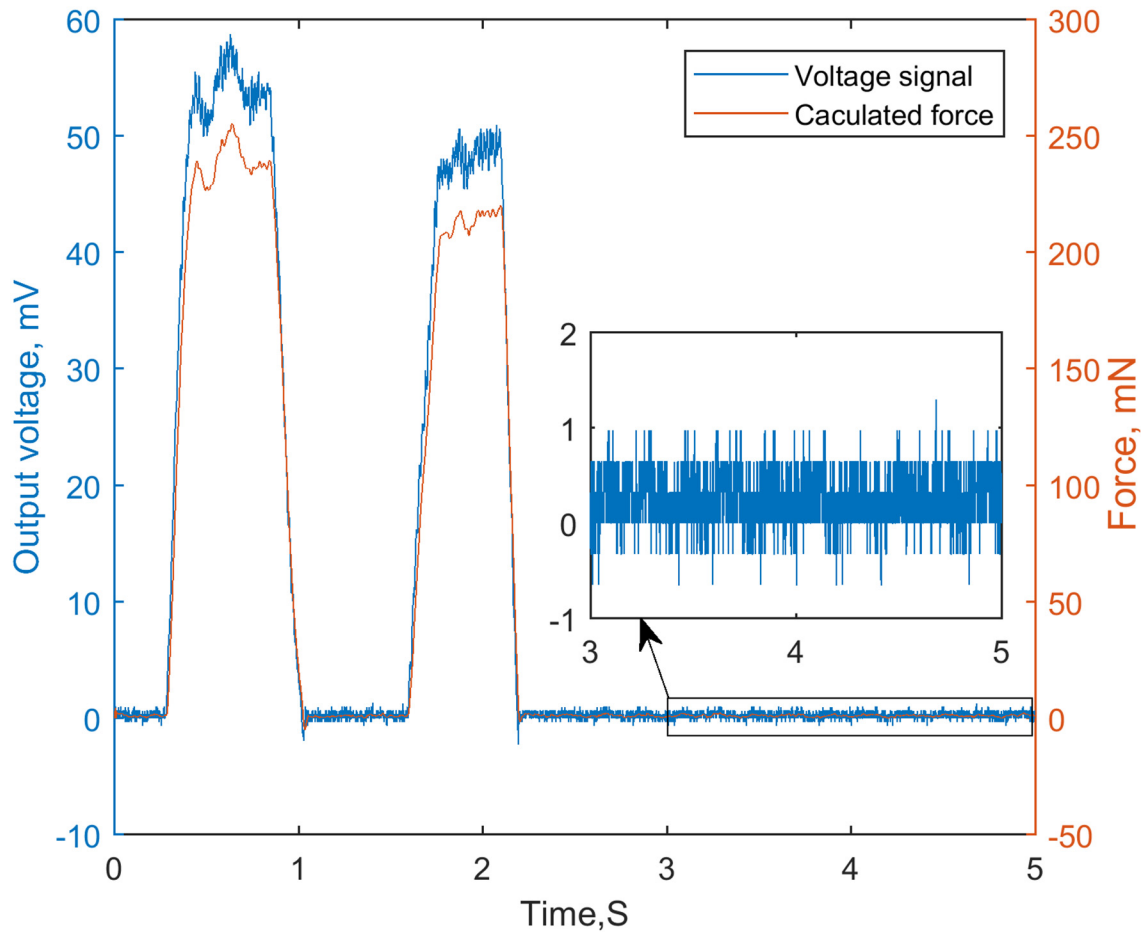
Figure 5-18 Signal-to-Noise Ratio analysis © [2017] IEEE

## 5.3 Specifications of the uniaxial (normal) force sensor and sensor array

In this section, the specifications of the tested normal tactile force sensor and normal tactile force sensor array have been discussed.

As shown in Table 5-2, the specifications of the normal tactile force sensor have been summarized. Two types of prototype devices have been listed. The input DC power could be from 1 volt to 3 volts, with one channel of differential output. The sensor can be packaged using either flip-chip or wire-bonding. The sensitivity of the normal tactile force sensor has been tested as 0.7 mV/mN•V.

Table 5-2 Specifications of the normal tactile force sensor

| Parameter | Specified |
|---|---|
| **Dimensions** | |
| Normal force sensor - Type 1 [um] | 500 × 500 × 350 |
| Normal force sensor - Type 2 [um] | 3000 × 3000 × 350 |
| **Material** | |
| Carrier | N-type Silicon |
| Sensor element | P-type silicon by Boron |
| **Connectivity** | |
| Flip-Chip | Yes |
| Wire-bonding pad [um] | Type 1: 125 × 125<br><br>Type 2: 1000 × 1000 |
| Input | 1 - 3V DC |
| Output | 0.7 mV/mN•V |
| Nominal resistance | 120 Ω +/- 24 Ω |
| Resistance Tolerance | +/- 10% |
| Loading range | 300 mN on die |
| Number of channels | 1 differential |
| **Thermal Properties** | |
| Reference Temperature | 20°C (68°F) |
| Service Temperature | -10 ~ 85 °C |
| Static measurements | -10 ~ 85 °C |
| Dynamic measurement | -10 ~ 85 °C |

The limitations of the normal tactile force sensor are that the mesa and membrane are fragile, to achieving the suitable sensitivity for mN-level force measurements. Another limitation for the 3-mm die is that the footprint is large, which is not economical for mass production. However, with reduced size of sensor pads, the footprint can be drastically smaller.

The specifications of the normal tactile force sensor array have been included in Table 5-3. The sensor array has the spatial resolution of 2 mm, which is defined by the lookup table density. The functional area is 10 mm × 10 mm, which is the space bounded by the four tactile sensors. The

limitation of the normal tactile sensor array is addressed in its functional area. But as the proof-of-concept, it is fully functional to demonstrate the mechanism of the sandwiched-array structure. The following multi-axis tactile sensor array also proved that the scalability of the sensor array structure.

Table 5-3 Specifications of the normal tactile force sensor array

| Array configuration | 2×2 |
|---|---|
| Cell geometry | 3 mm× 3mm |
| Pitch | 10 mm |
| Force range | 1 - 30 mN |
| Spatial resolution | 2 mm(can be smaller by the characterization) |
| Sensitivity | 0.3 mV/mN•V |
| Functional area | 10 mm ×10 mm |
| Signal channels | 4 Differential |

## 5.4 Characterizations and tests on the multi-axis sensor

Sensors packaged on the PCB board have their mesas exposed for applying forces. Considering its diameter, the top of the mesa only has the space for a sharp probe. Common probe paired with force meters would not fit for such a confined area (see Figure 5-19). Therefore, a similar test setup as previously used for normal force sensors was introduced for characterizing the multi-axis sensor in the normal direction.
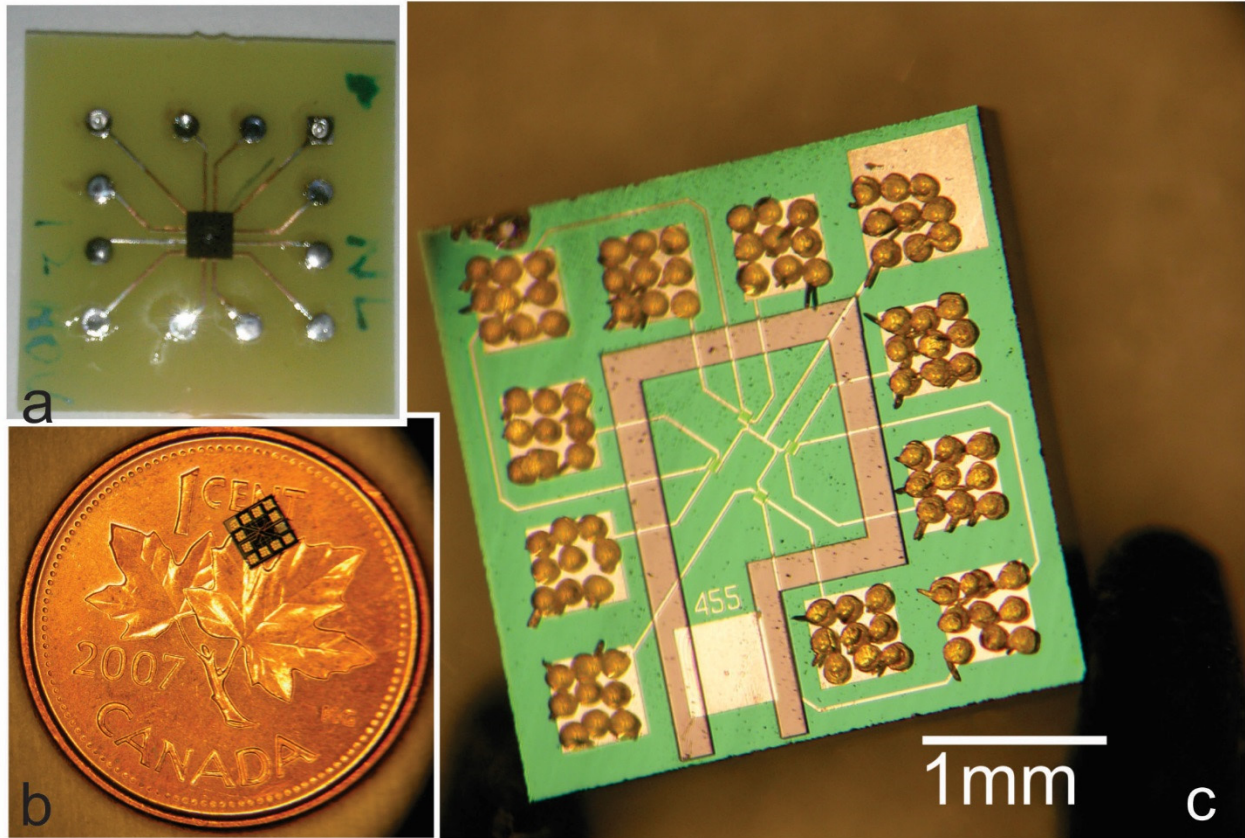
Figure 5-19 Packaged multi-axis sensor and its footprint (a: packaged sensor; b: sensor on a penny; c: sensor with gold bumps) © [2018] IEEE

Applying normal forces from 10 mN to 30 mN, outputs of the multi-axis tactile sensor have been recorded as depicted in Figure 5-20, exhibiting some extent of nonlinearity according to the trendline of data points. This is a problematic issue for future applications due to the complexity with the nonlinearity. Moreover, the outputs from element *E2* plateaued after the normal force reached 10 mN, which could not be explained by the nonlinearity caused by the structural feature, leaving this characterization approach questionable.
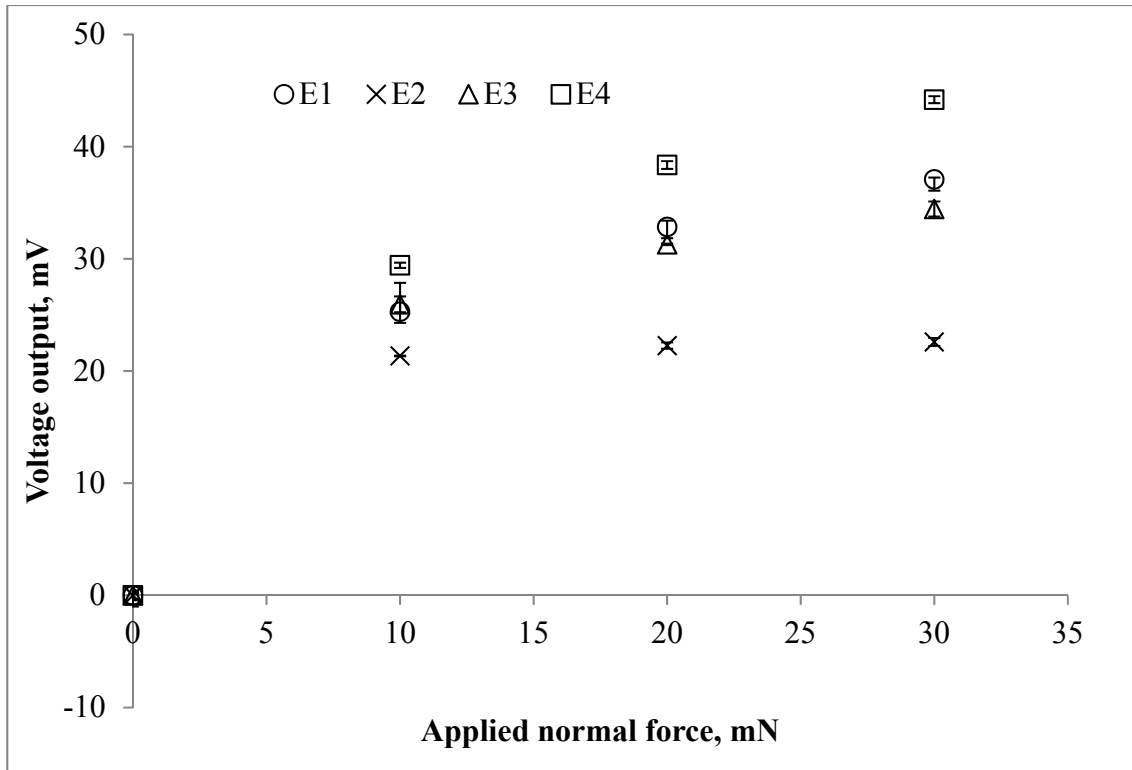
Figure 5-20 Outputs from a multi-axis tactile sensor applied normal forces (Membrane diameter of 1000um)

Behaviors of this multi-axis tactile sensor on the shear force have been studied by applying the horizontal force from 10 mN to 30 mN. A nonlinearity was observed from the outputs of *E1* and *E4*, which were supposed to be two symmetric slopes separated by the zero-axis according to the simulation. Notably, the outputs form *E2* and *E4* were twisted to higher order curves (see Figure 5-21), leading to the need of amendments on the test setup.

122
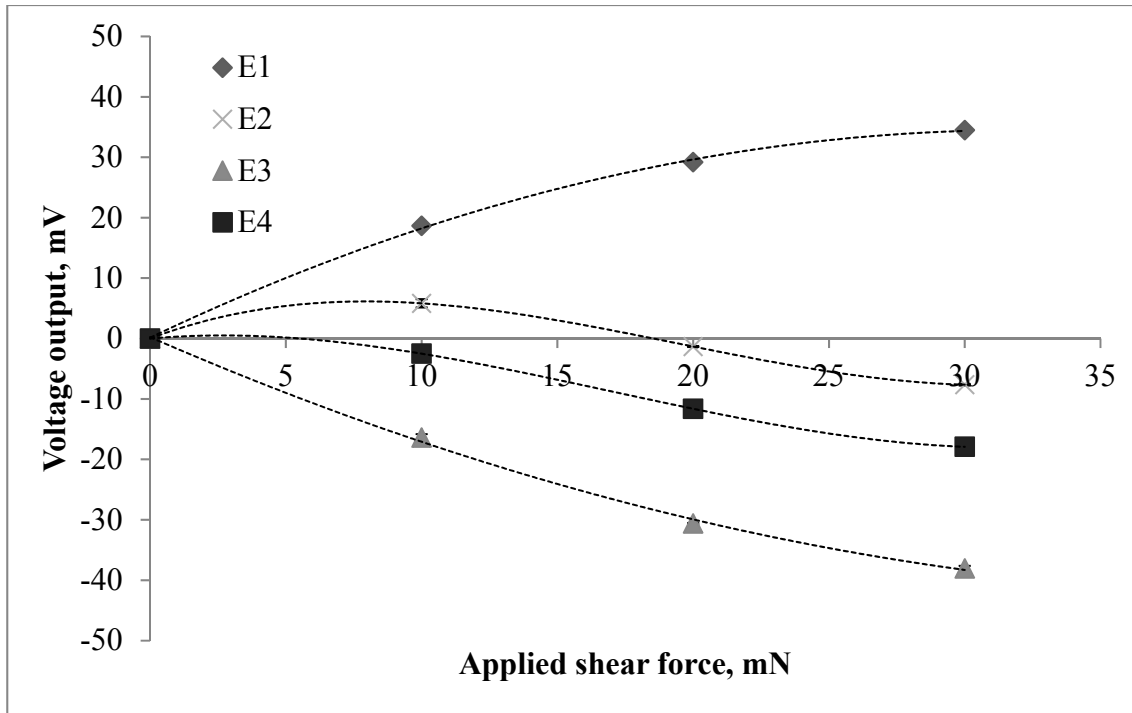
Figure 5-21 Outputs from the tactile sensor with the membrane diameter of 1000um on shear forces

Since normal force sensors with a membrane diameter below 500 um have been characterized and demonstrated satisfactory linear response comparing with simulations. Therefore, more tests were performed on multi-axis tactile sensor with smaller membrane diameters, for instance, the diameter of 400 um, as drawn in Figure 5-22. Nonetheless, outputs from element *E2* could not be explained since the nonlinearity root has been ruled out.
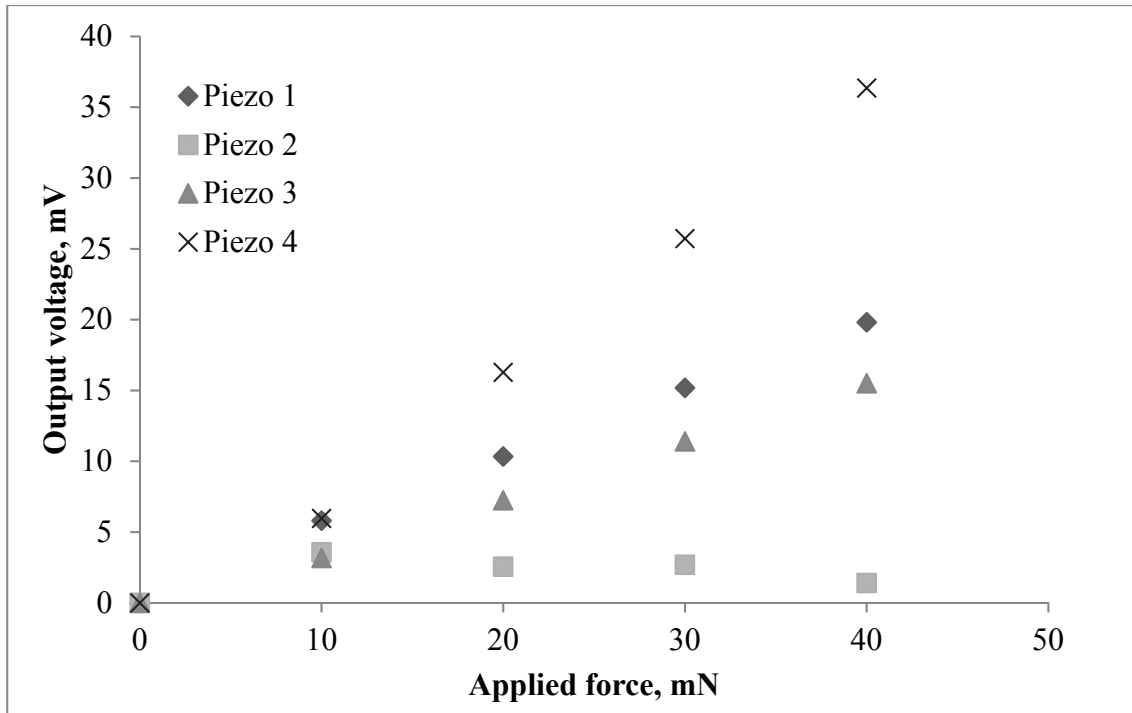
Figure 5-22 Outputs from multi-axis tactile sensor with the membrane diameter of 400 um on normal forces

A steel arm with a tungsten probe as the end actuator was used for applying various loads on mesas for the above tests. Commonly, the compliance of the steel rod would not be noticed or sensed since the force range interested in this work was at level of mN. The displacement from the probe caused by the reaction force from the mesa had been underestimated. To solve this issue, a piece of silicon wafer was diced into long strips, which were used to replace the steel arm. The tungsten probe was glued on the silicon strip. Repeated tests were performed on the sensor with a membrane diameter of 400 um. The linearity of this sensor restored by replacing the probe arm with the silicon substrate.
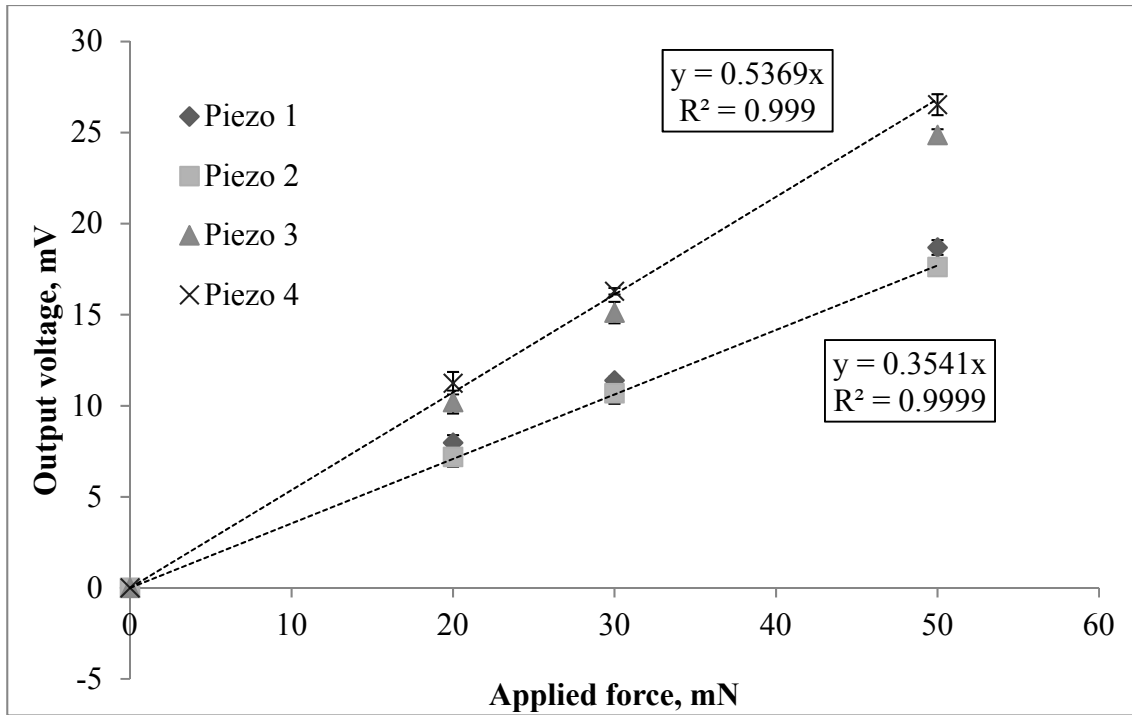
Figure 5-23 Outputs from the tactile sensor with the membrane diameter of 400 um probed by normal forces through the silicon arm

Using the silicon arm with a tungsten probe, data have been collected again from the multi-axis sensor with the membrane diameter of 1000 um for its responses on normal forces. The nonlinearity remained, but the outputs plateau disappeared within the applied force range (see Figure 5-24). This proved that the steel arm used in previous tests caused the unexplained features of the outputs.
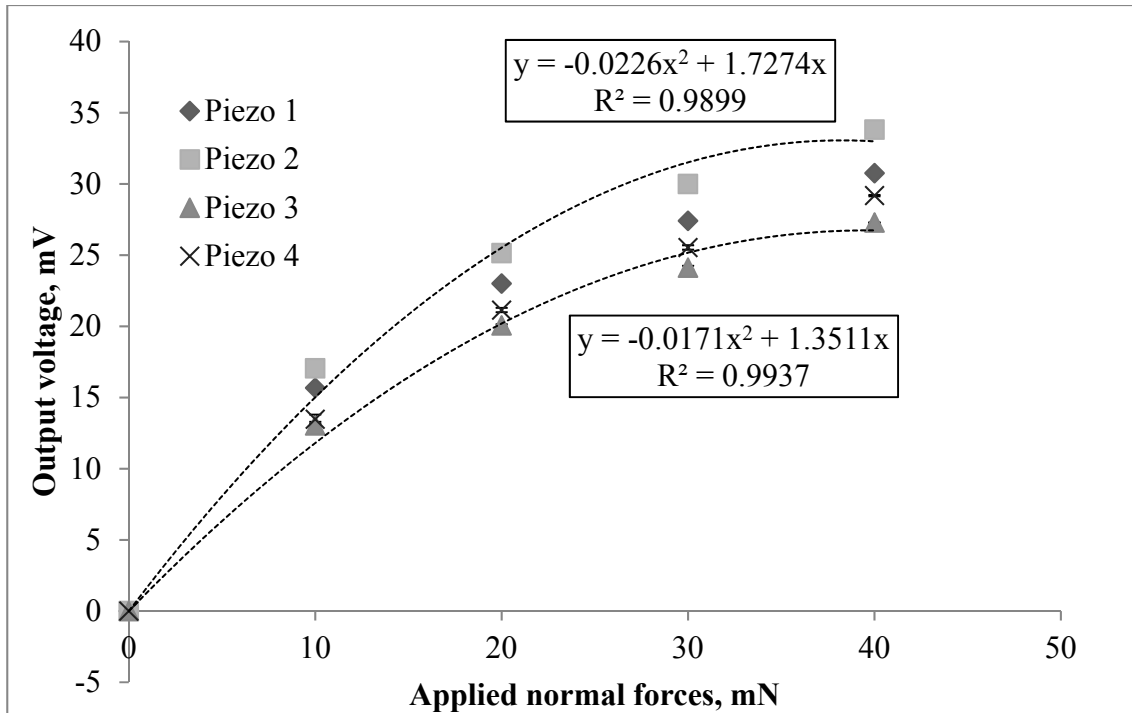
Figure 5-24 Outputs of a multi-axis tactile sensor with the membrane diameter of 1000 um applied by normal forces using a silicon arm
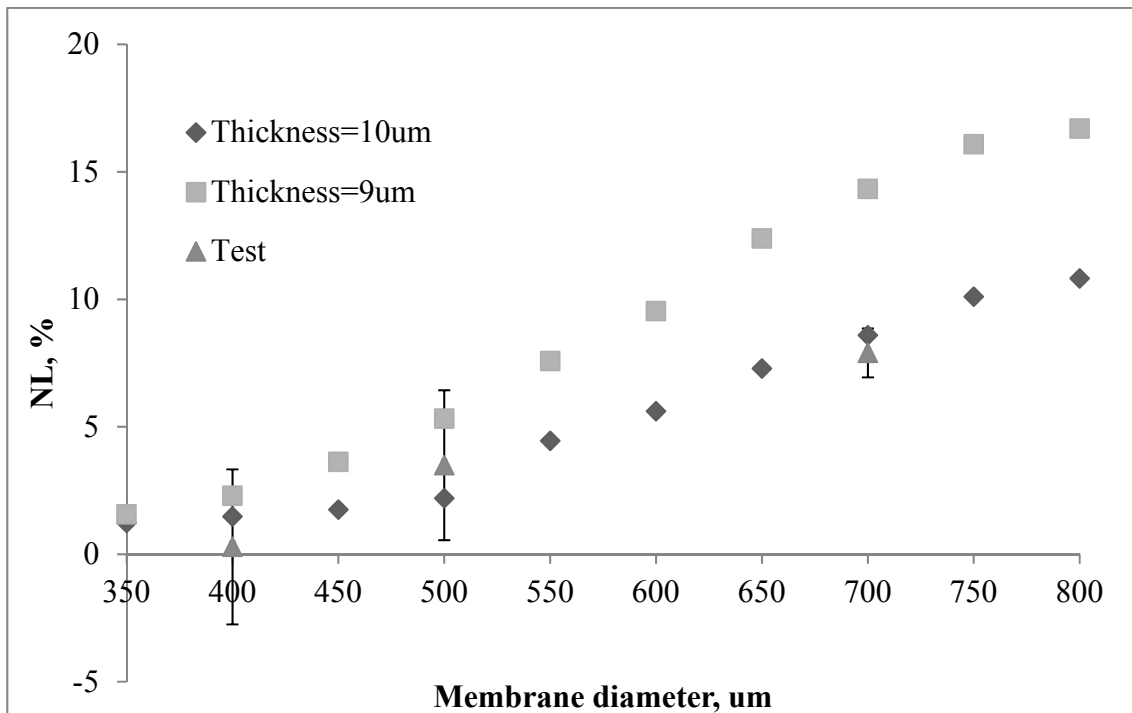


Figure 5-25 Nonlinearity analysis with respected to the diameter of sensor membrane

Nonlinearities in the sensor performances result from a variety of reasons, which can be categorized into three groups, including status changing, geometric nonlinearity and the material

nonlinearity. Due to the brittleness of crystal silicon, the first and third potential reasons can be opted out here. It is reasonable to assume that the geometric nonlinearity dominates the nonlinear behavior of the forces sensor. To validate this, by aggressively increasing the diameter of the multi-axis sensor membrane to 1 mm, this nonlinearity was observed in the responses to the normal force.
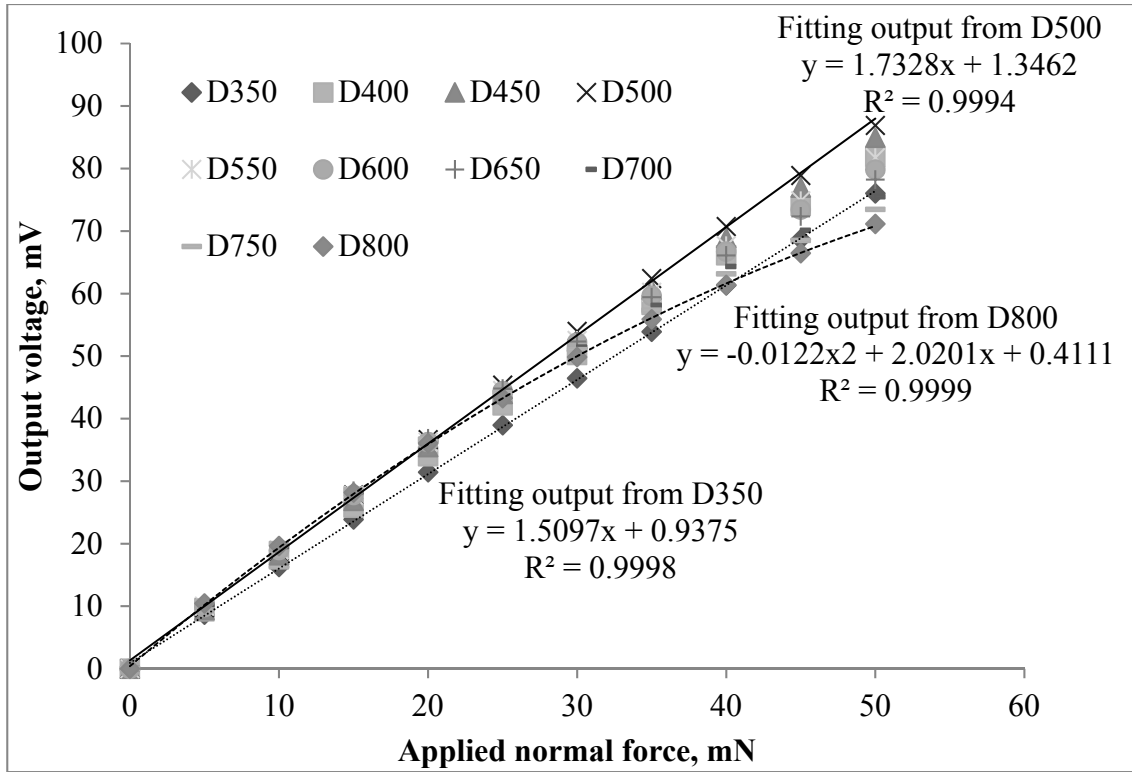


Figure 5-26 Simulation outputs from sensors with different membrane diameters, applied normal force

To investigate the nonlinear behavior of the sensor output from the normal forces, simulations have been performed on sensors with different membrane diameters. The membrane thickness was 10 um. The sensors were subjected to a normal force up to 50 mN. Their outputs have been plotted in Figure 5-26. As can be seen, the outputs from the sensors of which the diameters were less than 500 um presented linear responses, whilst the outputs form the sensors of which the diameters were larger than 500 um indicated nonlinear scenarios within the force range.

In order to quantify the nonlinearity of different sensor designs, the simulated responses were analyzed based on the equation below[38]:

$$NL(\%) = \left| \frac{V_{out}(F_{max}/2) - 1/2 V_{out}(F_{max})}{V_{out}(F_{max})} 100\% \right| \tag{5-2}$$

As plotted in Figure 5-25, the nonlinearity of sensor outputs increased as the membrane diameter in the sensor became larger. The test results from three different sensor designs (400 um, 500 um, and 700 um as the membrane diameter) have also approved the simulation results. Therefore, the recommended diameter of the sensor membrane should be around 500 um, considering the thickness of the membrane is 10 um (as the SOI wafer device layer).

## 5.5 Characterization and test on the multi-axis sensor array
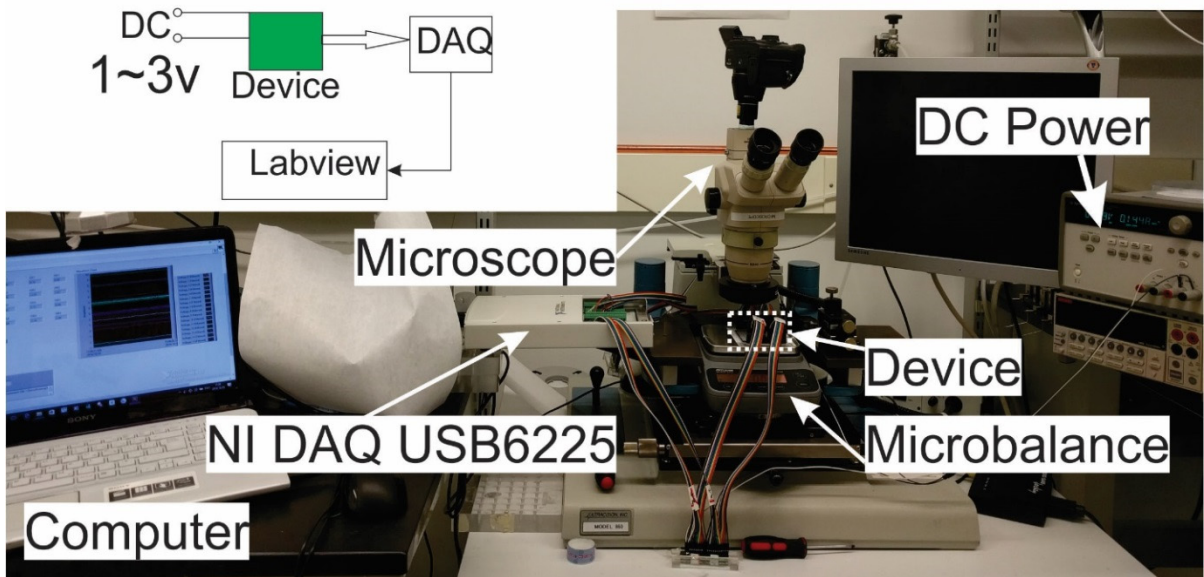


Figure 5-27 Test setup for multi-axis sensor array and schematic structure

For testing and characterizing the performance of the sensor array, the benchtop test setup has been arranged as shown in Figure 5-27. The tactile sensor array was placed on the top of a microbalance with a resolution of 1 mN and powered by a DC voltage source at 1 volt. Signals coming out of the sensor array were fed into a data acquisition card (DAQ, USB-6225 from National Instrument Inc.) and processed by the LabVIEW® on the computer including the sampling and filtering.
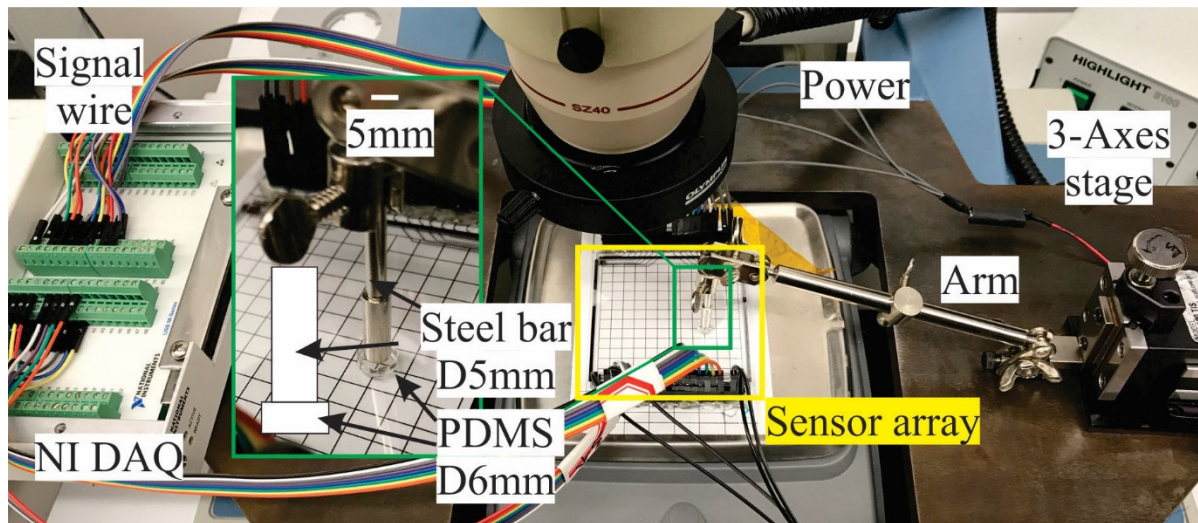
Figure 5-28 Probe tests using a PDMS cushion © [2018] IEEE

Similarly, as the test procedure for the uniaxial sensor array, the steel bar and the PDMS cushion have been used for justifying the methodology that applying forces by a sharp probe is as appropriate as the distributed load applied by the PDMS cushion. This is a close form of emulating the finger contact. The reason has been explained that the Young's modulus ($E$) of the glass is several orders higher than the human finger tissue or the PDMS. Typically, Young's modulus of the human finger tissue was below 0.25 MPa, if the applied force was below 10 N[152]. Whereas, the $E$ of the glass was more than 70 GPa (from Corning Willow® glass datasheets). The fingertip deformation would comply with the profile of the glass cover at a low tactile force level within the scope of this work. The glass cover deformation would remain the same although intuitively the size of contact area using a fingertip was larger than the probe. This conclusion could also be drawn from the test results from using a circular PDMS (polydimethylsiloxane) cushion with a thickness of 5 mm to mimic the fingertip contacting area(see Figure 5-28), considering the Young's modulus of PDMS was within range of 0.36 MPa -1 MPa[69]. The outputs from sensors remained the same level with/without the PDMS cushion if a 0.2-N normal force was applied on its top. Therefore, for the ease of controlling the locations where the forces applied, the rest of tests were done by using a sharp probe under the microscope.
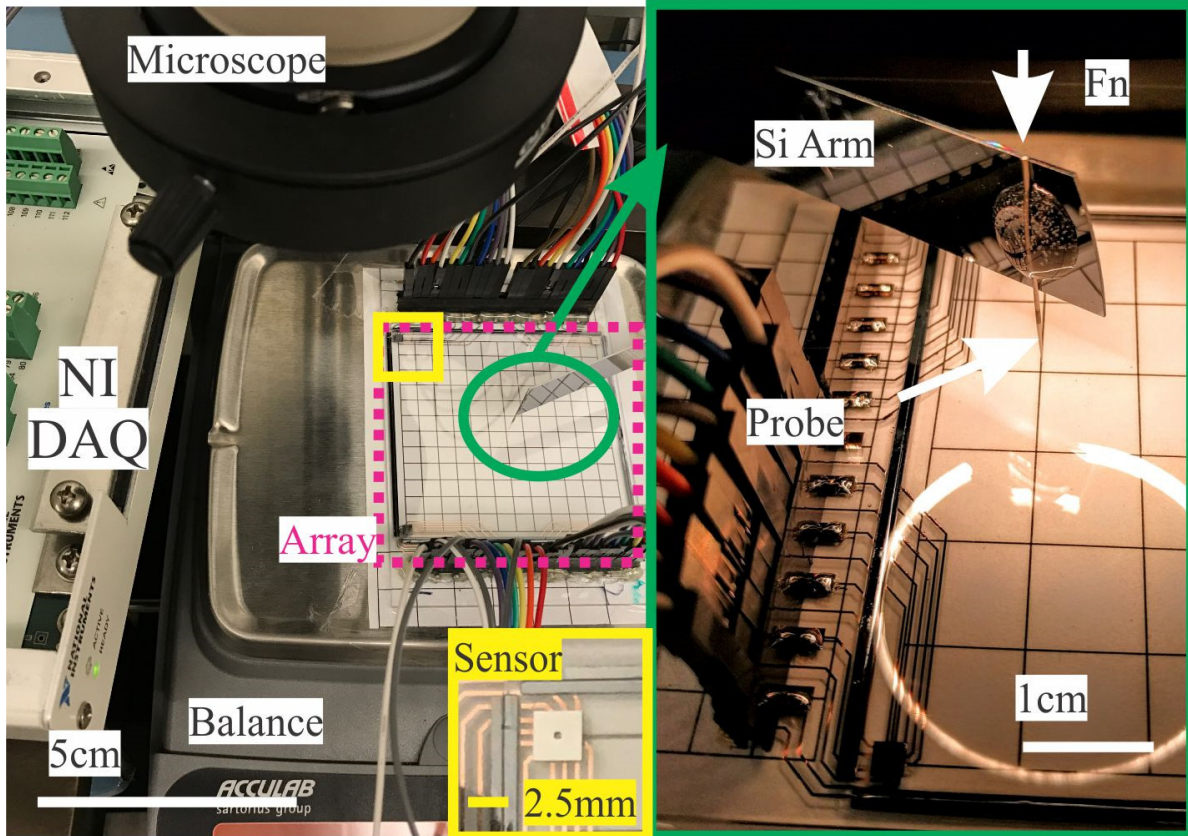
Figure 5-29 Test setup for normal loading (top left); for shear force (bottom) © [2018] IEEE

A close capture of the benchtop test setup has been illustrated in Figure 5-29. The tactile sensor array has been placed on the top of a microbalance with the resolution of 1 mN. A white paper printed with a grid with a mesh size of 5 mm was flattened underneath the sensor array, due to the advantage that the main area of the array was transparent. The purpose of the grid was to clarify the locations of the applied force in the characterization. An extended arm was made by the silicon wafer strip, mounted with a tungsten probe which would be used for applying the pressing force. Tests were done by applying a fixed-amplitude pressing force at various locations based on the printed grid. Responses from all piezoresistive elements were collected and plotted in Figure 5-30, which would be discussed in following sessions.
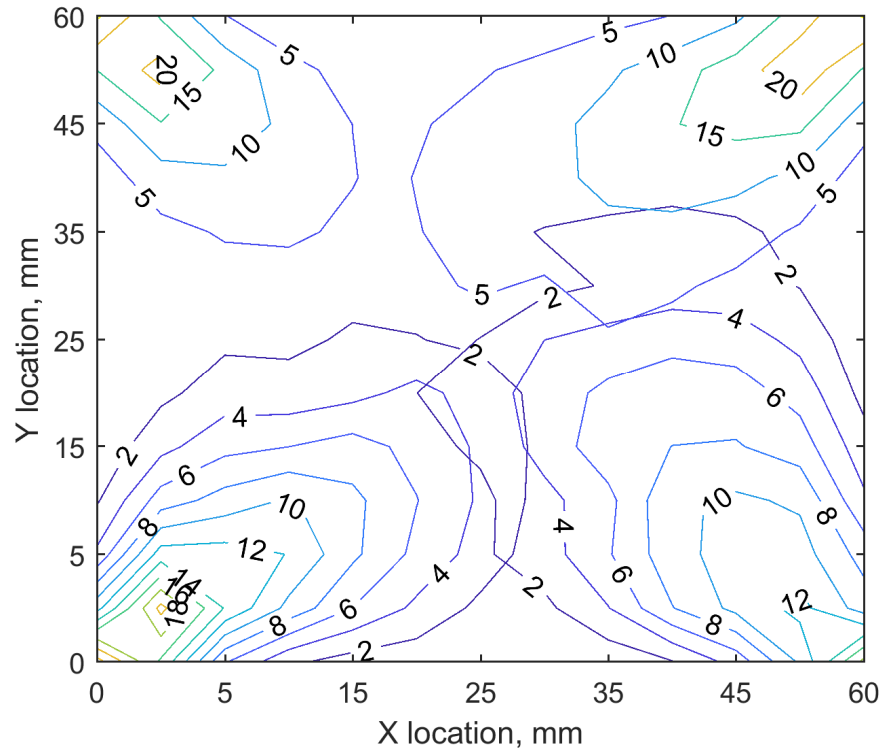
Figure 5-30 Complete probe tests over the multi-axis sensor array by an incremental distance of 2.5 mm © [2018] IEEE

Numerical analysis regarding the sensor array behavior has been done using the Finite Element Method in ANSYS® and analyzed in Chapter 3. A known force with the amplitude of 100 mN in the normal direction was applied on the cover glass of the sensor array, with response data collected from different locations. The incremental steps for the probe tests was 2.5 mm in either $x$ or $y$ direction that the 60 mm × 60 mm area was probed. The mean output values from four tactels have been calculated and plotted (refer to Figure 3-25). The experimental results in terms of applying the normal force on the sensor array have been shown in Figure 5-30, indicating the similar pattern comparing with the simulation responses. Moreover, the peak values of the sensor array at four corners from the tests were larger while the outputs were smaller at the central area, comparing with those values from the simulation, owing to fabrication variations and packaging defects at the prototype corners. Quantitatively, the experimental responses of the sensor array regarding tactile forces applied at different locations can be characterized into a lookup table. This table can be used for the trajectory and force analysis, which would be discussed in detail by the next section.

At any location, the output voltage can be calculated as a linear equation

$$V_{i,j,l} = K_{i,j,l}F \qquad i = 1,2,3,4; j = 1,2,3..n; l = 1,2,3..n$$

Where $i$ denoting the tactel number and $j,l$ denoting the element index in the benchmark matrices. The element density in benchmark matrices was determined by the probing data density, i.e. the incremental step when the test was performed. The $j$, $l$ could be larger if a smaller incremental distance was preferred. For instance, if the incremental step was 1 mm, then $n = 60$;

Considering practical tests with a reasonable and cost-effective data density, benchmark matrices can be built using $K_{i,j,l}$ from the four tactile sensors using the mean outputs. The matrices scheme has been shown in Figure 5-31. Therefore, if a tactile force was applied at a random location, a group of current signatures $K_{cr}$ formed a seed vector, which would be used by the polling technique to quantify the location and force of the tactile event.
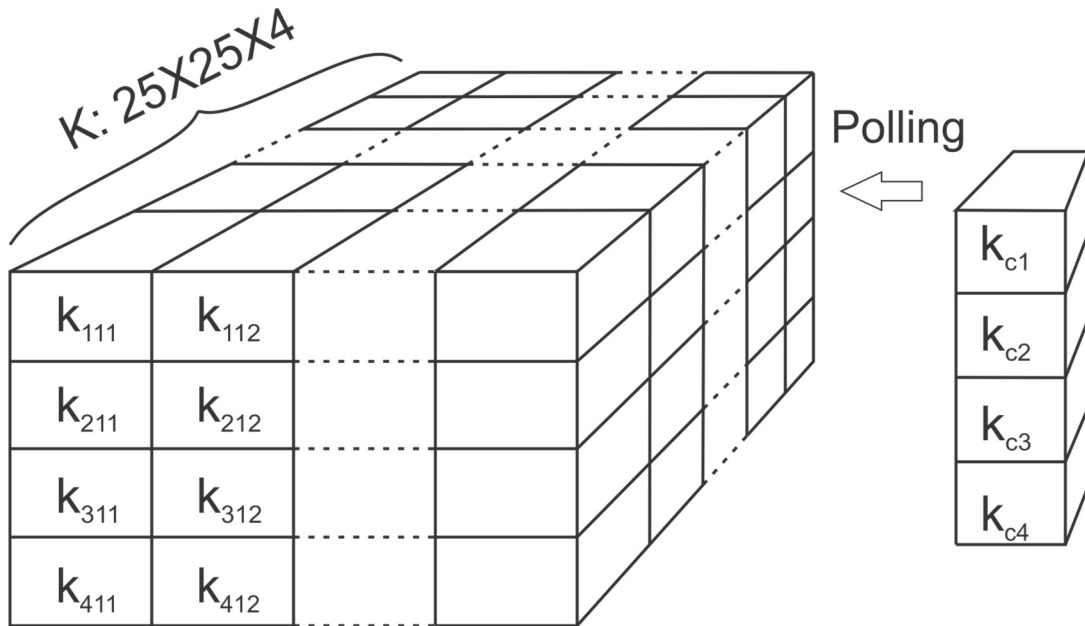


Figure 5-31 Data polling scheme from benchmark matrices © [2018] IEEE

The benchmark matrices were formed by the output voltages from the sensor array. The average values from 4 channels of each tacel were filled in the corresponding positions as the $K_{i,j,l}$. The tested output voltages from an unknown force provided another set of 16 channels of data. Calculating the mean values from these tested values, the polling signature vector $K_{cr}$ can be formed. In the polling calculation, the minimum sum of square errors was calculated to identify the location of the signature vector in the benchmark matrices according to Equation 5-3:

$$f_{j,l} = \min \Sigma \left(K_{r,j,l} - K_{cr}\right)^2 \qquad \text{Equation 5-3}$$

The calculated residuals can be sequenced to find the index of the minimum sum error. This index value indicated the location information of the applied force. As shown in Figure 5-32 and Figure 5-33, the trophy point demonstrated the corresponding location of the applied force.
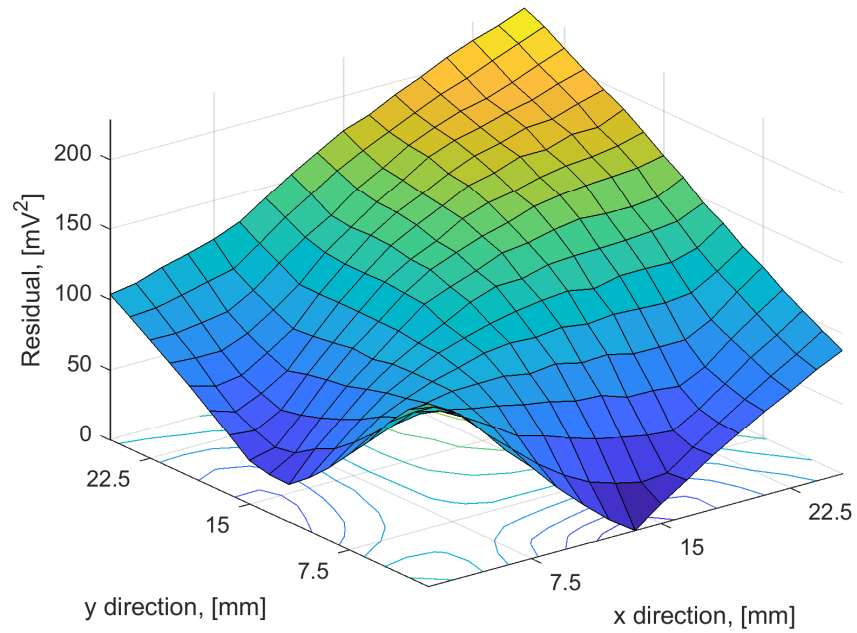


Figure 5-32 Residual of minimizing the square error corelated with the location at one edge
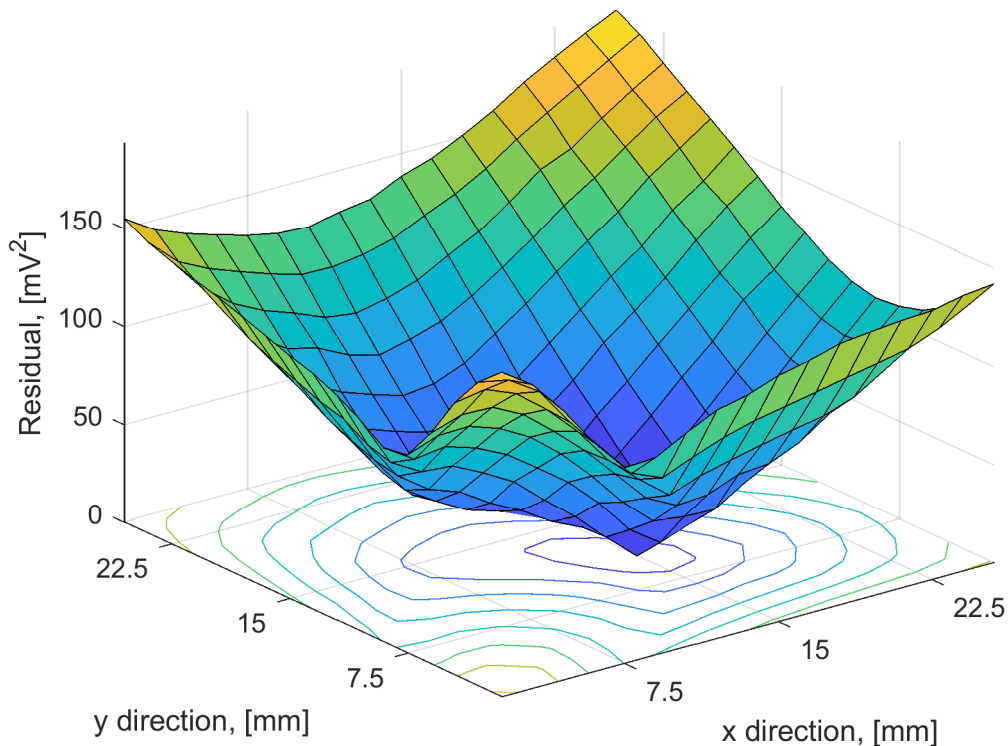
Figure 5-33 Residual of minimizing the square error corelated with the location

The polling technique would be an easier way to solve this type of problem because the high computational power of computer can be used. This numerical solution was better than solving inversed problems "on the fly", which were multiple high order surface equations regarding the outputs pattern. A simple test has been performed to validate this approach. This test was to interpret the tactile event by drawing a continuous character "U" on the sensor array. The original signals from the four tactels have been recorded and plotted in Figure 5-34. Similarly, peak values of the output voltages from the sensor array shifted sequentially, as the tactile event was approaching the nearest tactel. The location transitions of the applying force were calculated from the shifting slopes between one and another sensor. By the polling method mentioned in the above section, the force and location information of the drawing event has been displayed as the color-scale image t presented in Figure 5-35. Due to the sparsity of benchmark matrices, a "U" character can be recognized from the plot with a satisfactory resolution. Force amplitude has been solved accordingly shown with the color-scale.
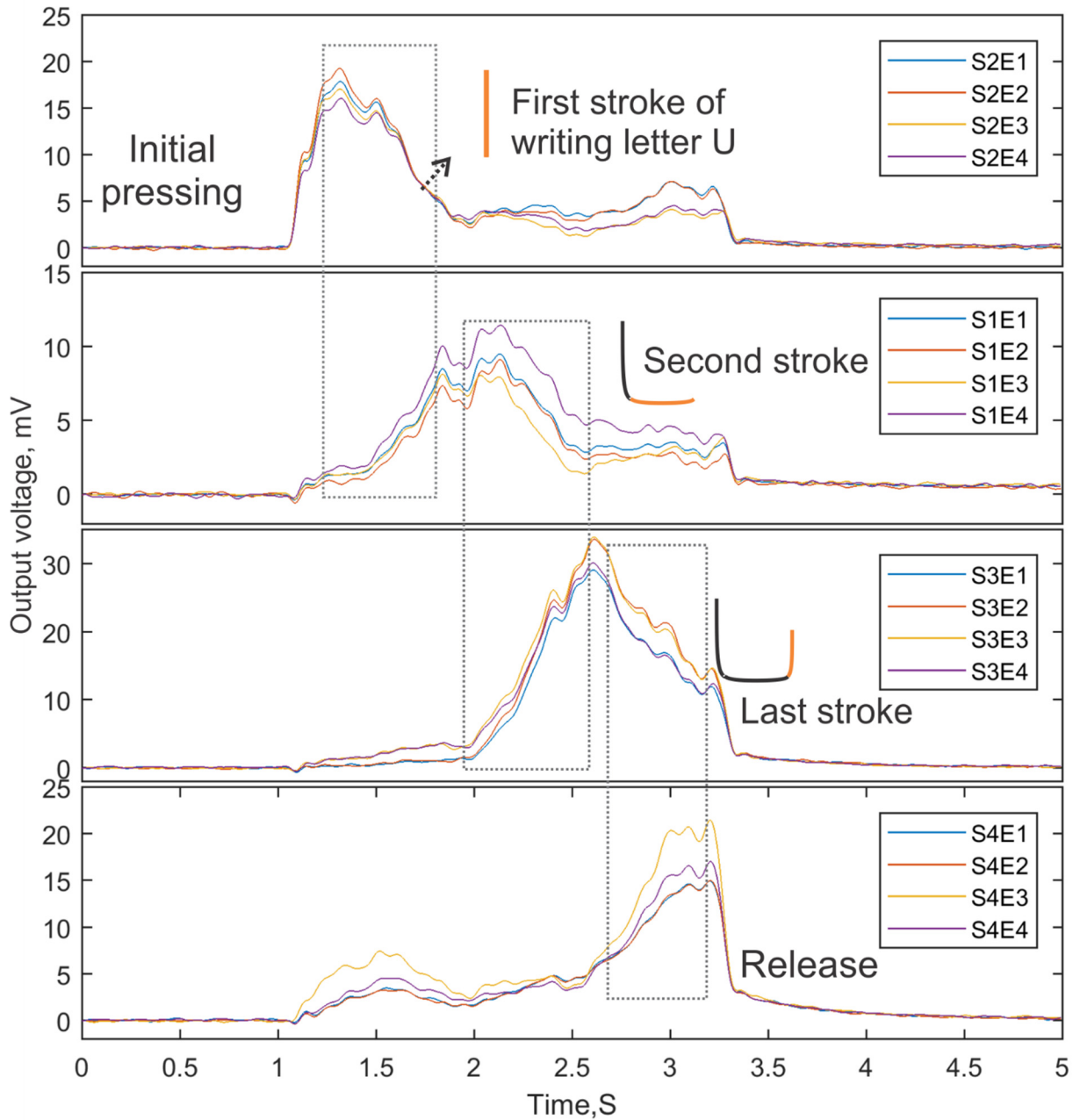
Figure 5-34 Original signal acquired by drawing a "U" on the sensor array © [2018] IEEE
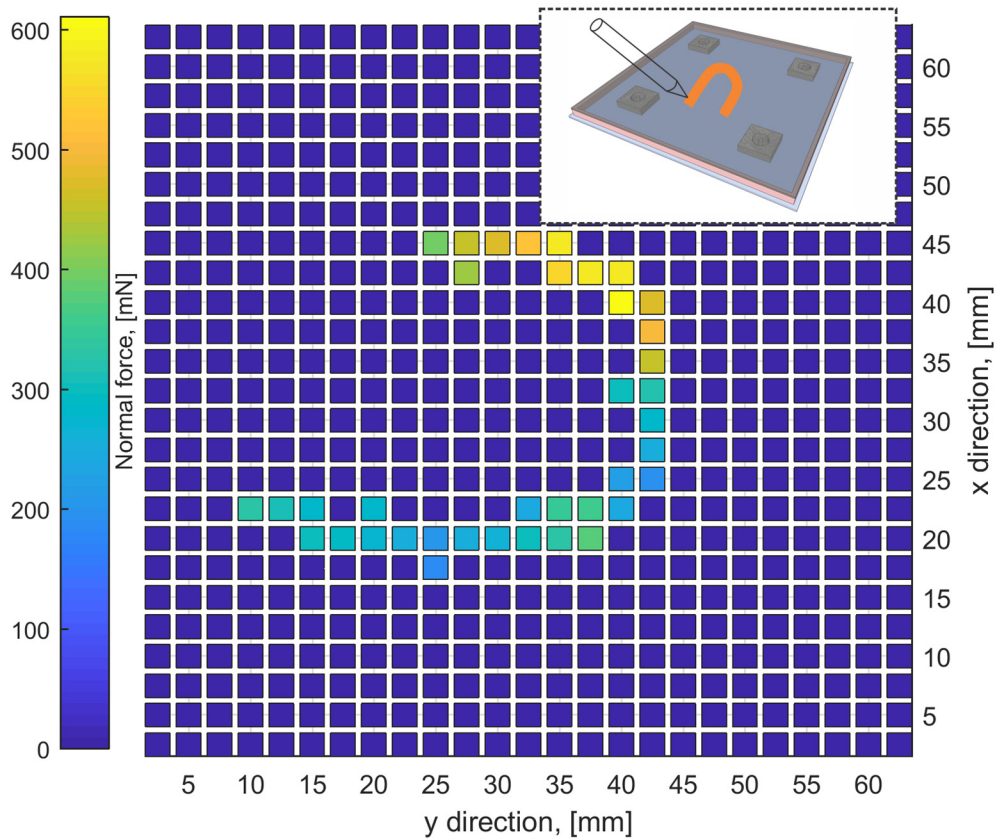
Figure 5-35 Tactile event locations and the normal force amplitude © [2018] IEEE
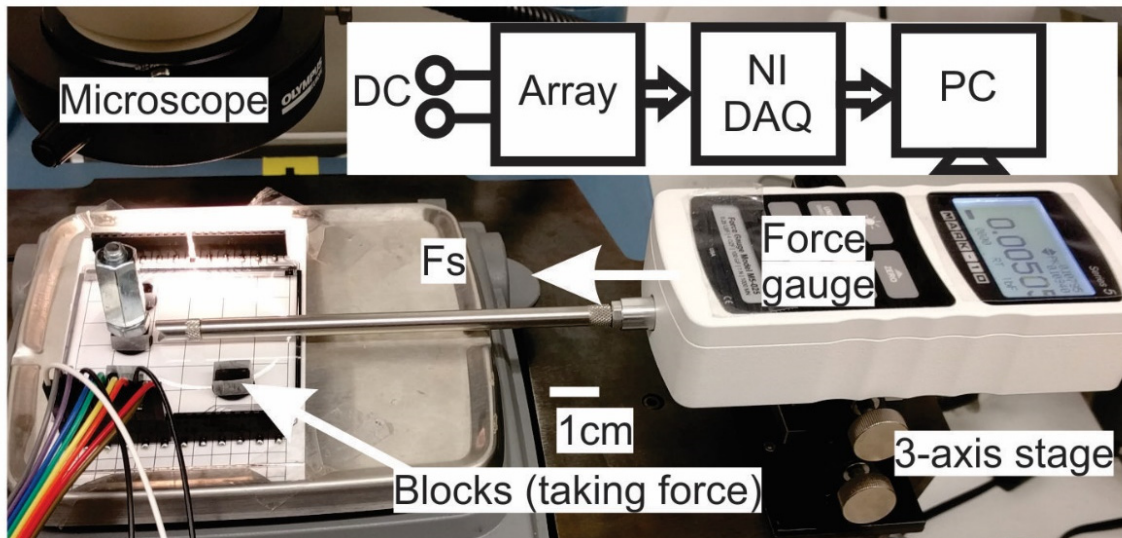


Figure 5-36 Setup for sensor array evaluated on shear forces © [2018] IEEE

To measure the outputs of sensor array in terms of shear forces, the previous benchtop setup has been modified as depicted in Figure 5-36. A uniaxial force gauge with a resolution of 0.1 mN

was mounted on the top of a three-axes manipulation stage to align with the sensor array. Plastic blocks were glued on top of the sensor array at several locations. Their weights were negligible comparing with the known preloading on the top during tests. The reason for adding up a preloading from the normal direction was due to the shear force would not exist in common tactile events without a pressing force, realistically.
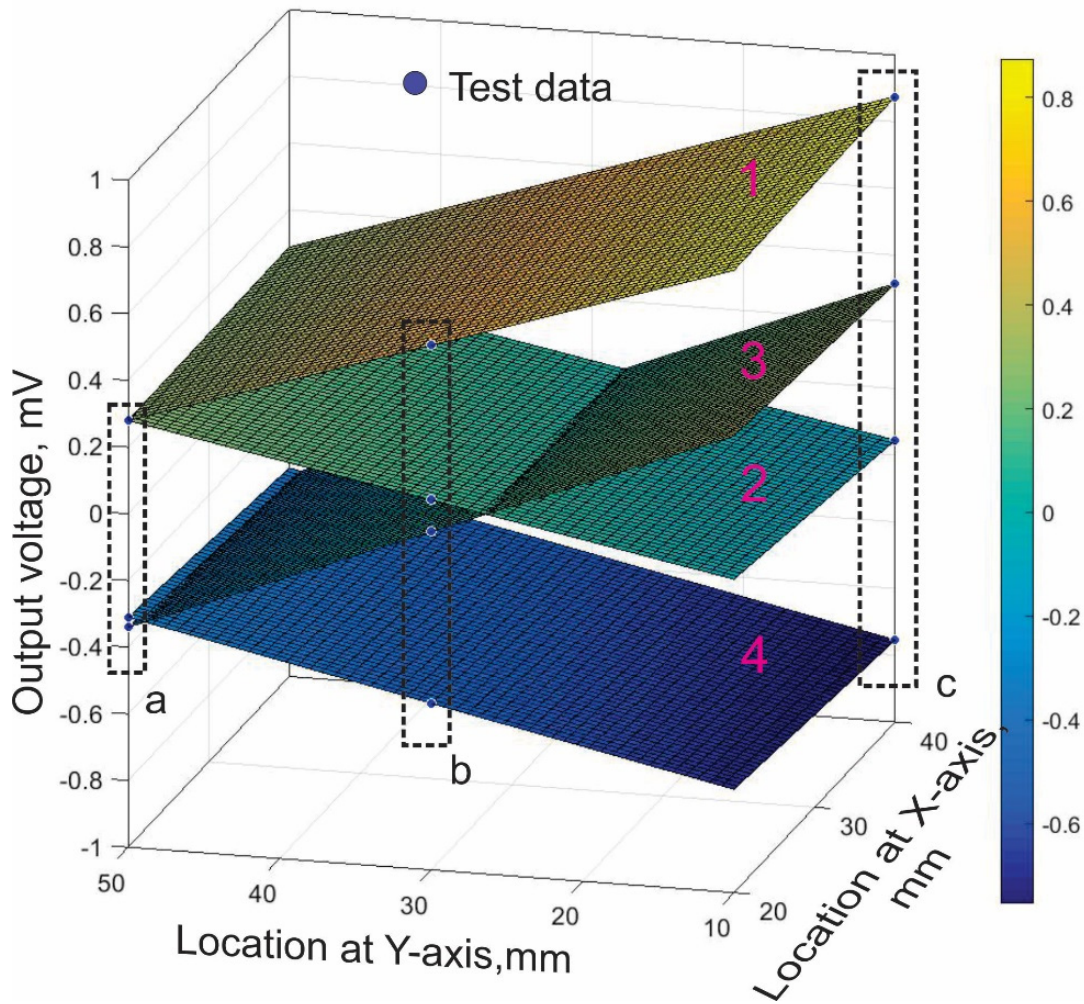


Figure 5-37 Test results from one sensor of applying 100 mN shear force at three locations on the array in x-direction © [2018] IEEE

Since the sensor array was embodied by four multi-axis tactels, its performance of sensing the shear force need to be evaluated. The results from four elements (denoted by *E1, E2, E3, E4*) within one tactel formed four fitting planes. This indicated the shear force output in *x*-direction linearly proportional with its location on *y*-axis, or vice versa. In other words, responses of the shear force from each of piezoresistive elements formed a flat plane (see Figure 5-38), which

showed that the sensor responses were linear. Besides the outputs were only related with the location at the axis which was perpendicular to the direction of the applied force. Notably, the sum of outputs from one sensor at any point within the sensing area, in terms of the shear force, remained zero. This characteristic was the signature of the configuration of sensor array, which would be useful for future decoupling of the multi-axis force and location.
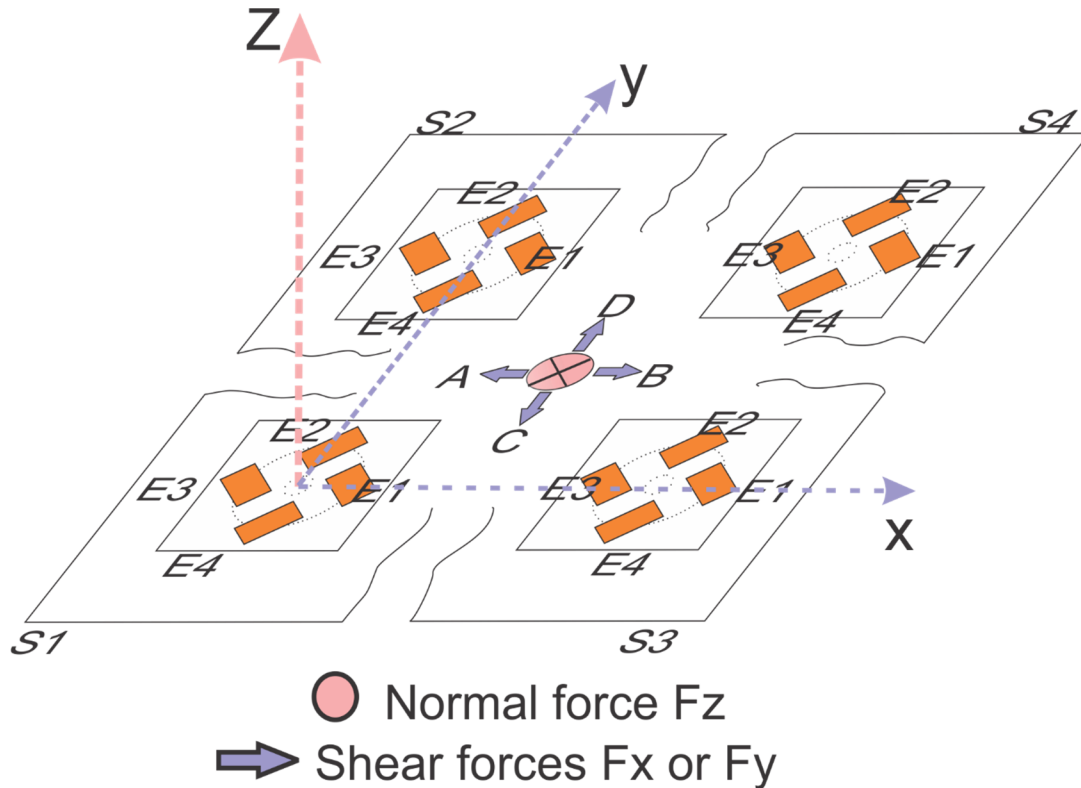


Figure 5-38 Test scheme on shear force at four directions (A, B, C, D respectively) with preloading of normal forces © [2018] IEEE

Shown in Figure 5-38, a qualitative test scheme was depicted. One finger was deployed to press the central area of the sensor array, applying shear forces at four different directions (A-B-C-D) sequentially. In this process, the normal force was applied as the preloading. The four tactile sensors in the array were labeled as *S1, S2, S3, S4*, respectively. Each sensor had four elements marked as *E1, E2, E3, E4*. Table 5-4 showed the anticipated responses of these 16 elements in the sensor array corresponding to the shear forces in the four directions, according to the shear test scheme. A conclusion could be drawn that the responses of four sensors from the shear force were identical. But increments from sensing elements swapped with respect to different directions. This phenomenon could be utilized for further characterization of the shear force, which would be discussed later. The anticipated response of the sensor array had been verified by the test results

as shown in Figure 5-39. For instance, comparing results of stage *C* and stage *D* for sensor 1(*S1*), the two outputs from *S1E2* and *S1E4* plateaued; then these outputs switched positions with each other which indicating a reversed direction of the applied shear force. The gap amplitude between plateaus could be calculated to be the amplitude of the shear force later.

Table 5-4 Responses analysis of all 16 elements in terms of applying shear forces in four directions with a normal force preloading (++ stands for the increasing of output voltage, -- stands for the decreasing of output voltage, o stands for slightly changing either increasing or decreasing.) © [2018] IEEE

|  | A | B | C | D |  | A | B | C | D |
|---|---|---|---|---|---|---|---|---|---|
| S1E1 | -- | ++ | o | o | S2E1 | -- | ++ | o | o |
| S1E2 | o | o | -- | ++ | S2E2 | o | o | -- | ++ |
| S1E3 | ++ | -- | o | o | S2E3 | ++ | -- | o | o |
| S1E4 | o | o | ++ | -- | S2E4 | o | o | ++ | -- |
| S3E1 | -- | ++ | o | o | S4E1 | -- | ++ | o | o |
| S3E2 | o | o | -- | ++ | S4E2 | o | o | -- | ++ |
| S3E3 | ++ | -- | o | o | S4E3 | ++ | -- | o | o |
| S3E4 | o | o | ++ | -- | S4E4 | o | o | ++ | -- |
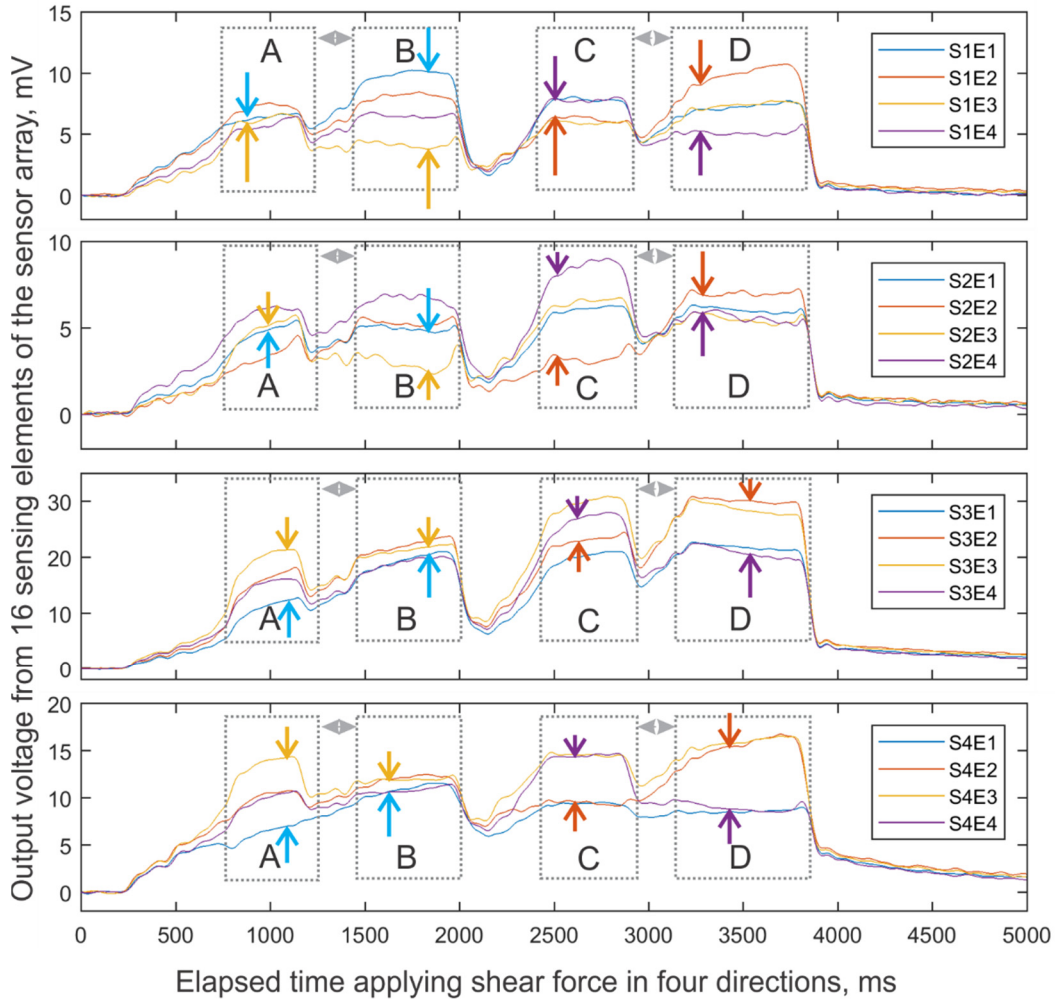
Figure 5-39 Response of the sensor array from the manipulation of one finger at central area

© [2018] IEEE

## 5.6 Force and location calculation

Simulations have been done by applying a 200-mN normal loading combined with the tuned shear force component in the x-direction for demonstrating the force decoupling calculations. The location (x: 45 mm, y: 36 mm) is randomly chosen to be close to *S4* as a general position, which is not on any symmetric axis.
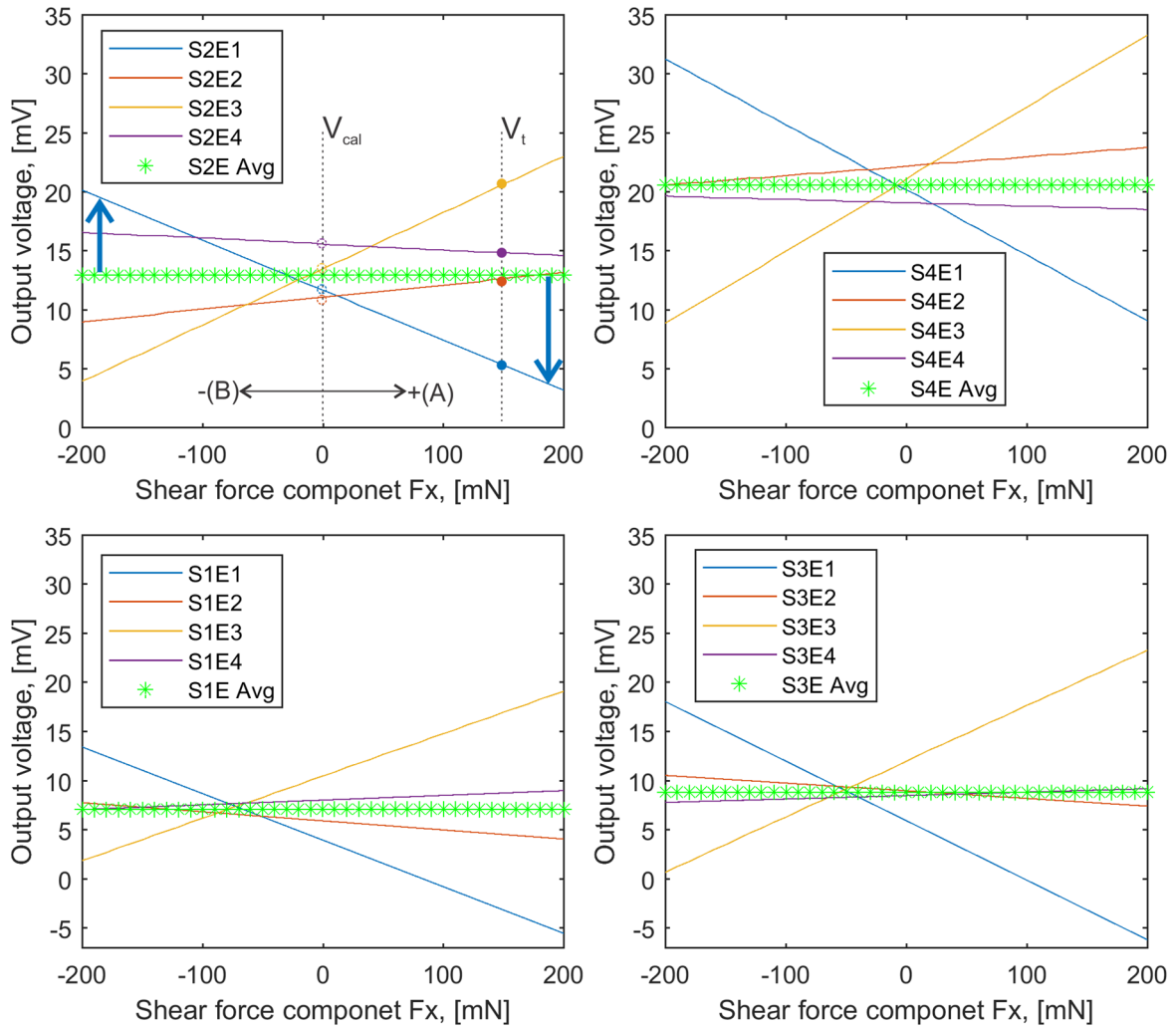
Figure 5-40 Simulations of applying a 200-mN normal force with tuned shear force in x-direction at a fixed location close to S4 (The output shifting of S2E1 has been marked by two blue arrows as the shear forces change directions; Solid dots indicate voltage readouts $V_t$ from sensors; Hollow dots indicate the voltages $V_{cal}$ if no shear forces applied) © [2018] IEEE

As shown in Figure 5-40, the mean voltage outputs have been plotted by the green dots calculated from the four sensing elements in each tactel. In the simulation, $V_t$ stands for the real-time voltage outputs from sensors, denoted for the measured knowns. The $V_{cal}$ denotes the output voltages generated by the normal force component, which needs to be calculated. The calculations of $V_{cal}$ are performed based on multiplying the difference ratio comparing the $V_{avg}$ (green line) and the mean value of prestored voltage values $V_{pre}$ (voltages at 100 mN) at the location in the previous probing test. The force components could be calculated by the equation 5-4:

$$\begin{cases} F_z = V_{Avg}K_z \\ F_x = \Delta(V^{E3} - V^{E1})K_S^{E3E1} \\ F_y = \Delta(V^{E4} - V^{E2})K_S^{E2E4} \\ V_{cal} = V_{Avg}/mean(V_{pre}) * V_{pre} \end{cases}$$

Equation 5-4

Where $K_s$ denoting the shear sensitivity matrices, $K_z$ standing for the normal sensitivity matrices, and $\Delta$ standing for the subtraction using $V_t$ and $V_{cal}$.

The "U" letter tests have been simulated in ANSYS® using FEM with a normal force combined by other shear force components. The letter was drawn following the sequence of *A-B-C-D-E-F*, see Figure 5-41.
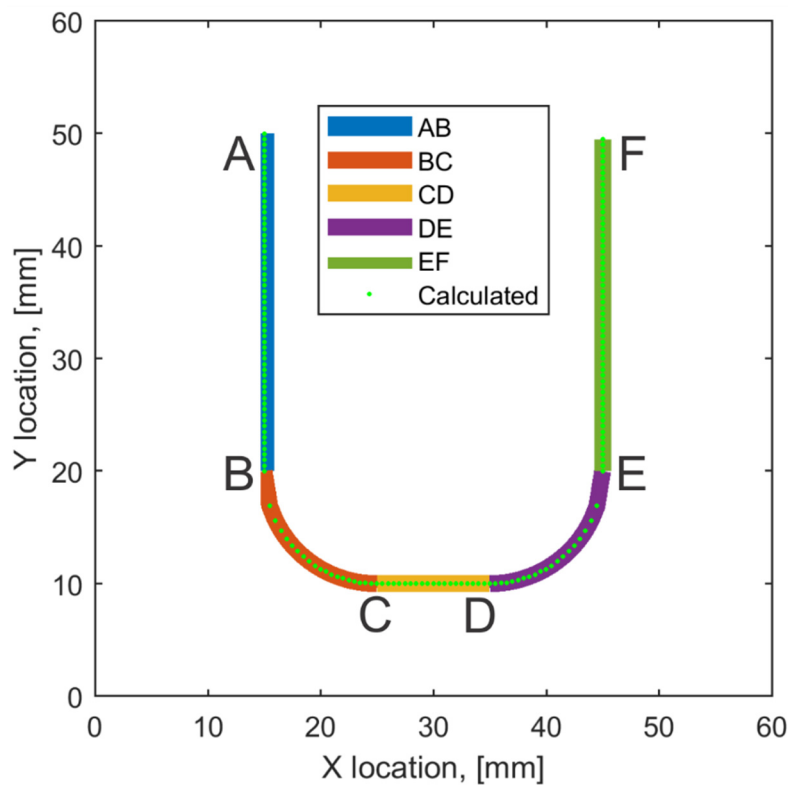


Figure 5-41 The layouts for drawing a U letter on the sensor array © [2018] IEEE

Two tests have been emulated. First, the multi-axis force combined with three force components (*Fx* + *Fy* + *Fz*) were applied with the five strokes to draw the "U" as shown in Figure 5-42 by the bold lines, denoted as the T1 group. Another batch of simulations have been performed by utilizing only the normal force component (*Fz*) for the letter, noted as *T2* tests.
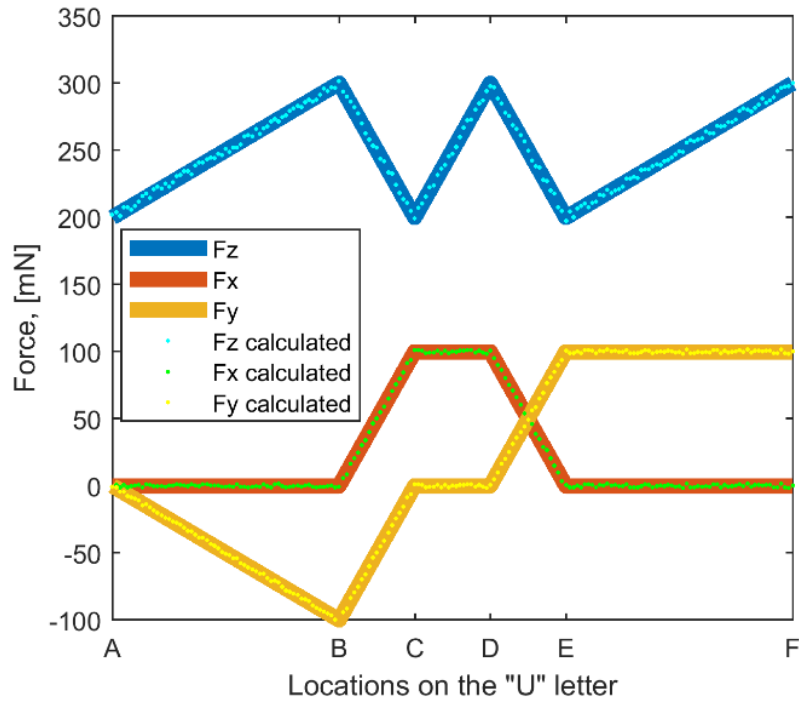


Figure 5-42 Comparison between input forces and calculated force components in the simulations of drawing the U letter © [2018] IEEE

Comparing outputs from the two scenarios (*T1* and *T2*) of the sensor array, were plotted in Figure 5-43.The sensor array outputs were quite different due to the participation of shear force components. The mean voltage outputs from these four tactels have been compared under the two scenarios in Figure 5-44, which validated the previous assumption that the outputs generated by the normal force component were irrelevant to the shear force components. The calculated forces and locations have been displayed with color dots, where the simulation inputs values were the bold lines in Figure 5-41, indicating the well agreements.
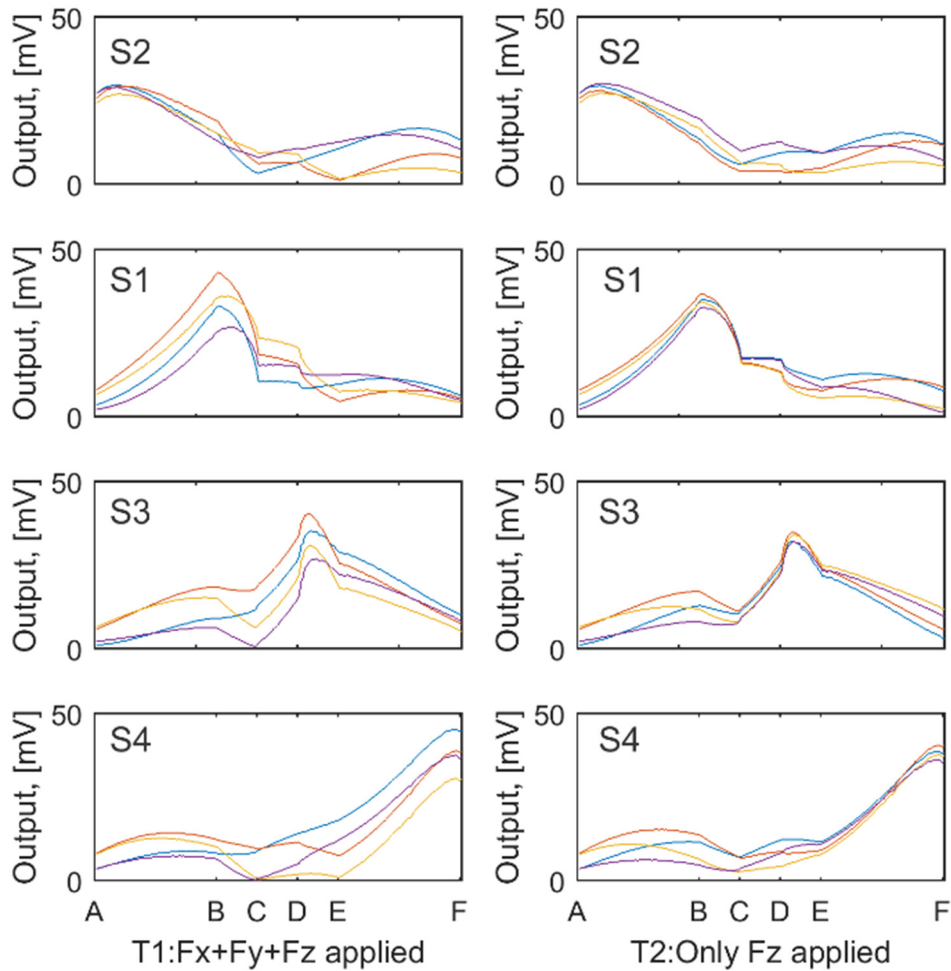


Figure 5-43 Outputs from the sensor array under two different loading conditions for drawing the letter "U" © [2018] IEEE
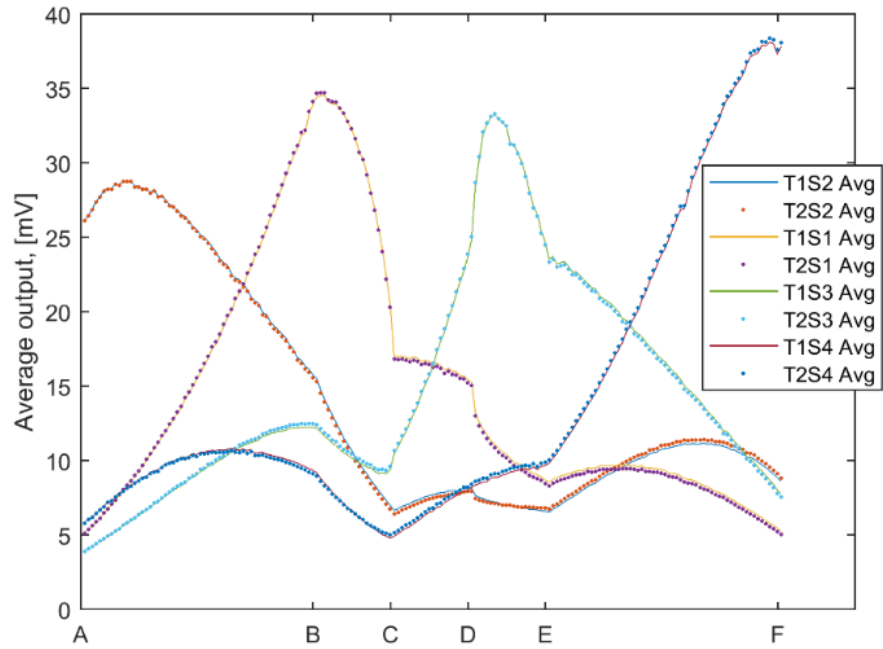
Figure 5-44 Mean voltage outputs comparison © [2018] IEEE

Since the sensor array is formed by four multi-axis tactile sensors, the channels of data are redundant (16 signals for 3 unknowns), which is the advantage of this work. The redundant feature enables a better performance in the calculation of the $F_x$, $F_y$, $F_z$, because the data with less noises could be selected as the inputs.

Although qualitative analysis on the response of shear forces from different directions has confirmed the function of proposed sensor array, further quantitative discussion must be done to quantify the shear force amplitude. To achieve this, the first step was to analyze the waveform from Figure 5-39 to extract the normal force component. This was done by polling the sensor response fingerprints from the benchmark matrices. The results of applied normal force components have been plotted in Figure 5-45. The shear force eventually could be calculated as plotted in Figure 5-46, by substituting the proper outputs to equation $F = K_s(x, y)V$, where $K_s$ was the shear sensitivity. The output plateau shifted in amplitude ranking, i.e. the highest plateau or lowest trough, indicating direction shifting of shear force.
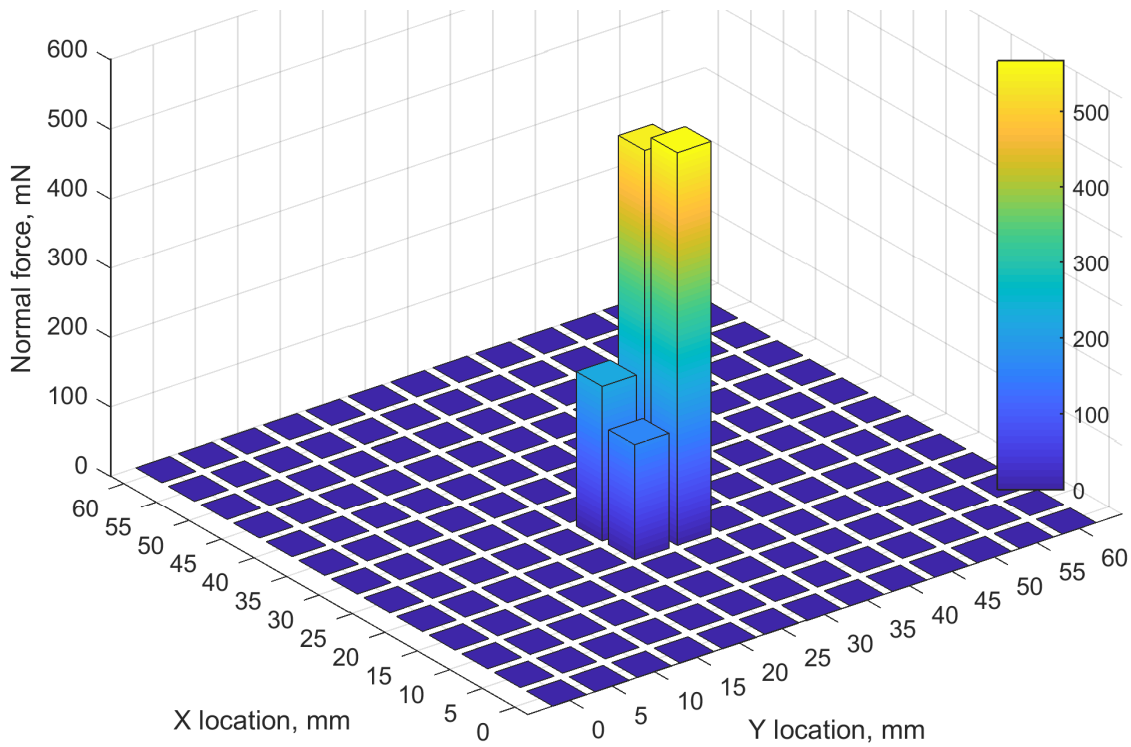


Figure 5-45 Normal force component as applying shear force
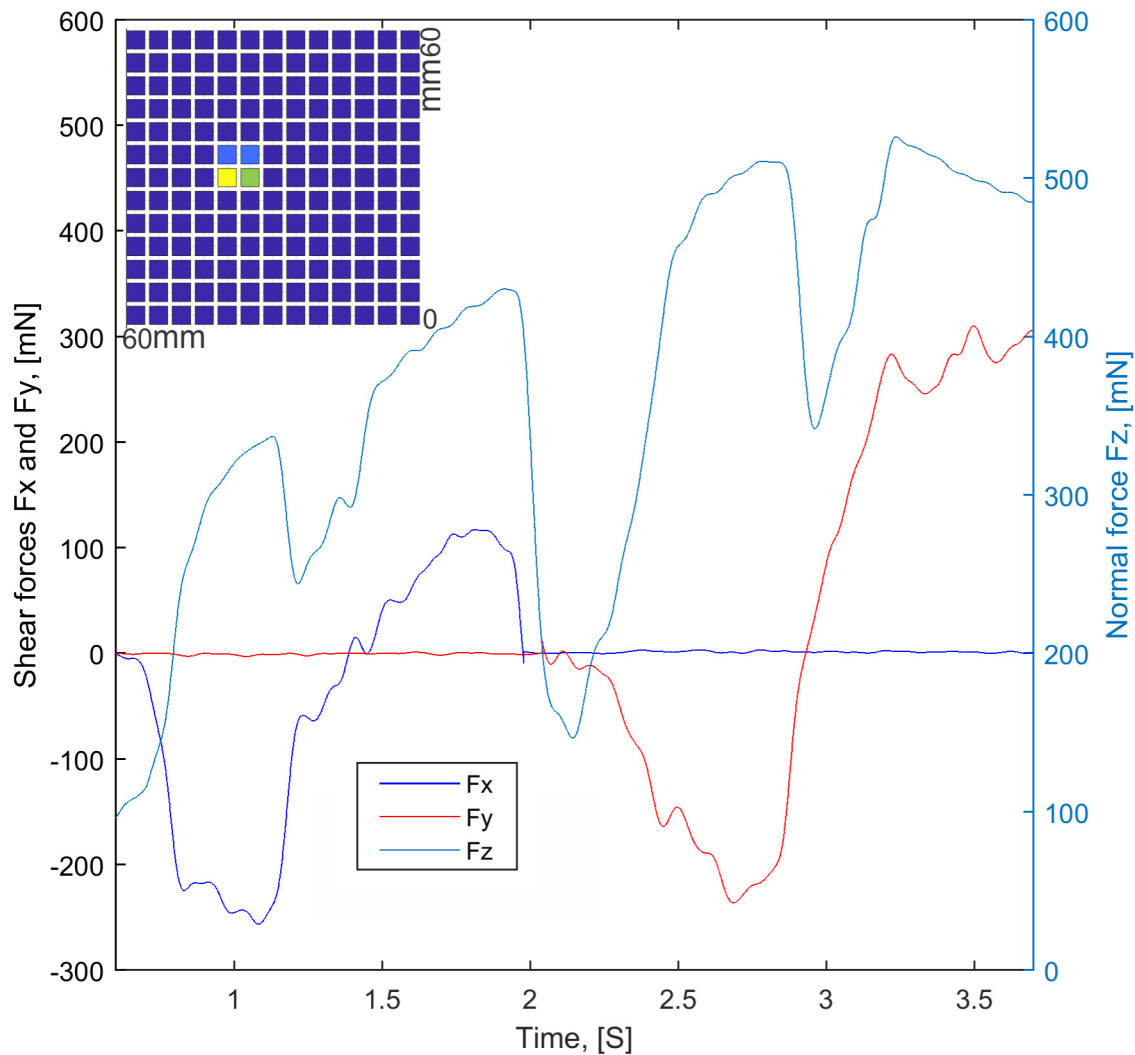
Figure 5-46 Shear force extraction and quantization © [2018] IEEE

To decouple the force components $F_x$, $F_y$, and $F_z$, some proximations have been made. The assumption was the linear interpolation if the force fell at the position between two adjacent calibrated points. Assuming the true *sensitivity fingerprints* within one *pitch* distance would form a convex curve, as shown in Figure 5-47, the approximation error $Z_{Err}$ for the normal force could be denoted by equation (5-5):

$$Z_{Err} = \frac{V_{zt} - V_{zinp}}{V_{zt}} * 100\% \tag{5-5}$$

Where $V_{zinp}$ standing for the linearly interpolated voltages between two calibrated points, and $V_{zt}$ standing for the mean values of actual tests from each tactel. For shear force calculations, as seen in Figure 5-48, the variations between the interpolated value $V_{zinp}$ and the actual value $V_{zt}$

would not influence the calculations for the voltage portions in $V_t$ generated by the shear components. Put another way, the outputs portions ($V^{E3}$-$V^{E1}$ or $V^{E4}$-$V^{E2}$) for calculating the shear forces from the sensing elements within each tactel maintain intact. Therefore, the shear forces error is only related with the half value of the calibration resolution (2.5 mm) and the running noise level (0.25 mV from the SNR-analysis).
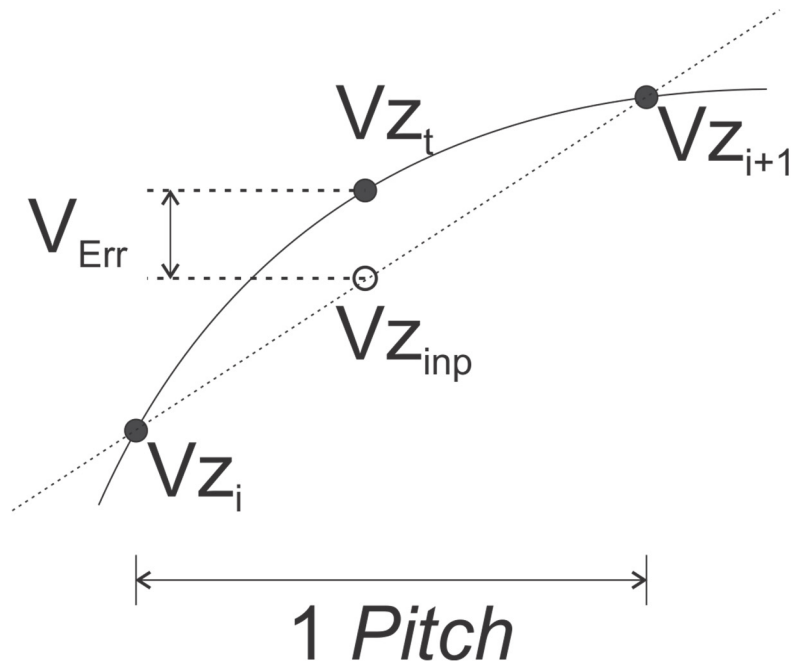


Figure 5-47 Scheme of the proximation in normal force calculations © [2018] IEEE
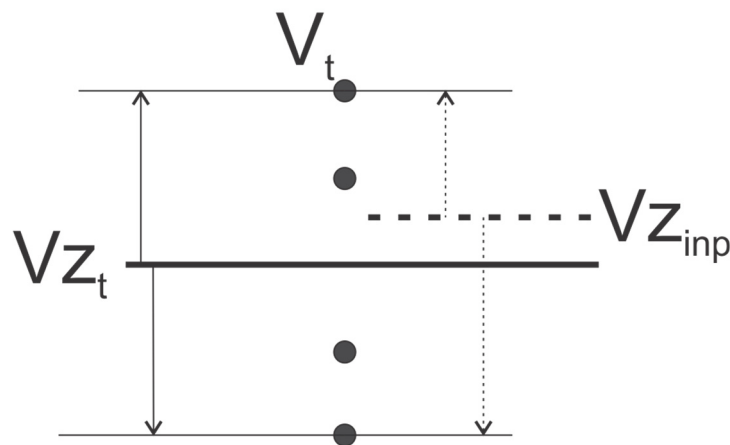


Figure 5-48 Scheme of the proximation irrelevance in shear force calculations © [2018] IEEE

The error analysis has been done by FEM simulations with a incremental step size of 1.5 mm. From Figure 5-49, the normal force error level is within ± 1.5% FS. The shear force error level is

within ± 2.5% FS as shown in Figure 5-50 and Figure 5-51, considering the 0.25-mV tested noise floor. Using the multi-axis forces as input gestures for HCIs in the practical application context, the variations within 1 gram-force in the measurement could be tolerated.
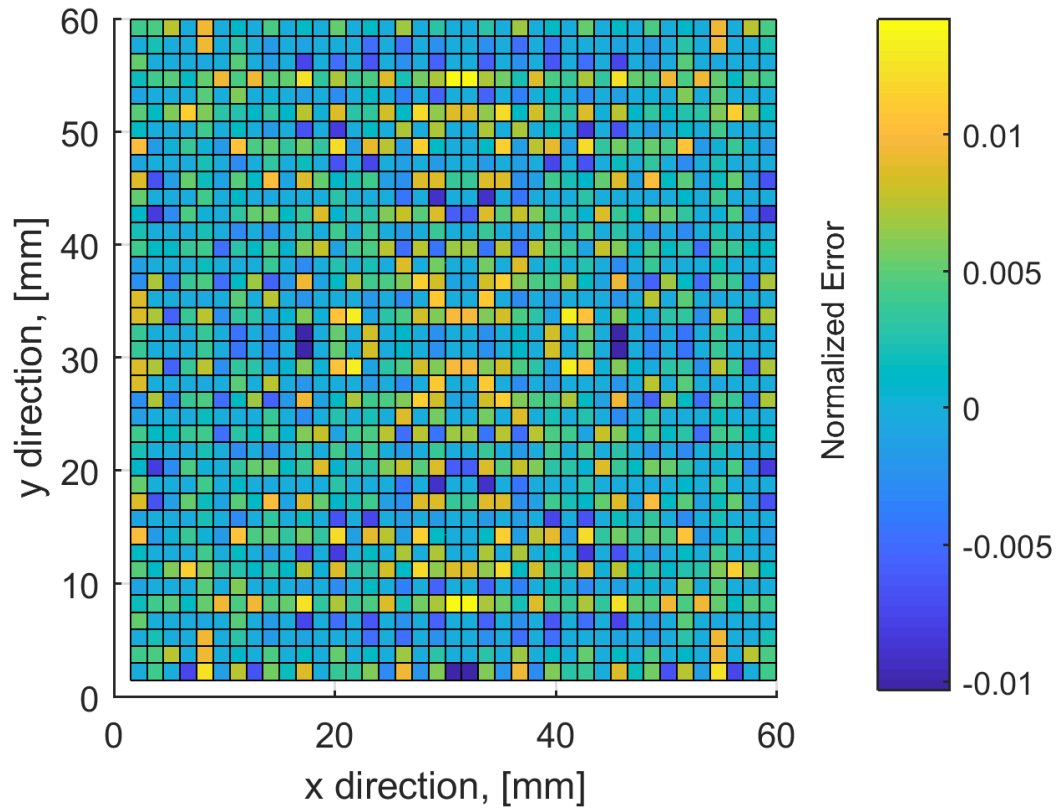


Figure 5-49 Calculated normal force error $Z_{Err}$ distribution across the sensor array © [2018] IEEE
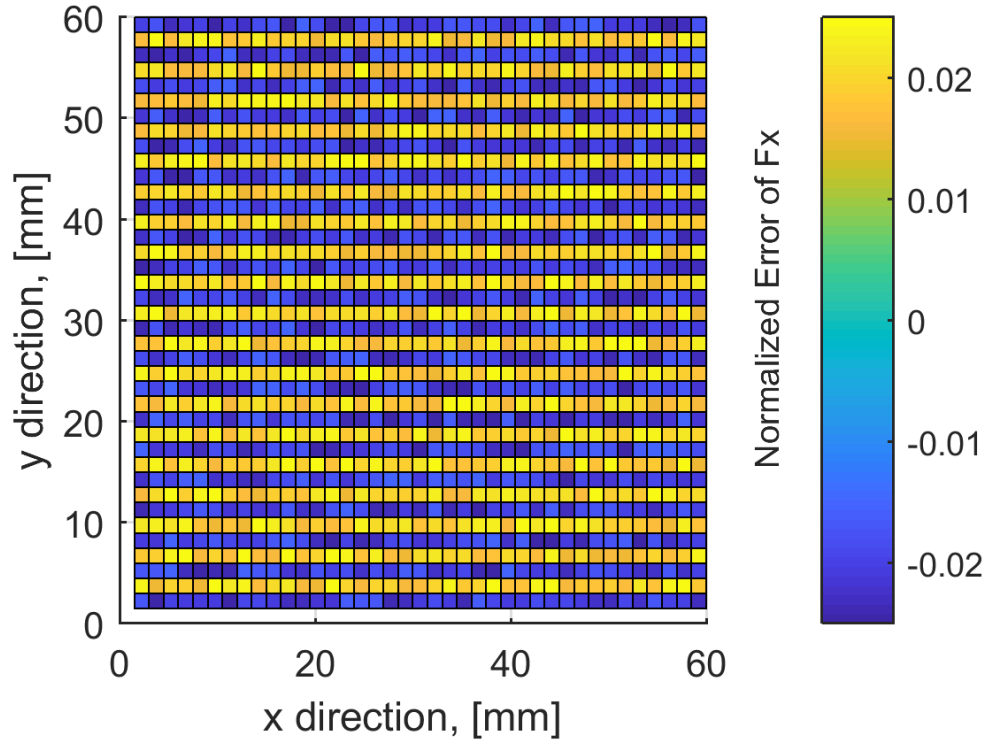
Figure 5-50 Error analysis of the shear force $F_x$ © [2018] IEEE
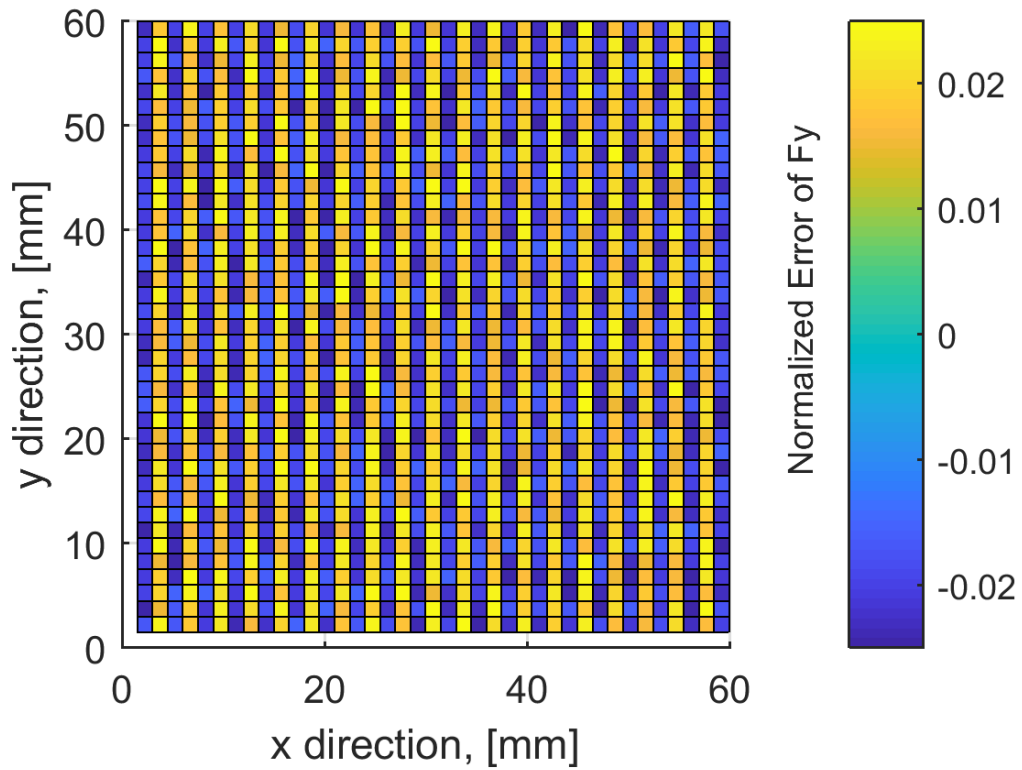


Figure 5-51 Error analysis of the shear force $F_y$ © [2018] IEEE
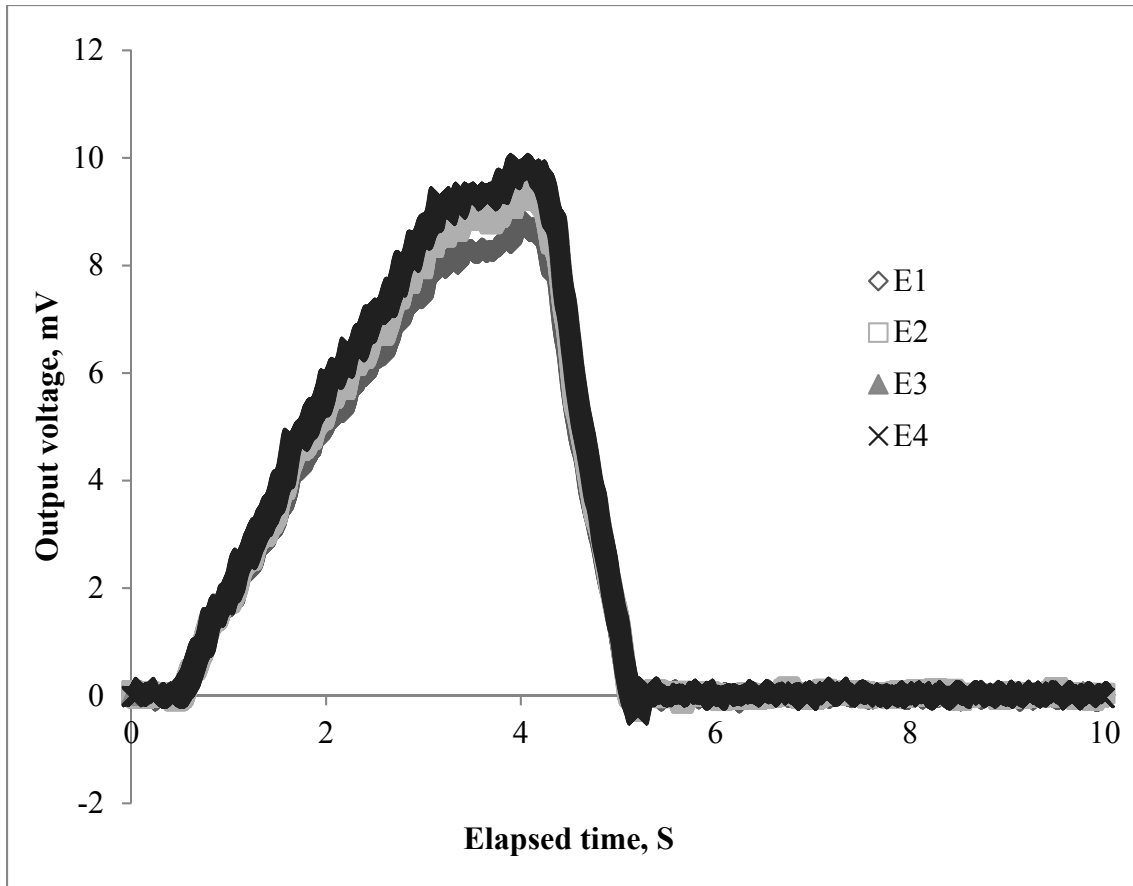
Figure 5-52 Outputs from four elements in one sensor for signal-to-noise ratio analysis

Signal-to-Noise Ratio of the sensor array has been investigated by applying a normal force with peak value at about 100 mN. Signals collected from one multi-axis tactel have been plotted in Figure 5-52, within an elapsed time of about 4 seconds. This was done using the steel bar and PDMS cushion, therefore, output slopes increased steadily as the effect of applying a force had been extended due to the softness of PDMS. Notably, at the end of releasing the force, a tiny diving peak below zero was found, which was possibly because the PDMS cushion stick with the bottom of steel bar and the glass.
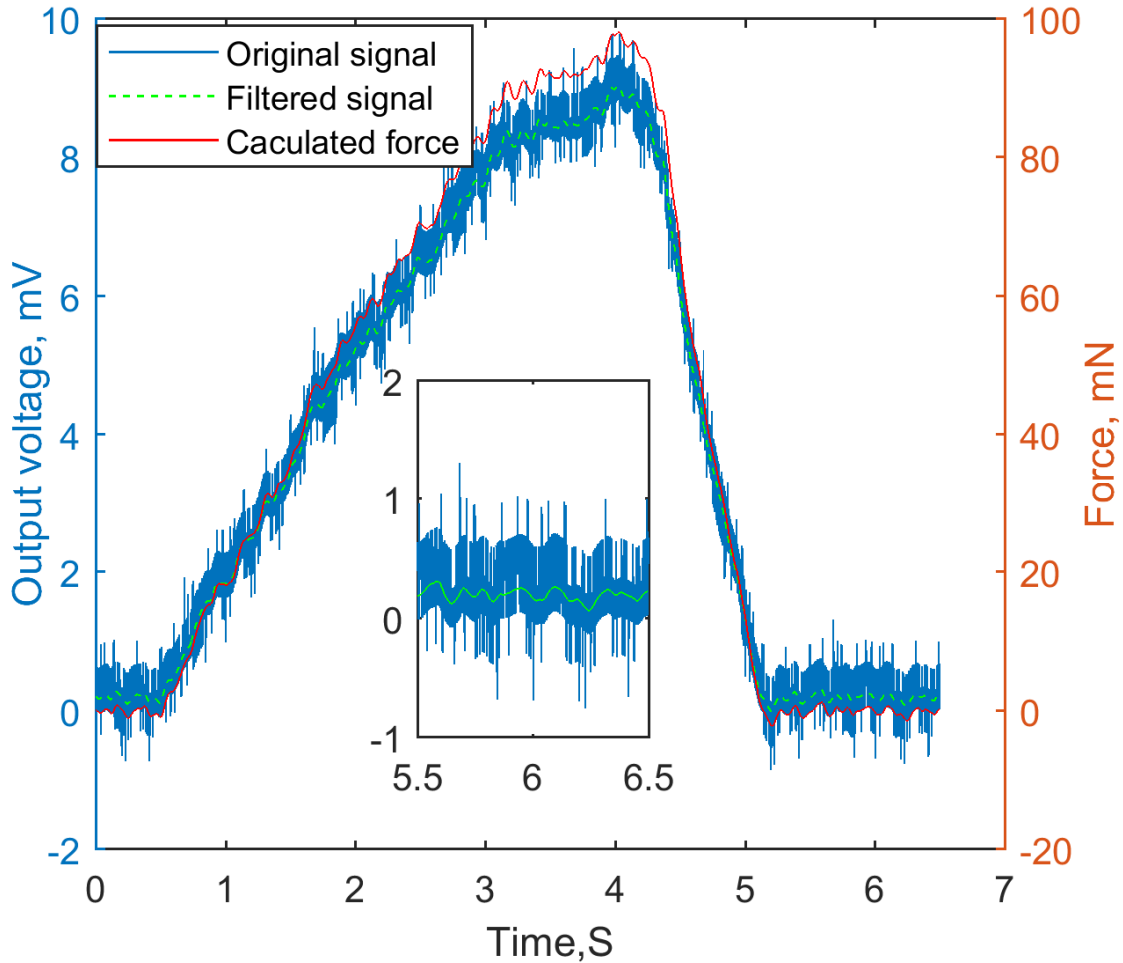
Figure 5-53 Signal-to-Noise ratio analysis © [2018] IEEE

Applied by a 100-mN normal force, the unfiltered original data has a 1.5-mV level of noise, whereas the filtered data has about a 0.25-mV noise-level after passing by a digital low-pass filter. SNR could be calculated by equation SNR = $P_{signal}/P_{noise}$. Considering the maximum force range of the sensor array, SNR were calculated as 32.3 FS and 194 FS for the unfiltered and the filtered data (see Figure 5-53), respectively.

A press-and-release test has been performed to study the behavior of the sensor array using the sharp tungsten probe and PDMS cushion. The stickiness of PDMS on the glass surface was confirmed by comparing two outputs from such probing, which has been presented in Figure 5-54. Around 4.4 second, the negative spike indicated that the PDMS cushion detached from the cover glass with a pulling force before completely separating from glass surface. The secondary slope captured between 3.6 s and 4.2 s was probably caused by the squeezed PDMS cushion releasing

back to normal geometry. This releasing provided a small reaction force onto the glass surface. Whereas, in the plot of using tungsten probe, both phenomena disappeared.
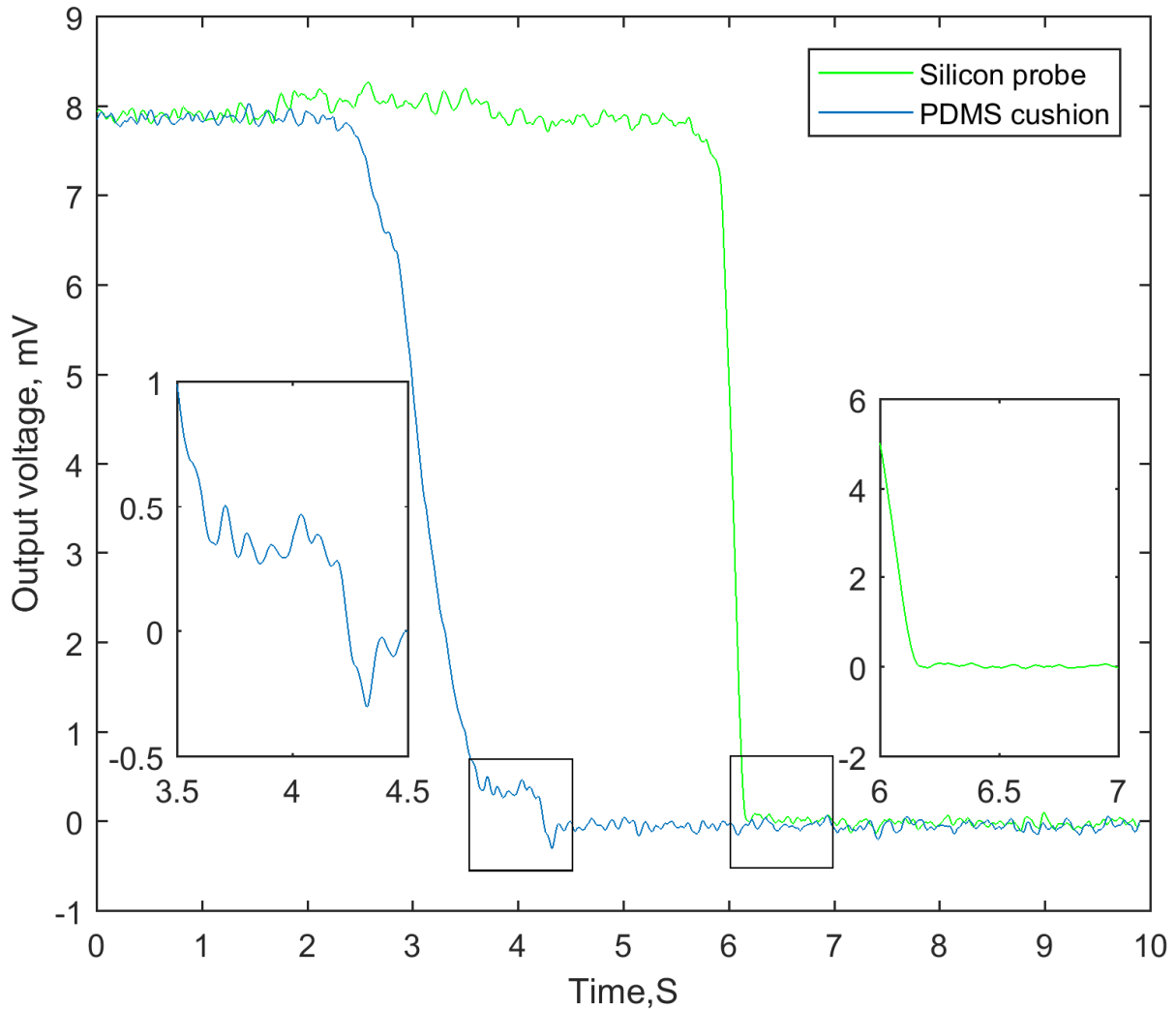


Figure 5-54 PDMS elastic effect during the force releasing

## 5.7 Specifications of the multi-axis tactile sensor and the multi-axis tactile sensor array

The specifications of the multi-axis tactile sensor have been listed in Table 5-5. As can be seen, the tactile sensor has a footprint of $2.5 \times 2.5 \times 0.35$ mm, 4 differential outputs and the ability for three-axes force measurement. For using as bare devices, the multi-axis tactile sensor is fragile. However, this can be avoided by carefully packaging the sensor or eliminating any overloading scenario.

Table 5-5 Specifications of the multi-axis tactile sensor

| Parameter | Specifications |
|---|---|
| Dimensions (mm) | 2.5 × 2.5 × 0.35 |
| **Material** | |
| Carrier | N-type Si |
| Sensor Element | P-type Si (Boron doped) |
| **Connectivity** | |
| Flip-chip | Yes |
| Wire-bonding Pad (um) | 450 × 450 |
| Input | 1 - 3V DC |
| Output | *Fz:* 0. 7mV/mN•V<br>*Fx & Fy:* 0.15 mV/mN•V |
| Nominal Resistance | 50 Ω +/- 6 Ω |
| Resistance Tolerance | +/- 10% |
| Maximum Loading Range | *Fz:* 300 mN<br>*Fx & Fy:* 100 mN<br>(on the die) |
| Number of Channels | 4 differentials |
| **Thermal Properties** | |
| Reference Temperature | 20°C (68°F) |

The multi-axis tactile sensor array has been introduced with specifications enclosed in Table 5-6. The sensor array has a spatial resolution of 2.5 mm with respect to sensing the tactile location. In terms of multi-axis force measurement, the sensor array has a sensitivity of 0.35 mV/mN•V and 0.15 mV/mN•V in the normal and shear direction, respectively. The limitations of the current sensor array are addressed as follows: the power consumption could be large due to the low overall resistance; a lack of global analytical solution to acquire the location and force information although the author has proposed a successful numerical solution. However, the power consumption can be reduced by increasing the Boron doping level of the tactels or applying pulsated DC power to the sensor array.

Table 5-6 Specifications of the multi-axis tactile sensor array

| Array Configuration | 2×2 |
|---|---|
| Cell Geometry | 2.5 mm× 2.5 mm |
| Footprint | 65 mm× 65 mm |
| Force range | $Fz:$ 1- 500 mN<br>$Fx$ & $Fy:$ 300 mN |
| Spatial Resolution | 2.5 mm (can be smaller by the characterization) |
| Sensitivity | Z: 0.35 mV/mN•V<br>X & Y: 0.15 mV/mN•V |
| Functional area | 60 mm ×60 mm |
| Signal channels | 16 Differential |

# Chapter 6.  Tuning force range of the tactile sensor

The packaging induced sensitivity tunability has been studied by modifying the tactile sensor for various force ranges. The sensor was designed for the normal tactile sensor array for touchscreen applications, with a force range in the millinewton level[137]. The sensor structure has been used as part of the modified assembly as shown in Figure 6-1. The sensor was structured with a circular membrane with its diameter of 400 um in a square-shape silicon die (3 mm × 3 mm). A four-terminal-gauge has been doped at the edge of the circular membrane, as the core piezoresistive sensing element. At the backside of the membrane, a cylinder mesa (boss) was built by the DRIE. Modifications on the force sensing range in the packaging phase has been done by adding a polymer dome into the void between the mesa and the vertical sidewall over the membrane. Owing to the filling material as a partial support, the overall deflection of the membrane would be affected, increasing the sensing range although lowering the sensitivity.
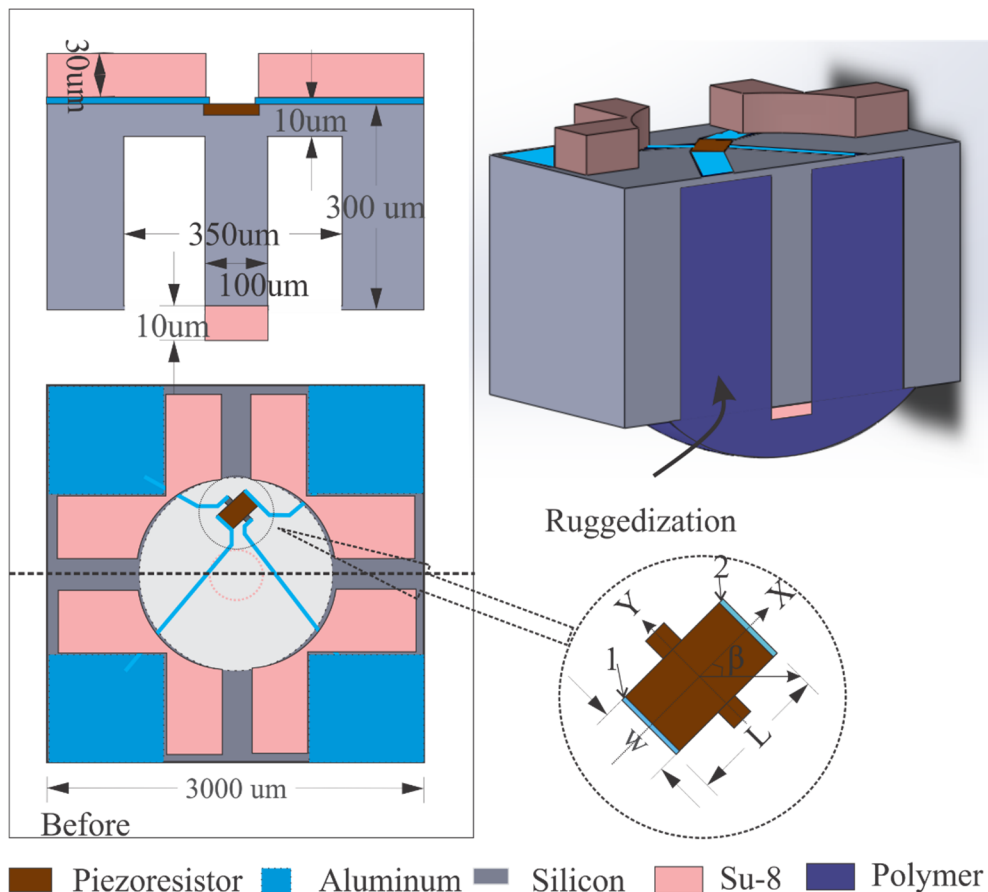


Figure 6-1 Sensor geometry and schematic view of packaging modification ruggedized by polymer

## 6.1 Ruggedization material

Usually, silicon-based MEMS devices are fragile including the one used for the sensor array in previous chapters, by having a standing-alone silicon mesa at the backside. Besides, the 10-um silicon membrane is also vulnerable in the packaging phase. The mesa and membrane could be easily smashed by the overload in flip-chip procedure. To enhance the robustness and the sensing range, two polymer materials have been used including the PDMS (polydimethylsiloxane) and the PU (Polyurethane). The two candidates have been elected to demonstrate the feasibility of modifying the force range of the tactile sensor, owing to their different material strengths and good biocompatibility. The material properties of both PDMS and PU have been listed below in Table 6-1, which have also been adopted in FEM simulations.

Table 6-1 Basic material property of PDMS and PU

| Material | Young's modulus | Poisson ratio | Biocompatibility |
|---|---|---|---|
| PDMS (Dow Corning sylgard® 184) | 0.36- 1MPa | 0.5 | Excellent[37, 153] |
| PU (Normag NR-906) | 0.69-2.07GPa | 0.45-0.5 | Good[154, 155] |

## 6.2 Fabrication and packaging
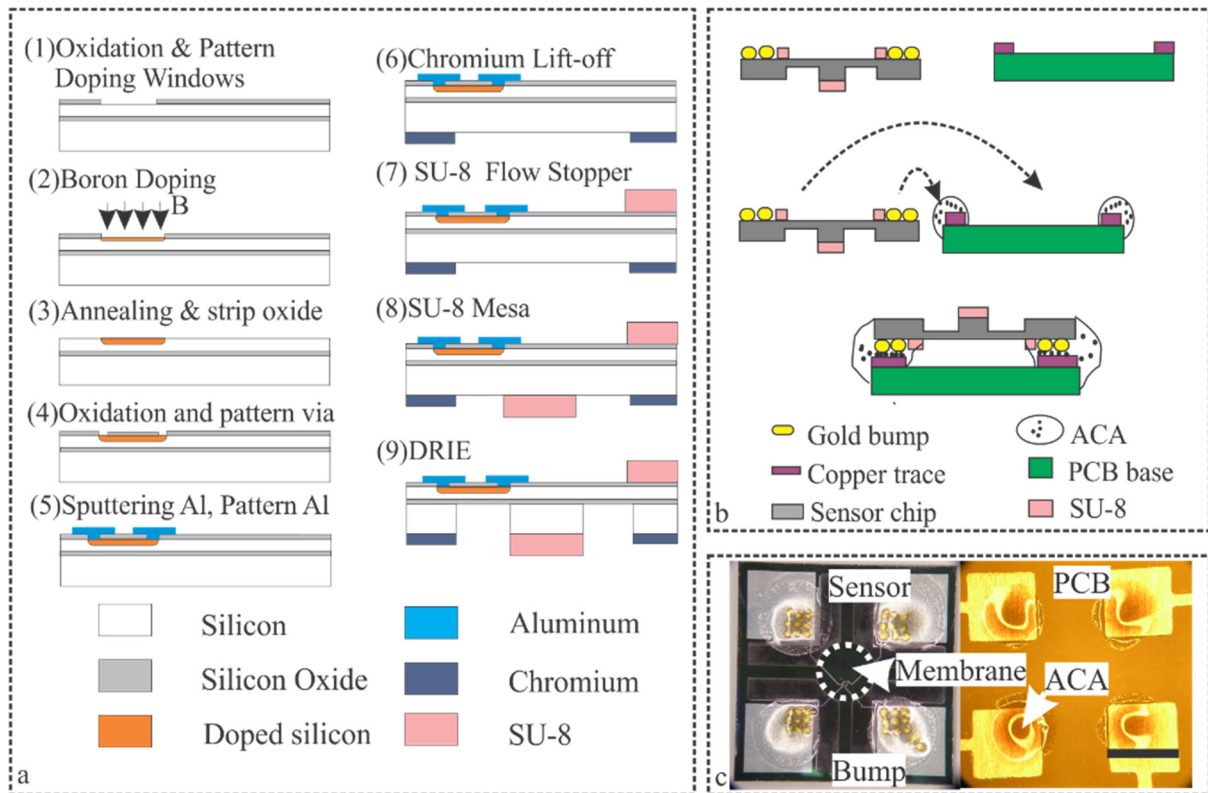


Figure 6-2 a: Fabrication process flow; b: Packaging procedures; c: applying anisotropic conductive adhesive (ACA) and frontside of the device (scale bar: 1mm)

The tactile sensor fabrication process flow has been presented in Figure 6-2 a, which started from an SOI (silicon-on-insulator) wafer. Firstly, the wafer was processed by a wet thermal oxidation and patterned by a BOE (buffered oxide etching) to form the mask layer for a following boron doping. The boron doping was performed in a quartz furnace at 900 °C for 45 minutes. Afterwards, the wafer was annealed at 1000 °C for 2.5 hours. Then the oxide mask was stripped off by another BOE. Another layer of thermal oxide was built and patterned to form the contact via. An Al layer was sputtered on the top of the oxide layer which had contact via in it. This layer of Al was patterned to make the electrical pads and traces for the power input and signal outputs. A procedure named chromium lift-off was done to define the backside etching region. The SU-8 flow stopper and mesa were installed by the photolithography at the top side of the wafer and in the to-be-etched region at the backside, respectively. Bonded on a carrier wafer, then the devices had been etched to form the membrane by the deep reactive ion etching(DRIE). After dicing the wafer, an individual sensor was flipped on the top of a polished PCB (printed circuit board) spread

with a few anisotropic conductive adhesive(ACA) to enhance the electrical connection and bond strength, using the flip-chip machine. Figure 6-2 c has depicted both the device with gold bumps and the PCB with ACA. After this initial packaging on the flip-chip machine, two kinds of polymer including the PDMS and PU were squeezed on the backside to fill the etched void and cover the mesa as displayed in Figure 6-3.
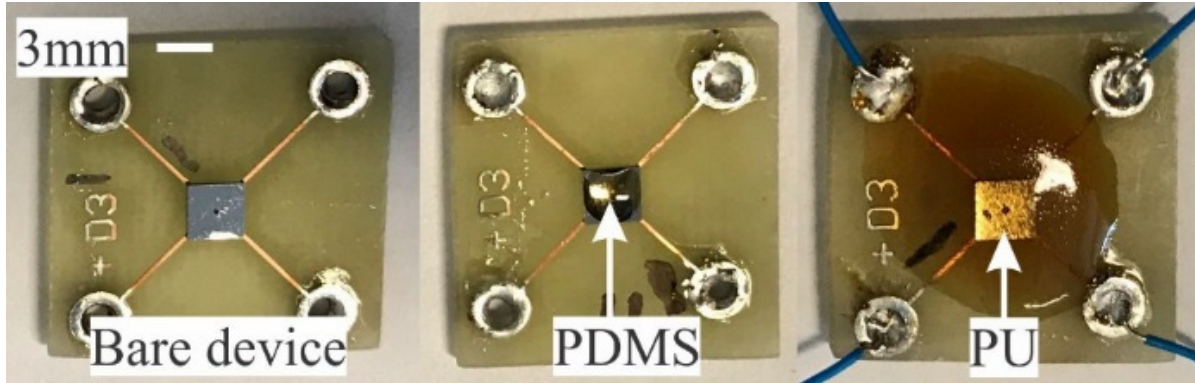


Figure 6-3 Ruggedized assembly comparing with bare device

Both the normally packaged and ruggedized sensors have been characterized with the corresponding range of known forces in the normal direction. Benchtop setups have been shown in Figure 6-4 for the characterization. The ruggedized sensors were mounted on a corner iron which was placed on the top of a Z-axis stage for changing its height. A force gauge with exchangeable probe tips has been used for applying the known force, sitting on the top of an x-y axes stage. Therefore, under the observation through the microscope, forces could be applied on mesas or polymer caps. Sensors were powered by a DC source at 1 volt. Signals were feed in either a multimeter which was with a millivolt resolution or the data acquisition card for further analysis.
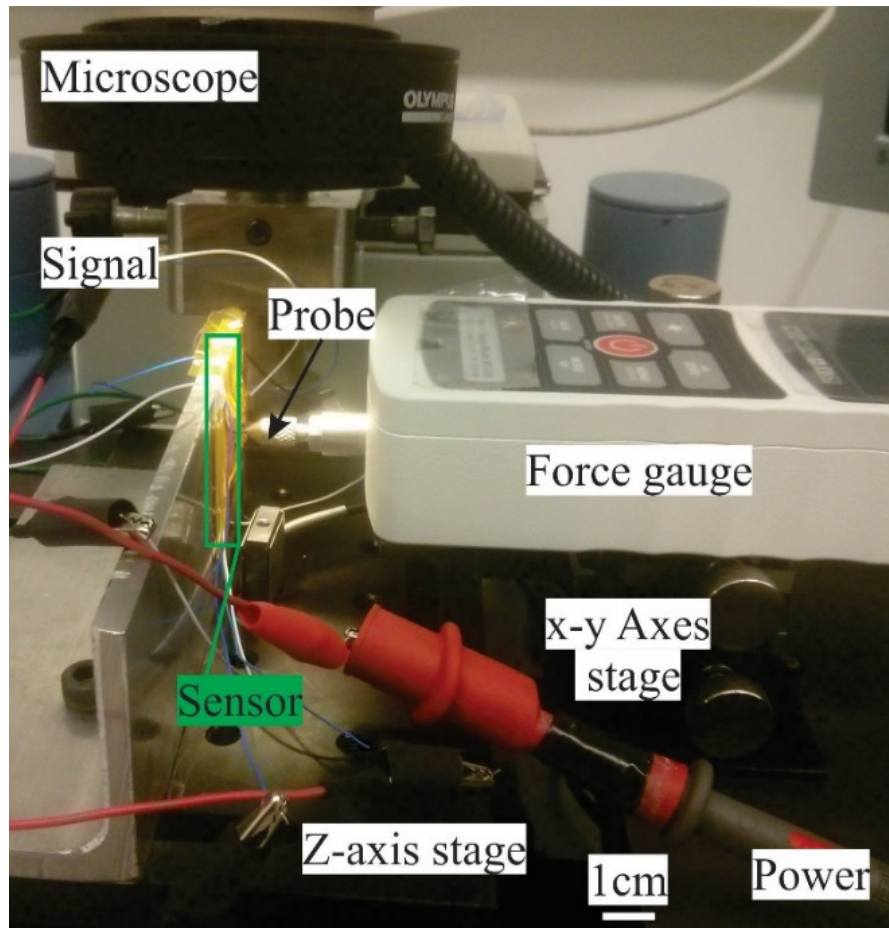
Figure 6-4 Characterization setup for sensor

As a proof-of-concept, devices with modified force ranges by the tuning methodology could be potentially applied for the physiological signals monitoring. This work provided several case tests including the lip closure force measurement, heart rate at the wrist, and finger strength tests. For the lip force measurement, the sensor ruggedized by the PDMS was chosen due to its appropriate force range for the compliant lip tissue. After placing the sensor between two lips and holding naturally, the author tested the sensor in two ways including pressing it with lips lightly and purging lips to apply more force on the sensor. In terms of monitoring the heart rate, the same type of PDMS ruggedized sensor was mounted by a rubber band at the wrist position where the radial artery was. The fluctuations of the vascular pressure caused the changing forces applied on the mounted sensor. For the finger strength evaluation, a test was done by placing the sensor between the thumb and index finger. Motions including press-and-release for four times and rubbing the PU dome for four times have been applied on it. Schematic drawings combined with photos captions have been attached below to demonstrate the qualitative test setups and procedures.

160

## 6.3 Results and discussion

Packaging induced property change could be detrimental for the MEMS development, which might compromise the designated performance of devices. The pristine devices could be characterized by applying the known normal force and evaluated the performance. As shown in Figure 6-5, the sensitivity of the tactile sensor was calibrated as 0.76 mV/mN·V with the maximum output voltage peaking at 80mV, demonstrating a good linearity within the range of 1 - 35 mN. Ruggedizing the void between the mesa and membrane with PDMS, the projected force range was enlarged to 1 - 400 mN if the outputs reaching the level of 70 mV. Then the force range would be more than 13 folds of the bare device capability, according to the output voltage (5.2 mV) at 30 mN (see Figure 6-6). Similarly, the voltage output of PU ruggedized sensor was around 15 mV, which offered a projected force range of 0.001 - 93 N if output reaching 70 mV. This enabled the device to have the capability to measure 3100 folds of the former maximum sensing force.
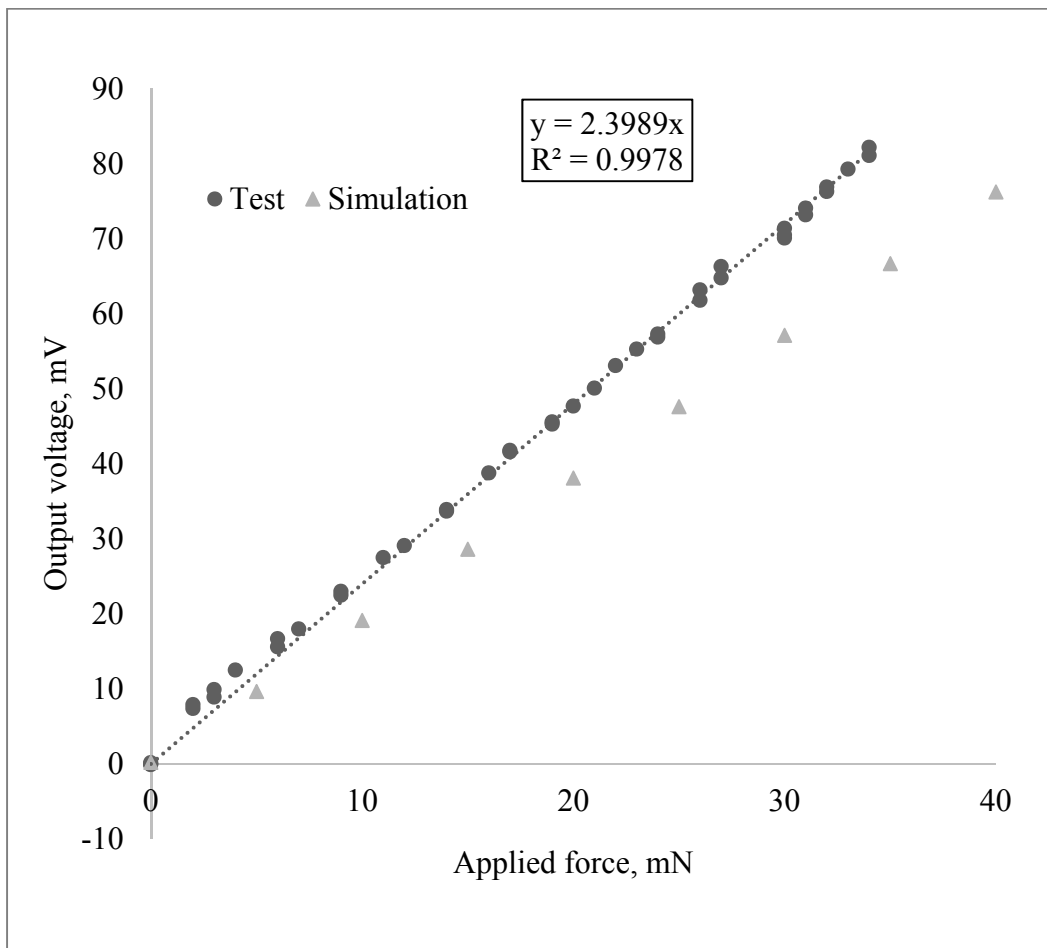


Figure 6-5 Characterization of a packaged sensor by applying force in normal direction on the mesa
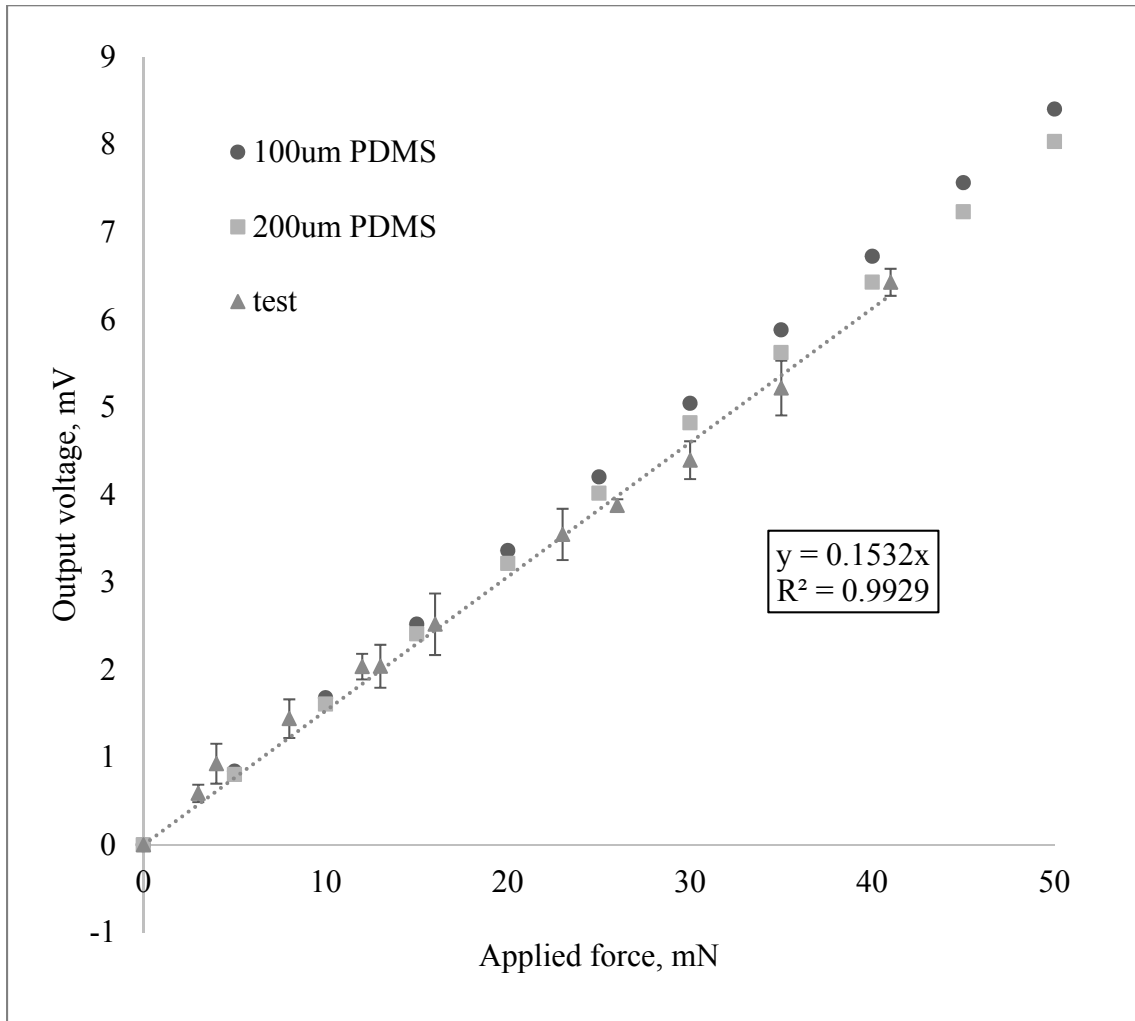
Figure 6-6 Characterization with ruggedized sensor by PDMS
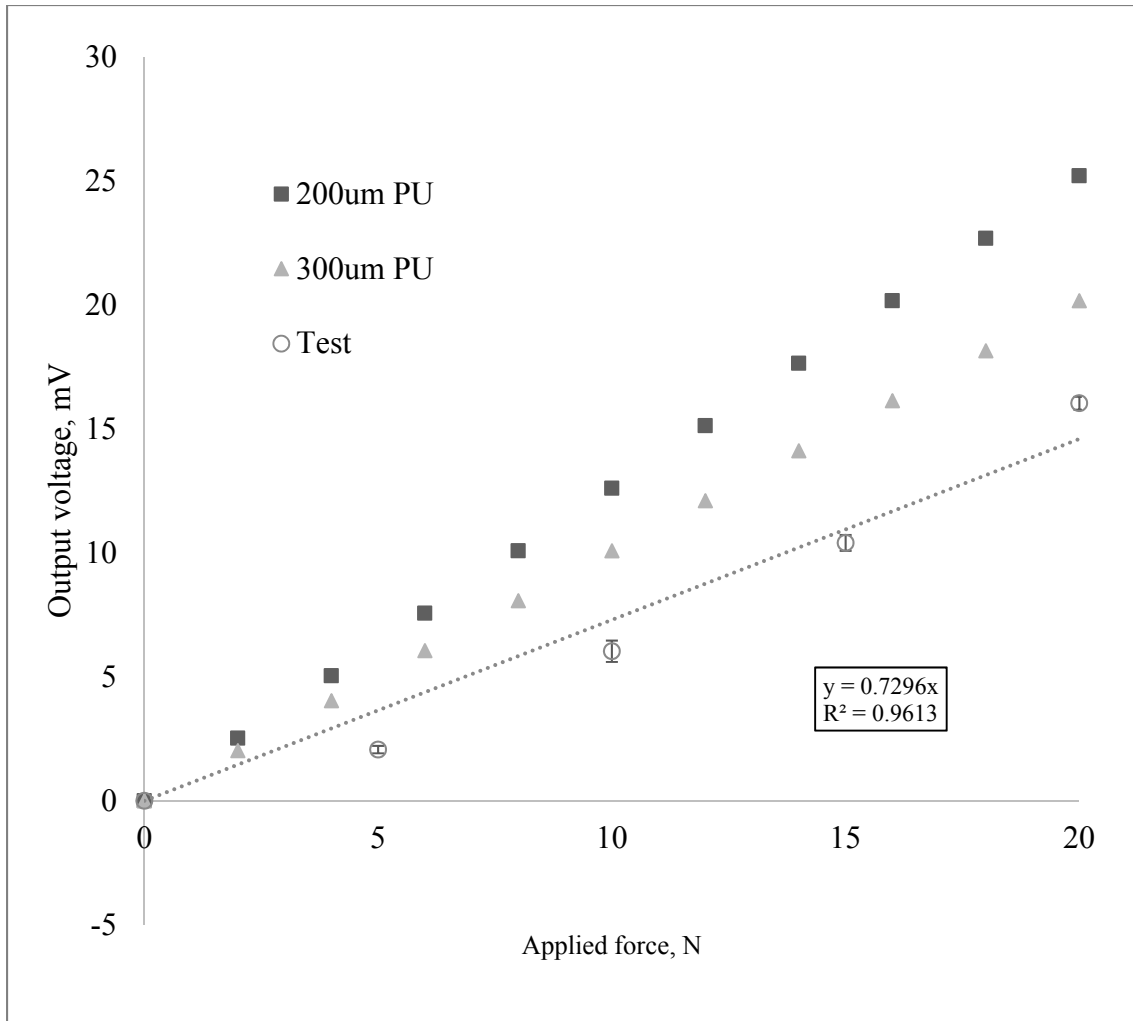
Figure 6-7 Characterization of ruggedized sensor by PU
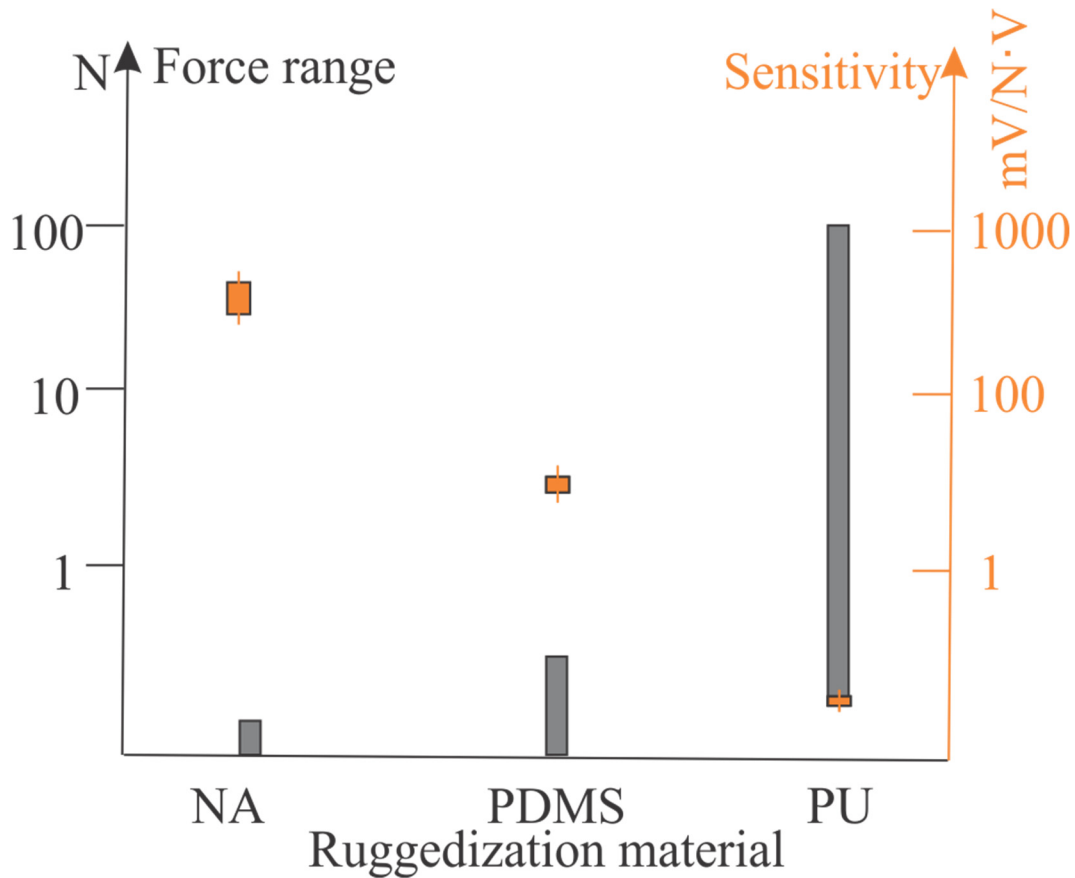
Figure 6-8 Packaging induced force range tunability (NA: Not Applied)

Sensing range changes of this tactile sensor induced by packaging materials such as PDMS and PU could vary from ten-fold to thousands-fold. These changes were expanding the force range from millinewton-level to hundred-newton-level (see Figure 6-8). Notably, the trade-off between the sensitivity and the full-scale force range has been made by the packaging modifications. The cultivation of the sensing range on a specific tactile sensor in the packaging phase could skip the previous development steps such as mask printing, fabrication flow, signal characteristics study, accelerating the application progress.

## 6.4 Case study

Lips are one of the essential facial organs for the human life activities such as keeping the food inside the mouth, speaking, expressing emotion, tactile sensation. It also has highly cosmetic value for the personal appearance. The proper lip closure force is one of parameters to evaluate the function of lips, as one of the common test for patients after the plastic surgery[40], or those with verbal challenges[156]. Common measurements of lip closure forces require bulky instruments, which uses a long rod stuffing into the mouth of testing objects[157]. Besides, the testing

equipment must be sanitized before the next test. Moreover, stuffing a huge alien object in the mouth of the test participant is mentally disruptive, especially for children or those people who have already overwhelmed by the plastic surgery recovery. Therefore, to develop a miniatured size, disposable force/pressure measurement element is helpful to mitigate these concerns. As captured in Figure 6-9, the natural lip closure pressure could raise the sensor output to about 1 mV. Therefore, lightly squeezing both lips could be sensed. With pursing lips, the output of this ruggedized sensor could peak to 3.3 mV which was equivalent to a lip closure pressure at 2.4 KPa.
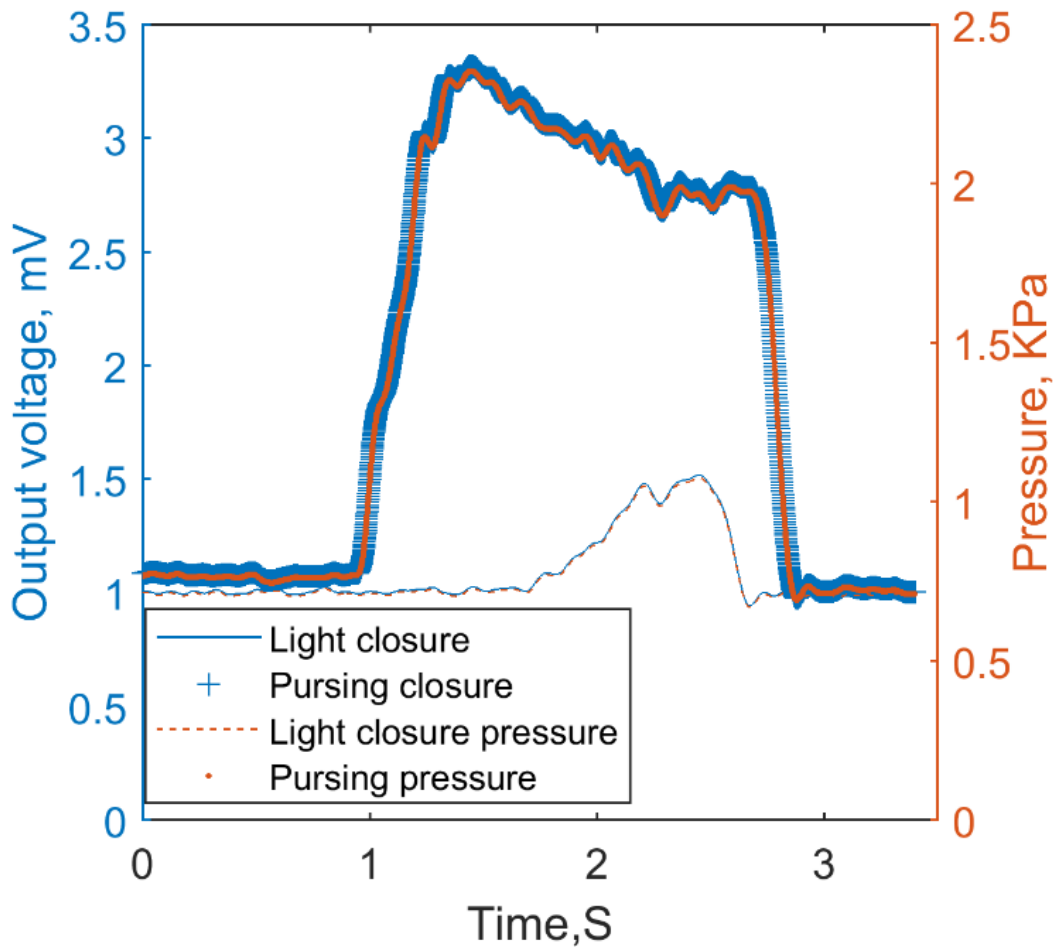


Figure 6-9 Lip closure force measurement

The average lip pressure (force) was around 0.2 KPa when the lips were at the rest position[158], or 40 KPa as maximum lip purging force (around 12.5 N)[157]. The maximum strength demonstrated huge variations due to gender differences and ages. The Young's modulus (E) of facial tissue was around 30 KPa including the lips[159], which was similar comparing with the silicone rubber EcoFlex® 0030[160](mix ratio at 1A:1B, E ≈ 29 KPa). Therefore, as captured in Figure 6-10, a phantom lip made by the EcoFlex® has been used to apply the similar level of

165

pressing force as the lip closure pressure on the PDMS ruggedized sensor. As shown in Figure 6-11, the slightly pressing could raise the sensor output up to about 1 mV which meant lightly squeezing both lips could be sensed. Notably, the output of the ruggedized sensor could reach 5.2 mV which was equivalent to the lip closure pressure at 4 KPa.
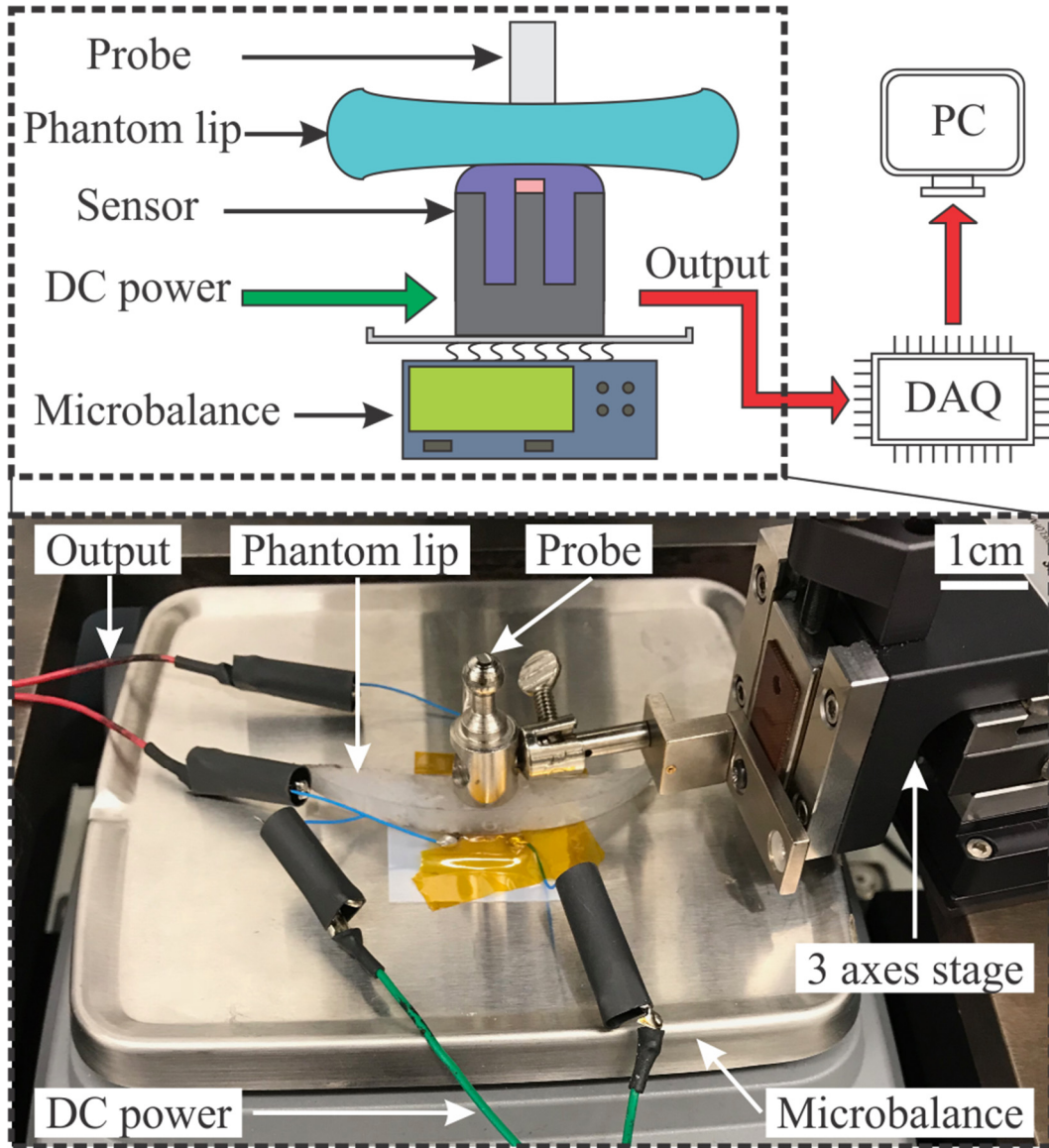


Figure 6-10 Test setup with the phantom lip
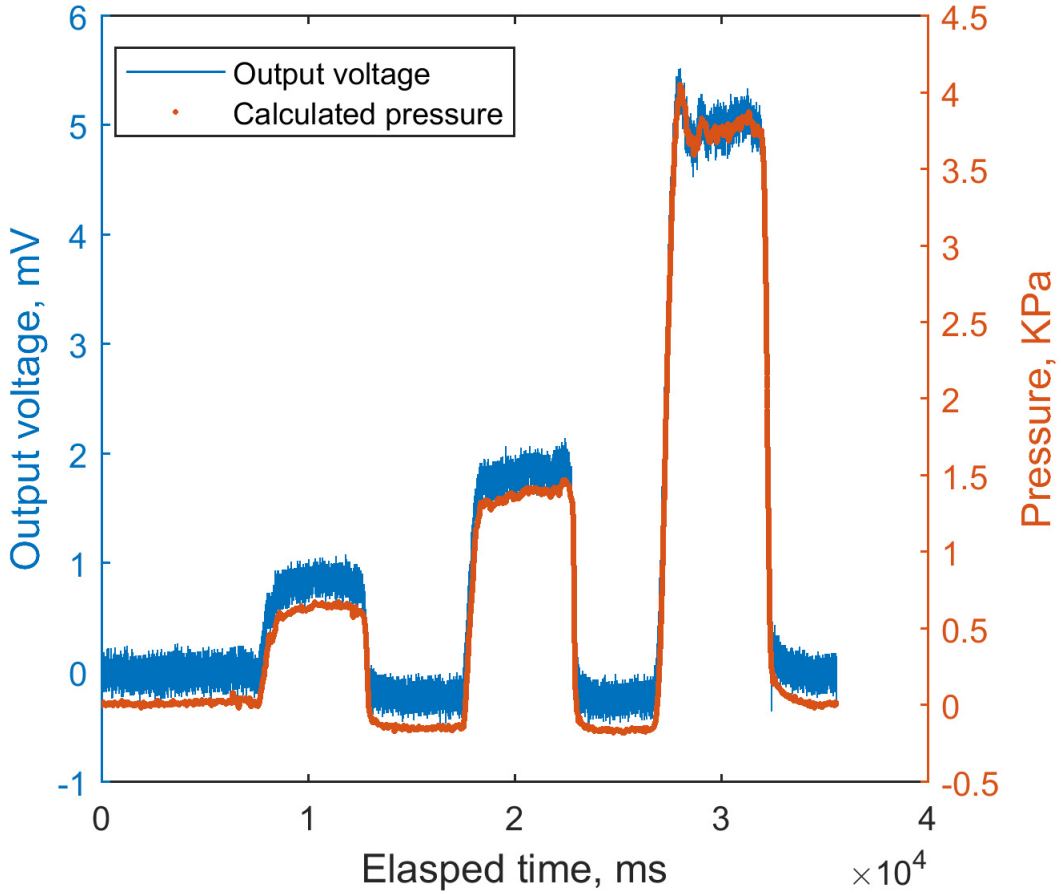
Figure 6-11 Lip closure force measurement

Heart is one of the most essential organs for the human to be alive. The heart rate is an important and straightforward parameter as an evaluation of whether the heart is in healthy shape or not. To measure the heart rate, numerous approaches have been developed including medical level monitoring systems, wearables as consuming electronics[161], implantable devices, etc. Among the medical devices adopted in hospitals, most of them are expensive and integrated with other instruments which are not portable. In terms of the consuming wearable electronics, most of them are based on the light detector, of which the accuracy easily gets affected by the ambient light or the sweat. Hereby, the contact-based devices are reliable in these scenarios. The wrist pulse is composed by two main parts including a primary wave and a secondary wave[162].With PDMS ruggedized sensor mounted on the wrist, heart rate signals could be sensed from the radial artery, where the pressure changes were found due to the blood flow fluctuations. By comparing with simulated ECG (electrocardiography) using MATLAB®, the heartbeat signal from the ruggedized sensor has been verified as $83 \pm 1$/min (see Figure 6-12). Notably, the sensor was preloaded at the pressure level of 7.5 KPa with the output of about 10.3 mV.
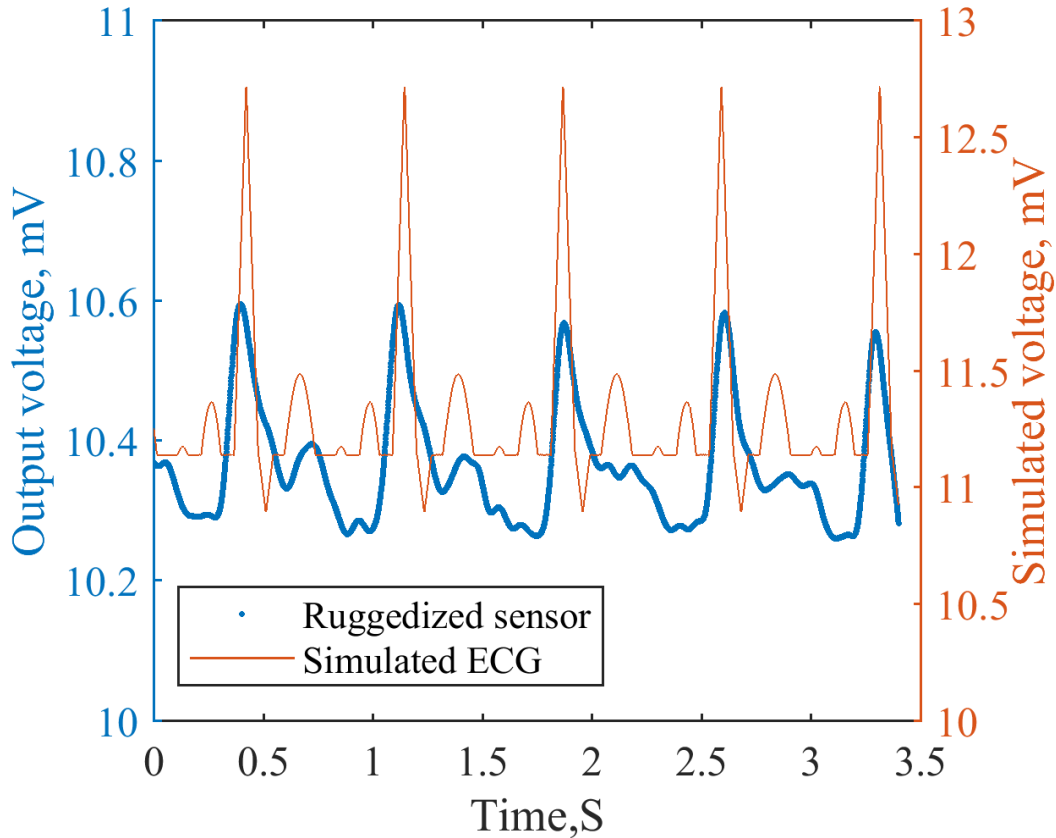
Figure 6-12 Heartbeat rate measurement

With PDMS ruggedized sensor pressed by a piece of silicone rubber mounted on an aluminum arm, emulated heart rate signals have also been evaluated. The pressure changes were found due to the up-and-down jack motion driven by a step motor connecting through a compliant shaft (see Figure 6-13). The heart rate at the wrist is composed by two main parts including the primary wave and the secondary wave[162, 163]. The emulated motion, which was also formed by two peaks as the two pulse components, has been captured by the tuned sensor as shown in Figure 6-14. The heart rate signal from the ruggedized sensor has been verified as $65 \pm 1$/min.
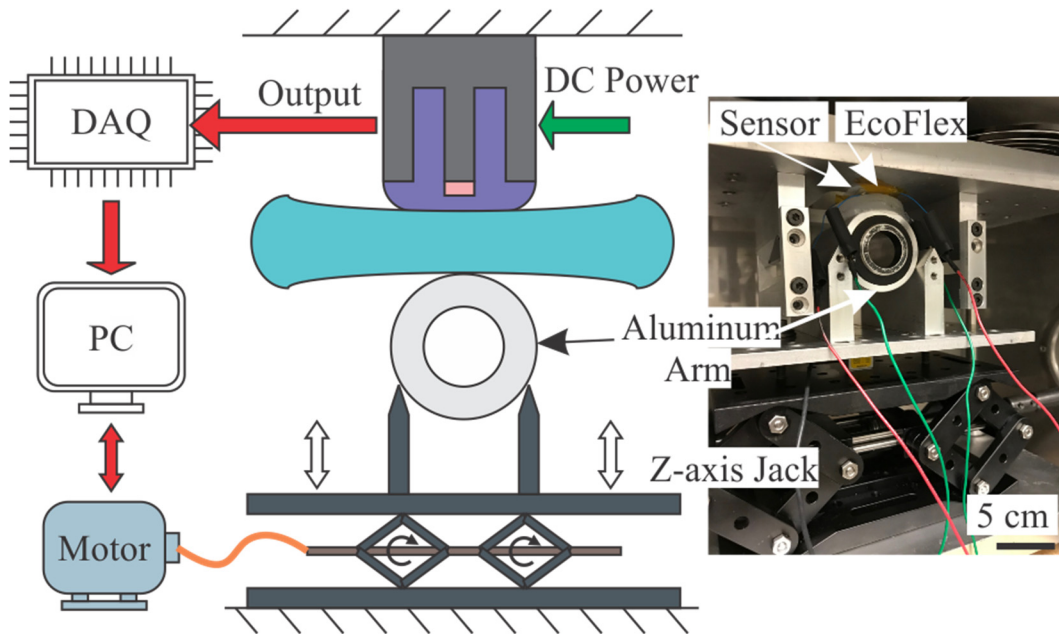
Figure 6-13 Apparatus for emulating the heart rate pulse with a step-motor-driven jack
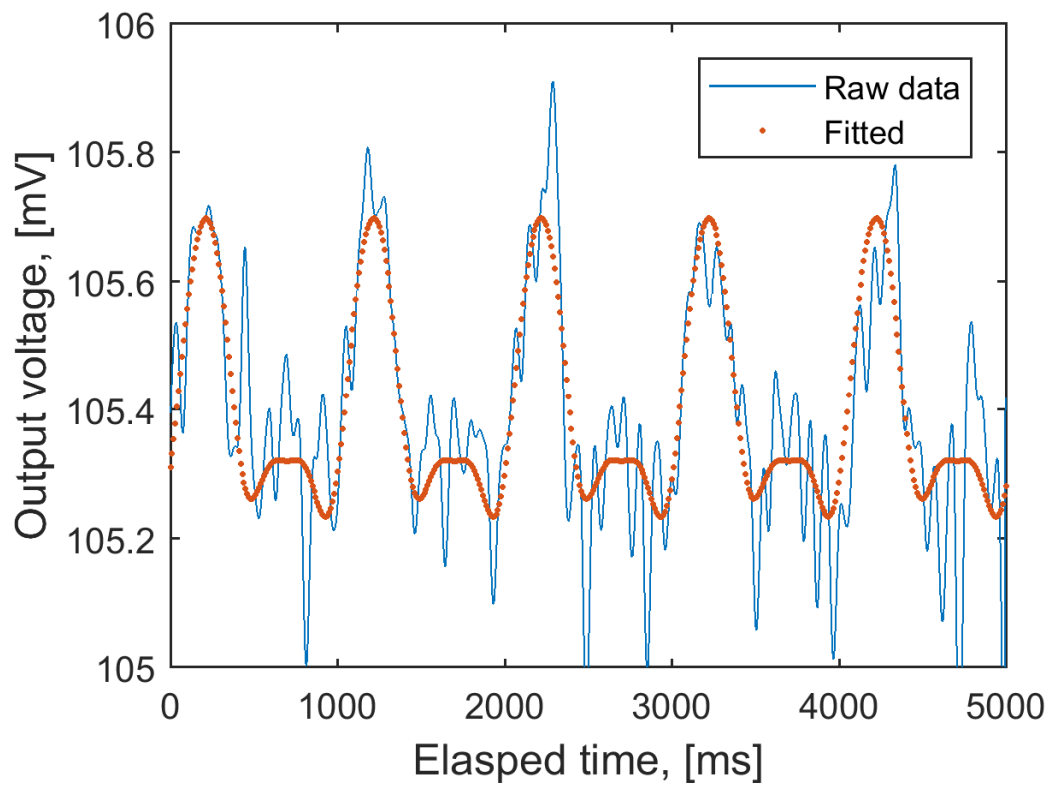


Figure 6-14 Emulated heart rate measurement
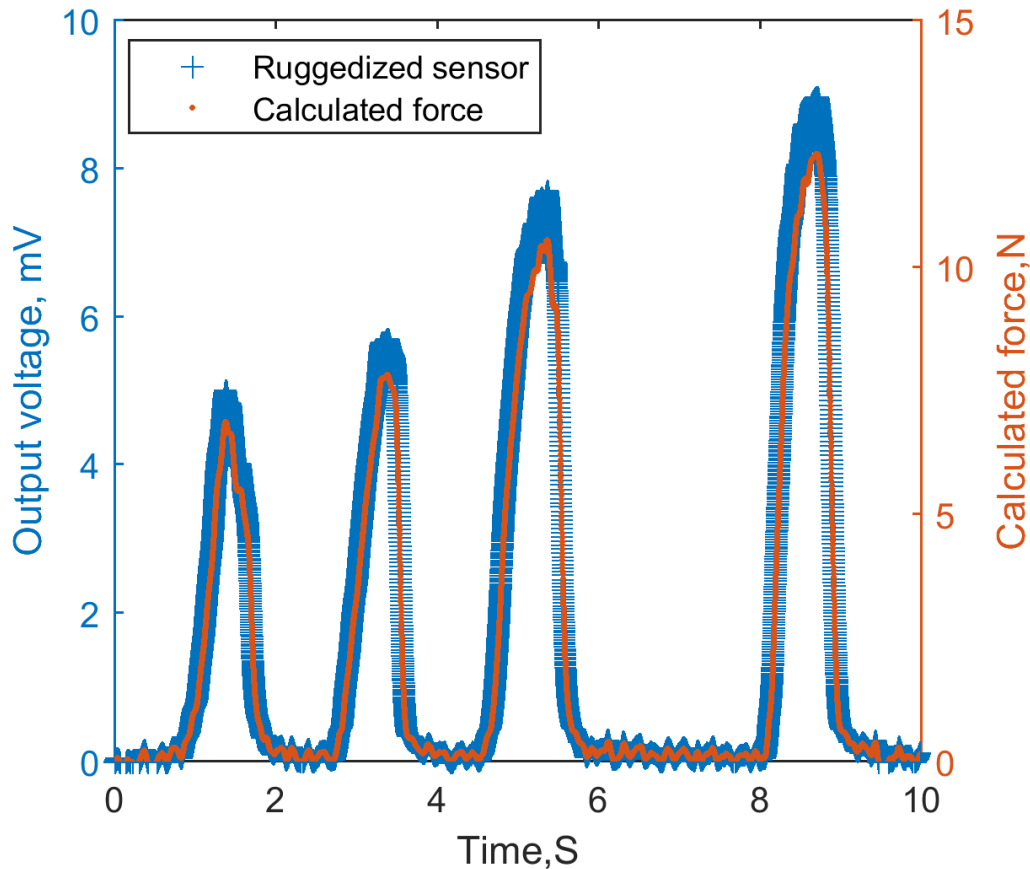
Figure 6-15 Pressing tests with the thumb and index finger

Hands are the most dexterous part in human body, containing significant number of degrees-of-freedoms. Therefore, to regain the strength and dexterity is the core process during the rehabilitation after surgeries such as finger transplantations, skin transplantations or fracture corrections. The finger strength would be one of the key parameters for evaluating the recovery procedures. To be powerful enough for daily grasping purposes, the finger pressing force has a range from several N to more than a hundred N. Therefore, as an exploration on the applications of the ruggedized sensor by PU, pressing the sensor with the thumb and index finger have been performed as qualitative tests. The forces during these four trials tests have been calculated according to previous characterizations. As can be seen in Figure 6-15, the peak force could reach 12.5 N. Therefore, the projected force range could be more than a thousand folds of the maximum force limit in the original tactile sensor.
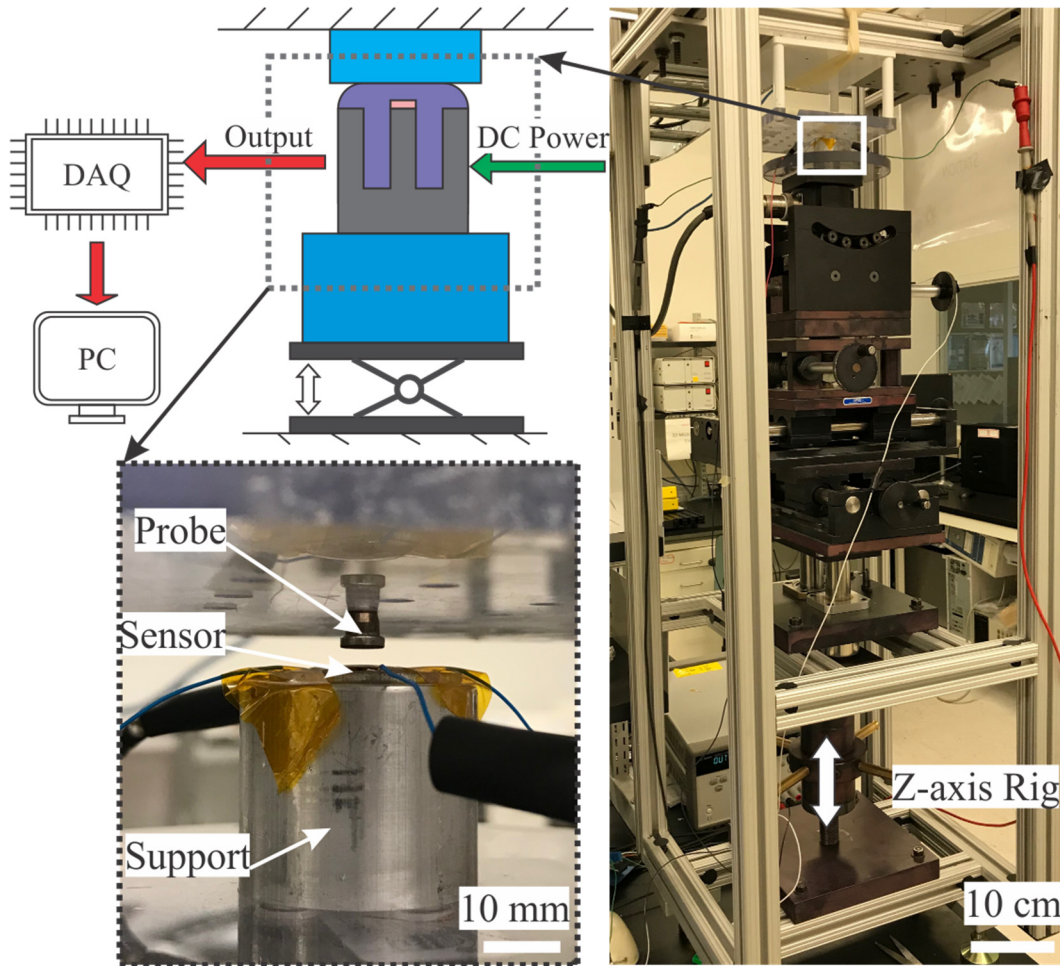
Figure 6-16 Test setup for applying pressing forces equivalent to the power of hands

As further exploits on the capability of the PU ruggedized sensor, tests done by pressing the sensor with a multi-axis test rig as shown in Figure 6-16. Forces during these tests have been calculated according to the previous characterizations. As can be seen in Figure 6-17, the peak force could reach 46 N, which is more than a thousand folds of the force limit in the pristine tactile sensor.
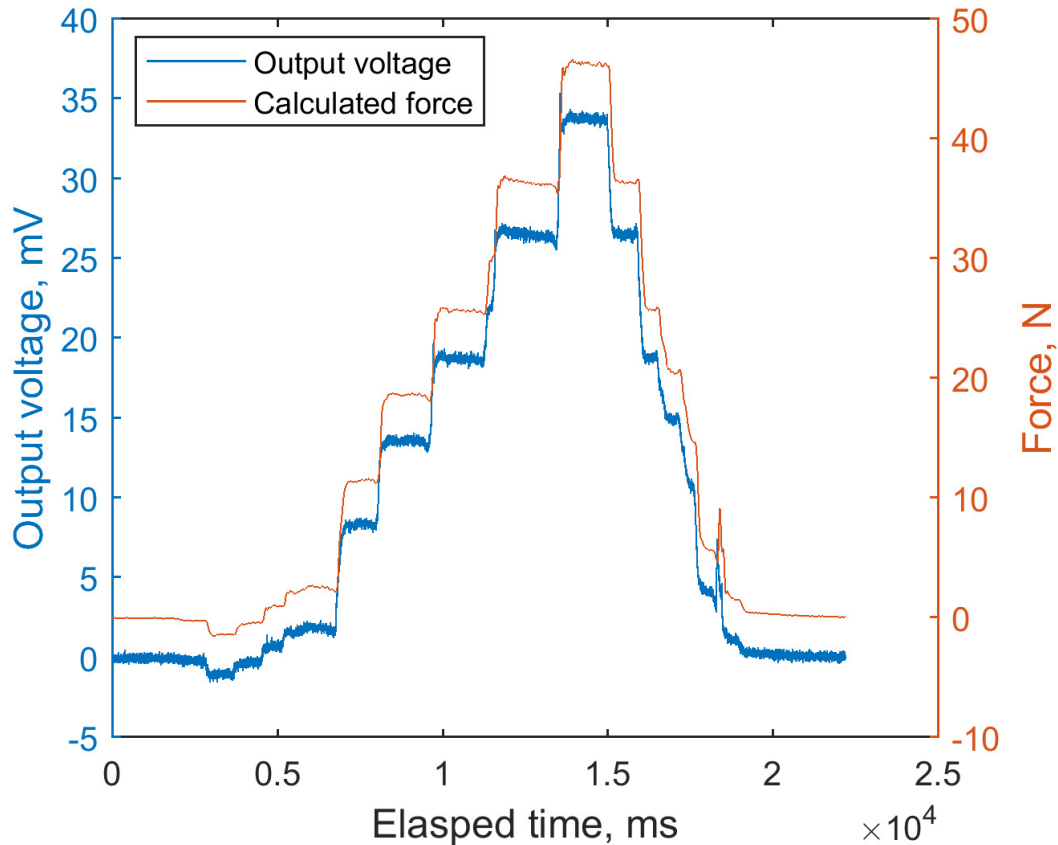
Figure 6-17 Pressing tests by z-axis rig

To evaluate the influence of the added PU on the shear force behavior, qualitative tests have been performed by rubbing the ruggedized sensor between the thumb and index finger. Results (see Figure 6-18) have demonstrated that the ability of sensing the shear force has been partially preserved, as negative spikes within the dash line rectangle could be observed from the plot. This was owing to the lateral deformation from the PU caused by frictions could be sensed by the mesa buried inside the PU bump. The conservation of the force orientation related performance could be utilized to package a multi-axis tactile sensor in the future and to uplift potentials for more applications regarding multi-axis force measurements.
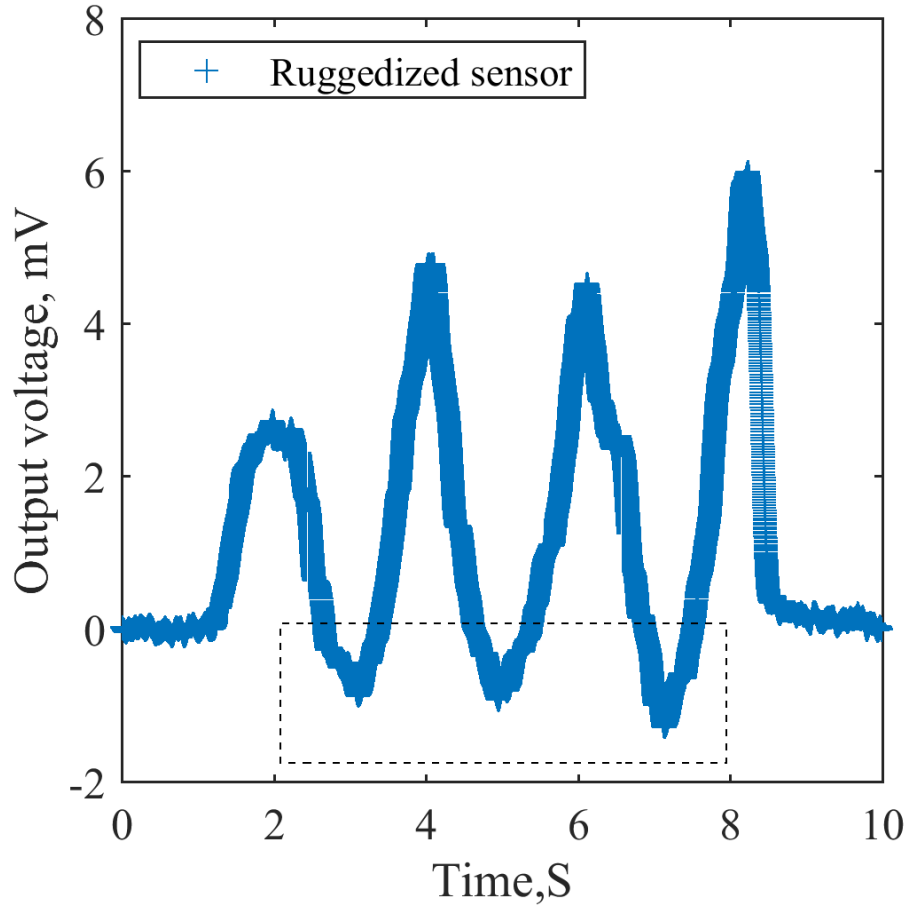
Figure 6-18 Rubbing the ruggedized sensor by the thumb and index finer

Signal-to-Noise ratio could be assessed by the equation: SNR = Psignal/Pnoise, which is the power of the signal divided by the power of the noise. As shown in Figure 6-19, the additive polymers on the tactile sensor have no observable influence in terms of signal quality comparing with that of pristine piezoresistive devices. The noise signal level could be observed as around 0.75 mV before the filtering and 0.2 mV afterwards, which presented the SNR values of 104 FS and 390 FS.
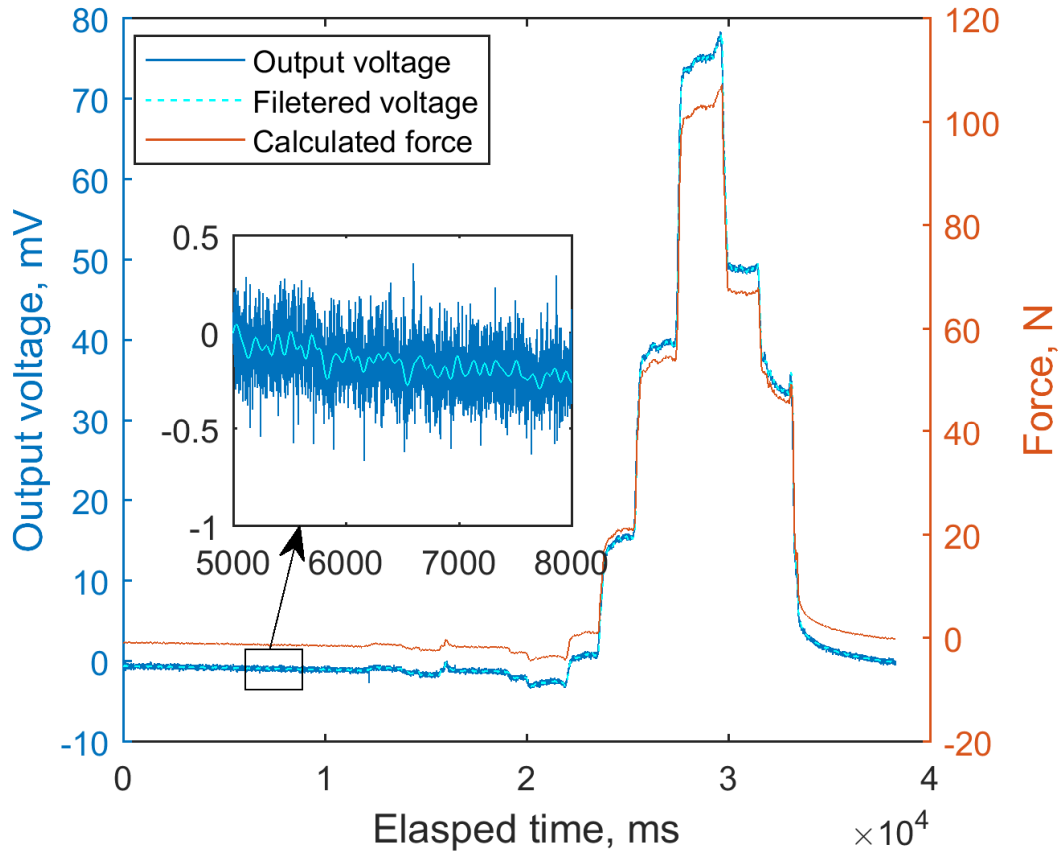
Figure 6-19 SNR analysis of ruggedized sensor by PU

# Chapter 7.  Conclusion and future work

## 7.1 Contributions of this work

The feasibility of a normal force tactile sensor array has been investigated using the finite element method. The response characteristics of the sensor array to normal forces at various locations has been analyzed based on geometric parameters such as pitches, membrane size, mesa diameter, etc.

The implementation of the normal force tactile sensor array has been performed by developing prototypes packaged as a $2 \times 2$ configuration. Both the tactile force and location information have been quantified using a lookup table approach based on the characterization fingerprints of each tactel at various locations on the sensor array.

A multi-axis tactile sensor array has been studied numerically and experimentally through a size of 60 mm $\times$ 60 mm prototyped system which utilized $2 \times 2$ multi-axis tactile sensors. Characterizations and tests have been performed to evaluate the performance with respect to sensing both the multi-axis tactile force and location information.

This work established a fabrication and packaging protocol for developing both the normal and multi-axis sensor arrays using SOI wafers and the PCBoG solution, accomplishing a compacter size and superior assembling coplanarity.

A methodology on tuning the range of tactile sensors by introducing different ruggedization materials in the packaging process has been proposed. This sheds light on diversifying applications for the physiological signals monitoring, providing different perspective on the development path of MEMS tactile devices.

## 7.2 Future work

The prototype in this work has a functional area with a size of 60 mm $\times$ 60 mm, which reaches the width of a common smart phone. Various devices such as tablets, control panels have larger size displays, which requires an expansion of the prototype.

The algorithm for solving the location and force information could be improved with more mathematic tools to achieving a higher efficiency for analyzing data "on-the-fly", such as trained artificial neural networks, etc.

The emphasis of this work has been addressed as providing the solution-in-one to measure the multi-axis tactile force and the tactile location. However, its application is still limited with one tactile point. Future work could have more efforts on decoupling more tactile points with the current configuration or utilizing the tactile sensor in other form (hetero-geometric) of sensor arrays for multi-point measurements.

With the presentation of Chapter 6, the author demonstrated several applications by tuning the sensitivity of the force sensor without involving changes on the mask design and the fabrication flow of the development. This methodology is worthy of more attentions for exploring the deployments of the multi-axis tactile sensor to diverse scenarios.

# Reference

[1]     H. Yousef, M. Boukallel, and K. Althoefer, "Tactile sensing for dexterous in-hand manipulation in robotics—A review," *Sensors and Actuators A: Physical,* vol. 167, pp. 171-187, 2011.

[2]     M. H. Lee and H. R. Nicholls, "Review Article Tactile sensing for mechatronics—a state of the art survey," *Mechatronics,* vol. 9, pp. 1-31, 2/1 1999.

[3]     S. Gao, V. Arcos, and A. Nathan, "Piezoelectric vs. Capacitive Based Force Sensing in Capacitive Touch Panels," *IEEE Access,* vol. 4, pp. 3769-3774, 2016.

[4]     A. Chaykina, S. Griebel, and L. Zentner, "Design, fabrication, and characterization of a compliant shear force sensor for a human–machine interface," *Sensors and Actuators A: Physical,* vol. 246, pp. 91-101, 8/1 2016.

[5]     J. Calpe-Maravilla, I. Medina, M. J. Martinez, and A. Carbajo, "Dual touch and gesture recognition in 4-wire resistive touchscreens," *2014 IEEE SENSORS,* pp. 787-790, 2-5 Nov. 2014.

[6]     W. Westerman, J. G. Elias, and A. Hedge, "Multi-Touch: A New Tactile 2-D Gesture Interface for Human-Computer Interaction," *Proceedings of the Human Factors and Ergonomics Society Annual Meeting,* vol. 45, pp. 632-636, October 1 2001.

[7]     L. John, W. Ying, and T. S. Huang, "Modeling the constraints of human hand motion," presented at the Proceedings of Workshop on Human Motion, 2000.

[8]     Y. Nakai, S. kudo, R. Okazaki, and H. Kajimoto, "Tangential force input for touch panels using bezel-aligned elastic pillars and a transparent sheet," presented at the Proceedings of the adjunct publication of the 27th annual ACM symposium on User interface software and technology, Honolulu, Hawaii, USA, 2014.

[9]     B. Lee, H. Lee, S.-C. Lim, H. Lee, S. Han, and J. Park, "Evaluation of human tangential force input performance," presented at the Proceedings of the SIGCHI Conference on Human Factors in Computing Systems, Austin, Texas, USA, 2012.

[10]    I. Campbell and R. Diestelhorst, "Microelectromechanical load sensor and methods of manufacturing the same," United States Patent US 20140007705A1, 2014.

[11]    Y. Nakai, S. Kudo, R. Okazaki, H. Kajimoto, and H. Kuribayashi, "Detection of tangential force for a touch panel using shear deformation of the gel," presented at the CHI '14 Extended Abstracts on Human Factors in Computing Systems, Toronto, Ontario, Canada, 2014.

[12]    C. Xiang-Cheng, L. Jia-Yi, G. Ren-Long, C. Jie, and L. Long-Tu, "Design and analysis of a piezoelectric material based touch screen with additional pressure and its acceleration measurement functions," *Smart Materials and Structures,* vol. 22, p. 125008, 2013.

[13]    B. Huppi, M. Grunthaner, J. Elias, S. Filliz, and S. Hotelling, "Ultrasound-based force sensing and touch sensing," United States Patent US 20170344143A1, 2017.

[14]    M. I. Tiwana, S. J. Redmond, and N. H. Lovell, "A review of tactile sensing technologies with applications in biomedical engineering," *Sensors and Actuators A: Physical,* vol. 179, pp. 17-31, 2012.

[15]    S. Ko, H. Shin, J. Lee, H. Jang, B. C. So, I. Yun*, et al.*, "Low noise capacitive sensor for multi-touch mobile handset's applications," in *2010 IEEE Asian Solid-State Circuits Conference*, 2010, pp. 1-4.

[16]    H.-K. Kim, S. Lee, and K.-S. Yun, "Capacitive tactile sensor array for touch screen application," *Sensors and Actuators A: Physical,* vol. 165, pp. 2-7, 2011.

[17] C.-Y. Huang, L. Lou, A. J. Danner, and C. Lee, "Transparent force sensing arrays with low power consumption using liquid crystal arrays," *Sensors and Actuators A: Physical,* vol. 190, pp. 136-140, 2/1 2013.

[18] K. Kim, K. R. Lee, W. H. Kim, K.-B. Park, T.-H. Kim, J.-S. Kim*, et al.*, "Polymer-based flexible tactile sensor up to 32×32 arrays integrated with interconnection terminals," *Sensors and Actuators A: Physical,* vol. 156, pp. 284-291, 2009.

[19] P. Saccomandi, L. Zollo, A. L. Ciancio, E. Schena, A. Fasano, C. M. Oddo*, et al.*, "Tactile piezoresistive sensors for robotic application: Design and metrological characterization," *2017 IEEE International Instrumentation and Measurement Technology Conference* pp. 1-6, 22-25 May 2017.

[20] W. Sang Min, K. Hoon-Sik, L. Nanshu, K. Dae-Gon, C. Del Solar, T. Duenas*, et al.*, "Piezoresistive Strain Sensors and Multiplexed Arrays Using Assemblies of Single-Crystalline Silicon Nanoribbons on Plastic Substrates," *Electron Devices, IEEE Transactions on,* vol. 58, pp. 4074-4078, 2011.

[21] A. Merve, S. Marco, A. Kossi, and P. Jamie, "Development and characterization of silicone embedded distributed piezoelectric sensors for contact detection," *Smart Materials and Structures,* vol. 24, p. 075030, 2015.

[22] W. Zheng, L. Wei, H. Qing, W. Ning, W. Chenxi, Y. Tingfang*, et al.*, "The design of infrared touch screen based on MCU," presented at the 2011 IEEE International Conference on Information and Automation, 2011.

[23] R. A. Brookhuis, T. S. J. Lammerink, and R. J. Wiegerink, "Differential capacitive sensing circuit for a multi-electrode capacitive force sensor," *Sensors and Actuators A: Physical,* vol. 234, pp. 168-179, 10/1 2015.

[24] Y. Zhao, Y. Zhao, and M. Zhao, "Novel force sensor based on a couple of fiber Bragg gratings," *Measurement,* vol. 38, pp. 30-33, 2005.

[25] A. Tibrewala, A. Phataralaoha, and S. Büttgenbach, "Development, fabrication and characterization of a 3D tactile sensor," *Journal of Micromechanics and Microengineering,* vol. 19, p. 125005, 2009.

[26] C.-C. Wen and W. Fang, "Tuning the sensing range and sensitivity of three axes tactile sensors using the polymer composite membrane," *Sensors and Actuators A: Physical,* vol. 145–146, pp. 14-22, 2008.

[27] S. Bae, H. Kim, Y. Lee, X. Xu, J.-S. Park, Y. Zheng*, et al.*, "Roll-to-roll production of 30-inch graphene films for transparent electrodes," *Nat Nano,* vol. 5, pp. 574-578, 2010.

[28] J. A. Muntjes, J. Hafner, M. Gortz, and W. Mokwa, "Studies on thinned flexible integrated capacitive pressure sensors in tactile sensor arrays for the use in robotics and prosthetics," presented at the 17th International Conference on Solid-State Sensors, Actuators and Microsystems 2013.

[29] M. Sohgawa, D. Hirashima, Y. Moriguchi, T. Uematsu, W. Mito, T. Kanashima*, et al.*, "Tactile sensor array using microcantilever with nickel–chromium alloy thin film of low temperature coefficient of resistance and its application to slippage detection," *Sensors and Actuators A: Physical,* vol. 186, pp. 32-37, 2012.

[30] T. Seiichi, T. Tomoyuki, M. Masato, I. Eiji, M. Kiyoshi, and S. Isao, "Transparent conductive-polymer strain sensors for touch input sheets of flexible displays," *Journal of Micromechanics and Microengineering,* vol. 20, p. 075017, 2010.

[31] G. Liang, Y. Wang, D. Mei, K. Xi, and Z. Chen, "Flexible Capacitive Tactile Sensor Array With Truncated Pyramids as Dielectric Layer for Three-Axis Force Measurement," *Journal of Microelectromechanical Systems,* vol. 24, pp. 1510-1519, 2015.

[32] D. J. Lipomi, M. Vosgueritchian, B. C. K. Tee, S. L. Hellstrom, J. A. Lee, C. H. Fox*, et al.*, "Skin-like pressure and strain sensors based on transparent elastic films of carbon nanotubes," *Nat Nano,* vol. 6, pp. 788-792, 2011.

[33] V. V. Meleshko, "Selected topics in the history of the two-dimensional biharmonic problem," *Applied Mechanics Reviews,* vol. 56, pp. 33-85, 2003.

[34] L. D. Harmon, "Automated Tactile Sensing," *The International Journal of Robotics Research,* vol. 1, pp. 3-32, June 1 1982.

[35] K. Noda, K. Hoshino, K. Matsumoto, and I. Shimoyama, "A shear stress sensor for tactile sensing with the piezoresistive cantilever standing in elastic material," *Sensors and Actuators A: Physical,* vol. 127, pp. 295-301, 3/13/ 2006.

[36] N. Jackson and J. Muthuswamy, "Flexible Chip-Scale Package and Interconnect for Implantable MEMS Movable Microelectrodes for the Brain," *Microelectromechanical Systems, Journal of,* vol. 18, pp. 396-404, 2009.

[37] A. J. T. Teo, A. Mishra, I. Park, Y.-J. Kim, W.-T. Park, and Y.-J. Yoon, "Polymeric Biomaterials for Medical Implants and Devices," *ACS Biomaterials Science & Engineering,* vol. 2, pp. 454-472, 04/11 2016.

[38] S. Marco, J. Samitier, O. Ruiz, J. R. Morante, and J. Esteve, "High-performance piezoresistive pressure sensors for biomedical applications using very thin structured membranes," *Measurement Science and Technology,* vol. 7, p. 1195, 1996.

[39] L. Hyung-kew, C. Sun-Il, and Y. Euisik, "A Flexible Polymer Tactile Sensor: Fabrication and Modular Expandability for Large Area Deployment," *Microelectromechanical Systems, Journal of,* vol. 15, pp. 1681-1686, 2006.

[40] K. Ueki, A. Moroi, M. Sotobori, Y. Ishihara, K. Marukawa, R. Iguchi*, et al.*, "Evaluation of recovery in lip closing pressure and occlusal force and contact area after orthognathic surgery," *Journal of Cranio-Maxillofacial Surgery,* vol. 42, pp. 1148-1153, 2014.

[41] J. G. da Silva, A. A. de Carvalho, and D. D. da Silva, "A strain gauge tactile sensor for finger-mounted applications," *Instrumentation and Measurement, IEEE Transactions on,* vol. 51, pp. 18-22, 2002.

[42] R. A. Brookhuis, H. Droogendijk, M. J. d. Boer, R. G. P. Sanders, T. S. J. Lammerink, R. J. Wiegerink*, et al.*, "Six-axis force–torque sensor with a large range for biomechanical applications," *Journal of Micromechanics and Microengineering,* vol. 24, p. 035015, 2014.

[43] L. Wang and D. J. Beebe, "A silicon-based shear force sensor: development and characterization," *Sensors and Actuators A: Physical,* vol. 84, pp. 33-44, 8/1 2000.

[44] S. Yu, J. N. Bradley, P. P. David, and E. Eniko, "A bulk microfabricated multi-axis capacitive cellular force sensor using transverse comb drives," *Journal of Micromechanics and Microengineering,* vol. 12, p. 832, 2002.

[45] F. Beyeler, S. Muntwyler, and B. J. Nelson, "A Six-Axis MEMS Force Torque Sensor With Micro-Newton and Nano-Newtonmeter Resolution," *Microelectromechanical Systems, Journal of,* vol. 18, pp. 433-441, 2009.

[46] M. Gnerlich, S. F. Perry, and S. Tatic-Lucic, "A submersible piezoresistive MEMS lateral force sensor for a diagnostic biomechanics platform," *Sensors and Actuators A: Physical,* vol. 188, pp. 111-119, 2012.

[47] C. Gehin, C. Barthod, and Y. Teisseyre, "Design and characterisation of a new force resonant sensor," *Sensors and Actuators A: Physical,* vol. 84, pp. 65-69, 8/1/ 2000.

[48] X. J. Zhang, S. Zappe, R. W. Bernstein, O. Sahin, C. C. Chen, M. Fish*, et al.*, "Micromachined silicon force sensor based on diffractive optical encoders for characterization of microinjection," *Sensors and Actuators A: Physical,* vol. 114, pp. 197-203, 9/1/ 2004.

[49] Z. Chi and K. Shida, "A new multifunctional tactile sensor for three-dimensional force measurement," *Sensors and Actuators A: Physical,* vol. 111, pp. 172-179, 3/15/ 2004.

[50] W. Wu, X. Wen, and Z. L. Wang, "Taxel-Addressable Matrix of Vertical-Nanowire Piezotronic Transistors for Active and Adaptive Tactile Imaging," *Science,* vol. 340, pp. 952-957, 2013.

[51] C. Roke, C. Melhuish, T. Pipe, D. Drury, and C. Chorley, "Lump localisation through a deformation-based tactile feedback system using a biologically inspired finger sensor," *Robotics and Autonomous Systems,* vol. 60, pp. 1442-1448, 2012.

[52] T. Nagao, Y. Hatamura, and H. Sato, "Development of a Flexible Grinding System with Six-Axis Force Sensor for Curved Surfaces," *CIRP Annals - Manufacturing Technology,* vol. 36, pp. 215-218, 1987.

[53] C. Yuan, L.-P. Luo, Q. Yuan, J. Wu, R.-J. Yan, H. Kim*, et al.*, "Development and evaluation of a compact 6-axis force/moment sensor with a serial structure for the humanoid robot foot," *Measurement,* vol. 70, pp. 110-122, 2015.

[54] M.-K. Kang, S. Lee, and J.-H. Kim, "Shape optimization of a mechanically decoupled six-axis force/torque sensor," *Sensors and Actuators A: Physical,* vol. 209, pp. 41-51, 3/1/ 2014.

[55] W. L. Jin and C. D. Mote Jr, "Development and calibration of a sub-millimeter three-component force sensor," *Sensors and Actuators A: Physical,* vol. 65, pp. 89-94, 2/15/ 1998.

[56] C. Pang, G.-Y. Lee, T.-i. Kim, S. M. Kim, H. N. Kim, S.-H. Ahn*, et al.*, "A flexible and highly sensitive strain-gauge sensor using reversible interlocking of nanofibres," *Nat Mater,* vol. 11, pp. 795-801, 2012.

[57] K. Lee, S. S. Lee, J. A. Lee, K.-C. Lee, and S. Ji, "Carbon nanotube film piezoresistors embedded in polymer membranes," *Applied Physics Letters,* vol. 96, p. 013511, 2010.

[58] D. M. Vogt, P. Yong-Lae, and R. J. Wood, "Design and Characterization of a Soft Multi-Axis Force Sensor Using Embedded Microfluidic Channels," *Sensors Journal, IEEE,* vol. 13, pp. 4056-4064, 2013.

[59] G.-S. Kim, D.-I. Kang, and S.-H. Rhee, "Design and fabrication of a six-component force/moment sensor," *Sensors and Actuators A: Physical,* vol. 77, pp. 209-220, 11/2/ 1999.

[60] J. Engel, J. Chen, Z. Fan, and C. Liu, "Polymer micromachined multimodal tactile sensors," *Sensors and Actuators A: Physical,* vol. 117, pp. 50-61, 1/3/ 2005.

[61] Y.-M. Huang, N.-C. Tsai, and J.-Y. Lai, "Development of tactile sensors for simultaneous, detection of normal and shear stresses," *Sensors and Actuators A: Physical,* vol. 159, pp. 189-195, 2010.

[62] M. Shikida, T. Shimizu, K. Sato, and K. Itoigawa, "Active tactile sensor for detecting contact force and hardness of an object," *Sensors and Actuators A: Physical,* vol. 103, pp. 213-218, 1/15/ 2003.

[63] T. Mei, W. J. Li, Y. Ge, Y. Chen, L. Ni, and M. H. Chan, "An integrated MEMS three-dimensional tactile sensor with large force range," *Sensors and Actuators A: Physical,* vol. 80, pp. 155-162, 3/10/ 2000.

[64] A. Tibrewala, A. Phataralaoha, and S. Büttgenbach, "Simulation, fabrication and characterization of a 3D piezoresistive force sensor," *Sensors and Actuators A: Physical,* vol. 147, pp. 430-435, 10/3/ 2008.

[65] M. Doelle, C. Peters, P. Ruther, and O. Paul, "Piezo-FET stress-sensor arrays for wire-bonding characterization," *Microelectromechanical Systems, Journal of,* vol. 15, pp. 120-130, 2006.

[66] D. Dzung Viet, T. Toriyama, J. Wells, and S. Sugiyama, "Micro force-moment sensor with six-degree of freedom," presented at the Proceedings of 2001 International Symposium on Micromechatronics and Human Science,, 2001.

[67] E. T. Enikov and B. J. Nelson, "Three-dimensional microfabrication for a multi-degree-of-freedom capacitive force sensor using fibre-chip coupling," *Journal of Micromechanics and Microengineering,* vol. 10, p. 492, 2000.

[68] M. Leineweber, G. Pelz, M. Schmidt, H. Kappert, and G. Zimmer, "New tactile sensor chip with silicone rubber cover," *Sensors and Actuators A: Physical,* vol. 84, pp. 236-245, 9/1/ 2000.

[69] S. H. Jeong, S. Zhang, K. Hjort, J. Hilborn, and Z. Wu, "PDMS-Based Elastomer Tuned Soft, Stretchable, and Sticky for Epidermal Electronics," *Advanced Materials,* vol. 28, pp. 5830-5836, 2016.

[70] P. Valdastri, S. Roccella, L. Beccai, E. Cattin, A. Menciassi, M. C. Carrozza*, et al.*, "Characterization of a novel hybrid silicon three-axial force sensor," *Sensors and Actuators A: Physical,* vol. 123–124, pp. 249-257, 9/23/ 2005.

[71] H. M. H. Gharib, "An investigation of using n-Si piezoresistive behavior to develop a three-dimensional stress sensing rosette," Doctor of Philosophy Department of Mechanical Engineering University of Alberta, 2013.

[72] C. S. Smith, "Piezoresistance Effect in Germanium and Silicon," *Physical Review,* vol. 94, pp. 42-49, 04/01/ 1954.

[73] O. N. Tufte and E. L. Stelzer, "Piezoresistive Properties of Silicon Diffused Layers," *Journal of Applied Physics,* vol. 34, pp. 313-318, 1963.

[74] O. N. Tufte and E. L. Stelzer, "Piezoresistive Properties of Heavily Doped n-Type Silicon," *Physical Review,* vol. 133, pp. A1705-A1716, 03/16/ 1964.

[75] Y. Kanda and Y. Kanda, "A graphical representation of the piezoresistance coefficients in silicon," *IEEE Transactions on Electron Devices,* vol. 29, pp. 64-70, 1982.

[76] Y. Kanda, "Piezoresistance effect of silicon," *Sensors and Actuators A: Physical,* vol. 28, pp. 83-91, 1991.

[77] Y. Kanda and K. Suzuki, "Origin of the shear piezoresistance coefficient $\pi_{44}$ of n-type silicon," *Physical Review B,* vol. 43, pp. 6754-6756, 03/15/ 1991.

[78] Y. Kanda and M. Migitaka, "Effect of mechanical stress on the offset voltages of hall devices in Si IC," *physica status solidi (a),* vol. 35, pp. K115-K118, 1976.

[79] M. Doelle, D. Mager, P. Ruther, and O. Paul, "Geometry optimization for planar piezoresistive stress sensors based on the pseudo-Hall effect," *Sensors and Actuators A: Physical,* vol. 127, pp. 261-269, 3/13/ 2006.

[80] N. Kentaro, O. Hiroaki, I. Eiji, M. Kiyoshi, and S. Isao, "Flexible tactile sensor for shear stress measurement using transferred sub-µm-thick Si piezoresistive cantilevers," *Journal of Micromechanics and Microengineering,* vol. 22, p. 115025, 2012.

[81] A. Partridge, J. K. Reynolds, B. W. Chui, E. M. Chow, A. M. Fitzgerald, L. Zhang, *et al.*, "A high-performance planar piezoresistive accelerometer," *Journal of Microelectromechanical Systems,* vol. 9, pp. 58-66, 2000.

[82] A. L. Roy, H. Sarkar, A. Dutta, and T. K. Bhattacharyya, "A high precision SOI MEMS–CMOS ±4g piezoresistive accelerometer," *Sensors and Actuators A: Physical,* vol. 210, pp. 77-85, 04/01/ 2014.

[83] Y. Kanda and A. Yasukawa, "Hall-effect devices as strain and pressure sensors," *Sensors and Actuators,* vol. 2, pp. 283-296, 1981.

[84] Y. Kanda and A. Yasukawa, "Optimum design considerations for silicon piezoresistive pressure sensors," *Sensors and Actuators A: Physical,* vol. 62, pp. 539-542, 1997.

[85] M.-H. Bao, W.-J. Qi, and Y. Wang, "Geometric design rules of four-terminal gauge for pressure sensors," *Sensors and Actuators,* vol. 18, pp. 149-156, 6/15/ 1989.

[86] M. Bao and Y. Wang, "Analysis and design of a four-terminal silicon pressure sensor at the centre of a diaphragm," *Sensors and Actuators,* vol. 12, pp. 49-56, 1987.

[87] A. V. Gridchin and V. A. Gridchin, "The four-terminal piezotransducer: theory and comparison with piezoresistive bridge," *Sensors and Actuators A: Physical,* vol. 58, pp. 219-223, 3/30/ 1997.

[88] A. V. Gridchin, "The four-terminal silicon piezotransducer: history and future," presented at the Proceedings of 5th Annual International Siberian Workshop on Electron Devices and Materials, 2004.

[89] A. V. Gridchin, "A three-terminal silicon piezotransducer: general consideration and estimation of sensitivity," presented at the Proceedings 4th Annual Siberian Russian Workshop on Electron Devices and Materials 2003.

[90] G. O. Coraucci, M. R. Finardi, and F. Fruett, "A Multi-Terminal Pressure Sensor with enhanced sensitivity," *TRANSDUCERS 2009. International Solid-State Sensors, Actuators and Microsystems Conference,* pp. 1122-1125, 21-25 June 2009.

[91] G. Coraucci and F. Fruett, "A theoretical study of a novel multi-terminal pressure sensor based on the transversal piezoresistive effect," *ECS Transactions,* vol. 9, pp. 561-569, 2007.

[92] U. Gowrishetty, K. M. Walsh, J. Aebersold, D. Jackson, H. Millar, and T. Roussel, "Development of Ultra-Miniaturized Piezoresistive Pressure Sensors for Biomedical Applications," presented at the 17th Biennial University/Government/Industry Micro/Nano Symposium, 2008.

[93] D. C. Benfield, "A Study of Six-Axis MEMS Sensors for Load Detection in Biomedical Applications," Doctor of Philosophy Thesis, Mechanical Engineering University of Alberta, 2012.

[94] D. Benfield, S. Yue, E. Lou, and W. A. Moussa, "Design and calibration of a six-axis MEMS sensor array for use in scoliosis correction surgery," *Journal of Micromechanics and Microengineering,* vol. 24, p. 085008, 2014.

[95] D. Benfield and W. A. Moussa, "Piezoresistive load sensor," United States Patent US 20130239700A1, 2013.

[96] W. A. Moussa and D. Benfield, "Piezoresistive load sensor," Canada Patent CA2806486C, 2017.

[97] H. H. Gharib and W. A. Moussa, "On the Feasibility of a New Approach for Developing a Piezoresistive 3D Stress Sensing Rosette," *IEEE Sensors Journal,* vol. 11, pp. 1861-1871, 2011.

[98]  A. Mohammed, W. Moussa, and E. Lou, "High-Performance Piezoresistive MEMS Strain Sensor with Low Thermal Sensitivity," *Sensors,* vol. 11, p. 1819, 2011.

[99]  P. Kopystynski and E. Obermeier, "An interchangeable silicon pressure sensor with on-chip compensation circuitry," *Sensors and Actuators,* vol. 18, pp. 239-245, 07/01/ 1989.

[100]  J. Li, G. Hu, Y. Zhou, C. Zou, W. Peng, and J. Alam SM, "Study on Temperature and Synthetic Compensation of Piezo-Resistive Differential Pressure Sensors by Coupled Simulated Annealing and Simplex Optimized Kernel Extreme Learning Machine," *Sensors,* vol. 17, p. 894, 2017.

[101]  C. Pramanik, T. Islam, and H. Saha, "Temperature compensation of piezoresistive micro-machined porous silicon pressure sensor by ANN," *Microelectronics Reliability,* vol. 46, pp. 343-351, 02/01/ 2006.

[102]  M. E. Gibari, C. L. Bleis, G. Lirzin, B. Lauzier, S. Ginestar, J. Tissier*, et al.*, "Thermal drift compensation of piezoresistive implantable blood pressure sensors with low cost analog solutions," presented at the 29th International Conference on Microelectronics, 2017.

[103]  D. Lee, S. Cho, H. Ryu, Y. Pu, S. Yoo, M. Lee*, et al.*, "A Highly Linear, AEC-Q100 Compliant Signal Conditioning IC for Automotive Piezo-Resistive Pressure Sensors," *IEEE Transactions on Industrial Electronics,* vol. PP, pp. 1-1, 2018.

[104]  H. R. Nicholls and M. H. Lee, "A Survey of Robot Tactile Sensing Technology," *The International Journal of Robotics Research,* vol. 8, pp. 3-30, 1989.

[105]  E. A. Johnson, "Touch Displays: A Programmed Man-Machine Interface," *Ergonomics,* vol. 10, pp. 271-277, 03/01 1967.

[106]  H. Tsujioka, K. Hashimoto, and N. Shiraishi, "Coordinates input device," United States Patent US005.518078A, May 21, 1996

[107]  D. M. Usher, "Comparison of a touch-sensitive VDU and computer-aided keypad for plant control," *Displays,* vol. 4, pp. 157-161, 1983.

[108]  W. H. Ko and Q. Wang, "Touch mode capacitive pressure sensors," *Sensors and Actuators A: Physical,* vol. 75, pp. 242-251, 06/08/ 1999.

[109]  J. Y. Han, "Low-cost multi-touch sensing through frustrated total internal reflection," presented at the Proceedings of the 18th annual ACM symposium on User interface software and technology, Seattle, WA, USA, 2005.

[110]  M. Takasaki, H. Kotani, T. Mizuno, and T. Nara, "Transparent surface acoustic wave tactile display," presented at the 2005 IEEE/RSJ International Conference on Intelligent Robots and Systems, 2005.

[111]  Y. Tae-Heon, K. Sang-Youn, K. Chong-Hui, K. Dong-Soo, and W. J. Book, "Development of a miniature pin-array tactile module using elastic and electromagnetic force for mobile devices," presented at the EuroHaptics conference and Symposium on Haptic Interfaces for Virtual Environment and Teleoperator Systems. World Haptics. Third Joint, 2009.

[112]  M. Hirsch, D. Lanman, H. Holtzman, and R. Raskar, "BiDi screen: a thin, depth-sensing LCD for 3D interaction using light fields," *ACM Trans. Graph.,* vol. 28, pp. 1-9, 2009.

[113]  R. N. Aguilar and G. C. M. Meijer, "Fast interface electronics for a resistive touch-screen," presented at the Proceedings of IEEE Sensors, 2002.

[114]  J. Li, J. Liang, L. Li, F. Ren, W. Hu, J. Li*, et al.*, "Healable Capacitive Touch Screen Sensors Based on Transparent Composite Electrodes Comprising Silver Nanowires and a Furan/Maleimide Diels–Alder Cycloaddition Polymer," *ACS Nano,* vol. 8, pp. 12874-12882, 12/23 2014.

[115] H. Tian, Y. Yang, D. Xie, T.-L. Ren, Y. Shu, C.-J. Zhou, *et al.*, "A novel flexible capacitive touch pad based on graphene oxide film," *Nanoscale,* vol. 5, pp. 890-894, 2013.

[116] T. H. Hwang, W. H. Cui, I. S. Yang, and O. K. Kwon, "A highly area-efficient controller for capacitive touch screen panel systems," *IEEE Transactions on Consumer Electronics,* vol. 56, pp. 1115-1122, 2010.

[117] P. Dietz and D. Leigh, "DiamondTouch: a multi-user touch technology," presented at the Proceedings of the 14th annual ACM symposium on User interface software and technology, Orlando, Florida, 2001.

[118] H. R. Kim, Y. K. Choi, S. H. Byun, S. W. Kim, K. H. Choi, H. Y. Ahn, *et al.*, "A mobile-display-driver IC embedding a capacitive-touch-screen controller system," presented at the IEEE International Solid-State Circuits Conference 2010.

[119] L. M. Faller, S. Mühlbacher-Karrer, and H. Zangl, "Inkjet-printing rapid prototyping of a robust and flexible capacitive touch panel," presented at the IEEE SENSORS, 2016.

[120] S. Smith and B. Sherwood, "Educational uses of the PLATO computer system," *Science,* vol. 192, pp. 344-352, April 23 1976.

[121] A. M. Hlady, "A touch sensitive X-Y position encoder for computer input," presented at the Proceedings of joint computer conference, Las Vegas, Nevada, 1969.

[122] J. A. Paradiso, K. Hsiao, J. Strickon, J. Lifton, and A. Adler, "Sensor systems for interactive surfaces," *IBM Systems Journal,* vol. 39, pp. 892-914, 2000.

[123] Z. L. Wang, "Triboelectric Nanogenerators as New Energy Technology for Self-Powered Systems and as Active Mechanical and Chemical Sensors," *ACS Nano,* vol. 7, pp. 9533-9557, 11/26/ 2013.

[124] Z. Wang, R. Jiang, G. Li, Y. Chen, Z. Tang, Y. Wang, *et al.*, "Flexible Dual-Mode Tactile Sensor Derived from Three-Dimensional Porous Carbon Architecture," *ACS Applied Materials & Interfaces,* vol. 9, pp. 22685-22693, 07/12 2017.

[125] C. Harrison and S. Hudson, "Using shear as a supplemental two-dimensional input channel for rich touchscreen interaction," presented at the Proceedings of the SIGCHI Conference on Human Factors in Computing Systems, Austin, Texas, USA, 2012.

[126] K. Salah, "A TSV to TSV, A TSV to Metal interconnects, and A TSV to active device coupling capacitance: Analysis and recommendations," presented at the 10th International Conference on Design & Technology of Integrated Systems in Nanoscale Era, 2015.

[127] N. Ranganathan, K. Prasad, N. Balasubramanian, and K. L. Pey, "A study of thermo-mechanical stress and its impact on through-silicon vias," *Journal of Micromechanics and Microengineering,* vol. 18, p. 075018, 2008.

[128] Y. Qiu, S. Yue, W. A. Moussa, and P. Mousavi, "Vacuum-Assisted Through Silicon via Filling Method With Ag-Based Epoxy," *IEEE Transactions on Components, Packaging and Manufacturing Technology,* vol. 6, pp. 1475-1481, 2016.

[129] M. Bouchoucha, L. L. Chapelon, P. Chausse, S. Moreau, and N. Sillon, "Through Silicon Via polymer filling for 3D-WLP applications," presented at the 3rd Electronics System Integration Technology Conference ESTC, 2010.

[130] M. Motoyoshi, "Through-Silicon Via (TSV)," *Proceedings of the IEEE,* vol. 97, pp. 43-48, 2009.

[131] M. J. Wolf, T. Dretschkow, B. Wunderle, N. Jurgensen, G. Engelmann, O. Ehrmann, *et al.*, "High aspect ratio TSV copper filling with different seed layers," presented at the 58th Electronic Components and Technology Conference, 2008.

[132] Y. K. Jee, J. Yu, K. W. Park, and T. S. Oh, "Zinc and Tin-Zinc Via-Filling for the Formation of Through-Silicon Vias in a System-in-Package," *Journal of Electronic Materials,* vol. 38, pp. 685-690, 05/01/ 2009.

[133] Y.-K. Ko, H. T. Fujii, Y. S. Sato, C.-W. Lee, and S. Yoo, "High-speed TSV filling with molten solder," *Microelectronic Engineering,* vol. 89, pp. 62-64, 01/01/ 2012.

[134] D. Pradeep, S. Jaakko, P. Harri, and M. Philippe, "The application of dry photoresists in fabricating cost-effective tapered through-silicon vias and redistribution lines in a single step," *Journal of Micromechanics and Microengineering,* vol. 21, p. 025020, 2011.

[135] B. David, L. Edmond, and A. M. Walied, "A packaging solution utilizing adhesive-filled TSVs and flip–chip methods," *Journal of Micromechanics and Microengineering,* vol. 22, p. 065009, 2012.

[136] S. Timoshenko, *Theory of plates and shells*, 2d ed. ed. New York :: McGraw-Hill, 1959.

[137] S. Yue, W. Moussa, and L. R. Williston, "Feasibility on a piezoresistive tactile normal force sensor array," *Applied Physics A,* vol. 116, pp. 409-414, 08/01 2014.

[138] B. David, Y. Shichao, L. Edmond, and A. M. Walied, "Design and calibration of a six-axis MEMS sensor array for use in scoliosis correction surgery," *Journal of Micromechanics and Microengineering,* vol. 24, p. 085008, 2014.

[139] R. Ziermann, J. von Berg, E. Obermeier, F. Wischmeyer, E. Niemann, H. Möller*, et al.*, "High temperature piezoresistive β-SiC-on-SOI pressure sensor with on chip SiC thermistor," *Materials Science and Engineering: B,* vol. 61-62, pp. 576-578, 07/30/ 1999.

[140] S. Yue and W. A. Moussa, "A Piezoresistive Tactile Sensor Array for Touchscreen Panels," *IEEE Sensors Journal,* vol. PP, pp. 1-1, 2017.

[141] S. Yue, Y. Qiu, and W. A. Moussa, "A Multi-Axis Tactile Sensor Array for Touchscreen Applications," *Journal of Microelectromechanical Systems,* vol. PP, pp. 1-11, 2018.

[142] M. J. Madou, *Fundamentals of Microfabrication: The Science of Miniaturization, Second Edition*: Taylor & Francis, 2002.

[143] R. C. Jaeger, *Introduction to microelectronic fabrication / Richard C. Jaeger*: Addison-Wesley Pub. Co., 1988.

[144] J. Lindhard, M. Scharff, and H. E. Schiøtt, "Range concepts and heavy ion ranges," *Det Kongelige Danske Videnskabernes Selskab,* vol. 33, 1963.

[145] K. L. Brown and G. W. Tautfest, "Faraday‐Cup Monitors for High‐Energy Electron Beams," *Review of Scientific Instruments,* vol. 27, pp. 696-702, 1956.

[146] M. Morita, T. Ohmi, E. Hasegawa, M. Kawakami, and M. Ohwada, "Growth of native oxide on a silicon surface," *Journal of Applied Physics,* vol. 68, pp. 1272-1281, 1990.

[147] S. L. Matlow and E. L. Ralph, "Ohmic Aluminum‐n‐Type Silicon Contact," *Journal of Applied Physics,* vol. 30, pp. 541-543, 1959.

[148] S. Franssila, *Introduction to microfabrication.*: Chichester, West Sussex, England ; Hoboken, NJ : John Wiley & Sons, 2nd ed., 2010.

[149] F. M. Smits, "Measurement of Sheet Resistivities with the Four-Point Probe," *Bell System Technical Journal,* vol. 37, pp. 711-718, 1958.

[150] J. E. Clayton, C. M. H. Chen, W. R. Cook, and F. A. Harrison, "Assembly technique for a fine-pitch, low-noise interface; Joining a CdZnTe pixel-array detector and custom VLSI chip with Au stud bumps and conductive epoxy," presented at the IEEE Nuclear Science Symposium, 2003.

[151] M. Rezaeisaray, J. Lueke, M. El Gowini, S. Yue, D. Raboud, and W. Moussa, "Overcoming Some of the Challenges in 3D Micro-Assembly Techniques to Package MEMS Devices," *Austin J Nanomed Nanotechnol,* vol. 2, p. 1032, 2014.

[152] C. Oprişan, V. Cârlescu, A. Barnea, P. Gh, D. N. Olaru, and P. Gh, "Experimental determination of the Young's modulus for the fingers with application in prehension systems for small cylindrical objects," *IOP Conference Series: Materials Science and Engineering,* vol. 147, p. 012058, 2016.

[153] S. Pal, *Biomaterials and Its Characterization.* Boston, MA: Springer US, 2014.

[154] D. J. Martin, L. A. Poole Warren, P. A. Gunatillake, S. J. McCarthy, G. F. Meijs, and K. Schindhelm, "Polydimethylsiloxane/polyether-mixed macrodiol-based polyurethane elastomers: biostability," *Biomaterials,* vol. 21, pp. 1021-1029, 05/01/ 2000.

[155] Q. Chen, J. D. Mangadlao, J. Wallat, A. De Leon, J. K. Pokorski, and R. C. Advincula, "3D Printing Biocompatible Polyurethane/Poly(lactic acid)/Graphene Oxide Nanocomposites: Anisotropic Properties," *ACS Applied Materials & Interfaces,* vol. 9, pp. 4015-4023, 02/01 2017.

[156] H. Lambrechts, E. De Baets, S. Fieuws, and G. Willems, "Lip and tongue pressure in orthodontic patients," *The European Journal of Orthodontics,* vol. 32, pp. 466-471, 8/1/ 2010.

[157] K. Nakatsuka, T. Adachi, T. Kato, M. Oishi, M. Murakami, Y. Okada*, et al.*, "Reliability of novel multidirectional lip‐closing force measurement system," *Journal of Oral Rehabilitation,* vol. 38, pp. 18-26, 2011.

[158] U. Thüer and B. Ingervall, "Pressure from the lips on the teeth and malocclusion," *Am J Orthod Dentofacial Orthop,* vol. 90, 1986.

[159] V. Luboz, E. Promayon, and Y. Payan, "Linear Elastic Properties of the Facial Soft Tissues Using an Aspiration Device: Towards Patient Specific Characterization," *Annals of Biomedical Engineering,* vol. 42, pp. 2369-2378, 11/01/ 2014.

[160] P. Boonvisut, R. Jackson, and M. C. Çavuşoğlu, "Estimation of Soft Tissue Mechanical Parameters from Robotic Manipulation Data," *IEEE International Conference on Robotics and Automation,* pp. 4667-4674, May 14-18 2012.

[161] I. Fine, A. V. Kaminsky, and L. Shenkman, "A new sensor for stress measurement based on blood flow fluctuations," presented at the SPIE BiOS, 2016.

[162] Y. Chen, L. Zhang, D. Zhang, and D. Zhang, "Wrist pulse signal diagnosis using modified Gaussian models and Fuzzy C-Means classification," *Medical Engineering & Physics,* vol. 31, pp. 1283-1289, 12/01/ 2009.

[163] P. Wang, W. Zuo, and D. Zhang, "A Compound Pressure Signal Acquisition System for Multichannel Wrist Pulse Signal Analysis," *IEEE Transactions on Instrumentation and Measurement,* vol. 63, pp. 1556-1565, 2014.

# Appendices

Appendix A 1 Resistance from test structures

| Location within SET | From Design* | Measured Resistance**, Ω | | | | |
|---|---|---|---|---|---|---|
| | | Resistor SET A | Resistor SET B | Resistor SET C | Resistor SET D | Resistor SET F*** |
| 1 | 350 | 468.91 | 678.97 | 369.99 | 353.63 | 5255.47 |
| 2 | 350 | 552.15 | 414.56 | 376.78 | 353.22 | 5285.71 |
| 3 | 450 | 461.07 | 462.96 | 459.65 | 441.61 | 471.70 |
| 4 | 450 | 458.29 | 451.55 | 453.16 | 444.55 | 485.54 |
| 5 | 50 | 62.07 | 29.81 | 38.58 | 34.66 | 31.97 |
| 6 | 50 | 78.23 | 44.71 | 34.09 | 7.04 | 42.57 |
| 7 | 50 | 76.17 | 71.47 | 64.94 | 48.61 | 79.66 |
| 8 | 50 | 228.22 | 190.39 | 28.30 | 71.64 | 1428.57 |
| 9 | 450 | 441.62 | 455.74 | 434.56 | 435.23 | 431.47 |
| 10 | 450 | 458.25 | 470.22 | 440.28 | 436.09 | 446.84 |
| 11 | 450 | 468.43 | 489.10 | 464.29 | 459.13 | 484.82 |
| 12 | 450 | 516.27 | 502.18 | 489.30 | 475.25 | 3478.26 |
| 13 | 950 | 942.62 | 933.06 | 940.70 | 931.17 | 930.23 |
| 14 | 950 | 962.34 | 959.33 | 978.72 | 950.41 | 967.40 |
| 15 | 950 | 991.38 | 985.01 | 1036.04 | 996.75 | 1041.90 |
| 16 | 2450 | 2486.49 | 2453.33 | 2516.78 | 2475.25 | 2450.98 |
| 17 | 2450 | 2513.66 | 2507.46 | 2622.38 | 2508.36 | 2551.02 |

*Assuming 50Ω.sq and using the mask design to estimate resistance. This excludes probe-to-probe resistance, contact resistance and Al track contributions.

**I-V curves were obtained for 85 resistor structures and the values above were taken from the I-V data just prior to current compliance being reached on the measurement unit. All I-V curves were linear up to the compliance limit (post ohmic anneal).

***Discolouration of aluminium tracks in this area post ohmic anneal.
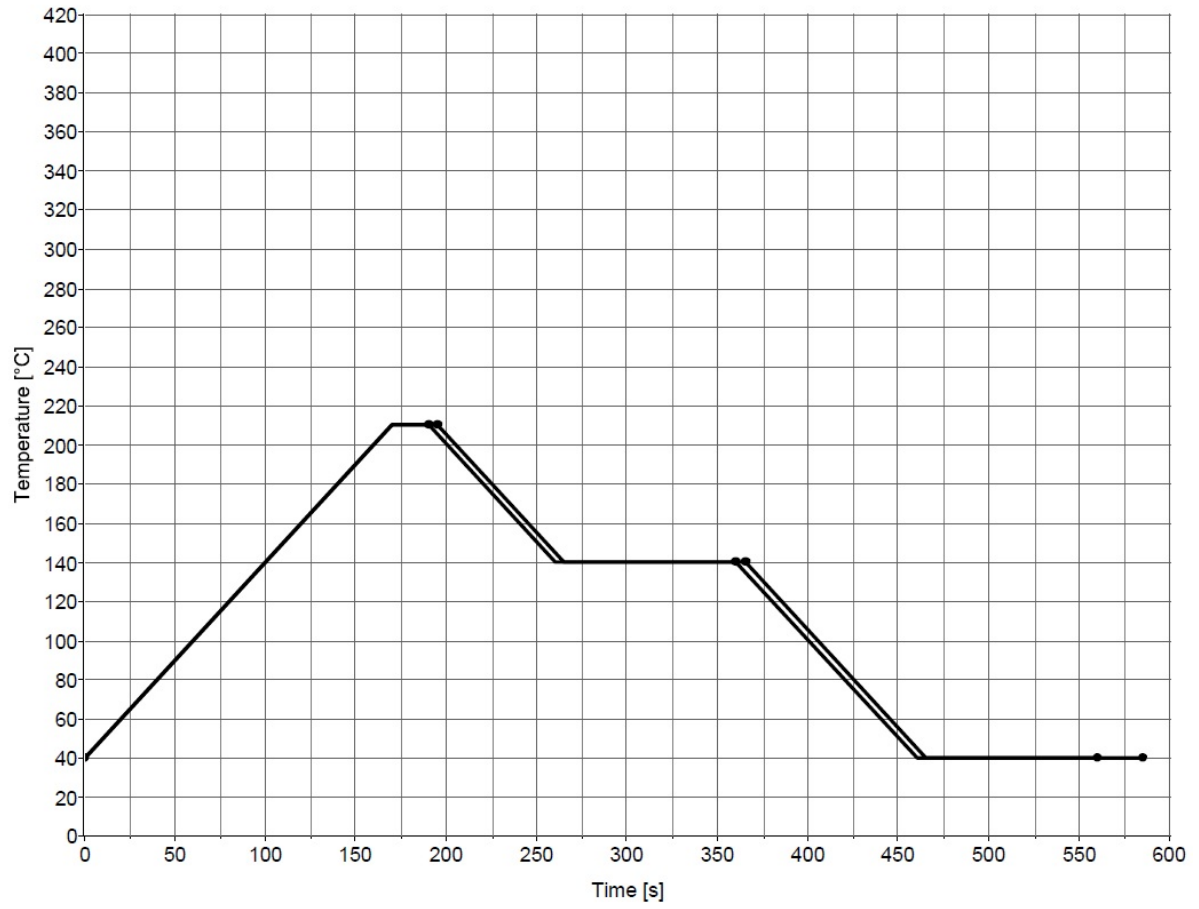
Appendix A 2 Configuration of thermal curing profile for ACA

# Appendix A 3 Simulation codes

```
/title, Silicon 4-Terminal Sensor w/Downward force
application
    *Do,GlobalVar,0,2,1
    !Parsav,all,parameters,,
    !/clear,nostart
    !Parres,change,parameters,,
/prep7
!* Silicon Contact Pressure Plate (Using uMKSV units)
!* Piezo Material Properties & Element Definition
!* Element Definition (p-type Si)
ET,1,SOLID227,101        !20 Node Tetrahedral Piezo
!* Stiffness (MPa)
c11= 16.57e4
c12= 6.39e4
c44= 7.96e4
tb,ANEL,1,,0
tbdata,1,c11,c12,c12
tbdata,7,c11,c12
tbdata,12,c11
tbdata,16,c44
tbdata,19,c44
tbdata,21,c44
!* Resistivity (TOhm*m)
mp,RSVX,1,7.8e-8
!* Piezoresistive Stress (MPa)^(-1)
p11= 6.5e-5
p12= -1.1e-5
p44= 138e-5
tb,PZRS,1
tbdata,1,p11,p12,p12
tbdata,7,p12,p11,p12
tbdata,13,p12,p12,p11
tbdata,22,p44
tbdata,29,p44
tbdata,36,p44
!********************************************
!* Silicon Material Properties & Element Definition
!********************************************
    ET,2,SOLID187
!* Stiffness (MPa)
c11= 16.57e4
c12= 6.39e4
c44= 7.96e4
tb,ANEL,2,,0
tbdata,1,c11,c12,c12
tbdata,7,c11,c12
tbdata,12,c11
tbdata,16,c44
tbdata,19,c44
tbdata,21,c44
ET,3,SOLID187
MP,EX,3,50              ! Young's Modulus
MP,PRXY,3,0.3
    !********************
!* Geometry Definition  for Piezoresistive simulation
!********************
/prep7
SilW = 500                    !Base square width
```

```
SilH = 300                    !Base square height
MembW = 300                   !Membrane cutout
    MembH = 290               !Membrane cutout
    L = 65                    !Piezoresistor
Length
W = 40          !Piezoresistor Width
b = 10                        !Signal arm width,
    a = 10                            !Signal
arm length,
    PieD = 5                  !Piezoresistor
depth, um
BLC5,0,0,SilW,SilW,SilH       !Define silicon
                              !Cut out material
    MemRad = 175
MemHeight = 290
CYL4,0,0,MemRad,,,,MemHeight
!VGEN,,2,,,,,MembD,,,1 !use with cyl/blc
VSBV,1,2
    !******Build the piezoresistor **************
    local,11
local,12,0,0,MemRad-20,SilH,45  !Coordinate systems for
piezo bit
    local,17,0,0,MemRad-20+5000,SilH,45
    local,18,0,5000,MemRad-20,SilH,45
    local,19,0,5000,MemRad-20+5000,SilH,45
    !Coordinate system for silicon
local,16,0,0,0,0,45
    !Pad 1 Keypoints
csys,12
    WPCSYS,-1,12,
k,101,-W/2,-L/2
k,102,W/2,-L/2
k,103,W/2,-b/2
k,104,W/2+a,-b/2
k,105,W/2+a,b/2
k,106,W/2,b/2
k,107,W/2,L/2
k,108,-W/2,L/2
k,109,-W/2,b/2
k,110,-W/2-a,b/2
k,111,-W/2-a,-b/2
k,112,-W/2,-b/2
a,101,102,103,104,105,106,107,108,109,110,111,112
    VOFFST,1,-PieD              !make pad areas
into volumes
    VOVLAP,ALL            !Overlap volume command
    !Build Mesa
local,13,0,0,0,-10
    wpcsys,-1,13
MesaR = 50
MesaH = 300
CYL4,0,0,MesaR,,,,MesaH
    vadd,2,3      !get volume 4
    !**********************
    !build array
    !**************************
    wpcsys,-1,11
Vsel,s,volu,,1,,,
    vsel,a,volu,,4,4,,
```

189

```
    Offset=5000                                          ESYS,16                    !Mesh
    vgen,2,all,,,0,Offset,0                          Piezoresistors
    vgen,2,1,4,,1*Offset,0,0 ! It will select all volumes    TYPE,1
after generating new ones.                           MAT,1
!*******************                                  ESIZE,MeshSizPie
!* Geometry Definition  for Mechanical simulation     VMESH,1
!*******************                                      TYPE,1
    BLC5,-Offset,0,SilW,SilW,SilH          !Define    MAT,1
silicon Base                                         ESIZE,MeshSizPie
CYL4,-Offset,0,MemRad,,,,MemHeight                   VMESH,2
!VGEN,,2,,,,,MembD,,,1 !use with cyl/blc                 TYPE,1
VSBV,9,10           !Cut out material                MAT,1
    local,14,0,-Offset,0,-10! from z original offset 10um    ESIZE,MeshSizPie
    wpcsys,-1,14                                      VMESH,5
CYL4,0,0,MesaR,,,,MesaH                                  TYPE,1
    vadd,9,11                                         MAT,1
    !****** Build sensor array for Mechanical         ESIZE,MeshSizPie
***********************                               VMESH,6
    vgen,2,10,,,0,Offset,0                               TYPE,2
    vgen,2,10,,,0,2*Offset,0                         MAT,2
    vgen,2,10,,,0,-Offset,0                          ESIZE,SilW/MeshDiv
    vgen,2,10,,,Offset,2*Offset,0                    VMESH,3,2
    vgen,2,10,,,Offset,-Offset,0                        TYPE,2
    vgen,2,10,,,2*Offset,-Offset,0                   MAT,2
    vgen,2,10,,,2*Offset,2*Offset,0                  ESIZE,SilW/MeshDiv
    vgen,2,10,,,3*Offset,2*Offset,0                  VMESH,4,1
    vgen,2,10,,,3*Offset,Offset,0                       TYPE,2
    vgen,2,10,,,3*Offset,0,0
    vgen,2,10,,,3*Offset,-Offset,0                      MAT,2
    !***************************                      ESIZE,SilW/MeshDiv
    ! build film                                        VMESH,7,5
    !***************************                         TYPE,2
    wpcsys,-1,13                                     MAT,2
    FilW=Offset*3+SilW                               ESIZE,SilW/MeshDiv
    FilH=500                                         VMESH,8,6
    CenterX=FilW/2-Offset-SilW/2                        TYPE,2
    CenterY=CenterX                                  MAT,2
    blc5,CenterX,CenterY,FilW,FilW,-FilH             ESIZE,SilW/MeshDiv
    !****build a cylinder for even meshing at pressure    VMESH,9,19
region                                                  TYPE,2
    !***********************                          MAT,2
    PressMoveX=500*GlobalVar                         ESIZE,SilW/MeshDiv
    !PressMoveY=288.645*10                           VMESH,20
    PressMoveY=500*GlobalVar                            Type,3
    !PressOffset=PressMoveX+Offset                      Mat,3
                                                        Mopt,expnd,1
    csys,11                                             !Smrtsize,2
    local,40,0,Offset-PressMoveX,Offset-PressMoveY,-    Esize,FilH/2
10      !Coordinate for applying pressure               vmesh,23
    wpcsys,-1,40                                        Type,3
    CYL4,0,0,3000,,,,                                   Mat,3
    voffset,255,-FilH                                   Mopt,expnd,1
    vovlap,21,22                                        !Smrtsize,2
    Vglue,7,23                                          Esize,FilH/2
    !vglue,11,19                                        vmesh,24
    !***************************                         !***************************
!* Meshing                                           !* Boundary Condition Application
!***************************                          !***************************
    MeshSizPie=5                                         csys,11
    MeshSizPie2=10                                   nsel,s,loc,z,SilH
    MeshDiv=25                                       nsel,u,loc,x,-SilW/2+100,SilW/2-100
                                                         nsel,u,loc,x,-SilW/2+100+Offset,SilW/2-100+Offset
```

190

```
    nsel,u,loc,x,-SilW/2+100-Offset,SilW/2-100-Offset
    nsel,u,loc,x,-SilW/2+100+2*Offset,SilW/2-
100+2*Offset
    nsel,u,loc,y,-SilW/2+100,SilW/2-100
    nsel,u,loc,y,-SilW/2+100+Offset,SilW/2-100+Offset
    nsel,u,loc,y,-SilW/2+100-Offset,SilW/2-100-Offset
    nsel,u,loc,y,-SilW/2+100+2*Offset,SilW/2-
100+2*Offset
    d,all,all,0
    !*******Left bottom sensor coord 12
************Zero Voltage Conditions
csys,12
    nsel,s,loc,y,-L/2
nsel,r,loc,x,-W/2,W/2
nsel,r,loc,z,0,D
d,all,volt,0
    !Source (3V) Voltage Conditions
csys,12
    nsel,s,loc,y,L/2
nsel,r,loc,x,-W/2,W/2
nsel,r,loc,z,0,D
d,all,volt,3
    !Get Sensor Output Nodes
!Sensor 1 Left
csys,12
nsel,s,loc,x,-W/2-a
nsel,r,loc,y,-b/2,b/2
nsel,r,loc,z,0,D
cp,11,volt,all
*get,nL1,node,0,num,min
nsel,all
!Sensor 1 Right
nsel,s,loc,x,W/2+a
nsel,r,loc,y,-b/2,b/2
nsel,r,loc,z,0,D
cp,12,volt,all
*get,nR1,node,0,num,min
nsel,all
    !*********Left top sensor coord
17***************Zero Voltage Conditions
csys,17
    nsel,s,loc,y,-L/2
nsel,r,loc,x,-W/2,W/2
nsel,r,loc,z,0,D
d,all,volt,0
    !Source (3V) Voltage Conditions
csys,17
    nsel,s,loc,y,L/2
nsel,r,loc,x,-W/2,W/2
nsel,r,loc,z,0,D
d,all,volt,3
    !Get Sensor Output Nodes
!Sensor 1 Left
csys,17
nsel,s,loc,x,-W/2-a
nsel,r,loc,y,-b/2,b/2
nsel,r,loc,z,0,D
cp,13,volt,all
*get,nL2,node,0,num,min
nsel,all
!Sensor 1 Right
nsel,s,loc,x,W/2+a

    nsel,r,loc,y,-b/2,b/2
nsel,r,loc,z,0,D
cp,14,volt,all
*get,nR2,node,0,num,min
nsel,all
    !*********Right bottom sensor coord
    !***************Zero Voltage Conditions
csys,18
    nsel,s,loc,y,-L/2
nsel,r,loc,x,-W/2,W/2
nsel,r,loc,z,0,D
d,all,volt,0
    !Source (3V) Voltage Conditions
csys,18
    nsel,s,loc,y,L/2
nsel,r,loc,x,-W/2,W/2
nsel,r,loc,z,0,D
d,all,volt,3
    !Get Sensor Output Nodes
!Sensor 1 Left
csys,18
nsel,s,loc,x,-W/2-a
nsel,r,loc,y,-b/2,b/2
nsel,r,loc,z,0,D
cp,15,volt,all
*get,nL3,node,0,num,min
nsel,all
!Sensor 1 Right
nsel,s,loc,x,W/2+a
nsel,r,loc,y,-b/2,b/2

    nsel,r,loc,z,0,D
cp,16,volt,all
*get,nR3,node,0,num,min
nsel,all
    !*********Right top senso coord csys,19
    nsel,s,loc,y,-L/2
nsel,r,loc,x,-W/2,W/2
nsel,r,loc,z,0,D
d,all,volt,0
    !Source (3V) Voltage Conditions
csys,19
nsel,s,loc,y,L/2
nsel,r,loc,x,-W/2,W/2
nsel,r,loc,z,0,D
d,all,volt,3
    !Get Sensor Output Nodes
!Sensor 1 Left
csys,19
nsel,s,loc,x,-W/2-a
nsel,r,loc,y,-b/2,b/2
nsel,r,loc,z,0,D
cp,17,volt,all
*get,nL4,node,0,num,min
nsel,all
!Sensor 1 Right
nsel,s,loc,x,W/2+a
nsel,r,loc,y,-b/2,b/2
nsel,r,loc,z,0,D
cp,18,volt,all
*get,nR4,node,0,num,min
nsel,all
```

```
    !*****************fix edge of the film
    Csys,11
    Nsel,s,loc,x,-(FilW/2-CenterX)-1000,-(FilW/2-
CenterX),
    !d,all,all,0
    D,all,UZ,0
    Nsel,s,loc,y,-(FilW/2-CenterY)-1000,-(FilW/2-
CenterY),
    !d,all,all,0
    d,all,UZ,0
    Csys,11
    Nsel,s,loc,x,(FilW/2+CenterX),(FilW/2+CenterX)+100
0,
    !d,all,all,0
    D,all,UZ,0
    Csys,11
    Nsel,s,loc,y,(FilW/2+CenterY),(FilW/2+CenterY)+100
0,
    !d,all,all,0
    D,ALL,UZ,0
    !*********************Pressure applied
    !***choose the circular region
    Local,30,0,-PressMoveX+Offset,Offset-PressMoveY,0
    wpcsys,-1,30
    CSWPLA,30,CYLIN
    nsel,s,loc,x,0,3000
    nsel,u,loc,z,-(FilH-10),FilH
    *get,nC1,node,0,count
/com, NN = %(nC1)%
F,ALL,FZ,(100E3*cos(0/180*3.14159))/nC
    !F,ALL,FY,(-4000E3*sin(0/180*3.14159))/nC1
                ! nsel,all
    !*****************************
!* Solution
!*******************************
/pbc,u,,1
/pbc,volt,,1
/pbc,cp,,1
/pnum,type,1
/number,1
eplot
fini
/solu                  ! Solution
antype,static
cnvtol,volt,1,.0001        ! Optional to prevent a warning
message
solve
fini
!*******************************
!* Post Processing
!*******************************
!* Examine Voltages
/post26
    Nsol,2,nR1,voltA,
    Nsol,3,nL1,voltB,
    Nsol,4,nR2,voltC,
    Nsol,5,nL2,voltD,
    Nsol,6,nR3,voltE,
    Nsol,7,nL3,voltF,
    Nsol,8,nR4,voltG,
    Nsol,9,nL4,voltH,
    *GET,size,VARI,,NSETS
```

```
    *DIM,output2,ARRAY,size,9,1, , ,
    VGET,output2(1,1),1, ,0
    VGET,output2(1,2),2, ,0
    VGET,output2(1,3),3, ,0
    VGET,output2(1,4),4, ,0
    VGET,output2(1,5),5, ,0
    VGET,output2(1,6),6, ,0
    VGET,output2(1,7),7, ,0
    VGET,output2(1,8),8, ,0
    VGET,output2(1,9),9, ,0
    !Create txt output file, with the value of F as its name
    *CFOPEN,%5%,txt,,APPEND
    !Write the array to the file
    *VWRITE,output2(1,2),output2(1,3),output2(1,4),outp
ut2(1,5),output2(1,6),output2(1,7),output2(1,8),output2(1,9
),
    (E18.9,T20,E18.9,T40,E18.9,T60,E18.9,T80,E18.9,T1
00,E18.9,T120,E18.9,T140,E18.9,T160)
    !close file
    *CFCLOSE
    !Start over by removing all geometry and elements
    /prep7
    Vclear,all
    !Vdele,all
    Aclear,all
    Adele,all
    Lclear,all
    Ldele,all
    Kdele,all
    !*del,output2
    csdele,all
    !increment do loop
    *enddo
```

192

## Appendix A 4 Matlab® codes

```
x(isnan(x),:)=;
y(isnan(y),:)=;
% ele_list=['s1e1','s1e2','s1e3','s1e4'];
% xsqm=reshape(x,13,13)
%% group D (60,60)
s1e1=VarName4;
s1e2=VarName5;
s1e3=VarName6;
s1e4=VarName7;
%% group A (0, 60)
s2e1=VarName8;
s2e2=VarName9;
s2e3=VarName10;
s2e4=VarName11;
%% group B  (0,0)
s3e1=VarName14;%%%broken element
s3e2=VarName13;
s3e3=VarName14;
s3e4=VarName15;

%% group C (60,0)
s4e1=VarName16;
s4e2=17;
s4e3=VarName18;
s4e4=VarName19;

% %  eliminate the NAN in the matrix
s1e1(isnan(s1e1),:)=[];
s1e2(isnan(s1e2),:)=[];
s1e3(isnan(s1e3),:)=[];
s1e4(isnan(s1e4),:)=[];

s2e1(isnan(s2e1),:)=[];
s2e2(isnan(s2e2),:)=[];
s2e3(isnan(s2e3),:)=[];
s2e4(isnan(s2e4),:)=[];

s3e1(isnan(s3e1),:)=[];
s3e2(isnan(s3e2),:)=[];
s3e3(isnan(s3e3),:)=[];
s3e4(isnan(s3e4),:)=[];

s4e1(isnan(s4e1),:)=[];
s4e2(isnan(s4e2),:)=[];
s4e3(isnan(s4e3),:)=[];
s4e4(isnan(s4e4),:)=[];


% % reshape the vector to a square matrix
s1e1=reshape(s1e1,13,13);
s1e2=reshape(s1e2,13,13);
s1e3=reshape(s1e3,13,13);
s1e4=reshape(s1e4,13,13);

s2e1=reshape(s2e1,13,13);
s2e2=reshape(s2e2,13,13);
s2e3=reshape(s2e3,13,13);
s2e4=reshape(s2e4,13,13);

s3e1=reshape(s3e1,13,13);
s3e2=reshape(s3e2,13,13);
s3e3=reshape(s3e3,13,13);
s3e4=reshape(s3e4,13,13);

s4e1=reshape(s4e1,13,13);
s4e2=reshape(s4e2,13,13);
s4e3=reshape(s4e3,13,13);
s4e4=reshape(s4e4,13,13);
```

```
    s1eabs=abs(s1e1)+abs(s1e2)+abs(s1e3)+abs(
s1e4);
    s1eabs=s1eabs/4;
    s2eabs=abs(s2e1)+abs(s2e2)+abs(s2e3)+abs(
s2e4);
    s2eabs=s2eabs/4;
    s3eabs=abs(s3e1)+abs(s3e2)+abs(s3e3)+abs(
s3e4);
    s3eabs=s3eabs/4;
    s4eabs=abs(s4e1)+abs(s4e2)+abs(s4e3)+abs(
s4e4);
    s4eabs=s4eabs/4;
    % %  build a 3 dimensinal matrix to store
the benchmark matrice
    % % which including the sum of absolute
value of voltages
    % % standing for the characterization
matrices
    rr=rand(13,13,16);
    rr(:,:,1)=s1e1(:,:);
    rr(:,:,2)=s1e2(:,:);
    rr(:,:,3)=s1e3(:,:);
    rr(:,:,4)=s1e4(:,:);

    rr(:,:,5)=s2e1(:,:);
    rr(:,:,6)=s2e2(:,:);
    rr(:,:,7)=s2e3(:,:);
    rr(:,:,8)=s2e4(:,:);

    rr(:,:,9)=s3e1(:,:);
    rr(:,:,10)=s3e2(:,:);
    rr(:,:,11)=s3e3(:,:);
    rr(:,:,12)=s3e4(:,:);

    rr(:,:,13)=s4e1(:,:);
    rr(:,:,14)=s4e2(:,:);
    rr(:,:,15)=s4e3(:,:);
    rr(:,:,16)=s4e4(:,:);

    % % rr store the benchmark matrice
    tt=rand(4,4);
    % bar3_stacked(rr4(:,:,1));
    impua=importdata('U A test.xlsx');
    % % impua.Sheet1(1,3); m stans for row, n
stands for column (m, n)
    % % size(impua.Sheet1(:,1))   [5000, 1]
    % % size(impua.Sheet1(:,:))   [5000,17]
V1..V16 plus smaple number

    %% contains a broken signal
    y1=impua.Sheet1(1:5000,2)-
mean(impua.Sheet1(1:20,2));
    y2=impua.Sheet1(1:5000,3)-
mean(impua.Sheet1(1:20,3));
    y3=impua.Sheet1(1:5000,4)-
mean(impua.Sheet1(1:20,4));
    y4=impua.Sheet1(1:5000,5)-
mean(impua.Sheet1(1:20,5));

    y5=impua.Sheet1(1:5000,6)-
mean(impua.Sheet1(1:20,6));
    y6=impua.Sheet1(1:5000,7)-
mean(impua.Sheet1(1:20,7));
    y7=impua.Sheet1(1:5000,8)-
mean(impua.Sheet1(1:20,8));
    y8=impua.Sheet1(1:5000,9)-
mean(impua.Sheet1(1:20,9));

    y9=impua.Sheet1(1:5000,10)-
mean(impua.Sheet1(1:20,10));
```

```matlab
    y10=impua.Sheet1(1:5000,11)-
mean(impua.Sheet1(1:20,11));
    y11=impua.Sheet1(1:5000,12)-
mean(impua.Sheet1(1:20,12));
    y12=impua.Sheet1(1:5000,13)-
mean(impua.Sheet1(1:20,13));

    y13=impua.Sheet1(1:5000,14)-
mean(impua.Sheet1(1:20,14));
    y14=impua.Sheet1(1:5000,15)-
mean(impua.Sheet1(1:20,15));
    y15=impua.Sheet1(1:5000,16)-
mean(impua.Sheet1(1:20,16));
    y16=impua.Sheet1(1:5000,17)-
mean(impua.Sheet1(1:20,17));

    % %  y1-y4 sensor 3 ,broken y2
    plot(y1(1:4900))
    hold on
    plot(y2(1:4900))
    plot(y3(1:4900))
    plot(y4(1:4900))
    plot(y5(1:4900))
    hold on
    plot(y6(1:4900))
    plot(y7(1:4900))
    plot(y8(1:4900))
    plot(y9(1:4900))
    hold on
    plot(y10(1:4900))
    plot(y11(1:4900))
    plot(y12(1:4900))
    plot(y13(1:4900))

    plot(y14(1:4900))
    plot(y15(1:4900))
    plot(y16(1:4900))


    trilb=tril(ones(13,13));
    % % flip(trilb)
    trirt=triu(ones(13,13));
    trirb=flip(trirt);
    % % qua=and(trilb,trirt);
    rr12=rand(13,13,12);
    rr12(:,:,1:4)=rr4;
    quotient=zeros(13,13);
    quotient1=rr4(:,:,1);
    quotient2=rr4(:,:,2);
    quotient3=rr4(:,:,3);
    %% calculate the voltage quotient, using
the largest outputs divided by
    %% the smaller 3 voltages, this will
generate large numbers
    %% make the benchmark matrices more
irregular
    for i=1:13
        for j=1:13

quotient12(i,j)=quotient1(i,j)/quotient2(i,j
);
        end
    end
    % for i=1:13
    %     for j=1:13
    %
quotient12(i,j)=quotient12(i,j)*trirb(i,j);
    %     end
    % end
    quotient1=rr4(:,:,1);
    quotient4=rr4(:,:,4);

    for i=1:13
        for j=1:13

quotient14(i,j)=quotient(i,j)/quotient2(i,j)
;
        end
    end
    for i=1:13
        for j=1:13

quotient13(i,j)=quotient(i,j)/quotient3(i,j)
;
        end
    end

    % for i=1:13
    %     for j=1:13
    %
quotient14(i,j)=quotient14(i,j)*trirb(i,j);
    %     end
    % end
    zeromat=zeros(6,13);
    quotient12(1:6,:)=zeros(6,13);%% chop the
matrice to a quater;
    quotient12(:,1:6)=zeros(13,6);
    quotient14(1:6,:)=zeros(6,13);%% chop the
matrice to a quater;
    quotient14(:,1:6)=zeros(13,6);
    quotient13(1:6,:)=zeros(6,13);%% chop the
matrice to a quater;
    quotient13(:,1:6)=zeros(13,6);

    % % quotient41
    % % quotient43
    for i=1:13
        for j=1:13

quotient41(i,j)=quotient4(i,j)/quotient1(i,j
);
        end
    end
    for i=1:13
        for j=1:13

quotient43(i,j)=quotient4(i,j)/quotient3(i,j
);
        end
    end

    for i=1:13
        for j=1:13

quotient42(i,j)=quotient4(i,j)/quotient2(i,j
);
        end
    end
    quotient41(8:13,:)=zeros(6,13);%% chop
the matrice to a quater;
    quotient41(:,1:6)=zeros(13,6);
    quotient43(8:13,:)=zeros(6,13);%% chop
the matrice to a quater;
    quotient43(:,1:6)=zeros(13,6);
    quotient42(8:13,:)=zeros(6,13);%% chop
the matrice to a quater;
    quotient42(:,1:6)=zeros(13,6);

    % % quotient34
    % % quotient32
```

```matlab
    for i=1:13
        for j=1:13

quotient34(i,j)=quotient3(i,j)/quotient4(i,j
);
        end
    end
    for i=1:13
        for j=1:13

quotient32(i,j)=quotient3(i,j)/quotient2(i,j
);
        end
    end

    for i=1:13
        for j=1:13

quotient31(i,j)=quotient3(i,j)/quotient1(i,j
);
        end
    end

    quotient34(8:13,:)=zeros(6,13);%% chop
the matrice to a quater;
    quotient34(:,8:13)=zeros(13,6);
    quotient32(8:13,:)=zeros(6,13);%% chop
the matrice to a quater;
    quotient32(:,8:13)=zeros(13,6);
    quotient31(8:13,:)=zeros(6,13);%% chop
the matrice to a quater;
    quotient31(:,8:13)=zeros(13,6);

    % % quotient23
    % % quotient21
    for i=1:13
        for j=1:13

quotient23(i,j)=quotient2(i,j)/quotient3(i,j
);
        end
    end
    for i=1:13
        for j=1:13

quotient21(i,j)=quotient2(i,j)/quotient1(i,j
);
        end
    end

    for i=1:13
        for j=1:13

quotient24(i,j)=quotient2(i,j)/quotient4(i,j
);
        end
    end
    quotient23(1:6,:)=zeros(6,13);%% chop the
matrice to a quater;
    quotient23(:,8:13)=zeros(13,6);
    quotient21(1:6,:)=zeros(6,13);%% chop the
matrice to a quater;
    quotient21(:,8:13)=zeros(13,6);
    quotient24(1:6,:)=zeros(6,13);%% chop the
matrice to a quater;
    quotient24(:,8:13)=zeros(13,6);
    rr16=rand(13,13,12);
    rr16(:,:,1:4)=rr4;
    rr16(:,:,5)=quotient12;
    rr16(:,:,6)=quotient14;
    rr16(:,:,7)=quotient23;
    rr16(:,:,8)=quotient21;
    rr16(:,:,9)=quotient34;
    rr16(:,:,10)=quotient32;
    rr16(:,:,11)=quotient41;
    rr16(:,:,12)=quotient43;
    rr16(:,:,13)=quotient13;
    rr16(:,:,14)=quotient24;
    rr16(:,:,15)=quotient31;
    rr16(:,:,16)=quotient42;


    %% observe the sum of bmmat 1 and 2 in
voltages
    rrtest=zeros(13,13);
    % rrtest=rr4(:,:,4)+rr4(:,:,1);
    for i=1:13
        for j=1:13

rrtest(i,j)=rr4(i,j,4)+rr4(i,j,1);
        end
    end
    bar3(rrtest);


    %% assemble the four curve surface as
data flow
    rr4=rand(13,13,4);
    rr4(:,:,1)=s4eabs(:,:)';  %%
    rr4(:,:,2)=s1eabs(:,:);
    rr4(:,:,3)=s2eabs(:,:)';
    rr4(:,:,4)=s3eabs(:,:);
    rr4org=rr4;

    rr4(:,:,1)=flip(flip(rr4(:,:,1))');
    rr4(:,:,2)=rr4(:,:,2)';
    rr4(:,:,3)=flip(flip(rr4(:,:,3))');
    rr4(:,:,4)=rr4(:,:,4)';

    Amax=max(max(rr4(:,:,1)));
    Bmax=max(max(rr4(:,:,2)));
    Cmax=max(max(rr4(:,:,3)));
    Dmax=max(max(rr4(:,:,4)));
    %% all voltages are elevated to the same
level of Amax
    rr4(:,:,2)=Cmax/Bmax*rr4(:,:,2);
    rr4(:,:,1)=Cmax/Amax*rr4(:,:,1);
    rr4(:,:,4)=Cmax/Dmax*rr4(:,:,4);
    % % rr4(:,:,:)
    % % rr4 store the location benchmark
matrice
    bar3_stacked(rr4);


    %% using voltage as key
    bmmat=formbmmat(rr4);
    bmmat2=formbmmat2(rr4);
    %%
    rrtest=zeros(13,13);
    % rrtest=rr4(:,:,4)+rr4(:,:,1);
    for i=1:13
        for j=1:13

rrtest(i,j)=bmmat(i,j,5)+bmmat(i,j,6);
        end
    end
    bar3(rrtest(1:7,1:7));
[X,Y]=volt2xy2(y5,y6,y7,y8,y9,y10,y11,y12,y1
3,y14,y15,y16,y1,y2,y3,y4,bmmat,Amax,Bmax,Cm
ax,Dmax);
```

```matlab
    plot(X(1250:3200),Y(1250:3200),'ro');
    % X(find(X),:)=1;
    % Y(find(Y),:)=1;
    [fxid,fyid,forcemat]=xy2force(y5,y6,y7,y8
,y9,y10,y11,y12,y13,y14,y15,y16,y1,y2,y3,y4,
X,Y,bmmat,rr4org);
    %
scatter3(fxid(find(fxid)),fyid(find(fyid)),f
orcemat(find(forcemat)));
    % hold on
    %
plot(fxid(find(fxid)),fyid(find(fyid)),'ro')
;
    force=calavg(fxid(find(fxid)),fyid(find(f
yid)),forcemat(find(forcemat)));
    force=force';
    bforce=bar3(force);
    colorbar
    for k = 1:length(bforce)
        zdata = bforce(k).ZData;
        bforce(k).CData = zdata;
        bforce(k).FaceColor = 'interp';
    end
```